NANOSCALE MECHANICS OF DISORDERED BIOMOLECULES IN BRAIN

by

MD ISHAK KHAN

DISSERTATION

Submitted in partial fulfillment of the requirements

for the degree of Doctor of Philosophy in Mechanical Engineering at

The University of Texas at Arlington

December, 2020

Arlington, Texas

Supervising Committee:

Ashfaq Adnan, Supervising Professor

Kent Lawrence

Hyejin Moon

Md Rassel Raihan

Sheikh Fahad Ferdous

ABSTRACT

NANOSCALE MECHANICS OF DISORDERED BIOMOLECULES IN BRAIN

Md Ishak Khan, Ph.D.

The University of Texas at Arlington, 2020

Supervising Professor: Ashfaq Adnan

The long-term objective of this dissertation is to link blast-induced traumatic brain injury (TBI) with multiscale, multiphysics damage evolution in the brain using experimentally verifiable computations and simulations. The short-term goal is to conduct modeling and simulation to correlate dynamic mechanical loading to damage in sub-axonal components. It is known that the interior of the brain at the macroscale (10^{-1} m) is composed of two distinct components, the grey matter, and the white matter. Within the cortex, the grey matter primarily takes the form of cortical columns (mesoscale: 10^{-3} m), which are six layered structures, each composed of 8-10 thousand neurons with unmyelinated axons. White matter, on the other hand, consists of the myelinated axons structured as fiber tracts, whose cell bodies are in the grey matter. Structurally, a single neuron (microscale: 10^{-6} m) is composed of a soft cell body (soma), fibrous dendrite branches, and an axon fiber. Both axons and dendrites are supported by the cytoskeleton (nanoscale: 10-9 m), which is primarily composed of neurofilaments, microfilaments, tau proteins and microtubules. As such, strain rate dependent studies are particularly important for characterizing cytoskeletal components and hence obtaining molecular level insight on neurological disorder and/or damage, such as Traumatic Brain Injury (TBI). Of all the elements of the cytoskeleton, tau protein and NF lacks understanding due to presence of unstructured portions in the structure. Due to the length scale of cytoskeletal components, they

are suitable for molecular level computational studies. In this thesis, we have developed reliable predicted structures for the disordered molecules such as tau protein and neurofilaments. Then we have captured the stress-strain response of tau protein, neurofilaments, actin, spectrin, and actin-spectrin interaction model under different mechano-biological scenario.

In the first study, we have shown the effect of strain rate on single tau, dimerized tau, and tau-MT interface interaction. In the second study, we have incorporated domain and residue focused phosphorylation in tau. Therefore, this study addresses the behavior of tau according to the phosphorylated state and attempts to find out the effect of this post-translational modification. The first and second studies have successfully provided crucial insights regarding rate dependent aspects of tau, and structural and chemical response of this cytoskeletal component. In the third study, we have performed similar strain rate dependent tests on the sidearms of NF isoforms. The fourth study has taken tau and NF studies further and characterized tau and NF behavior by fitting their relaxation data to established viscoelastic models. In the fifth study, high strain rate response of actin, spectrin, and actin-spectrin interaction model have been determined.

Based on the five studies performed, we have particularly enhanced the existent computational model, which does not include all elements of axon such as tau protein and NFs. Furthermore, we have also aided the finite element modeling of axon model, as due to the inclusion of the insight and deformation aspects of tau protein and NFs it will be more realistic and comprehensive. Therefore, our study is impactful in the sense is that it will pave the pathway to develop a bottom up approach of computational axon modeling.

ACKNOWLEDGEMENTS

I am grateful to Dr. Ashfaq Adnan for providing helpful supervision throughout my PhD. My sincere thanks to Dr. Kent Lawrence, Dr. Hyejin Moon, and Dr. Rassel Raihan for their valuable insights regarding my thesis, Dr. Sheikh Fahad Ferdous for insight regarding the actin and spectrin modeling, Dr. Kathleen Gilpin for insight regarding behavior of intrinsically disordered proteins (IDPs), and Dr. Jun Liao for providing access to Simpleware ScanIP software. Also, my acknowledgement goes to the Office of Naval Research (ONR) for funding the research, and Texas Advanced Computing Center (TACC) for providing the high-performance service units. Finally, I owe Multiscale Mechanics and Physics Laboratory (MMPL) members for insight regarding Molecular Dynamics (MD) and Finite Element Analysis (FEA) concepts.

DEDICATION

To my loving wife Oishi and daughter Sameerah.

LIST OF FIGURES

Figure No.	Figure Caption	Page No.
1.1	A simplified classification of biopolymers.	1
1.2	Protein types in cytoskeleton.	2
1.3	MT structure showing helically arranged repetitive α and β-tubulin subunits.	6
1.4	Tau protein interacting with MT.	12
1.5	NF isoforms.	16
1.6	Globular actin (G-actin), which is the structural unit of MF, and the filamentous actin (F-actin) which is formed by polymerization of G-actin.	19
1.7	Atomic model of filamentous actin (F-actin).	20
2.1	Stress vs strain plot of single tau projection domain.	42
2.2	Single tau unfolding and stretching.	43
2.3	Stress vs strain plot of dimerized tau.	45
2.4	Stages observed during the pull of one protein in the dimerized tau model.	46
2.5	Stress vs strain graph and potential energy graph for the tau-MT system.	49
2.6	Observation during the pulling of single tau towards the –x direction away from MT surface.	50
2.7	Stress vs strain graph and potential energy graph for the dimer-MT system.	53
2.8	Observation during the dimerized tau pulling away from MT surface.	54
3.1a	Stress vs strain plot of single tau projection domain.	76
3.1b	Different stages of the tensile test on single tau.	79
3.2a	Stress vs strain graph and potential energy for dimerized tau.	81
3.2b	Stages observed during the pull of one protein in the dimerized tau model.	82
3.3a	Stress vs strain graph and potential energy graph for the tau-MT system.	87

3.3b	Observation during pulling of tau along –x direction away from tubulin surface.	88
3.4a	Stress vs strain graph and potential energy graph for the tau-MT system (residue focused phosphorylation).	92
3.4b	Stages observed during the pull of one protein in the tau-MT model.	93
3.5b	Snapshots of different times during the 1ns NVT equilibration for normal and phosphorylated tau.	97
3.5c	Projection domain mass center distance of the proteins as a function of time.	101
4.1	Stress vs strain graphs at two strain rates for the pulled tail domain of a. NFL, b. NFH.	120
4.2	Snapshots at different timesteps during the tensile test performed on NFL and NFH.	121
4.3	Potential energy vs time for NFL and NFH during the entire equilibration time (1ns).	123
4.4	Overall mass center distance and sidearm mass center distance for a. NFL, b. NFH.	123
4.5	Snapshots at different timesteps during equilibration (accumulation test).	125
5.1	Pre-relaxation stretching for tau protein.	136
5.2	Modulus, E(t) vs time for 1ns relaxation tests for tau protein.	137
5.3	Fitting the E(t) vs time curve of the tau relaxation test data to 3 parameter Maxwell model.	137
5.4	Determining G(t) and B(t) for the assumed Poisson’s ratios for tau protein.	139
5.5	Pre-relaxation stretching for NFL.	142
5.6	Modulus, E(t) vs time for 1ns relaxation tests for NFL.	143

5.7	Fitting the E(t) vs time curve of the NFL relaxation test data to 3 parameter Maxwell model.	143
5.8	Determining G(t) and B(t) for the assumed Poisson's ratios for NFL.	145
6.1	Different Domains of G-actin and F-actin formed by polymerization.	151
6.2	Actin filament decoration with cofilin.	155
6.3	Depiction of forced unfolding of spectrin.	161
6.4	Representation of actin-spectrin network.	163
6.5	Stress-strain response of 6-actin system for two strain rates.	172
6.6	Snapshots of tensile test on 6-actin system at strain rate $1x10^{8}s^{-1}$.	173
6.7	Snapshots of tensile test on 6-actin system at strain rate $1x109s^{-1}$.	174
6.8	Stress-strain response of 12-actin system for two strain rates.	176
6.9	Snapshots of tensile test on 12-actin system at strain rate $1x10^{8}s^{-1}$.	177
6.10	Snapshots of tensile test on 12-actin system at strain rate $1x109s^{-1}$.	178
6.11	Stress-strain response of α-spectrin system for two strain rates.	179
6.12	Snapshots of tensile test on α-spectrin system at strain rate $1x10^{8}s^{-1}$.	180
6.13	Snapshots of tensile test on α-spectrin system at strain rate $1x10^{9}s^{-1}$.	181
6.14	Stress-strain response of β-spectrin system for two strain rates.	182
6.15	Snapshots of tensile test on β-spectrin system at strain rate $1x10^{8}s^{-1}$.	182
6.16	Snapshots of tensile test on β-spectrin system at strain rate $1x10^{9}s^{-1}$.	183
6.17	Actin-spectrin interaction at strain rate $1x10^{8}s^{-1}$.	185
6.18	Actin-spectrin interaction at strain rate $1x10^{9}s^{-1}$.	188
7.1	Viscoelastic shear lag model.	197
7.2	FEM axon model under construction.	198
7.3	Determination of damage-prone areas in an FEM model of cerebral cortex.	199
A1.1	Predicted tau protein structure models from i-TASSER.	205

A2.1	Equilibration: Potential energy vs time.	209
A2.2	Equilibration: Structural snapshot of the tau protein.	210
A2.3	Tensile test: Stress vs strain and energy plots.	211
A2.4	Cartoon representation of the PDB file of the initial structure.	212
A2.5	Tensile test: Structural snapshot of the tau protein.	212
A2.6	Comparison between the explicit and implicit system stress-strain relation.	218
A3.1	Potential energy vs time for two models.	220
A3.2	Stress vs strain for two models.	221
A4.1	Dimerized tau: potential energy vs time for the domain phosphorylated systems.	222
A4.2	Tau-MT interaction: potential energy vs time for the domain phosphorylated systems.	223
A4.3	Tau-MT interaction: potential energy vs time for the residue phosphorylated systems.	223
A4.4	Tau accumulation test: 2 tau system: potential energy vs time during the 1ns equilibration.	224
A4.5	Tau accumulation test: 3 tau system: potential energy vs time during the 1ns equilibration.	224
A4.6	Tau accumulation test: 4 tau system: potential energy vs time during the 1ns equilibration.	225
A4.7	Tau accumulation test: 6 tau system: potential energy vs time during the 1ns equilibration.	225
A5.1	Comparison between CHARMM and OPLS tensile test results for α-spectrin.	227
A5.2	Tensile test snapshots at 0%, 5%, and 10% strain for α-spectrin created by a-c) OPLS, d-f) CHARMM.	228

LIST OF TABLES

Table No.	Table Title	Page No.
1.1	Exemplary Finding: Stiffness of Axonal Cytoskeletal Components from Current Literature.	24
1.2	Behaviors, Properties, or Aspects Studied/Determined by Using Computational Approaches on Cytoskeletal Components.	27
2.1	Unfolding stiffness and stretching stiffness of the projection domain of single tau.	42
3.1	Selection of phosphorylation sites in tau protein based on earlier studies.	69
3.2	Unfolding stiffness and stretching stiffness of single tau for phosphorylation in different domains.	73
3.3	Observation of tau-MT interaction for phosphorylation at different domains (strain rate: $2x10^9$ s^{-1}).	75
5.1	Maxwell Model Parameters from Tau Relaxation Test.	138
5.2	Maxwell Model Shear Modulus and Bulk Modulus Parameters for Tau.	141
5.3	Maxwell Model Parameters from NFL Relaxation Test.	144
5.4	Maxwell Model Shear Modulus and Bulk Modulus Parameters for NFL.	147
6.1	Actin, Spectrin, and Actin-Spectrin Network: Mechanical Behavior Insight	165
6.2	Simulation setup for tensile tests on actin, spectrin, and actin-spectrin models.	170
6.3	Stiffness summary from the tensile tests on actin and spectrin models.	184
A2.1	Gradual Progression of Unfolding of Single Tau.	214

TABLE OF CONTENTS

	Page No.
Abstract	ii
Acknowledgements	v
List of Figures	vii
List of Tables	xii
Chapter 1: Introduction, Background, Motivation, and Scientific Impact	1
1.1 Introduction: Biopolymers and Traumatic Brain Injury	1
1.2 Axonal Cytoskeletal Components of Neuron	4
1.3 Modeling Axonal Cytoskeletal Components of Neuron	6
1.3.1 Microtubules	6
1.3.2 Insights on MT Mechanical Properties	11
1.3.3 Tau Proteins	12
1.3.4 Insights on Tau Mechanical Properties	16
1.3.5 Neurofilaments	16
1.3.6 Insights on NF Mechanical Properties	18
1.3.7 Microfilaments	19
1.3.8 Insights on MF Mechanical Properties	23
1.4 Stiffness of Axonal Cytoskeletal Components of Neuron	23
1.5 Conclusion	26
1.6 Studies Performed to Address Current Limitations	32
Chapter 2: Effect of Strain Rate on Tau Protein	33
2.1 Introduction	33
2.2 Method	38
2.3 Results	40

2.3.1 Single Tau Deformation 40
2.3.2 Dimerized Tau Deformation 44
2.3.3 Tau-MT Interaction 47
2.4 Discussion 54
2.5 Conclusion 58
Chapter 3: Effect of Phosphorylation on Tau Protein 61
3.1 Introduction 61
3.2 Method 68
3.3 Results 74
3.3.1 Domain Focused Phosphorylation 74
3.3.1.1 Single Tau Unfolding and Stretching 74
3.3.1.2 Dimerized Tau Separation 80
3.3.1.3 Tau-MT Interaction 85
3.3.2 Residue Focused Phosphorylation 90
3.3.2.1 Tau-MT Interaction: Normal vs Phosphorylated Tau 90
3.3.2.2 Tau Accumulation Test 95
3.4 Discussion 103
3.5 Conclusion 108
Chapter 4: Effect of Strain Rate on Neurofilaments 110
4.1 Introduction 110
4.1.1 NF Structure 110
4.1.2 Modifications in NF structures: Polymerization and Phosphorylation 112
4.1.3 Other Parameters Affecting NF Network, Structure and Properties 114
4.1.4 NF Properties 115
4.2 Method 116

4.3 Results 118

4.3.1 Effect of Strain Rate on Neurofilaments 118

4.3.2 NF Accumulation Test 121

4.4 Discussion 126

4.5 Conclusion 129

Chapter 5: Viscoelastic Properties of Tau Protein and Neurofilaments 130

5.1 Introduction 130

5.2 Method 132

5.3 Results 135

5.3.1 Viscoelastic Modeling of Tau Protein 135

5.3.2 Viscoelastic Modeling of Neurofilaments 141

5.4 Discussion 147

5.5 Conclusion 148

Chapter 6: Mechanical Behavior of Actin-Spectrin Skeleton in Axon 150

6.1 Introduction 150

6.1.1 Relevance of Actin, Spectrin, and Periodic Actin-Spectrin Lattice 150

6.1.2 Insights on Actin, Spectrin, and Periodic Actin-Spectrin Network 151

6.1.3 Summary of the Literature Review 164

6.2 Method 168

6.2.1 Tensile Test on 6-actin and 12-actin Models 168

6.2.2 Tensile Test on α-spectrin and β-spectrin 168

6.2.3 Determination of Actin-Spectrin Interaction 169

6.2.4 Stress-Strain Calculation and Tensile Test Schemes 169

6.3 Results 172

6.3.1 Tensile Property of Actin 172

6.3.2 Tensile Property of Spectrin 179
6.3.3 Actin-Spectrin Interaction 185
6.4 Discussion 190
6.4.1 Mechanical Behavior of Actin in TBI Scenario 191
6.4.2 Mechanical Behavior of Spectrin in TBI Scenario 192
6.4.3 Actin-Spectrin Interaction in TBI Scenario 192
6.5 Conclusion 193
Chapter 7: Summary and Future Studies 195
7.1 Summary 195
7.2 Implementation of the MD Studies 196
7.3 Future Direction 198
Appendix 201
Appendix 1: Predicted Structure of Tau Protein 202
A1.1 i-TASSER Methodology 202
A1.2 Predicted Structure of Tau Protein from i-TASSER 204
A1.3 Limitations of the Prediction of Tau, which is an IDP 205
Appendix 2: MD Simulation: Explicit vs Implicit Solvent 207
A2.1 Difference Between Explicit and Implicit Solvation 207
A2.2 Equilibration and Tensile Test Comparison 209
Appendix 3: i-TASSER Predicted Models: Comparative Reliability 220
Appendix 4: Potential Energy vs Time Graphs for Phosphorylation Effect on Tau. 222
Appendix 5: Comparison Between CHARMM and OPLS: Tensile Test on α-Spectrin 227
References 230
VITA 278

CHAPTER 1

INTRODUCTION, BACKGROUND, MOTIVATION, AND SCIENTIFIC IMPACT

1.1 Introduction: Biopolymers and Traumatic Brain Injury

Neural cytoskeletal components are essentially polymers of protein, and therefore, they can be classified as biopolymers. Biopolymers, due to their sustainability, are considered highly important and versatile ingredients, and they have multi-dimensional applications, from structural to biomedical. The studies included in this thesis will be limited to the structural aspects of axonal cytoskeletal components.

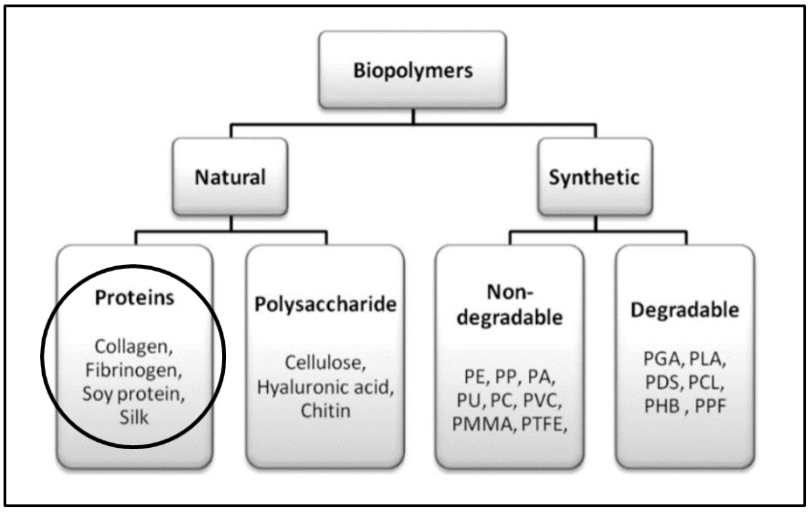

Figure 1.1: A simplified classification of biopolymers (Ekiert et al., 2015). The natural biopolymers include proteins, which is the type of cytoskeletal components (MT, Tau protein, MF, NF, etc.).

In order to determine the mechanical properties and behavior of proteins, molecular level strain rate dependent tests play important role. In many cases, there is drastic change of damage and deformation aspects of biomolecules according to the applied strain rate. And therefore, computational studies which are performed to determine the mechanical properties of such biomolecules generally include mechanical

tests emphasized on strain rate. Characterizing deformation and damage criteria for all the cytoskeletal components is particularly important, as they provide crucial insight on traumatic brain injury (TBI) and other neurological disorders. It is relevant to mention that when mentioning neuronal cytoskeleton, we are interested in both ordered and disordered protein structures. Fig. 1.2 clarifies the position of cytoskeletal components in the protein family.

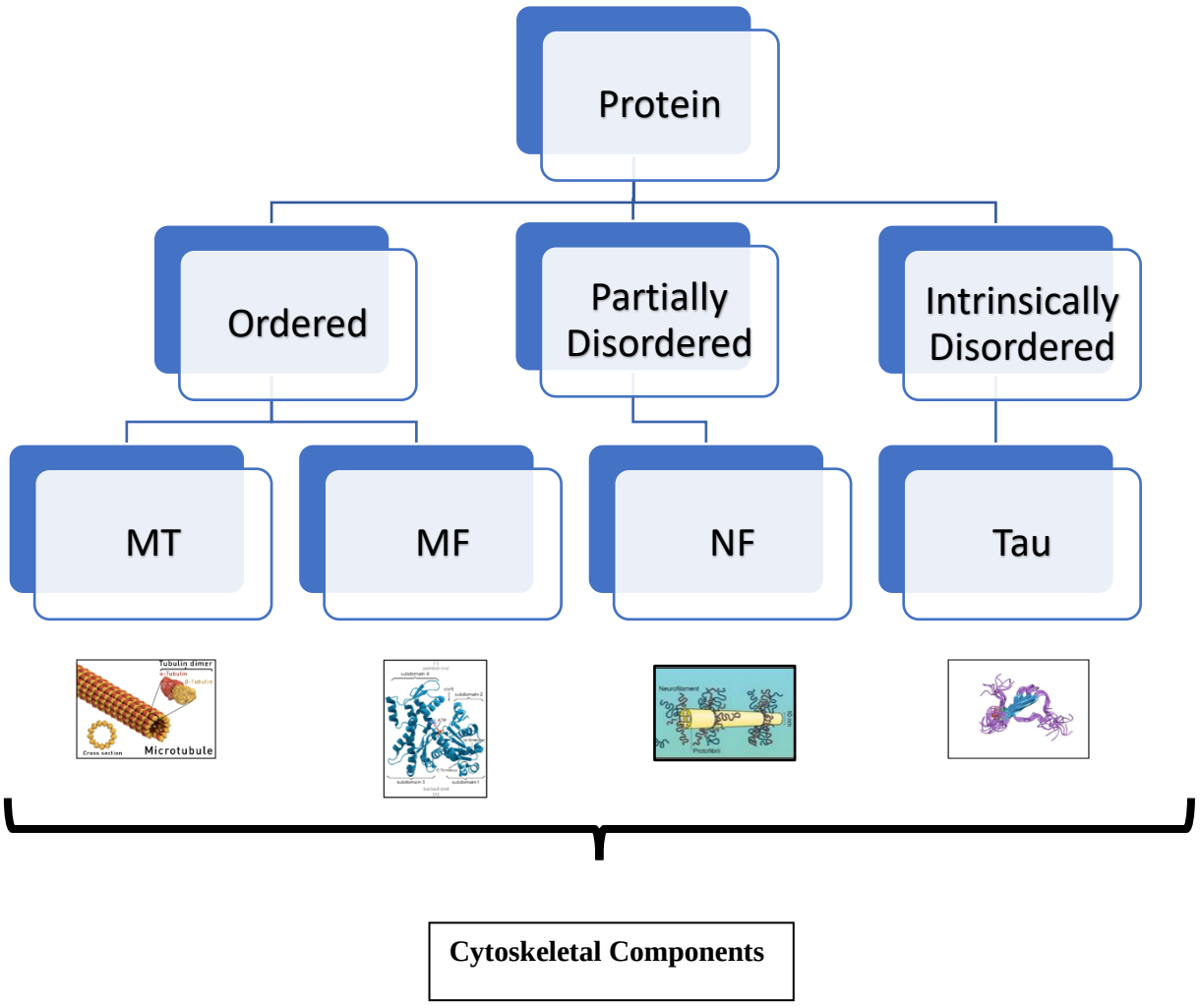

Figure 1.2: Protein types in cytoskeletal components. The major component MT is a specifically defined and conserved protein, while tau protein and NF contain disordered portions in the structure.

TBI has been a familiar topic of research for the last few decades, because due to use of improvised explosive devices (IED) and frequent impact injuries, soldiers and athletes are affected on a regular basis. The post-traumatic stress disorder (PTSD) affected soldiers are thousands in numbers and attempts to manufacture superior battlefront gear and sports gear have been rampant. Quantification of the threshold of damage in brain, which can be considered as significant, requires the quantification of damage in cytoskeletal components. Therefore, we can take a bottom-up approach to develop a computational model of axon, before which we have to obtain sufficient insight on cytoskeletal components themselves. This thesis first takes a deep dive into the current scenario and recent advancements on modeling cytoskeletal components to justify the approach. Then we point out four different questions which have not been answered from the computational perspective over the years and solve them one by one in four independent studies. Finally, we propose the possibility of development of a holistic axon model, after justifying the scientific impact of such approach. The following discussion is the comprehensive literature review we have performed on computational approaches on cytoskeletal components.

The principal component of axonal cytoskeleton is MT, and therefore, there have been numerous computational approaches for holistic axon modeling and explaining their stiffness and damage, focusing on microtubule polymerization and cross-link dynamics by analyzing response under different stretches and stretch rates (de Rooij and Kuhl, 2018). Such studies show the importance of molecular level mechanisms which affect cellular level force and respective component properties, such as stiffness and damage criteria when they are under the application of loading. Many a study have analyzed by focusing on solely on MTs while taking a reasonable conjecture of the mechanical properties of the cross-link and other elements, and some studies have attempted finding out the properties and behavior on individual component level, which will be discussed in the later part of the manuscript.

In order to approach the modeling axon and cytoskeletal components by using MD simulations, many force field potentials have been developed and used, such as CHARMM (Brooks et al., 2009), DREIDING (Mayo et al., 1990), AMBER (Wang et al., 2004), OPLS (Damm et al., 1997), etc. However, selection of a

particular force field for a specific set of simulation depends on several parameters, such as overall biomolecule system, required calculation involved, user experience, available resources, and convenience. Similar considerations are also existent in case of Finite Element Methods (FEM), and the usable interfaces or software can vary from user to user. Currently for continuum scale computational studies of relevant systems use software such as ANSYS (Stolarski et al., 2018), ABAQUS (Wu et al., 1997), etc.

We will discuss in detail on computational approaches on MTs, tau proteins, NFs, and MFs. At the end, we will provide a brief and organized summary of the advancements the computational studies have made, and an exemplary table summarizing our stiffness-focused literature review. It is to be mentioned that for the continuum level modeling (such as FEM modeling), theoretical constitutive relations are used. In order to maintain relevance and find the interrelation convenient, we have mentioned the theoretical works as well.

1.2 Axonal Cytoskeletal Components of Neuron

Eukaryotic neurons contain elaborate cytoskeleton in the cytoplasm. There are three major components of "neural" cytoskeleton: i. microtubules (MT), ii. a subset of intermediate filaments (IF) which is called neurofilaments (NF), and iii. microfilaments (MF). The crosslinks between MT bundles (majorly microtubule associated protein tau) are highly significant to determine the stability of MT, and eventually, the entire cytoskeleton. Therefore, our discussion will contain a brief yet separate section about tau protein.

The principal component of axonal cytoskeleton is microtubule (MT), and therefore, there have been numerous computational approaches for holistic axon modeling and explaining their stiffness and damage, focusing on microtubule polymerization and cross-link dynamics by analyzing response under different stretches and stretch rates (de Rooij and Kuhl, 2018). Such studies show the importance of molecular level mechanisms which affect cellular level force and respective component properties, such as stiffness and damage criteria when they are under the application of loading. Many a study have analyzed by focusing on solely on MTs while taking a reasonable conjecture of the mechanical properties of the cross-link and

other elements, and some studies have attempted finding out the properties and behavior on individual component level, which will be discussed in the later part of the manuscript.

Our discussion will be heavily focused on molecular level simulations, as they have been particularly convenient in determining the component level behavior and properties of neural cytoskeletal components. In order to approach the modeling axon and cytoskeletal components by using MD simulations, many force field potentials have been developed and used, such as CHARMM (Brooks et al., 2009), DREIDING (Mayo et al., 1990), AMBER (Wang et al., 2004), OPLS (Damm et al., 1997), etc. Each one of the force field potentials have improved themselves in their consecutive versions, e.g. all atom CHARMM22 has been improved by deriving its dihedral potential corrected variation, namely CHARMM22/CMAP (Mackerell Jr et al., 2004). In short, the earlier versions of the potentials covered basic bond and angle interactions, but the later versions have facilitated capturing the realistic structural behavior by incorporating backbone orientation, dihedral mapping, etc.

However, selection of a force field for a specific set of simulation depends on several parameters, such as overall biomolecule system, required calculation involved, user experience, available resources, and convenience. Similar considerations are also existent in case of Finite Element Methods (FEM), and the usable interfaces or software can vary from user to user. Currently for continuum scale computational studies of relevant systems use software such as ANSYS (Stolarski et al., 2018), ABAQUS (Wu et al., 1997), etc. We admit the specific limitations of such software due to the nuances of element definition and meshing maneuvers irrespective of their diversity. However, capturing the realistic continuum phenomena and characterizing material behavior is possible for neural cytoskeletal components in some cases by using such FEM approaches. In both approaches (molecular and continuum), the computational capability has increased significantly, facilitating the capture of more detailed, smaller length scale, and higher time scale phenomena.

We will discuss in detail on computational approaches on MTs, tau proteins, NFs, and MFs. At the end, we will provide a brief and organized summary of the advancements the computational studies have made, and

an exemplary table summarizing our stiffness-focused literature review. It is to be mentioned that for the continuum level modeling (such as FEM modeling), theoretical constitutive relations are used. To maintain relevance, we have mentioned the works heavily focused on theory of constitutive modeling in appropriate cases. The purpose of this review is two-fold: a) obtaining insight on the accomplishments of computational approaches to model neural cytoskeletal components, b) pinpointing the limitations of the existent studies in order to set possible future works, which will facilitate a comprehensive set of information on these components.

1.3 Modeling Axonal Cytoskeletal Components of Neuron

1.3.1 Microtubules

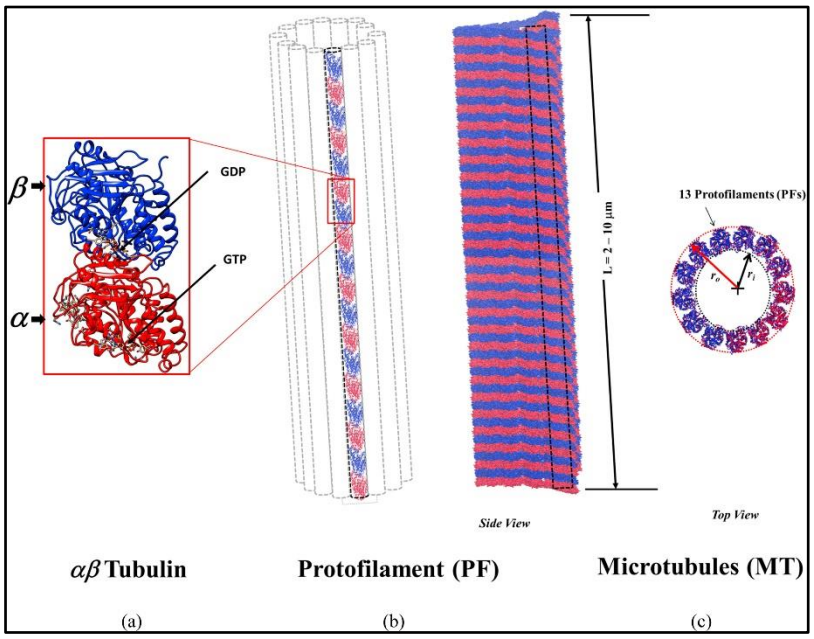

Figure 1.3: MT structure showing helically arranged repetitive α and β-tubulin subunits. Reference: Adnan et al (2018) (Adnan et al., 2018).

As it is the largest component of axonal cytoskeleton formed by repetitive helical arrangement of α and β-tubulin subunits (Fig. 1.3), MT is the most convenient one to study, and therefore, there have been numerous computational approaches to determine its properties and behavior using MD simulation, CG modeling, and FEA approach. This section contains the recent studies of such nature.

Molecular level modeling of MT has not always been performed by fully atomistic simulation, and the approaches have been diverse. For example, approaches for determining MT Young's modulus have yielded results which differ by several orders of magnitude, and the approaches can differ from structural mechanics modeling (Zhang and Wang, 2014) to MD simulation (Wells and Aksimentiev, 2010), CG modeling (Feng and Liang, 2012), FEM approach (Barreto et al., 2013), etc.

MD simulation has been particularly successful to determine MT properties and behavior. One of the reasons is that although it is the largest cytoskeletal component, it is convenient to model in the length scale appropriate for MD simulation. Therefore, in independent MD studies, MT properties are revealed by performing allostery, bending, tension, twisting, energetics of inter-protofilament interaction study, etc. on atomistic MD model (Enemark et al., 2008; Gebremichael et al., 2008; Mitra and Sept, 2008; Sept et al., 2003; SONCINI et al., 2009; Wells and Aksimentiev, 2010; Zeiger and Layton, 2008). Such models have been applied in an extended fashion in later MD works to analyze different deformation modes such as dilation, stretching, bending, etc. on MT, and finding the MT rigidity (Dima and Joshi, 2008; Grafmüller and Voth, 2011; Wu and Adnan, 2018). Properties of MT subunits are also determined by MD simulation studies, such as axial and circumferential elastic moduli, in-depth analysis of atomistic to supramolecular properties of tubulin, study on effect of MT stabilizing drug on the structure, GTP hydrolysis on intrinsic dimer bending, etc. (Carpenter et al., 2006; Deriu et al., 2007; Gebremichael et al., 2008; Kerssemakers et al., 2006; Mitra and Sept, 2008; Zeiger and Layton, 2008), and overcome the limitations of earlier continuum level studies, which attempted to capture tubulin and MT dynamics and behavior (Tuszyński et al., 2005a, 2005b). Moreover, Amyloid fibril, the structure of which is very relatable to MTs, has also been

mechanically characterized by MD simulation (Yoon et al., 2011). The mechanics of the molecular level structure has been captured by diverse approaches, such as Brownian motion study (Zakharov et al., 2015).

From a simplified point of view, MTs can be considered as nano-fibrous structure, with tau protein as their crosslinks, and therefore, they can be designed as nanofiber reinforced nanocomposites using atomistic based continuum model (Adnan et al., 2018). This study reveals unique viscoelastic nature of axon, and the effect of their behavior during traumatic brain injury (TBI). Such computational studies are, as a result, important regarding determination of axon response for brain injury and neuropathology. The collaboration between continuum scale and atomistic based studies is that such concoction can overcome the limitations of both approaches (lacking finer scale details, and scale limitations along with computational expense, respectively) (Xiang and Liew, 2012), by using different techniques at disposal, such as interatomic potentials and continuum homogenization. This study has determined the viscoelastic nature, and Young's modulus for MTs, which agrees with prior studies. In a separate study, the same group has developed a shear lag model by considering both MT and tau proteins as viscoelastic materials, and used atomistic based calculations to develop continuum scale model (ADNAN et al., 2015). Such study is inspired by earlier approaches, which used atomistic based continuum approach to predict elastic modulus of MT, as well as other mechanical response, such as transverse compression, orthotropic elastic properties, and other dynamic responses (Jiang et al., 2008; Liew et al., 2011; Sept and MacKintosh, 2010; Vogt, 2008; Xiang and Liew, 2013). However, the exclusivity of this study is that they have been able to develop a phase diagram for quantification of damage criteria, by considering both MT failure at high strain rate, and MT sliding at low strain rate. It is worth to mention that such shear lag model is strengthened by earlier studies, which suggested that viscoelasticity (and dynamic binding) of (or between) tau proteins leads to the unique strain rate dependent failure of MT (Ahmadzadeh et al., 2015, 2014). In other words, at lower strain rate, MTs (eventually, axon) can be stretched reversibly, while at higher strain rate, their stretch can lead to axon failure. By using MD simulations, not only structure level properties of MT are determined, but also subunit

level aspects are investigated (Enemark et al., 2008). Such studies bolster the usage of molecular level studies, as they agree with previous experimental data on MT stiffness.

The frequent trade-off between MD simulation modeling of MT and continuum level study is that continuum level study can capture larger length scale and time scale behavior, but lacks atomistic details, as reflected over and over again in recent studies (ADNAN et al., 2015; An and Gao, 2010; Sim and Sept, 2013). The promising aspect of MD simulation advancement is that, although it is computationally demanding, the fully atomistic simulation of 13 helically aligned repeating subunits of MT protofilament has been performed, which has been considered the pathway for similar studies (Wells and Aksimentiev, 2010). In order to overcome the limitations of MD simulation and normal mode analysis (NMR), multiscale modeling (Hemmat et al., 2018) by using several approaches, such as anisotropic elastic network modeling (ENM) has been found to be convenient (Deriu et al., 2010), as such approach can handle the entire MT level phenomena. Furthermore, they have been able to find stretching and bending properties, using the entire MT model developed by CG simulation, which is detailed to several hundreds of nanometers, which can be directly compared to existent experimental data. Coarsening of MT structure has also been utilized in other studies, which attempted to determine MT properties such as elastic modulus, and tension, compression, or torsion properties (Feng and Liang, 2012; Lazarus et al., 2015). CG mechanochemical models, in separate studies, have been utilized to find out the dynamic behavior of MT (Ji and Feng, 2011; Peter and Mofrad, 2012), such as characterization of sheet-ended MTs, analysis of distribution of interaction energy, and finding out radial indentation process of MT, along with the assembly, growth, structure, and deformation mechanics of such biomolecule. Multiscale modeling of MT has also been applied to investigate diverse phenomena, such as electric field effect on MT (Setayandeh and Lohrasebi, 2016).

CG modeling has been particularly useful to determine specific MT behavior and dynamics, such as their severing mechanism, nano mechanics, and bending behavior (Theisen et al., 2013, 2012). This has been possible because unlike fully atomistic MD simulation, they can account for large number of atoms and eventually, can address holistic properties. This approach facilitates to observe certain MT phenomena

which was otherwise impossible to observe except by experimental techniques, as such biological phenomena are driven by enzymes and mechano-chemical activities. The properties that have been determined for MT by using MD simulations (such as elastic properties, mechanical deformation, force generation at shrinkage of filament, length dependence on persistence length, collapse and catastrophe of the MT structure, etc.), have also been calculated and analyzed in depth by CG simulations, a handful of which have considered plasticity explicitly (Ding and Xu, 2011; Gardel et al., 2004; Mahadevan and Mitchison, 2005; Molodtsov et al., 2005; VanBuren et al., 2005; Wu et al., 2009).

Aside from the MD and CG approaches, continuum level models have also been developed for cytoskeletal components, keeping in consideration that MT contributes most in the tensile and compressive properties of axon, using FEA (Barreto et al., 2013; Sandor Kasas et al., 2004). FEM has been particularly successful to account for the nanometer-level structure, deformation, instability, indentation response, elastic response, oscillation modes, and collapse of MT (de Pablo et al., 2003; S Kasas et al., 2004; Sandor Kasas et al., 2004; Kis et al., 2002; Schaap et al., 2006). Numerous continuum level models have been developed for MT to capture the mechanical response. Some of the models have attempted to relate the MT response with beam theory, while others focused on specific responses, such as buckling, bending, torsion, transverse compression, lateral interaction, shear response, rotation response, vibration, orthotropic elastic properties, or other dynamic phenomena on MT (Civalek and Demir, 2011; Demir and Civalek, 2013; Gu et al., 2009; Hawkins et al., 2010; S Kasas et al., 2004; Li et al., 2006; Li, 2008; Liew et al., 2015; Nishimura et al., 2006; Qian et al., 2007; Shen, 2010a, 2010b, 2010c; Shi et al., 2008; Wada and Netz, 2006; Wang et al., 2006b, 2006a; Wang and Zhang, 2008; Wu et al., 2012) (N.B. such studies have been performed since 1990's, but we have only cited the studies which were published recently in order to signify the impact of the recent approaches, considering that the computational capability and efficiency have been manifold since 2000's). Such approaches have facilitated the development of single cell model for force induced interactions in cytoskeletal components. These studies are particularly important because they have been able to include component level and holistic level properties in the modeling, which is necessary to obtain

insight on the components. FEA studies have also been performed by focusing on specific response of MTs, such as buckling parameters and bending stiffness, by using nonlocal beam model of MT protein (Civalek and Demir, 2016), and multiscale CG model of MT (Deriu et al., 2012a). These studies are significant because they give us crucial insight on the effect of the length scale of MTs on buckling response, and they have found that the buckling loads increase markedly with the increase of elastic matrix parameter for all type boundary conditions and microtubule types. Actually, buckling has been studied in depth by FEM approaches, for example by taking their individual state and bundled state into consideration (Soheilypour et al., 2015). In other studies on MT in continuum scale (such as anisotropic FEM shell modeling), specific parameters such as persistence length, tension and torsion behavior, modulus of rigidity, etc. (Shahinnejad et al., 2013), along with the dependence of persistence length on contour length has been computationally determined (Gao et al., 2010). Moreover, viscoelasticity of MT has also been taken into consideration by modeling MT as standard linear solid model to capture axonal MT rupture in recent FEM study (Shamloo et al., 2015). By considering the diversity and success of determination of mechanical properties of MT by FEM approach, we can assert that such approach is no less important than MD simulation and CG modeling.

1.3.2 Insights on MT Mechanical Properties:

1. Being the largest component of cytoskeleton, MT length scale is convenient for computational studies, and it has been subjected to numerous analyses. The studies are not only limited to MT properties, but also extended to interactions with other components.

2. Different approaches to determine mechanical properties of MT has generated results which vary by several orders.

3. Atomistic simulation studies have been able to address particular dynamic behavior of MT, such as stretching, tension, bending, twisting, etc. Also, they have determined elastic properties of MT

in both atomic and supramolecular level. Despite being computationally expensive, full MT modeling has been possible due to computational advances.

4. Atomistic based continuum level studies have addressed the particular limitations of both continuum level and fully atomistic level studies.

5. CG studies have been able to characterize dynamic behavior of MTs. Furthermore, they have determined the interaction energy properties and molecular level deformation mechanics, including severing mechanism of MTs.

6. Mechanical properties, such as tensile and compression properties, as well as viscoelastic behavior of MT have been determined by FEM studies, too. They have been particularly successful to address the bundled behavior of MT due to convenience of length scale.

1.3.3 Tau Proteins

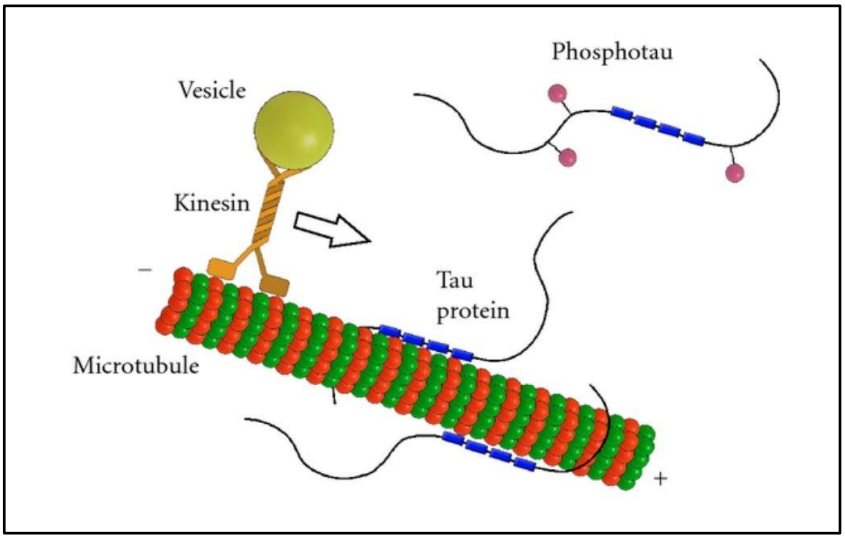

Figure 1.4: Tau protein interacting with MT. Reference: Kolarova et al (2012) (Kolarova et al., 2012).

Tau protein, as a structural element of neuronal cytoskeleton, provides support for MTs. As a protein, it does not stay on its own, rather it creates electrostatically bonded dimers. Mainly it contains three domains: projection domain, MT binding repeats, and tail. The dimers are obtained by the electrostatic "zipper" bonding or overlapping between the projection domains of two adjacent tau proteins. Surface force apparatus experimentation by Rosenberg et al depicts the tau-MT interaction in detail (Rosenberg et al., 2008), where quantification of binding interaction is obtained by comparing adhesion energies for bare mica surface to tau protein covered surface vs tau protein covered surface to tau protein covered surface.

As a biomarker of Alzheimer's disease (AD) and several other neuropathology, tau protein is an important cytoskeletal component. Furthermore, it determines the stability of MTs, which further signifies the importance of tau property studies. Due to existence of disordered portions in the structure of tau protein, it has been less studied, and the behavior as well as properties lack sufficient validation. This section will, therefore, will be a concise one, discussing the recent computational approaches on tau protein.

One unique aspect of tau protein is its intrinsic disorder. In other words, lack of specific 3D conformation makes it difficult to find its properties and behavior experimentally. One way to address this dilemma is to use a combination of microscopic studies along with molecular dynamics simulation. For example, protein folding and unfolding has been studied and validated by using a combination of atomic force microscopy (AFM) and steered molecular dynamics (SMD) approach (Isralewitz et al., 2001). Similarly, neutron scattering approach can use molecular dynamics simulations as a supplement to find out intrinsically disordered protein (IDP) behavior, such as of tau (Fichou et al., 2015). It is to be noted for the relevance of tau protein and NFs that a wide range of predictors are available to predict IDP structures with a certain level of confidence (Li et al., 2015), and some of them have been used for quite a few years in a large span of computational works (Kelley et al., 2015; Zhang, 2008), but the detail discussion on their algorithms and the reliability of the predicted structures are out of the scope of this manuscript.

However, as taus are crosslinks for the MTs (see Fig. 1.4), some mathematical modeling of MT have used tau protein data obtained from single cell spectroscopy study and viscoelastic insight on tau – leading to

modeling MT as elastic element and tau as viscoelastic element (Ahmadzadeh et al., 2014). Our earlier studies essentially address the lack of computational tau study by using molecular dynamics simulation, and specifically determines strain rate effect on tau and phosphorylation effect – both domain focused and residue focused. Furthermore, these studies also determine the tau-MT interface interaction, and their accumulation tendency with respect to phosphorylation state, which gives us important insight on tau modeling. It is important to note that most of the computational work on tau protein is functionality focused, not structure, and therefore, structural modeling of tau protein is still non-existent in literature.

As a highly solvable protein, tau protein is hypothesized to have dominant tau-water interface interaction which determines its characteristics, and comparison of neutron scattering study with MD simulation of powder-formed intrinsically disordered protein (IDP) tau which quantifies protein hydration rate, strengthens this finding (Fichou et al., 2015). Although such studies have been performed earlier on several other proteins such as lysozyme and green-fluorescent proteins, such study on an IDP is of its first kind, making MD simulation very promising in this area, by a. addressing the challenging task of modeling an IDP which has several conformation in solvated state, and b. raising the possibility of extending such study for other IDPs. Some standalone studies, however, focused on specific parameters, such as possibility of formation of tau protein fibril at high temperature, experimental validation of which bolsters the findings (Luo et al., 2013). However, from total mechanical standpoint, the authors have not found any computational studies on tau protein properties, although it has been asserted in early experimental works (Wegmann et al., 2011), and used in later computational modeling of MT (Ahmadzadeh et al., 2014). In continuum level MT modeling studies, tau protein is modeled as crosslinks, and in some cases the attachment and detachment of tau to MT surface is expressed as thermally activated phenomenon (de Rooij and Kuhl, 2018), while in other cases its viscoelasticity is pronounced (Ahmadzadeh et al., 2014).

In numerous studies regarding tau, phosphorylation is an important phenomenon, as it is hypothesized that it manipulates the ability of tau protein to affect the MT stability, including Monte Carlo simulation of tau which specifically analyzes the effect of phosphorylation, dephosphorylation and moderate

phosphorylation on separation and accumulation of tau, or maintaining tau-tau equilibrium distance(Jho et al., 2010). This diverse study facilitates the reader to obtain insight on tau protein behavior on MT surface attached state and free (dissolved in water) state. Furthermore, hyperphosphorylation has been found to be related with paired helical filament (PHF) and neurofibrillary tangle (NFT) formation, which is a certain marker of neuropathology, and this specific aspect has been addressed in some MD simulation studies (Lyons et al., 2014), by analyzing the phosphorylation effect on peptide fragment of tau, which found that all phosphorylation patterns disrupted the structure of tau protein.

Finally, using of predicted structure to analyze IDPs has observed significant improvement over the last two decades, and might be considered as a work-around procedure to circumvent the limitations of experimental approaches on IDPs. For example, in a separate study, MD simulation on predicted structure of tau (predicted by i-TASSER) was performed to determine the electrostatic behavior, which corresponds to experimental results, such as tau preferring a contracted conformation in fluid, and an extended conformation while interacting with MT (Castro et al., 2019). Also, in some cases in some cases the formation of reliable predicted structure is obtained by obeying the stereochemical compatibility (used i-TASSER to predict tau structure) (Battisti and Tenenbaum, 2012), and and can be implemented in tau aggregation studies (Dułak et al., 2018).

From this section it is evident that although there are numerous computational studies on tau, they have been mostly focusing on the hydrophobic surface effect or charged portion effect of tau domains, and there are very few computational studies on tau protein addressing mechanical properties, and many aspects of this cytoskeletal component is still unknown. Some studies have focused on phosphorylation, but they have been inconclusive on how it affects the mechanical properties. However, our group have performed MD simulation studies specifically to address this shortcoming, and determined the strain rate effect on tau (and NF), domain-focused and residue-focused phosphorylation effect on tau, and viscoelastic modeling of tau protein (and NF) by relaxation simulation.

1.3.4 Insights on Tau Mechanical Properties:

1. As a biological marker of neurological diseases and structural crosslinks of MTs, tau is an important cytoskeletal component, but it is not studied in a comprehensive manner, and their properties and behavior are not existent in literature due to being an intrinsically disordered protein.
2. Due to them being IDP, tau proteins are mostly studied based on their functionality, not structure.
3. There is very few structural modeling of tau-MT interface, and viscoelasticity of tau is hypothesized as the dominant parameter to alter MT behavior.
4. Phosphorylation has been conjectured as a very important parameter to control the dynamics of tau, but further studies revealed that multiple parameters have significant role to determine overall tau behavior.
5. Therefore, computational studies can be a convenient way to determine specific mechanical properties of tau, such as rate-dependent properties, and effect of phosphorylation on mechanical properties of tau.
6. In order to obtain effective solutions to the aspects mentioned in point 5 above, using reliable predicted structures might be a good approach in appropriate tau protein studies.

1.3.5 Neurofilaments

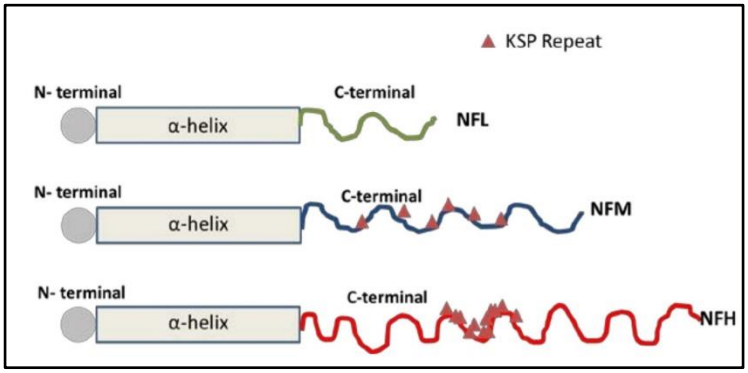

Figure 1.5: Neurofilament isoforms, highlighting the extent of the tail region of the structure. Reference: Jayanthi et al (2014) (Jayanthi, 2014).

Neurofilaments (NFs) are major cytoskeletal components of vertebrate myelinated axons. The three isoforms of NFs have C-terminal disordered sidearms (or tails) which dictate the disruption of NF network and eventually (Fig. 1.5 shows structural representation of the isoforms), the propagation of motor neuron disorders. Modeling of NFs have been performed extensively from experimental point of view, especially using X-ray scattering and various microscopy techniques, and most of them have established the bottlebrush modeling scheme for NFs (Beck et al., 2012). This section will be discussing on computational studies on NFs and will be a brief one like the section on tau protein.

There have been detailed molecular level modeling studies on NF, which address specific aspects of NF properties, such as phosphorylation effect on sidearms (Adiga and Brenner, 2010), finding out conformational properties of NF by using Monte Carlo simulation (Jayanthi et al., 2013; Stevenson et al., 2011), effect of hydrophobic interactions and cations on NF structure (Lee et al., 2013), atomistic level modeling of NF isoform, etc. (Jayanthi, 2014).

Sequence based CG modeling of NFs also strengthens the bottlebrush modeling, for which essentially the physical structure and the effect of charged portions in the sidearms play the major role defining the model (Chang et al., 2009). This study analyzes the phosphorylation effect on all three isoforms of NF and finds that not only the length of the sidearm dictates the mechanical properties of NFs (in other words, number of phosphorylation sites is not the only parameter defining NF properties). The bottlebrush modeling that has been mentioned above is particularly important on NF structure studies, because not only it describes the NF network, but also NF-NF interaction, which is further asserted in other studies which concocted MC simulation and micrography results (Kumar et al., 2002). There have been similar approaches, such as bead-spring modeling of NF (CG modeling) to determine their conformational dynamics (Stevens and Hoh,

2010). These studies have suggested that conformation within the brush is important irrespective of filament length and plays an important role in all isoforms. In most of such conformational studies, it has been suggested that the interaction in the sidearm region dictates the overall behavior of NF, due to presence of charged portion in the sidearms, and their net effect on the attraction and repulsion within the network. NF-NF interaction study, which has attempted to analyze the "opposite brush interaction" and "inside brush interaction" between charged portions, has also strengthened such viewpoint, as such study has found that the net repulsion dictates sidearm spacing (Stevens and Hoh, 2011).

Going through the recent literatures on NF properties and behaviors, it has become clear that stoichiometric studies on NF are highly facilitated by Monte Carlo simulations, especially using CG models of NF structures (Kim et al., 2011). These studies have strongly suggested that NF has a self-sufficient and stable in-vivo structure, which means large changes in NF stoichiometry has little effect on the stability. CG modeling has also addressed several other aspects regarding NF structure and network, such as effect of ionic strength and pH on segment rearrangement upon phosphorylation (Zhulina and Leermakers, 2007a), determination of equilibrium structure of NF using self-consistent field analysis and CG modeling of NF tail (Zhulina and Leermakers, 2007b), effect of protein composition (Zhulina and Leermakers, 2010), etc.

The use of established CG models in different simulation studies shows the diverse applicability of such models in determining their properties and behavior using molecular studies.

1.3.6 Insights on NF Mechanical Properties:

1. Molecular level studies on NF has been able to find out post-translational modification effect on sidearms, conformational properties, isoform-specific behavior, interaction with water, etc.
2. CG modeling have strengthened the viewpoint that the effect of charged portion in the sidearms on NF isoforms play a dominant role to determine their behavior. They have also been able to address

specific structural and network aspects of NFs, such as effect of composition, ionic strength, and pH on segment rearrangement, and so on.

3. NF network modeling studies have given insight when the micrography studies are combined with Monte Carlo (MC) simulation. MC simulation has been successful to determine stoichiometric properties of NF.

1.3.7 Microfilaments

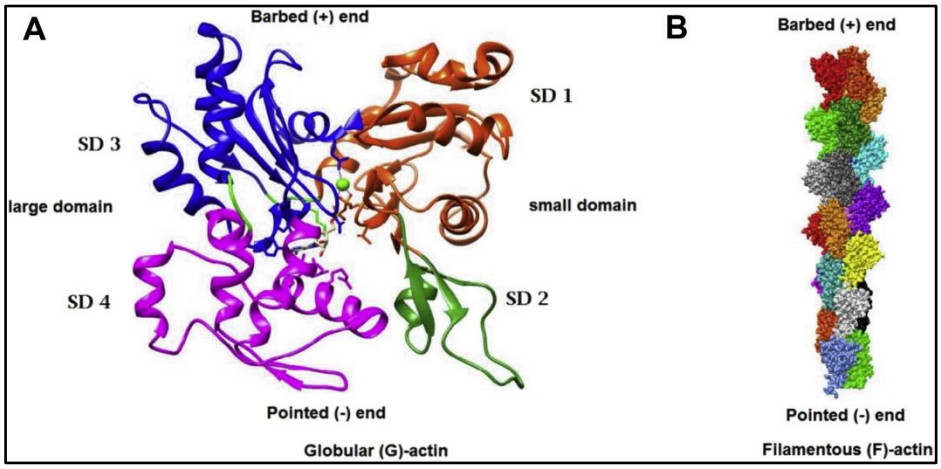

Figure 1.6: Globular actin (G-actin), which is the structural unit of MF, and the filamentous actin (F-actin) which is formed by polymerization of G-actin. Reference: Kumar et al (2017) (Kumar and Mansson, 2017).

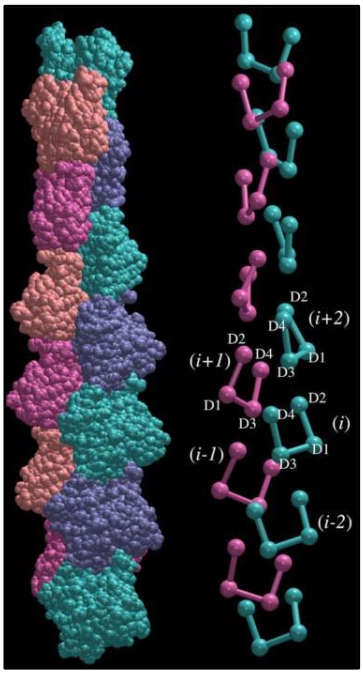

Figure 1.7: Atomic model of filamentous actin (F-actin) which is developed from the Holmes model (left) (Splettstoesser et al., 2011). The CG representation is also shown (right). Reference: Chu et al (2006) (Chu and Voth, 2006).

Microfilament (MF) contains very less disordered portion, and therefore, it has been studied thoroughly. The building block of MF is a globular actin (G-actin), polymerization of which leads to the filamentous version of the protein (F-actin), which is the functional block of MF. This section will be discussing recent advancements on MF and MF subunit studies by computational approaches. Fig. 1.6 shows a generic structural representation of MF, and Fig. 1.7 shows the model developed by atomistic level study.

There have been extremely structure-focused all-atom studies on microfilaments, which use familiar Oda (Oda et al., 2009) or Holmes (Dominguez and Holmes, 2011) model for atomistic studies on Actin, including their polymerization and depolymerization (Pfaendtner et al., 2010b, 2010a). However, due to the scale limitation, there has been multiscale approach (multiscale serial bead model) to model

microfilament networks (Li et al., 2013), through which we can obtain insight on biological mechanics to few micrometer length scale. This study is validated by previous experimental repertoires on single actin transverse vibration and axial tension analysis, and facilitates finding out mechanical behavior of actin filaments, as well as the importance of crosslinking in their structure and network behaviors (T Kim et al., 2009), and effect of actin binding proteins on the stiffness (Claessens et al., 2006). Actin dynamics and conformational structure depends on several parameters such as nucleotide state, and the specific effect of these diverse mechano-chemical effects and phenomena are studied in separate studies by molecular studies (Dalhaimer et al., 2008; Lee et al., 2011; Pfaendtner et al., 2009; Zheng et al., 2007). Moreover, some models have incorporated viscoelasticity in the atomistic actin network model. Not only such studies show the applicability of MD simulation on such structures, but also the evolution of the capability of structural modeling via this approach over the last two decades (Splettstoesser et al., 2011).

All-atom MD simulations have various approaches towards modeling large biopolymers such as actin to find out various mechanical properties, such as extensional and torsional stiffness (Matsushita et al., 2012, 2010), and in various occasions, steered molecular dynamics (SMD) has been particularly effective finding out mechanical properties of actin. For example, Kim et al has shown that SMD can demonstrate the effect of cofilin (an actin regulatory protein) on increasing the flexibility of actin filament (Kim et al., 2016), by performing tensile tests on various models of actin and actin-cofilactin model.

As a common remedy to the scale limitation to the all-atom modeling of the microfilament networks, coarse grained (CG) modeling has been found as a reliable approach (Jeon et al., 2008; Ming et al., 2003; Saunders and Voth, 2012). Therefore, there has been study which models microfilament network in CG approach, using MD simulation results (Chu and Voth, 2006). The methodology here is to model each sub-domain as a CG site, resulting in four sites per G-actin monomer, and design the filament using the average internal coordinates obtained from fully atomistic MD simulation – an approach which is particularly useful to find out the behavior of actin filament under different loading condition.

In order to simplify and utilize the results of all-atom MD simulations, CG technique has been found to be very promising, because study on actin filaments shown that the statistical distance between group of atoms in all-atom simulation can very well be used to parameterize the force field, and eventually, characterize the dynamics of protein via Brownian dynamics simulations (Deriu et al., 2012b). The coarsening of the model facilitates to run the simulation for a higher time scale, and therefore, these results can be extended to other subcellular structures. This study particularly analyses the effect of number of CG beads on the estimated persistence length of actin filament, which is determined by different approaches in other studies, as an important mechanical property.

CG modeling not only provides the insight on certain mechanical properties such as torsional rigidity and persistence length, but also gives important information about the filament heterogeneity and distinct conformations of actin filaments, which is otherwise not extractable by experimental maneuvers (Fan et al., 2012). This study essentially strengthens the reliability of MD and CG simulations on large biopolymers, as the results obtained on mechanical properties are consistent with experimental results. Some studies have also provided stochastic insight on the structure as well as mechanical deformation via CG modeling, which demonstrates the diversified scope of this approach (Yogurtcu et al., 2012). In separate study, both MD and CG approaches have been utilized to find out structural and mechanical properties of actin monomer, which further reveals the actin dynamics (Chu and Voth, 2005).

Continuum mechanics has played a major role for modeling actin networks in continuum domains, as a result of which, diverse models have populated in recent years, such as affine continuum mechanical model of F actin network with crosslinking and linker proteins (Holzapfel et al., 2014), multi-scale continuum analysis and computational model (Unterberger et al., 2013a), and study facilitating the vibrational data obtained from molecular characterization, eventually using it for continuum level modeling (Li, 2015). These types of models give further insights of experimental results by analyzing shear response of network models, and as mentioned earlier, motives of such study are to find out the applicability to other subcellular structures, and scope of cross-scale modeling of biopolymers. Viscoelasticity of cross-linked actin networks

has also been analyzed by performing finite element method (FEM) modeling, based on continuum-scale theoretical study (Unterberger et al., 2013b).

1.3.8 Insights on MF Mechanical Properties:

1. Due to having less disordered portion in the structure, MF model has been established with confidence, and molecular level studies have addressed the structure and network aspects, polymerization behavior, etc.
2. One particularly important aspect, that is, effect of actin binding protein on the behavior is studied thoroughly by computational studies on MF.
3. Load-dependent properties of MF has been determined by CG studies. However, they are also dependent on the molecular level studies.
4. Mechanical modeling by studying loading response of MF is studied by continuum scale modeling. Therefore, it can be stated that computational studies have facilitated thorough characterization of MF.

1.4 Stiffness of Axonal Cytoskeletal Components of Neuron

To characterize the neural cytoskeleton from the material perspective, it is important to determine the component level properties and behavior. Different approaches can be undertaken to characterize the components of a mechanical body, and several parameters can play significant role in defining certain behavior. However, tensile stiffness is an important mechanical parameter while defining the neural cytoskeletal component behavior.

We have performed a property-focused literature review to tabulate the properties (mostly stiffness values) that have been determined by several approaches earlier, along with the comprehensive review on cytoskeletal components. We have already mentioned that due to the convenience of the length scale of microtubule, properties are calculated for this structure to great extent in numerous literatures. Also, due to lack of disorder in MF structure, it has also been studied considerably. On the other hand, due to existence of disordered portion in the structure and extremely small length scale, tau protein and NF lack literature on their properties and behavior, which bolsters the importance on further computational investigations on them. Table 1.1 summarizes our property-focused review as an example and gives a glimpse on experimental validation of computational studies, which makes the computational approach more promising. It also strengthens our prior statement that the mechanical properties may vary by several orders.

Table 1.1: Exemplary Finding: Stiffness of Axonal Cytoskeletal Components from Current Literature

Cytoskeletal Component	Stiffness (Young's Modulus)	Reference No.	Comment
Microtubule	1.9 GPa	(Ahmadzadeh et al., 2014)	Electron Micrography studies, FEM
	1.5 GPa	(Peter and Mofrad, 2012)	From experiment
	1.9 GPa	(Suresh, 2007)	Information obtained from several references in this paper

	1.2 GPa	(Gittes et al., 1993)	For homogeneous and isotropic MT
	2 GPa	(ADNAN et al., 2015)	Viscoelastic shear lag model
Tau protein	5 MPa	(Peter and Mofrad, 2012; Shahinnejad et al., 2013)	Cross linking Tau Protein's Young's modulus from experiment, FEM
	10 MPa	(Wegmann et al., 2011)	Atomic Force Microscopy (AFM)
Neurofilaments	1-15 Pa	(Yao et al., 2010)	Linear elastic modulus of NF network as a function of concentration of NF and concentration of Mg.
	>100 Pa	(Leterrier et al., 1996)	Fluorescence and microscopy studies
	300-400 MPa	(Wagner et al., 2007)	For Intermediate Filaments (IF), not just NFs.
	1-5 GPa	(Suresh, 2007)	For Intermediate Filaments (IF), not just NFs.
Microfilaments	1.3-2.5 GPa	(Suresh, 2007)	This reference has used different works to validate the parameters used in their

	400 MPa-2.5 GPa	(Kim et al., 2015)	Steered Molecular Dynamics (SMD) simulation.

1.5 Conclusion

In this study, we have reviewed the current scenario and recent advancements on studies on cytoskeletal components which used computational approaches such as MD simulation, CG simulation, FEA analyses, etc. From our comprehensive literature review, the major findings can be summarized as shown below. It is to be noted that due to very conserved structure and lack of disorder in MT and MF structure respectively, they have been extensively studied, while due to being intrinsically disordered protein, and presence of disordered portion in isoforms, tau protein and NFs still lack comprehensive studies.

For all the cytoskeletal components, molecular level simulations can capture atomistic details, while continuum level studies can capture holistic structural dynamics. Therefore, this tradeoff will always be present, despite extreme advancement in computational capabilities over the recent years. We admit the necessity of experimental validation of such studies (which actually are present for numerous studies we have mentioned, and made clear by Table 1.1), and assert that in particular circumstances, computational repertoires provide certain convenience, and their impact on giving insight on dynamics, properties, and behavior of cytoskeletal components cannot be ignored. The parameters, properties or aspects that have been determined, analyzed, or extended through computational approaches are shown in the brief points in this section.

Behaviors, properties, or aspects studied/determined by using computational approaches on cytoskeletal components are summarized in Table 1.2.

Table 1.2: Behaviors, Properties, or Aspects Studied/Determined by Using Computational Approaches on Cytoskeletal Components

Cytoskeletal Component	Behavior, Property, or Aspect Studied	Reference (Last Name of the First Author, Publication Year, and Reference No.)
MT	Young's modulus	Zhang 2014(Zhang and Wang, 2014), Wells 2010(Wells and Aksimentiev, 2010), Feng 2012(Feng and Liang, 2012), Barreto 2013 (Barreto et al., 2013)
	Axial and circumferential moduli	Mitra 2008(Mitra and Sept, 2008), Gebremichael 2008(Gebremichael et al., 2008), Zeiger 2008(Zeiger and Layton, 2008), Deriu 2007(Deriu et al., 2007), Carpenter 2006(Carpenter et al., 2006), Kerssemarkers 2006(Kerssemakers et al., 2006)
	Orthotropic elastic properties	Jiang 2008(Jiang et al., 2008), Vogt 2008(Vogt, 2008), Sept 2010(Sept and MacKintosh, 2010), Xiang 2013(Xiang and Liew, 2013), Liew 2011(Liew et al., 2011)
	Physical response to mechanical loading and energetics of inter-protofilament interaction	Wells 2010(Wells and Aksimentiev, 2010), Feng 2012(Feng and Liang, 2012), Mitra

		2008(Mitra and Sept, 2008), Gebremichael 2008(Gebremichael et al., 2008), Enemark 2008(Enemark et al., 2008), Soncini 2009(SONCINI et al., 2009), Sept 2003(Sept et al., 2003), Zeiger 2008(Zeiger and Layton, 2008), Lazarus 2015(Lazarus et al., 2015)
	Deformation modes, rigidity	Wu 2018(Wu and Adnan, 2018), Dima 2008(Dima and Joshi, 2008), Grafmuller 2011(Grafmüller and Voth, 2011)
	Subunit behavior	Mitra 2008(Mitra and Sept, 2008), Gebremichael 2008(Gebremichael et al., 2008), Zeiger 2018(Zeiger and Layton, 2008), Deriu 2007(Deriu et al., 2007), Carpenter 2006(Carpenter et al., 2006), Kerssemakers 2006(Kerssemakers et al., 2006)
	Dynamic response	Jiang 2008(Jiang et al., 2008), Vogt 2008(Vogt, 2008), Sept 2010(Sept and MacKintosh, 2010), Xiang 2013(Xiang and Liew, 2013), Liew(Liew et al., 2011)

	Strain rate dependent failure mechanism	Ahmadzadeh 2014(Ahmadzadeh et al., 2014), Ahmadzadeh 2015(Ahmadzadeh et al., 2015)
	Severing mechanism	Theisen 2013(Theisen et al., 2013), Theisen 2012(Theisen et al., 2012)
	Oscillation modes and collapse, structure instability	Kasas 2004(Sandor Kasas et al., 2004), Kis 2002(Kis et al., 2002), Pablo 2003(de Pablo et al., 2003), Schaap 2006(Schaap et al., 2006), Kasas 2004(S Kasas et al., 2004)
	Viscoelastic response	Xiang 2012(Xiang and Liew, 2012), Adnan 2015(ADNAN et al., 2015), Ahmadzadeh 2014(Ahmadzadeh et al., 2014), Ahmadzadeh 2015(Ahmadzadeh et al., 2015), Shamloo 2015(Shamloo et al., 2015)
Tau Protein	Tau-water interaction	Fichou 2015(Fichou et al., 2015)
	Phosphorylation effect on mechanical behavior	Jho 2010(Jho et al., 2010), Lyons 2014(Lyons et al., 2014)
	Electrostatic properties	Rosenberg 2008(Rosenberg et al., 2008), Castro 2019(Castro et al., 2019), Battisti 2012(Battisti et al., 2012; Battisti and Tenenbaum, 2012)

	Aggregation behavior	Dulak 2018(Dułak et al., 2018)
NF	Phosphorylation effect on sidearms	Adiga 2010(Adiga and Brenner, 2010), Jayanthi 2013(Jayanthi et al., 2013), Stevenson 2011(Stevenson et al., 2011)
	Conformational properties and dynamic behavior	Stevens 2010(Stevens and Hoh, 2010), Stevens 2011(Stevens and Hoh, 2011)
	Effect of charged portion in structure and sidearm-sidearm interaction	Chang 2009(Chang et al., 2009), Kumar 2002(Kumar et al., 2002), Stevens 2011(Stevens and Hoh, 2011)
	Effect of ionic strength and pH	Zhulina 2007(Zhulina and Leermakers, 2007a)
	Effect of protein composition	Zhulina 2010(Zhulina and Leermakers, 2010)
MF	Extensional and torsional stiffness	Matsushita 2012(Matsushita et al., 2012), Matsushita 2010(Matsushita et al., 2010)
	Torsional rigidity, Persistence length	Fan 2012(Fan et al., 2012)
	Importance of crosslinks on structure and network behavior	Kim 2009(T Kim et al., 2009), Holzapfel 2014(Holzapfel et al., 2014), Unterberger 2013(Unterberger et al., 2013a)
	Effect of actin binding and severing on stiffness and flexibility	Claessens 2006(Claessens et al., 2006)

	Nucleotide state effect on conformational structure	Zheng 2007(Zheng et al., 2007), Pfaendtner 2009(Pfaendtner et al., 2009), Dalhaimer 2008(Dalhaimer et al., 2008), Lee 2011(Lee et al., 2011)
	Characterization of dynamics by behavior	Deriu 2012(Deriu et al., 2012b)
	Filament heterogeneity	Fan 2012(Fan et al., 2012)
	Mechanical deformation	Yogurtcu 2012(Yogurtcu et al., 2012)
	Vibration and shear response	Kim 2009(T Kim et al., 2009), Li 2015(Li, 2015)
	Viscoelastic behavior	Unterberger 2013(Unterberger et al., 2013b)

From Table 1.2 it is evident that studies on MT and MF are comprehensive. However, the specific aspects which have not been studied in detail, but possible by using computational maneuver are:

a. Tau: Rate-dependent mechanical properties, domain focused and residue focused phosphorylation effect on stiffness, strain rate effect, and viscoelastic behavior.

b. NF: Rate-dependent mechanical properties, viscoelastic characterization.

Therefore, it can be asserted computational approaches will be promising to address the limitations in such areas. We can also argue that the purposes mentioned in the introduction section of this manuscript is fulfilled in the sense that we have particularly found out the current standings and accomplishments of the

existent works on neural cytoskeletal components, and determined two areas of limitations which might be addressed by using computational (specifically molecular level simulation studies) approach.

1.6 Studies Performed to Address Current Limitations

The comprehensive literature review should be sufficient for the reader to be convinced that computational study is a reasonable way to handle the cytoskeleton problems, and that we require further insight on tau protein and NF. We have completed four studies and shown them in the following chapters as an attempt to address the lacking in our understanding on tau protein, NF, and actin-spectrin structure in the axonal cytoskeleton of neuron. The studies we have undertaken are:

1. Strain rate effect on tau,
2. Phosphorylation effect on tau,
3. Strain rate effect on NF, and
4. Viscoelastic modeling of tau and NF,
5. Mechanical behavior of actin-spectrin structure.

Completion of these studies, to the best knowledge of the author, has answered several unanswered questions regarding the structural behavior and response of tau, NF, and periodic axonal cytoskeleton lattice. From a broader perspective, these studies have provided important insight on mechanical behavior of the major axonal cytoskeletal components of neuron, paved the pathway for bottom-up axon modeling, and overall mechanical aspect of the cytoskeleton.

CHAPTER 2

EFFECT OF STRAIN RATE ON TAU PROTEIN

2.1 Introduction

Blast-induced TBI has been considered highly significant on the battlefield and in sports (Okie, 2005; Taylor and Ford, 2009). Numerous studies have been performed to address this injury mechanism and consequences from different perspectives, such as post-traumatic stress disorder, aggregation of neurological disorders, damage threshold of cytoskeletal components, etc. When head is impacted by blast-like mechanical force, the resulting pressure wave transmits to the interior of the brain. A major part of brain's interior is built on over 100 billion of neuron cells and its surrounding extra-cellular matrices. Structurally, a single neuron is composed of a soft cell body (soma), fibrous dendrite branches, and an axon fiber. Both axons and dendrites are supported by the cytoskeleton, which is primarily composed of neurofilaments, microfilaments, tau proteins and microtubules. Of these, the mechanical behavior of microfilaments and microtubules have been studied in depth, and of neurofilaments has been studied partially in the past. However, mechanical response of tau protein and its interaction with MT have not been studied in detail. One reason is the structural disorder in tau protein. It is known as an intrinsically disordered protein implying a definitive structural conformation of this protein is unavailable. As such, fundamental understandings of the responses of single tau protein, polymerized tau protein and tau-microtubule interfaces under high-rate mechanical forces are very important. Yet, comprehensive mechanical behavior of tau protein and tau-MT interaction are not available in the literature.

As tau protein is an intrinsically disordered protein (IDP), a brief introduction on IDP is relevant for this study. Intrinsically disordered proteins (IDP) are special proteins involved in many different cell-signaling pathways within the cell. They have unique capabilities of performing different functions based on conformations that occur due to different post-translational modifications, different binding substrates

(proteins, nucleic acids, fibers, etc.) and fewer of the order-promoting amino acids found within hydrophobic cores of proteins. These include tryptophan, cysteine, tyrosine, leucine, phenylalanine, isoleucine, and valine. On the other hand, the amino acid make-up of an IDP commonly includes an abundance of amino acids associated with disorder, including alanine, arginine, glycine, glutamine, serine, proline, glutamate, and lysine (Jorda et al., 2010). In recent years, IDPs have been more prominent in biomedical research in an effort to understand their variable roles. This paper discusses tau, which is heavily involved in Alzheimer's Disease (AD), but Parkinson's disease (alpha-synuclein), Amyotrophic Lateral Sclerosis (superoxide dismutase-1), and Huntington's Disease (poly-glutamine gene products) are also caused by IDPs (Uversky, 2010). Without stable conformations and singular, defined functions, IDPs are prone to aggregation and once aggregated, burden the cell's degradation machinery.

After clarification on IDPs, we can move on to the specific introduction on their deformation characteristics and mechanical behavior. Some recent works seek to obtain mechanical properties of MT or analyze the mechanism of damage and failure of axonal microtubules (Wells and Aksimentiev, 2010; Wu and Adnan, 2018). The structural unit of MT (the αβ-tubulin) has been determined earlier by electron crystallography (Nogales et al., 1998). Further studies have shown that there are two distinct sites at the C-terminal on each subunit, to which tau protein can be attached. One of them is the C terminal site, which contains the C-terminal 12 amino acids of MT, and another one is the internal site, which is situated at the last 1-3rd of C-terminal excluding the last 12 amino acids. Tau interacts with the C-terminal site by R1 or R1-R2 interrepeat, and with the internal site by the rest of the MT binding sites (R2-R4). It has also been proposed that tau-MT interaction can take place in two manners: i. tau may interact with only α or β subunit of an MT by the mechanism above or ii. tau may interact with both portions of α and β subunits (one with R1 or R1-R2 interrepeat, another with R2-R4) (Chau et al., 1998). Further studies on localization of tubulin binding sites for tau protein (Maccioni et al., 1988; SERRANO et al., 1985) strengthened the finding of Chau et al. As important is MT as an individual cytoskeletal component, so are the crosslinks between them, which are denoted by microtubule associated proteins (MAP), mainly tau. Tau is an intrinsically

disordered protein (IDP), and has no defined secondary structure (Rosenberg et al., 2008). However, there are numerous predictor software for obtaining secondary structures of proteins, such as i-TASSER (Zhang, 2008), Phyre2 (Kelley et al., 2015), etc. which can predict the structures of IDPs with a certain level of confidence. The details of the mechanism of predicting secondary structures is out of the scope of this manuscript, although relevant discussion is presented in the supplementary material.

Numerous studies regarding tau specifically discuss on phosphorylation and hyperphosphorylation, which are post-translational modifications. There have been separate studies on tau structure, which suggest that phosphorylation level plays a critical role to distinguish healthy tau from pathological tau (Becker and Przybylski, 2007), and it also has been hypothesized to alter the ability of tau to bind MTs as well as other functionalities (Hanger et al., 2009). Earlier Monte Carlo simulation study that has attempted to find out the threshold of tau pathology suggested that numerous candidate amino acids can be phosphorylated, but under pathological conditions around 7 of them are actually phosphorylated (Jho et al., 2010). The abnormally phosphorylated tau proteins are 3-4 times more phosphorylated than the normal ones, and ~2 sites per mole of tau protein can be phosphorylated in normal condition (Kenessey and Yen, 1993). Recently, cryo-EM technology has been able to obtain 3-4Å resolution image of paired helical filaments (PHF) in AD affected brains (Fitzpatrick et al., 2017), which is directly related to abnormal phosphorylation in tau.

Not only phosphorylation and dephosphorylation are relevant, but also the strain rate dependent structural response of tau regarding this study. In some simulation studies of microtubule bundles cross-linked with tau protein, the response under different levels of uniaxial tension for different distributions of cross-links and discontinuities have been observed, and the estimated Young's modulus used for calculation was 5MPa (Peter and Mofrad, 2012), although they have admitted that it is decidedly approximate, and tau-tau, tau-MT, etc. interactions are important candidates to determine the mechanical behavior. Their model showed that bundle failure occurred due to failure of cross-links. Tau proteins, through complementary dimerization with other tau proteins, form bridges to nearby microtubules to form bundles (Mandelkow et al., 1995). The

tau proteins have edge-to-edge distance of 20nm and hexagonal packing (Chen et al., 1992). Furthermore, computational models have been built to study the behavior of cytoskeletal filaments (Chandran and Mofrad, 2009; Mofrad, 2008) and cross-linked networks have also been investigated (Claessens et al., 2006; Taeyoon Kim et al., 2009; Silber et al., 2004). Earlier computational and theoretical models have shown that shear resistance provided by the cross-linked network greatly increases MT bending stiffness (Tolomeo and Holley, 1997), and found bundle stiffness regime (Bathe et al., 2008). Discrete bead-spring models have been widely used to build filament and network structure (Rodney et al., 2005; Sandersius and Newman, 2008). In another finite element analysis, the Young's Modulus of tau protein was assumed to be 5MPa (Shahinnejad et al., 2013), but elevated to 62.5 MPa in order to reduce the flexural behavior so that the spring constant can be the same as Peter et al (Peter and Mofrad, 2012). The tensile test results reasonably agree with that of Peter et al., and it also analyzed the behavior of bundle under torsion. Prior continuum and computational axon modeling gives us useful insights on tau protein, such as viscoelastic shear lag model (Ahmadzadeh et al., 2014), failure mechanism of axon study (de Rooij and Kuhl, 2018), and so on. The computational continuum models and rate-dependent tests can determine the properties of the cytoskeletal components such as microtubules, and therefore are relevant to the current study.

The structure and phosphorylation studies cannot depict the complete structural and functional scenario of tau, because another critical aspect of tau protein is the MT binding region, which can work as a backbone of the structure and from which the projection domain can spread around (Lee et al., 1989). Some recent studies have further clarified the position and structure of MT binding sites in tau, such as Rosenberg et al (Rosenberg et al., 2008). Each of the four binding regions of tau is around 18 amino acids (AA) long, separated by interrepeats of 13-14 AA length. The positively charged repeat or interrepeat region is believed to facilitate electrostatic interactions between tau and negatively charged surface of MT (Chau et al., 1998; SERRANO et al., 1985; Silber et al., 2004). In the N-terminal of the MT binding region, there is a positively charged and proline-rich region, which has phosphorylation sites responsible for the regulation of MT association to taus (Goode et al., 1997; Trinczek et al., 1995). The other portions of tau protein have

significant functionalities as well, such as the N-terminal region, which can contain zero to two negatively charged inserts (each 29AA long). The N terminus and proline-rich region make up the projection domain of tau protein, which extends outward from the MT surface and determines inter-MT distance in MT bundles (Chen et al., 1992). Other studies show that MT binding with tau is very fast, does not depend on the MT location in the axonal shaft and varies with MT curvature (Samsonov et al., 2004). Study of intrinsically disordered tau protein folding on MT shows that tau locally folds into a stable structure upon binding (Trinczek et al., 1995).

Aside from studying standalone tau protein response, our interest is to obtain insight on tau-MT interaction. Tau protein organization on MT can be described as a coating or surface decoration, as suggested by some works (Santarella et al., 2004). The mode of tau protein binding with MT has been studied, and it suggests that tau protein binds along as well as across protofilaments (Al-Bassam et al., 2002).

Now, while considering a feasible approach to computationally determine single tau, dimerized tau, and tau-MT behavior, we must consider the earlier studies that have been performed on intrinsically disordered proteins (IDPs). Therefore, by focusing on computational studies on IDPs (especially on tau proteins), we have found that recent years have observed significant improvement in computational studies by using predicted structure. Notable examples are electrostatic study (Castro et al., 2019). and aggregation behavior study on tau (Battisti et al., 2012). However, studies focusing on mechanical response of tau are still non-existent.

Based on the existing literature as discussed above, there are certain parameters yet undetermined, such as stiffness of single tau filament, required stretching for separation of dimerized tau proteins, tau-MT binding strength and whether MT subunit binding between themselves is stronger than tau-MT bond, etc. This study attempts to address these specific questions using atomistic computational method called molecular dynamics (MD). The rationale behind choosing this tool are twofold: 1) reliable experimentation at this length scale is rare and 2) MD is an appropriate tool to capture the molecular details of the elements involved. Specifically, for the single tau, we have obtained the secondary structure from i-TASSER

predictor software (Zhang, 2008). For dimerized tau, we have made the model with overlapped projection domain as depicted by Rosenberg et al (Rosenberg et al., 2008). For tau-MT interaction, we have used Chau et al proposals of interaction, where tau can interact with one or both subunits of MT (Chau et al., 1998). The effects of high strain rate on the deformation mechanism of single tau, dimerized tau and tau-MT interface are studied.

2.2 Method

The tau protein structure is obtained from the i-TASSER predictor software (Zhang, 2008). We have used the model with the C score of 1.06 (the C score is determined based on significance of threading template alignments and the convergence parameters of the structure assembly simulations) which we have assumed satisfactory for an IDP. For single tau protein, we have solvated the obtained structure with TIP3P water using CHARMM-GUI (Jo et al., 2008) solvator and quick-MD simulator modules. Required number of 0.15M KCl ions were added to obtain charge neutralization for explicit solvent simulations. The dimerized model was created by using UCSF Chimera (Pettersen et al., 2004), in which we have overlapped the projection domains of two identical tau proteins. We have used implicit solvent technique of CHARMM (Best et al., 2012) in LAMMPS (Plimpton, 1995) (pair_style lj/charmm/coul/charmm/implicit command) for dimerized tau, which facilitates a bigger box size, faster calculation and convenient observation of two tau system. The implicit solvent computes with a modification of adding an extra r^{-1} term for Coulombic energy calculation and skipping long range Coulombic energy calculations.

The MT structure is obtained from the existing model built by Wells et al (Wells and Aksimentiev, 2010), each subunit of which has one GTP or a GDP, along with one Mg^{2+} ion in the junction. By repeating the helically arranged 13 subunits periodically along the length direction, we have created a virtually infinite MT (similar methodology has been followed in the work of Wu et al for MT study (Wu and Adnan, 2018)). The tau-MT interaction system was created by placing the tau binding sites in close proximity to the MT

binding sites as proposed by Chau et al (Chau et al., 1998). We have used the implicit solvent technique for tau-MT as described above for dimerized tau.

With periodic boundary conditions in all three directions, we have equilibrated the structures for all cases (single tau, dimerized tau and tau-MT) for 100ps to minimize the potential energy at a targeted temperature of 310K. Single tau, dimerized tau and tau-MT contained 6424, 12848 and 33292 atoms respectively. The LJ potentials are used with inner and outer cutoff of 10Å and 12Å, respectively. Long range coulombic interactions are computed by pppm style, facilitating a particle-particle particle-mesh solver with a 3d mesh.

We have used CHARMM36 (Best et al., 2012; Brooks et al., 2009; MacKerell et al., 1998) potential parameters with appropriate CMAP corrections (Best et al., 2012) for all the simulations. Potentials for GDP and GTP are taken from that of ADP and ATP respectively (Wells and Aksimentiev, 2010). The equilibration was performed in NVT canonical ensemble, with the temperature damping parameter of 100fs.

In single tau protein tensile tests, we have fixed the MT binding domain and pulled the projection domain at different strain rates (10^8-$2x10^9$ s^{-1}) along x axis. For dimerized tau, we have fixed the MT binding domain of one protein and pulled away another binding domain along x axis (10^9 $s^{-1}$and $2x10^9$ s^{-1}). For tau-MT, While keeping the upper and lower few layers of atoms fixed of the MT, the tau protein was pulled away by few atoms of the projection domain (strain rate: 10^9 s^{-1} and $2x10^9$ s^{-1}). For the relevance of the simulations with explicit water molecules as solvent vs implicit water molecules, readers may refer to the supplementary materials of Wu et al (Wu and Adnan, 2018). Although biomolecule simulations are more realistic with explicit solvation, we have adopted implicit technique for dimerized tau and tau-MT due to the high box size required for the high stretch, and for convenient observation of unfolding, stretching and separation.

The stress-strain plots are obtained by the per-atom stress calculation and summation in LAMMPS. However, as the output is in (pressure x volume) unit, we must divide the obtained stress value by the volume of the protein (or certain portion of the protein). The general formulation used by stress per atom command is $P = (P_{xx}+P_{yy}+P_{zz})/ (3xV)$, where P_{xx}, P_{yy} and P_{zz} are the summations of stress/atom values for

all atoms in x, y, and z direction respectively, and V is the summation of volume of the atoms of the protein being considered. The approximated volume was obtained by Voronoi cell approximation, adapted from LAMMPS voro++ package (Rycroft, 2009). The strain is simply obtained by the displacement of the atoms from the initial position. All the tensile tests are performed in NVT ensemble, with 100fs temperature damping parameter. The visualizations of the tensile tests are carried out by OVITO software (Stukowski, 2010).

All of the simulations were carried out by the STAMPEDE2 supercomputer of Texas Advanced Computing Center (TACC).

2.3 Results

2.3.1 Single Tau Deformation

For the single tau model, we have performed the tensile tests at four different strain rates: 10^8, 5×10^8, 10^9 and 2×10^9 s^{-1}. The MT binding region atoms are fixed, and first few atoms of the projection domain are pulled at –x direction. The calculated stress-strain graphs are shown in Fig. 2.1.

It can be observed that the stress-strain response of a single tau can be divided into two regions - the "unfolding" and "stretching" regions. It is known that a typical tau protein has a tertiary "folded" structure, that is, a stable conformation of the filament with multiple folds in the structure. When the mechanical load is applied, first the folds disappear one after another because of breaking of the electrostatic and van der Waals forces between the folded portions of the filament (this phenomenon will be called as "unfolding" onwards in this manuscript). However, the mentioned forces are relatively weaker than chemical bonds, as they are merely the result of proximity and positioning (3D confirmation of the structural portions in space). Therefore, during the unfolding region (see Fig. 2.1) no significant rise of stiffness is observed. However, after the filament is free of the folded regions, the structurally linear filament will be deformed against the relatively stronger covalent bonds (this phenomenon will be called as "stretching" onwards in this study).

Therefore, in this region there will be higher stress developed and significant rise in stiffness will be observed, as shown in the "stretching region" in Fig. 2.1. The unfolding and stretching phenomena are clarified by simplified schematic in Fig. 2.2 as well.

In Fig. 2.1, multiple distinct slopes can be observed that reflect the stiffnesses of tau protein at different strain-states. Up to ~200% tensile strain, the slope is very small implying a relatively low unfolding stiffness of tau. After the unfolding is complete, we can observe pure stretching of the covalent bonds. Unfolding stiffness obtained from the strain of 0%-150%, while stretching stiffness is obtained from the strain of 200%-300% where another distinct change of slope is observed. Fig. 2.2 shows the unfolding and stretching snapshots. The unfolding stiffness and pure stretching stiffness values are shown in Table 2.1. According to Table 2.1 and Fig. 2.1, it can be inferred that a single tau exhibits viscoelastic behavior to some extent, and that its stiffness is strongly dependent on strain rate. With the increment of strain rate, tau acts as a stiffer material in both the unfolding and stretching zone, which is expected for viscoelastic soft biomaterial. The slope is in the Mega Pascal range: 0.5GPa or ~500MPa. From the existent literature we have not found any validated estimate of the stiffness of the projection domain of tau, but we have detail information regarding the stiffness of other cytoskeletal components, such as MT and microfilaments. Deformation studies and viscoelastic shear lag models of MT show that the MT stiffness can be in the giga pascal range (Ahmadzadeh et al., 2014; Peter and Mofrad, 2012). Studies on microfilament show that their stiffness can vary from few mega pascals to >2GPa (Higuchi et al., 1995a; Huxley et al., 1994a; Kim et al., 2015; Kojima et al., 1994a; Wakabayashi et al., 1994a). Therefore, we can assume that our results obtained for the tau protein stiffness, both in unfolding and stretching region, are reasonable.

Table 2.1: Unfolding stiffness and stretching stiffness of the projection domain of single tau

Strain Rate (s^{-1})	Unfolding Stiffness (MPa)	Stretching Stiffness (GPa)
10^8	50.1	0.076
$5x10^8$	129	0.549
10^9	284.9	1.198
$2x10^9$	500.5	2.399

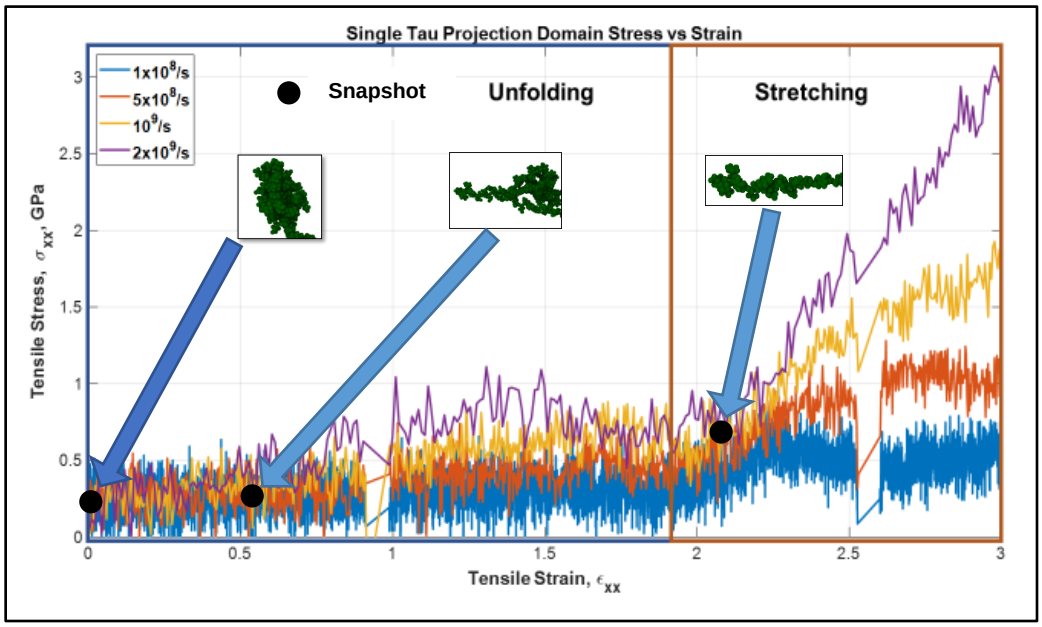

Figure 2.1: Stress vs strain plot of single tau projection domain. Up to ~200% strain, the protein keeps unfolding, and after that a sharp rise in the slope is observed, suggesting the pure stretching of covalent bonds. Unfolding and stretching zones are shown by rectangular boxes.

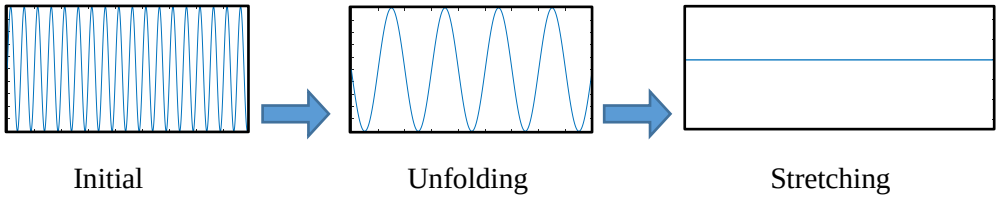

a. Simplified schematic for protein unfolding and stretching

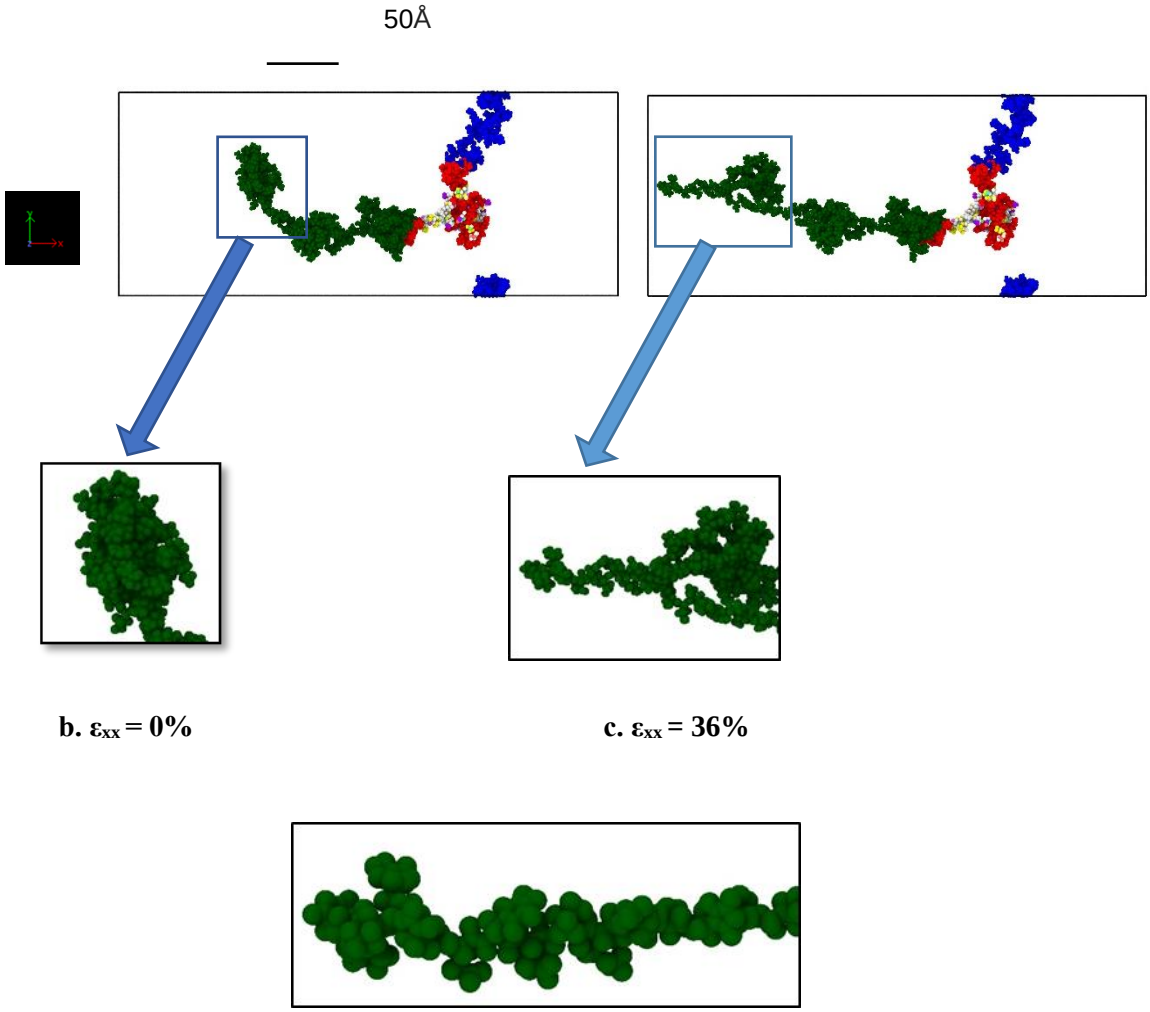

b. $\varepsilon_{xx} = 0\%$ **c. $\varepsilon_{xx} = 36\%$**

d. $\varepsilon_{xx} = 206\%$

Figure 2.2: a. Simplified schematic for tau protein unfolding and stretching. Initially, there are multiple folding (which are distinct from each other). When loading is applied, the van der Waals force and electrostatic force between the folded portions are broken, and therefore the structure unfolds. At extreme

strain, the structure becomes free of all the folds, and stretch to a relatively linear filament. b. Initial single tau structure (strain = 0%), c. tau protein being unfolded due to pulling at 10^9 s^{-1} (strain = 36%), d. tau protein being stretched (strain = 206%, only the projection domain is shown for the convenience of visualization). Color legends: green: projection domain, red: MT binding region, blue: N terminus or tail, white and the rest: interrepeats between the MT binding regions. The enlarged snapshots are for the first ~1100 atoms for convenient visualization. Water molecules are not shown.

2.3.2 Dimerized Tau Deformation

The dimerized tau model was similar to the single tau, except that we have fixed the MT binding site of one tau and pulled away the binding site of another tau to observe the developed stress and possible sliding out of tau projection domain at extreme strain. We have plotted the stress-strain curves (calculation procedure was similar to single tau) for the projection domain of the tau protein that has been pulled at the x direction, at the strain rate of 10^9 s^{-1} and $2x10^9$ s^{-1}. The implicit-solvent dimerized tau model shows several stages of tension during the test. We are referring to the protein with fixed MT binding region as protein 1, and the protein being pulled as protein 2. The stages observed are (for the strain rate of $2x10^9$ s^{-1}): i. Unfolding of protein 2 (up to 163% strain), ii. Stretching of protein 2 (up to 257% strain), iii. Unfolding of protein 1 (up to 334% strain), iv. Stretching of protein 1 (up to 395% strain), v. Disentanglement of the overlapped projection domains of the tau proteins (up to 721% strain), vi. Sliding out or projection domain along with stretching (very fast, occurs at around 722% to 758% strain region), and vii. Separation of proteins (~758% strain). For strain rate of 10^9 s^{-1}, the separation occurs just above the stretch of ~800%. Therefore, the observations imply that the separation of dimer also depends on the strain rate, and at a certain high strain rate, the separation occurs significantly early, although the stretch following the unfolding seems the same for both strain rates. It is to be noted that the separation stretch that are mentioned here are the percentage of strain at which the two dimers are visibly separated from each other, although the pulling away of one

tau from another starts earlier (around 30% of strain earlier), and before complete separation there are sub-stages of untangling of the overlapped projection domains of the two tau proteins.

Fig. 2.3a shows the stress-strain curves of the projection domain of protein 2 and Fig. 2.4 shows snapshots of the stages observed. The single tau study on this paper already shows that tau is highly stretchable. Therefore, when we are considering dimerized protein model, it is expected for both proteins to be highly stretched before the observation of sliding out of one projection domain out of another. This set of simulation provides new insight about shear mechanism and sliding threshold of dimerized tau, which is yet non-existent in literature. Fig. 2.3b shows the potential energy trend, and how the potential energy decreases drastically at the separation, irrespective of applied strain rate.

a

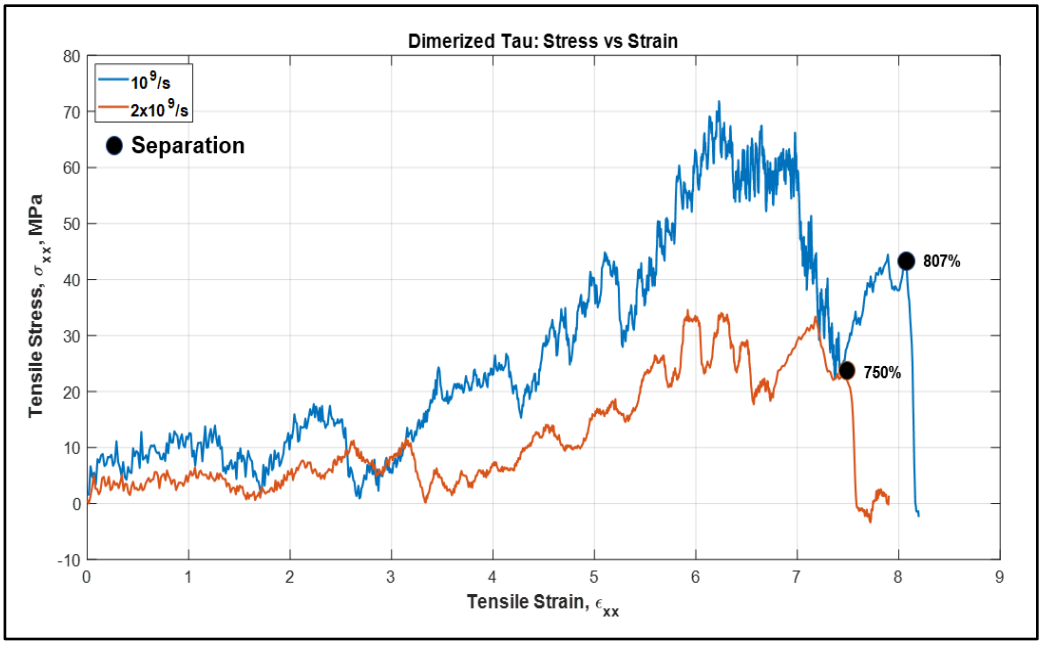

b

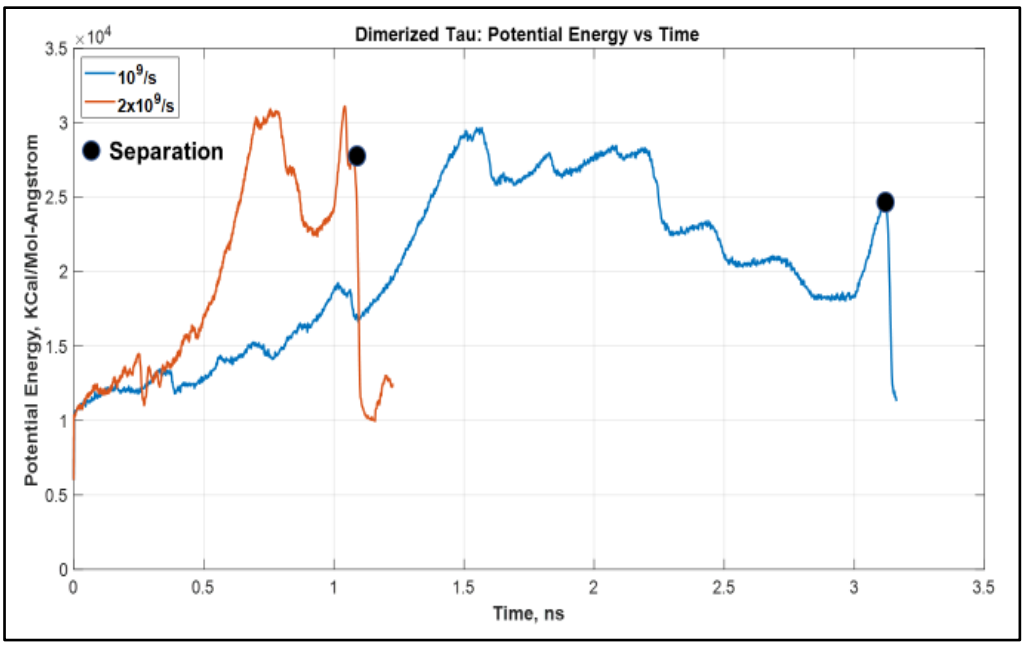

Figure 2.3: a. Stress-strain plot of protein 2 projection domain for two different strain rates. At lower strain rate, we observe development of stress at higher value and delayed separation, and vice versa. b. Potential energy vs time plot for the system.

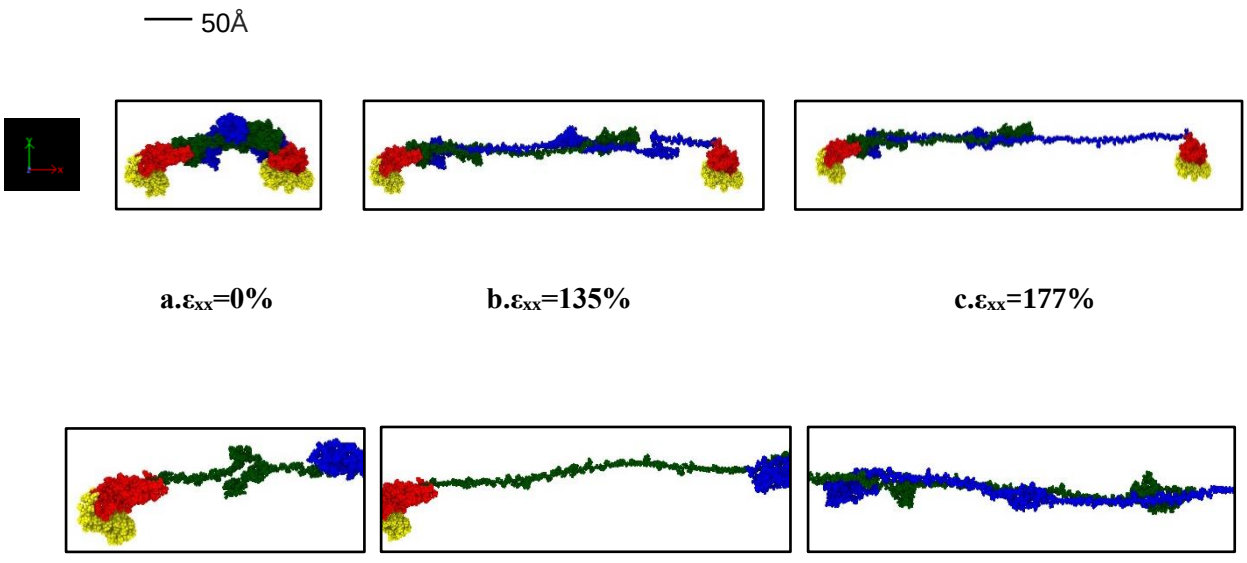

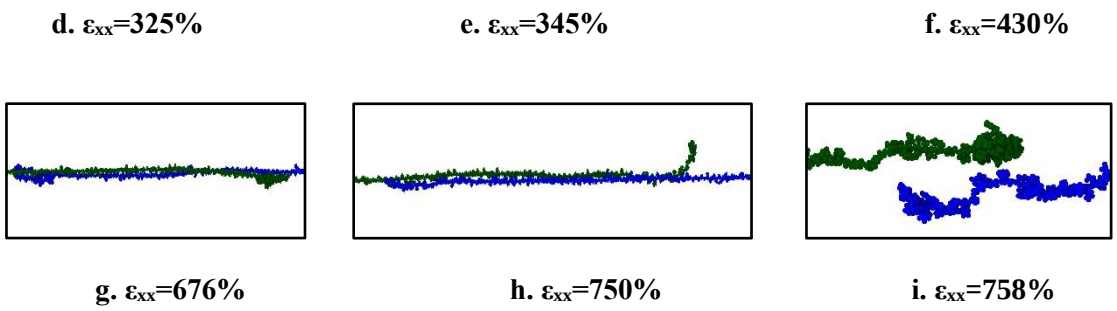

Figure 2.4: Stages observed during the pull of one protein in the dimerized tau model (for the strain rate of $2x10^9$ s^{-1}). a. Initial stage (strain: 0%), b. Unfolding of protein 2 (strain: 135%), c. Stretching of protein 2 (strain: 177%), d. Unfolding of protein 1 (strain: 325%), e. stretching of protein 1 (strain: 345%), f. Disentanglement of the overlapped projection domains of the tau proteins (strain: 430%), g. Continued disentanglement (strain: 676%), h. Sliding out of projection domain (strain: 750%), i. Separation of proteins (strain: 758%). Color legends: Green: Projection domain of protein 2, Blue: projection domain of protein 1, Red: MT binding region (including the interrepeats) for protein 1 and 2, Yellow: N terminal tails of protein 1 and 2.

2.3.3 Tau-MT Interaction

In order to determine the nature of single tau-MT interaction, one N-system MT adopted from Wells et al (Wells and Aksimentiev, 2010) was used. One tau protein MT binding site was attached to the surface of the MT. The tensile test results were quite straight-forward: the stretching is followed by unfolding in the projection domain of the tau structure, and even at these extreme strain rates, tau had to be stretched for >11 times of its initial length before getting completely separated from MT. The unfolding and stretching manners are similar to the single and dimerized tau tests, that is, projection domain gets unfolded for a long time, then gets significantly stretched, leading to eventual separation from the MT surface. As we have seen in case of the dimerized tau models, we observe earlier separation at higher strain rate and vice versa for

tau-MT models. We can conclude from the two strain rate results that at a certain strain rate range, the tau can be stretched significantly while still being attached to the MT surface. On the other hand, at higher strain rate, it is not allowed to be stretched in that manner, depicting the effect of strain rate. In the dimerized tau, we have observed development of higher stress in tau before final separation for lower strain rate. However, in tau-MT interaction, we have not observed any significant difference in the stress-strain trend for the two different strain rates, rather only in the separation stretch. The untangling sub-stages also take place before separation, as we have observed in dimerized tau. Fig. 2.5a shows stress-strain graphs for the applied strain rates, and Fig. 2.5b shows the potential energy graph, which suggests that potential energy decreases significantly at separation, for both cases. Fig. 2.6 shows various significant stages during pulling of single tau away from MT surface.

Lastly, we are also interested to find out the strain rate dependent nature of dimerized tau-MT interaction. We have attached a dimerized tau on the surface of MT in a similar way of single tau-MT model, and applied high strain rate. This simulation was to compare the relative strength of tau-MT bond to tau-tau bond, and as the simulation shows, tau-tau bond is much stronger than tau-MT bond, because although the pulled tau was stretched significantly at the higher strain rate (~360% before separation from MT surface), it did not disentangle from the other tau. Rather, the entire dimerized structure got separated from MT surface, suggesting that tau-tau bond is stronger than tau-MT bond. For the lower strain rate, the dimerized tau subunits got significant sliding over each other, but eventually got separated from the MT surface before getting entirely separated from each other (~825% before separation). Fig. 2.7 shows that potential energy significantly reduces at separation, and Fig. 2.8 shows different significant stages up to and at separation.

a

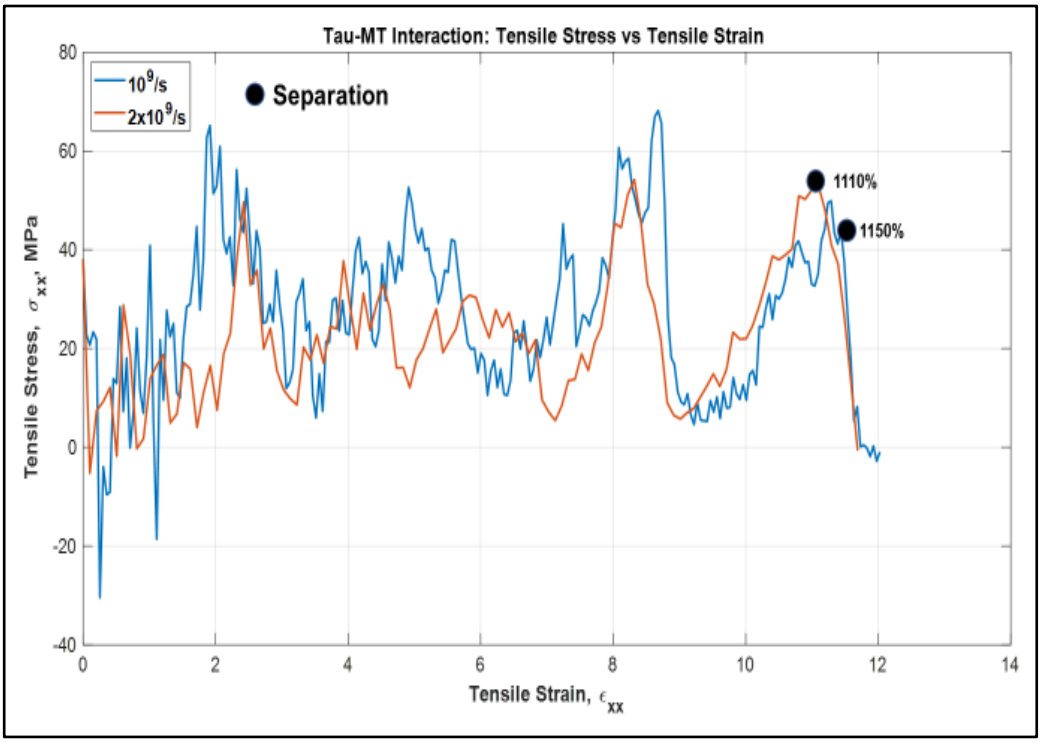
Tau-MT Interaction: Tensile Stress vs Tensile Strain
10^9/s
2x10^9/s
Separation
1110%
1150%
Tensile Stress, σxx, MPa
Tensile Strain, εxx
80
60
40
20
0
-20
-40
0
2
4
6
8
10
12
14

b

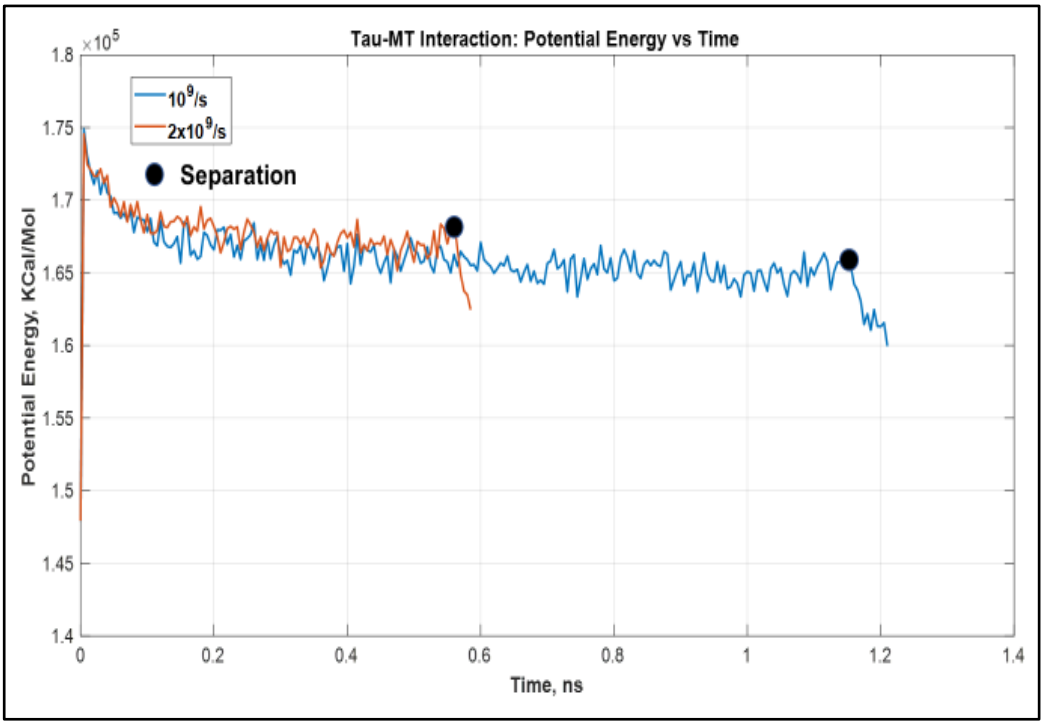

Figure 2.5: a. Stress vs Strain graph for the projection domain of tau during the pulling at different strain rates. The stress-strain trends are similar for both the strain rates, although the separation occurs at different strain. b. Potential energy vs time plot for the single tau-MT system.

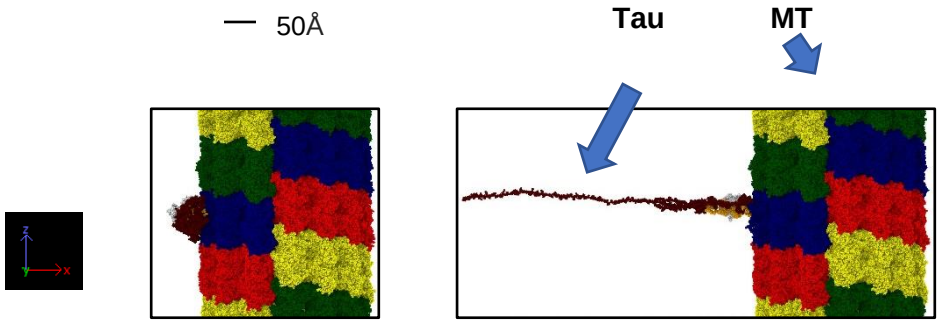

a. ε_{xx}=0% **b. ε_{xx}=409%**

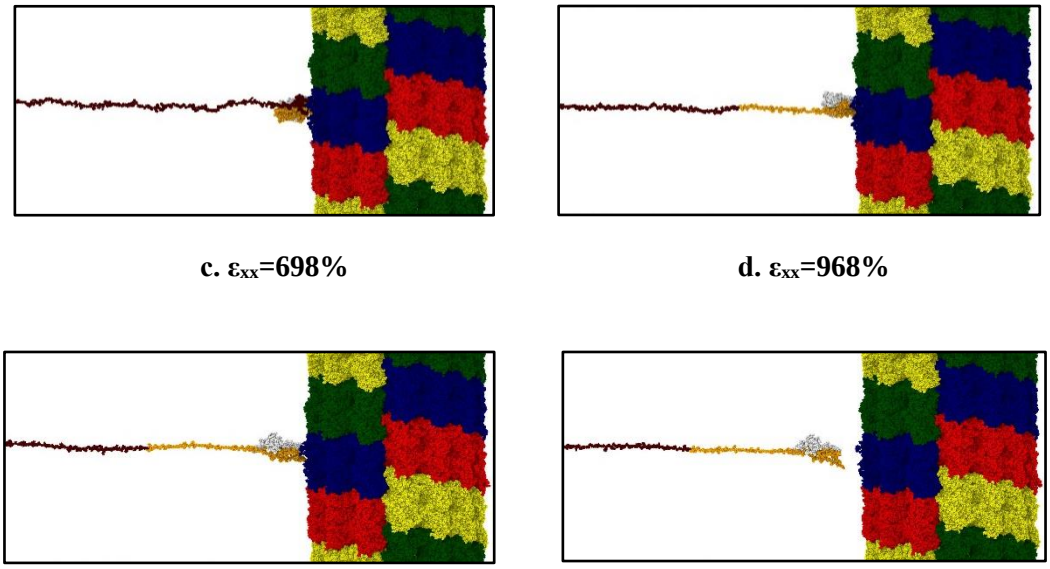

c. ε_{xx}=698% **d. ε_{xx}=968%**

e. ε_{xx}=1108% **f. ε_{xx}=1128%**

Figure 2.6: Observation during the pulling of single tau towards the -x direction (strain rate: $2x10^{9}$ s^{-1}) away from MT surface. a. Initial stage (strain: 0%), b. unfolding of tau projection domain (strain: 409%), c. stretching of tau projection domain (strain: 698%), d. stretching of MT binding region (strain: 968%), e. onset of separation (strain: 1108%), f. after complete separation (strain: 1128%). Color legends: Red, blue, green and yellow: repeating helical units of MT, maroon: projection domain of tau, orange: MT binding site atoms of tau (including the interrepeats), white: N terminus tail of tau.

a

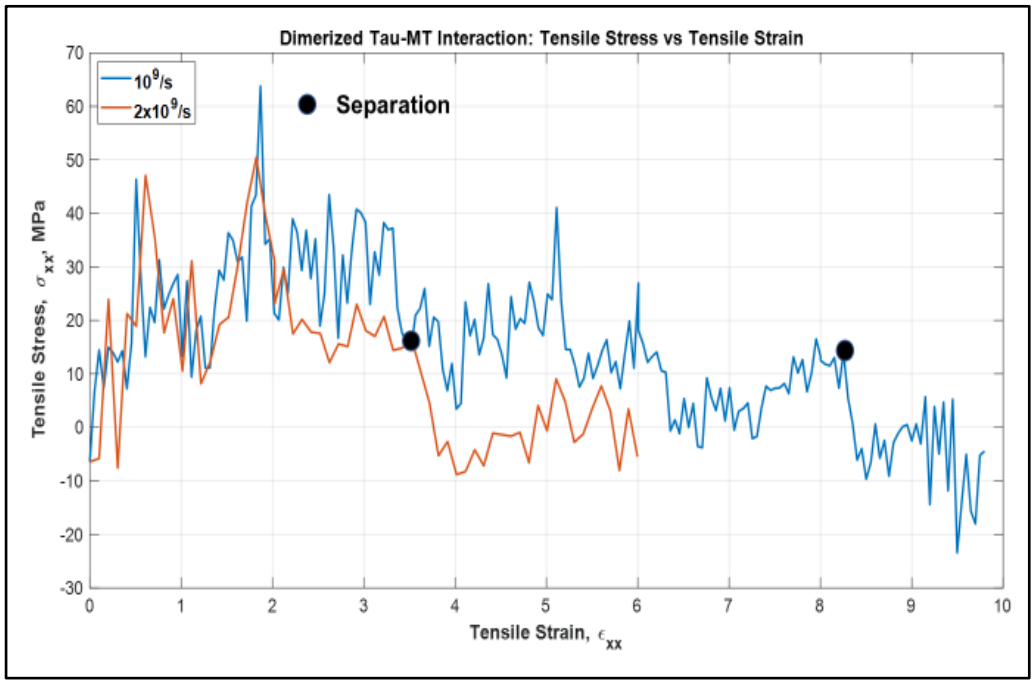
Dimerized Tau-MT Interaction: Tensile Stress vs Tensile Strain
10^9/s
2x10^9/s
Separation
Tensile Stress, σxx, MPa
Tensile Strain, εxx
70
60
50
40
30
20
10
0
-10
-20
-30
0
1
2
3
4
5
6
7
8
9
10

b

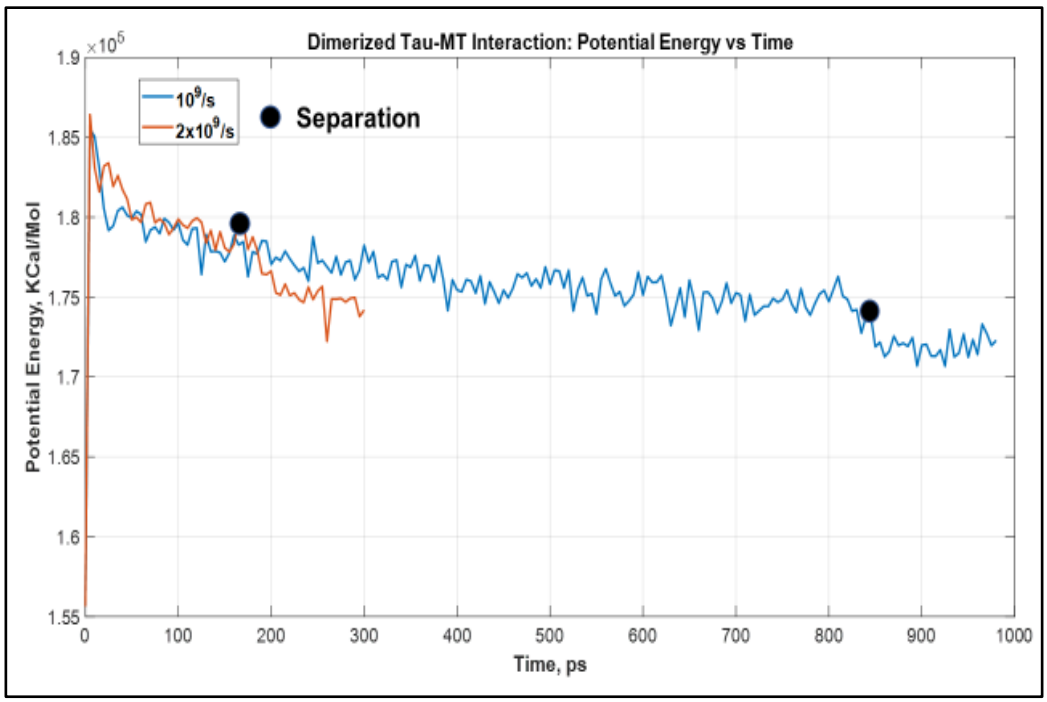

Figure 2.7: a. Stress vs Strain graph for the projection domain of tau during the pulling at different strain rates. The separation occurs early for higher strain rate (~360%), and much later for lower strain rate (~825%). b. Potential energy vs time plot for the dimerized tau-MT system. As expected, potential energy drastically reduces at separation (~360% strain for $2x10^9$ s^{-1}, ~825% strain for $1x10^9$ s^{-1}). For both cases, tau-tau bond is stronger than tau-MT bond.

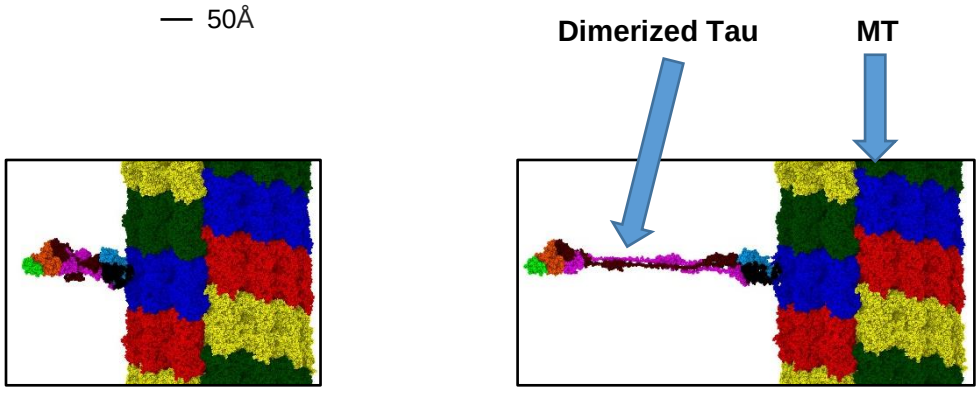

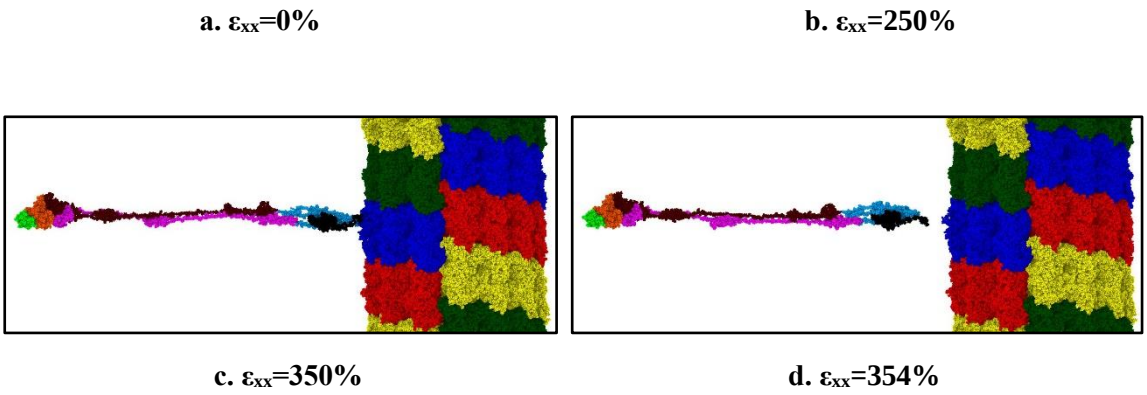

Figure 2.8: Observation during the dimerized tau pulling away from the MT surface (-x direction, strain rate: $2x10^9$ s^{-1}). a. Initial stage (strain: 0%), b. unfolding and stretching of tau (strain: 250%), c. onset of separation (strain: 350%), d. after separation (strain: ~354%). Color legends: Red, blue, green and yellow: repeating helical units of MT, maroon: projection domain of tau 1, orange: MT binding site atoms of tau 1(including the interrepeats), light green: tail domain of tau 1, purple: projection domain of tau 2, light blue: MT binding site atoms of tau 2(including the interrepeats), black: tail domain of tau 2.

2.4 Discussion

In this study, we have analyzed the response of tau protein and tau-MT interaction from a strictly mechanical point of view. We have performed tensile tests on a predicted structure of tau protein to determine the single tau projection domain stiffness, dimerized tau separation stretch, tau-MT separation stretch, and comparison between tau-tau vs tau-MT bond. For a disordered protein, the confidence score (C-score) of -0.03 has been assumed as reliable in our simulation. The detail of quantification of the reliability for a protein structure predicted by i-TASSER (Zhang, 2008) is discussed in the supplementary material of this manuscript.

Admittedly, the strain rates that we have applied fall into high to very high range, but it facilitates us to obtain an insight of sub-axonal level response of this particular neural cytoskeletal component. In reality,

the tissue level loading might be lower than the cellular level stress, meaning moderate level blow on the head may lead to high level tissue deformation, which eventually leads to extreme level of stress and failure in sub-axonal level components, supported by recent finite element method (FEM) studies on axon (Cloots et al., 2011, 2010). These studies show that axonal level anisotropy and cellular level heterogeneity might play instrumental role to determine failure criteria of the components, and injury level. Also, this level of strain rate is justified in the scenario of cavitation bubble collapse or blast wave exposure, which leads to intensely high stress in sub-axonal component (Wu and Adnan, 2018).

Earlier studies which modeled MT response under mechanical loading did not incorporate tau protein with detail mechanical properties, rather studied MT protofibril response where tau protein is considered as a viscoelastic spring (Ahmadzadeh et al., 2014), the properties of which were adapted from earlier characterization of pro- and anti-aggregant conformations of tau protein obtained by single molecule force spectroscopy (SMFS) (Wegmann et al., 2011). However, this study characterizes the response of only mutant conformation of the "repeat domain of tau", not the projection domain which is susceptible to unfolding and stretching under the application of high strain rate. Therefore, the current study is an effective extension of previous SMFS study with more comprehensive insight. In general, SMFS studies show the stretch of a molecule from force vs displacement perspective focusing on the detachment peak force at the contour length of the molecule used, but in TBI scenario, a more relevant representation is using directional stress vs strain which can perfectly differentiate between the unfolding and stretching region of a protein under pure mechanical loading.

For dimerized tau, we have re-generated the dimerized tau structure with overlapped projection domains depicted in the study of Rosenberg et al (Rosenberg et al., 2008). This study particularly established the importance of projection domain which determines the inter-MT distance in axonal bundle, as the tau-tau interaction is dependent on the length of projection domain, and interaction with a surface can be adhesive to repulsive (or a combination of both) based on the configuration. This study highlighted on the tau-tau interaction and tau-mica interaction, and substantiated that the interaction force is a function of projection

domain length. The current study undertakes the missing aspect of the study: effect of shear that the dimerized conformation is susceptible to when undergoing through a high mechanical stress. Essentially our study shows that the projection domains of dimerized tau proteins are strong against shear and sliding force, and that the scenario it undergoes in strictly mechanical loading is highly dynamic, consisting both unfolding and stretching of both proteins. It further fortifies the observation that proline-rich region and N terminus combination, which is the projection domain, is highly stretchable while in the dimerized conformation, although the individual tau proteins might reach the failure region earlier. This specific observation shows that mere electrostatic and van der Waals bonds between the negatively charged N terminal region of one tau protein and positively charged prolin-rich region of another tau protein are sufficient to withstand mechanical loading to significant extent. This mechanical behavior of tau is also highlighted in the MT modeling work performed earlier, where one of the key prediction is that tau protein may elongate differently, and according to the position along the MT bundle (Ahmadzadeh et al., 2015, 2014). This high ability of tau protein to stretch aligns with another prediction of the study, that is, tau elongation facilitates the sliding of MT. The increased rigidity of the prolin-rich region can also be held responsible for the particular behavior of tau projection domain as suggested by NMR spectroscopy studies (Mukrasch et al., 2007).

The tau-MT model in the current study is developed as per the proposal of Chau et al, which shows specific MT binding sites on tau can facilitate bonding with tau binding sites on MT (Chau et al., 1998; Nogales et al., 1998). The proposal suggests that tau-MT interaction is highly dynamic, and that one MT binding region can interact with one or both subunits of MT (α and β). In our model, the tau protein has been attached to the specific location of the helically arranged protofibril to ensure that tau interacts with the C-terminal site by only R1 or R1-R2 interrepeat, and with the internal site by the rest of the MT binding sites (R2-R4), which was the scheme suggested by Chau et al. This is a relevant representation of a TBI scenario, where the sub-axonal level stretch on the cytoskeletal component is high for a significant timespan, but tau-MT bond is sufficiently strong to withstand mechanical load as long as the entire projection domain is not

stretched. As stretching does not occur before unfolding of all the conformed portions of the projection domain, the MT structure instability is not invoked before the directional stress is developed in the MT binding region. The “jaw interaction” between the flanking domain of tau protein and acidic outside of MT surface is also responsible for such strong affinity, as seen between the projection domain and MT (partially), tail domain and MT (fully), suggesting that tau-MT bond is strong irrespective of the intervention of MT binding sites, which is proposed by earlier NMR studies (Mukrasch et al., 2007). However, in our case, both the intervention of flanking region and MT binding region are present, which facilitates stronger bond, as suggested by separate study (Preuss et al., 1997). Similar to dimerized tau system, this set of simulations shows that the interaction between charged portions (MT binding sites of tau and C-terminal as well as last 1/3rd portion of the C-terminal region excluding the terminal 12 amino acids) provides significant mechanical strength, even when susceptible to high to very high strain rate.

Finally, the dimerized tau-MT interaction system was a representation of more comprehensive scenario of TBI, in which there is a competition between the mechanical strength of tau-tau and tau-MT bond. As all of the involved regions in this case are charged (prolin-rich region of tau, negatively charged N-terminus region of tau, negatively charged outside surface of MT, etc.), we can assume that electrostatic interaction is more important in this case than the van der Waals bonds. The dimerized tau-MT bond shows that it requires development of more stress in tau-tau interaction region than required in tau-MT region, which suggests that prolin-rich region interaction with negatively charged projection domain is stronger than negatively charged MT surface interaction with positively charged MT binding sites, and under high strain rate, we can expect tau separation from MT surface. In case of multiple occasion of tau separation from MT surface in a single injury phenomenon, it may lead to the MT system collapse before the tau system collapse, as tau actually folds into stable conformation upon binding with MT (Kadavath et al., 2015).

As tau protein contains prolin-rich region, it is highly relevant to study its characteristics and assesses its behavior from neurodegenerative disease perspective. The importance of such prolin-rich proteins have been evident in separate neurodegenerative disorder studies (Gladkevich et al., 2007; Sochocka et al., 2019).

These proteins are heavily implicated in neurodegenerative diseases and traumatic brain injury, which tau is also involved in. The PRR is a speculative binding site in proteins, so future studies could include protein biochemistry experiments focused on protein-protein interactions.

Evident from the strength of the tau-MT bond demonstrated in this paper, despite having a fast binding kinetics, we suggest that the intrinsic disorder of tau facilitates this phenomenon. Tau regularly alters its conformation, so its inherent flexibility is a likely source of the protein's ability to remain bound despite increased strain rate. We suggest tau absorbs the strain throughout its length and relies on the strong capability of the projection domain to remain bound to the microtubule during events where the brain undergoes significant strain and stretch. The strength of the tau-MT bond is particularly important for the field of traumatic brain injury, where strain and axonal stretch is thought to be a primary mechanism of injury in traumatic brain injury (Chung et al., 2005). Future studies might include studying comparing the IDP-substrate bond of other IDPs to see if the high bond strength is a common feature across IDPs as compared with ordered proteins.

Lastly, it is also evident from our MD simulation study that incorporation of physical chemistry perspective (such as posttranslational modification like domain focused or residue focused phosphorylation) along with the mechanical viewpoint is important to obtain comprehensive insight on tau protein behavior. Also, in all the tensile tests, tau protein has shown the dependence on the applied strain rate as single tau behaves as a stiffer material at higher strain rate in both unfolding and stretching region and dimerized tau separation and tau-MT separation stretches have shown strong dependency on strain rate, which suggests the importance of a separate study of viscoelastic characterization of tau protein.

2.5 Conclusion

In this study, we have computationally determined the stiffness of projection domain of single tau protein and dimerized tau proteins, and the strength of tau-MT interface. From our MD simulations, the major findings can be summarized as below:

1. Single tau protein is highly stretchable and shows viscoelasticity. It shows unfolding to a great extent before being purely stretched. The unfolding stiffness range is between 50MPa and 500MPa, while stretching stiffness can be >2GPa. The stiffness in both regions increases with the increment of the strain rate.

2. Dimerized tau-tau bond is strong, and the dimer structure does not dissociate before being stretched at >7.5 times of the initial length.

3. Tau protein can be separated from MT only at very high stretch (>11 times of the initial length of tau), and tau-MT bond is stronger than the MT subunit bond. Also, from the dimerized tau-MT simulation, we have obtained that tau-tau bond is stronger than tau-MT bond. We can hypothesize about mechano-chemical events which can trigger MT-tau separation, which have the timescale(s) than MD simulation can capture.

4. Strain rate affects the separation stretch and developed stress in tau for dimerized tau model, while it only affects the separation stretch significantly for tau-MT model. Higher strain rate causes early separation, and vice versa.

Bottom-up computational modeling of axon requires mechanical characterization of individual components, and therefore, this study provides required insight on the strain rate dependent mechanical behavior of individual tau protein as well as tau-MT interface interaction. In injury biomechanics area and especially in multiscale traumatic brain injury (TBI) studies, these findings will play instrumental role to determine damage criteria at sub-axonal level. This molecular dynamics simulation study particularly finds out sub-axonal level response of neural cytoskeletal components, which are relevant to TBI scenario, where nanoscale injury propagates (axonal damage, MT instability, tau unfolding and stretching, tau-MT

separation) due to macroscale impact (head injury). To obtain more comprehensive insight on tau, we intend to perform studies incorporating physical chemistry parameters, and viscoelastic characterization.

CHAPTER 3

EFFECT OF PHOSPHORYLATION ON TAU PROTEIN

3.1 Introduction

Phosphorylation has been associated with traumatic brain injury (TBI), dementia, Alzheimer's disease (AD), formation of paired helical filaments (PHF) and neurofibrillary tangles (NFT) in tau and other neurodegenerations (Hawkins et al., 2013; Shultz et al., 2015). It can occur in different ways in tau, and while some modes can alter electrophoretic mobility of tau, some other modes cannot; and phosphorylation is correlated to AD PHF, causing cytoskeletal alterations (Baudier and Cole, 1987). Specifically, tau in AD brain is abnormally phosphorylated protein component of PHF (Grundke-Iqbal et al., 1986). Therefore, it has gained attention in the recent years in cytoskeletal modeling studies. In this section, we will discuss the effect of phosphorylation and dephosphorylation that incorporates significant structural and chemical changes to cytoskeletal components, especially on tau-MT interaction.

As tau protein is an intrinsically disordered protein (IDP), a brief introduction on IDP is relevant for this study (repeated in relevance, earlier discussed in our work on tau protein response under strict mechanical loading). Intrinsically disordered proteins (IDP) are special proteins involved in many different cell-signaling pathways within the cell. They have unique capabilities of performing different functions based on conformations that occur due to different post-translational modifications, different binding substrates (proteins, nucleic acids, fibers, etc.) and fewer of the order-promoting amino acids found within hydrophobic cores of proteins. These include tryptophan, cysteine, tyrosine, leucine, phenylalanine, isoleucine, and valine. On the other hand, the amino acid make-up of an IDP commonly includes an abundance of amino acids associated with disorder, including alanine, arginine, glycine, glutamine, serine, proline, glutamate, and lysine (Jorda et al., 2010). In recent years, IDPs have been more prominent in

biomedical research in an effort to understand their variable roles. This paper discusses tau, which is heavily involved in Alzheimer's Disease (AD), but Parkinson's disease (alpha-synuclein), Amyotrophic Lateral Sclerosis (superoxide dismutase-1), and Huntington's Disease (poly-glutamine gene products) are also caused by IDPs (Uversky, 2010). Without stable conformations and singular, defined functions, IDPs are prone to aggregation and once aggregated, burden the cell's degradation machinery.

After clarification on IDPs, we can move on to the specific introduction on phosphorylation effect on such proteins. Phosphorylation means attachment of a phosphoryl group to a molecule, and it has been considered important in protein functionalities, along with its counterpart named dephosphorylation. Phosphorylation has been shown to affect the activity of tau in vitro and microtubule associated protein activities in vivo, and it can be obtained by several protein kinases (Lindwall and Cole, 1984). Identification of the phosphorylated sites in abnormally phosphorylated protein samples is the approach to identify the respective kinases or phosphatases involved (Goedert et al., 1989). Cause of phosphorylation has been hypothesized as the function of several kinases and phosphatases (Churcher, 2006; Mazanetz and Fischer, 2007). Numerous studies have suggested that phosphorylated taus are less effective than non-phosphorylated ones on MT polymerization (Biernat et al., 1993; Bramblett et al., 1993; Cleveland et al., 1977). It has also been found as a developmentally regulated phenomenon (Dudek and Johnson, 1995; Mawal-Dewan et al., 1994; Ono et al., 1995), or in elaboration, we can say that extent of phosphorylation in fetal tau can be compared to that of PHF tau from AD PHF (Kenessey and Yen, 1993).

More importantly, it has been hypothesized to alter the ability of tau to bind microtubules (Buée et al., 2000), though the specific mechanism of phosphorylation in this regard is uncertain. Electron micrography study shows that dephosphorylated tau can facilitate rapid polymerization of microtubules (Lindwall and Cole, 1984), and also that partially purified microtubules contain kinase which is capable of re-phosphorylation of tau. The current conjecture is that the role of more than one enzymes (candidate kinases) might be related to phosphorylation and alteration of MT binding, and that kinase inhibitors can control the process of hyperphosphorylation, although existent review work admits that roles of MT associated kinases

and phosphatases are yet to be fully described (Billingsley and Kincaid, 1997), and it is not clear how many of them participate in tau phosphorylation in vivo (Buée et al., 2000). However, some specific studies have marked some kinases as related to controlling phosphorylation, such as GSK3, CDK5, MARK, etc. (Ferrer et al., 2005; Mazanetz and Fischer, 2007; Noble et al., 2005). Some studies on bovine and rat brains have shown that Calcium/calmodulin (CaM) dependent protein kinases can phosphorylate taus which is similar to AD lesions (Mandelkow and Mandelkow, 1998).

Phosphorylation "level" has been hypothesized as an important marker of tau pathology, because it is at different levels in normal (or healthy) tau, fetal tau, adult tau and AD affected brains (Brandt and Lee, 1993), and in general is related to the detachment from MTs, leading to changes in MT dynamics (Ballatore et al., 2007). Tau protein itself is a biomarker of AD, and both total and p-taus are increased in such disorders, as suggested by CSF studies (Sjögren et al., 2001). Experimentally it is found that levels of normal tau is significantly reduced in brain supernate from AD cases, or in other words, abnormally phosphorylated taus are increased in pathological scenarios (Khatoon et al., 1994; Köpke et al., 1993). Abnormal phosphorylation has been related to PHFs and AD and other neurodegenerative diseases, and therefore has obtained focus (Selkoe, 1991). However, there are some conflicting results in existence, which suggest that PHFs can be formed in a phosphorylation-independent manner also (Goedert et al., 1996). This "developmental regulation" aspect of phosphorylation is to be given proper attention, as different states of phosphorylation are observed in fetal and adult tau, and AD-like state similar to the fetal tau (Watanabe et al., 1993).

There have been separate studies on tau structure, which suggest that phosphorylation level plays a critical role to distinguish healthy tau from pathological tau (Becker and Przybylski, 2007), and it also has been hypothesized to alter the ability of tau to bind MTs as well as other functionalities (Hanger et al., 2009). Earlier Monte Carlo simulation study that has attempted to find out the threshold of tau pathology suggested that numerous candidate amino acids can be phosphorylated, but under pathological conditions around 7 of them are actually phosphorylated (Jho et al., 2010). The abnormally phosphorylated tau proteins are 3-4

times more phosphorylated than the normal ones, and around 2 sites per mole of tau protein can be phosphorylated in normal condition (Kenessey and Yen, 1993). Recently, cryo-EM technology has been able to obtain 3-4Å resolution image of paired helical filaments (PHF) in AD affected brains (Fitzpatrick et al., 2017), which is directly related to abnormal phosphorylation in tau. Total tau vs p-tau studies, in order to find CSF biomarkers for diagnosis of AD, have been plenty, and in general suggested that p-tau is higher in AD affected brains (Mulder et al., 2010). Differential diagnosis of AD with cerebrospinal fluid (CSF) levels of tau phosphorylated at Thr-231 showed that the level is significantly higher in AD affected samples (Buerger et al., 2002). Another study also showed that CSF level of tau phosphorylated at Ser-396 and Ser-404 can be diagnostic marker of AD (Hu et al., 2002). Also, separate CSF study on patients suggested in a similar way, that phosphorylated tau (p-tau) level is higher in AD brain than normal control group (Kandimalla et al., 2013). Therapeutic approaches targeting tau have recently focused on inhibiting tau fibril formation or dissolution of pre-existing aggregates, and thus preventing aberrantly phosphorylated and/or misfolded tau from forming more organized aggregates (Pickhardt et al., 2005). It is also believed that dephosphorylation is related to regaining MT functions and structural integrity (Ballatore et al., 2007). Furthermore, some phosphorylation related studies using separate phosphorylation dependent antibodies show that severity of the tau pathology (formation of PHF and NFT) can be related to this process in AD affected brains (Mandelkow et al., 1995).

Also, there are separate studies in existent literature that focus on phosphorylation of specific residue (such as Ser-262), which show that certain serine phosphorylation can strongly reduce binding of tau to MTs (Biernat et al., 1993) (Biernat et al). Early studies showed that different serine residue such as Ser-199, Ser-202, Ser-409, Ser-396 and threonine residues such as Thr-231 are phosphorylated in NFTs (Götz et al., 1995). Phosphorylation in Ser-202 has been suggested to recapitulate phosphorylation in developmental stage (Goedert et al., 1993). Thr-181 has been related to AD in separate researches, where phosphorylated Thr-181 quantification has been analyzed (Haense et al., 2008; Ravaglia et al., 2008; Vanmechelen et al., 2000). A review work has also found hyperphosphorylation in PHFs in general (Götz et al., 1995). In vivo

experiments has shown that green fluorescent protein (GFP) tau attaches with MT in a phosphorylation-dependent manner (Samsonov et al., 2004). Critical site-based phosphorylation (such as in Ser-262, Thr-231, Ser-396) studies show that it can reduce MT binding and form aggregation of tau, and also can be developmentally regulated (Biernat et al., 1993; Bramblett et al., 1993). Quantification of binding of MT with tau is determined by the stoichiometry, or number of tubulin dimer attached to tau in phosphorylated state – the results of which suggested that phosphorylation can significantly reduce the stoichiometry, and creating mutated isoform by switching Ser-262 with an Alanine residue showed less sensitivity to phosphorylation, making it an important regarding tau-MT interaction. These studies also strengthen the argument that the residues can be phosphorylated by activity of more than one kinase and assert that although phosphorylation in many candidate amino acids (AA) is possible, certain phosphorylated residues can have major effect on MT binding.

However, these studies also admit that the causal relationship between phosphorylation in specific site and reduced binding ability to MT, or pathology is debatable. Studies on monoclonal antibodies have been manifold, because it has been found that PHF tau reacts with certain antibodies in a phosphorylation-dependent manner, and these studies have suggested that phosphorylation in Ser-199 and/or Ser-202 might be related to switch of normal tau to AD-like state tau in a reversible manner (Biernat et al., 1992). Although it might seem that phosphorylation in single sites can lead to decreased level of MT binding, this phenomenon is thought as insufficient to eliminate MT binding altogether (Seubert et al., 1995). Also, phosphorylation mechanism can be more complex than depicted in the above discussion focusing on the effect of phosphorylation of specific sites, because in abnormal condition (PHF tau), clustering can occur to the sites, giving multiple phosphorylated peptides with possible mutually exclusive combinations of phosphorylation (Goedert et al., 1992). As there are numerous putative phosphorylation sites in tau, and in AD more than 30 sites are phosphorylated which are determined by mass spectrometry, identification of critical sites (which are involved in converting normal tau to a pathological one) is difficult. However, some studies have shown that Ser-262, Thr-231 and Ser-235 inhibits the binding to MT by ~35%, ~25% and

~10% respectively (Iqbal et al., 1989). Other studies suggest that candidate critical sites can be Ser-199/202/205, Thr-212, Thr-231/Ser-235, Ser-262/356 and Ser-404, while Thr-231, Ser-396 and Ser-422 can promote self-assembly of tau into filaments (Alonso et al., 2004) (quantification comes from phosphate per mole of tau studies, which suggests that 4-6 phosphates/mol of protein indicates pathology). The residue-specific studies suggest that MT binding domain and its vicinity are the most important candidates to examine the effect of phosphorylation, especially the R1-R2 inter-region, which is also the most potent region for MT polymerization (Goode and Feinstein, 1994; Panda et al., 1995). Site-specific phosphorylation can lead to loss of MT binding, and weakening of the neuronal cytoskeleton (Mandelkow et al., 1995). Specific domain-focused studies have targeted MT binding site residues to observe the phosphorylation effects (Scott et al., 1991). However, such studies are not conclusive, because the structural integration and disintegration mechanism is highly complex and modulated by other parameters than tau phosphorylation (Avila, 1990). Dephoshorylation has been found to restore the ability of PHF to bind, but it is not clear how phosphorylation sites outside the MT binding region can regulate tau-MT interactions (Garver et al., 1996).

We have already mentioned computational studies performed on tau-MT interaction as well. The other aspects of Monte Carlo simulation of tau-MT showed that due to charged nature of MT, electrostatic interaction is important to analyze their behavior, and while amino acids in tail domain of tau stay mostly apart from the MT surface, in bulk solution dephosporylated taus are separated due to coulomb repulsion between similarly charged isoforms, and moderate phosphorylation can decrease average intermolecular distance between dephosphorylated and phosphorylated taus, leading to their overlap (Jho et al., 2010).

Based on the discussion above, phosphorylation can be considered as a biomarker for decreasing tau-MT bonding, but deeper investigations are still needed on the parameters and mechanisms that control phosphorylation. There are different mechanisms, such as O-glycosylation which are hypothesized to negatively regulate phosphorylation, and believed to be involved in AD (Liu et al., 2004; Yuzwa et al.,

2008). Such investigations have suggested that reduced O-glycosylation can lead to hyperphosphorylation and eventually, the disorders we have mentioned above.

There are certain limitations in the studies on phosphorylation effect, although numerous studies exist in literature. To mention a few, the studies cannot clarify the mechanisms of the effect of phosphorylation on residues outside MT binding region, they cannot conclusively answer the zone-based phosphorylation effect and pathological threshold of tau protein, and they cannot form any specific causal reason between phosphorylation in specific sites and reduced tau-MT interaction. Furthermore, similar phosphorylation state can be observed in normal and diseased taus – which clearly indicate that phosphorylation is not a stand-alone parameter to determine pathology. This study attempts to answer certain questions which were incompletely or not answered in earlier studies on domain-focused or residue-focused tau studies, such as how the mechanical stiffness of single tau is altered due to phosphorylation in different domains, how the required stretch for separation in dimerized tau is affected by this phenomenon, or how the tau-MT interaction is changed (tau-MT interaction studies have proposed several probable mechanism including hyperphosphorylation in specific residues leading to decreased tau-MT binding, but inconclusively).

The MD simulations in the current study are designed accordingly: for single tau, we have obtained the secondary structure from i-TASSER (Zhang, 2008) predictor software and applied phosphorylation on relevant sites using CHARMM-GUI (Jo et al., 2008) to imitate phosphorylated condition. For domain focused phosphorylation, we have applied phosphorylation in different domains, while for residue focused phosphorylation, we have applied phosphorylation in specific residues (details in the "Method" section). For dimerized tau, we have made the models with overlapped projection domains as depicted by Rosenberg et al (Rosenberg et al., 2008). For tau-MT interaction, we have used Chau et al proposals of interaction, where tau can interact with one or both subunits of MT (Chau et al., 1998). We have applied phosphorylation to the dimerized and tau-MT models in the similar manner as single tau models. In the results and discussions section, we discuss on the tensile tests performed on all the models in detail.

3.2 Method

Tau protein has three domains in its structure: projection domain, MT binding domain, and tail domain. The projection domain of one tau creates electrostatic zipper bond with the projection domain of another tau – resulting in dimerized tau (Rosenberg et al., 2008). Furthermore, tau proteins attach themselves onto the surface of MT through the MT binding domain (Chau et al., 1998). Therefore, while designing tensile tests, there are three scenarios to be considered: first, single tau projection domain unfolding and stretching needs to be differentiated based on the applied strain rate; second, dimerized tau separation strain needs to be determined, and third, the tau-MT separation stretch needs to be determined. These specific scenarios are relevant to TBI scenario, as while susceptible to TBI, single tau projection domain gets significantly stretched, dimerized tau proteins become vulnerable to stress development in their overlapped projection domain areas, and tau gets stretched which leads to separation from MT surface. It is also important to differentiate their mechanical behavior according to their phosphorylated states. Therefore, in single tensile tests, we have stretched single tau projection domain while keeping the MT binding region fixed. In dimerized tau system, we have pulled the MT binding domain of one tau protein while keeping the MT binding domain of another tau. In tau-MT system, we have pulled the tau projection domain from MT surface, and determined at what strain the MT binding domain of the tau gets separated from the MT surface. At the end of the Method section, Table 3.2 shows the simulation box sizes used in this study.

By going through the recent computational approaches on intrinsically disordered proteins (IDPs), we have found that recent years have observed significant improvement in computational studies by using predicted structure. Notable examples are electrostatic study (Castro et al., 2019) and aggregation behavior study on tau (Battisti et al., 2012). The method used here is the similar to our earlier work on single tau, dimerized tau and tau-MT interaction models, except that we have incorporated new models with phosphorylation in different domains of tau to observe how chemical effects withstand extreme mechanical loading. It is already substantiated by recent review study that such molecular level study on mechanical behavior is required to obtain a comprehensive insight regarding tau (Khan et al., 2020a).

In the current study, the tau protein structure is obtained from i-TASSER predictor software. We have used the model with the C score of -0.03 (the C score is determined based on significance of threading template alignments and the convergence parameters of the structure assembly simulations) which we have assumed satisfactory for an IDP. We have used the quick-MD simulator module from CHARMM-GUI for applying phosphorylation. Phosphorylation was applied to these Serine (SER) residues for domain focused phosphorylation: a. for projection domain: 46, 56, 61, 64, 68, 113, 129, 131, 137, 184; b. for MT binding sites: 258, 262, 285, 289, 293, 305, 316, 320, 324, 341; and c. for N-terminus tail: 396, 400, 404, 409, 412, 413, 416, 422, 433, 435. Finally, for the set with phosphorylation in all domains, we mean that all the SER residues mentioned above are phosphorylated simultaneously. In case of residue focused phosphorylation, we have selected 7 residues which have been found at phosphorylated state widely in case of neuropathology such as formation of PHF or AD. These selected residues consist of six serine (SER) residues: 199, 202, 262, 396, 404, 409, and Threonine (THR) residue 231. The selection was made according to earlier studies, the reference list of which is shown in Table 3.1. We have focused on the residues which are found to have decreased tau-MT bonding in one or more studies.

Table 3.1: Selection of phosphorylation sites in tau protein based on earlier studies

Critical Phosphorylation Site	Reference No.
Ser199, Ser202, Ser396, Ser409, Thr231	(Biernat et al., 1992; Mandelkow and Mandelkow, 1998; Mandelkow et al., 1995; Pickhardt et al., 2005; Santarella et al., 2004; Trinczek et al., 1995)

Thr181	(Biernat et al., 1992; Fitzpatrick et al., 2017; Goedert et al., 1992, 1989; Götz et al., 1995)
Thr231	(Buerger et al., 2002; Haense et al., 2008)
Ser396, Ser404	(Bramblett et al., 1993; Hu et al., 2002; Kenessey and Yen, 1993)
Ser199, Ser202, Ser262	(Trinczek et al., 1995)
Ser199, Ser202, Ser205, Ser235, Ser262, Ser356, Thr212, Thr231	(Biernat et al., 1993; Goedert et al., 1993; Iqbal et al., 1989; Seubert et al., 1995)
R1-R2 inter-region	(Buée et al., 2000)

The dimerized model was created by using UCSF Chimera (Pettersen et al., 2004), in which we have overlapped the projection domains of two identical tau proteins. We have used implicit solvent technique of CHARMM in LAMMPS (pair_style lj/charmm/coul/charmm/implicit command) for the tensile tests of dimerized tau and tau-MT interaction, which facilitates a bigger box size, faster calculation and therefore, convenient observation of the protein systems we have built, at the cost of more realistic scenario of explicit water molecules, which would be computationally demanding at our required box sizes. The implicit solvent mechanism computes with a modification of adding an extra r^{-1} term for Coulombic energy calculation, which depicts a simpler calculation method for unsolvated biomolecules. The reader can find the relevance of using implicit solvent simulation for such cytoskeletal systems from the supplementary material of Wu et al (Wu and Adnan, 2018).

For domain focused phosphorylation, the MT structure is obtained from the existing model built by Wells et al (Wells and Aksimentiev, 2010). We have used the N system described in the paper, in which there are helically organized four subunits (two α, two β) and the same type of subunits are placed beside each other, each having one GTP or a GDP, along with one Mg^{2+} ion in the junction. The tau-MT interaction system was created by UCSF Chimera as well, where the tau binding sites are placed in close proximity of the MT binding sites as proposed by Chau et al (Chau et al., 1998). For residue focused phosphorylation, we have attached the MT binding sites of two different tau proteins on the MT surface, one being normal and the another phosphorylated at the 7 residues. The full MT structure is obtained by periodically repeating the helical structure along the length direction, creating a virtually infinite MT. In the accumulation test, we have created four (4) systems: 2 tau system, 3 tau system, 4 tau system, and 6 tau system. The 3 tau system is the reference system, while 2 tau system is created by removing the second protein from the 3 tau system, 4 tau system is created by offsetting protein 1 at 40Å distance in z-direction, 6 tau system is created by offsetting protein 1, 2, and 3 at 40Å distance in z-direction. In the reference 3 tau system, the tau proteins are placed in random orientation, in the vicinity of each other and in presence of explicit water molecules, and then equilibrated for 1ns at 310K NVT ensemble. The equilibration setting is the same for 2, 4, and 6 tau systems.

For the tensile tests, with periodic boundary conditions in all three directions, we have equilibrated the structures for all cases (single tau, dimerized tau and tau-MT) for 100ps to minimize the potential energy at a targeted temperature of 310K. Single tau, dimerized tau and tau-MT contained ~6400, ~12800 and ~33000 atoms respectively (the exact number of atoms varied according to the level of phosphorylation). The LJ potentials are used with inner and outer cutoff of 10Å and 12Å, respectively.

We have used CHARMM36 (Best et al., 2012; Brooks et al., 2009; MacKerell et al., 1998) potential parameters with appropriate CMAP corrections (Buck et al., 2006) for all the simulations. Potentials for GDP and GTP are taken from that of ADP and ATP respectively (Wells and Aksimentiev, 2010). The equilibration was performed in NVT canonical ensemble, with the temperature damping parameter of 100fs.

Tensile tests are performed in different manners for domain focused and residue focused phosphorylation. In the tensile test on single tau, we have fixed the MT binding domain and pulled the projection domain along x axis. For dimerized tau, we have fixed the MT binding domain of one protein and pulled away the MT binding domain of another protein along x axis. For tau-MT, we have fixed the microtubule subunits (the portions that are opposite of the tau binding sites on them) and pulled away the tau protein. Tau-MT tensile tests are done at high strain rate ($2x10^9$ s^{-1}). However, for residue focused phosphorylation, the upper and lower layers of the periodic MT structure were fixed, while few projection domain atoms of the attached tau proteins were pulled at two different strain rates (10^9 s^{-1} and $2x10^9$ s^{-1}). For the tau accumulation test, only 1ns equilibration was assumed sufficient to observe. The high strain rate on neural cytoskeletal components are relevant to TBI scenario, which we attempt to focus on particularly (Wu and Adnan, 2018).

LAMMPS allows to calculate the force on a group of atoms along with the displacement with convenience. Furthermore, stress-strain plots are obtained by the per-atom stress calculation and summation in LAMMPS. However, as the output is in (pressure x volume) unit, we must divide the obtained stress value by the volume of the protein (or certain portion of the protein). The general formulation used by stress per atom command is $P = (P_{xx}+P_{yy}+P_{zz})/ (3xV)$, where P_{xx}, P_{yy} and P_{zz} is the summation of stress/atom value for all atoms in x, y, and z direction respectively, and V is the summation of volume of the atoms of the protein being considered. The approximated volume was obtained by Voronoi cell approximation, adapted from LAMMPS voro++ package (Rycroft, 2009). The strain is simply obtained by the displacement of the atoms from the initial position. All the tensile tests are performed in NVT ensemble, with 100fs temperature damping parameter. The visualizations of the tensile tests are carried out by OVITO software (Stukowski, 2010).

All the simulations were carried out by the STAMPEDE2 supercomputer of Texas Advanced Computing Center (TACC).

Table 3.2: Simulation Box Sizes and Setup Used in this Study

Phosphorylation State	System	Simulation box size (nm x nm x nm)	Setup
Domain Phosphorylation	Single Tau	30 x 12 x 12	MT binding site is fixed and projection domain is pulled
	Dimerized Tau	200 x 20 x 15	MT binding site of one protein is fixed, MT binding site of another protein is pulled
	Tau-MT	200 x 20 x 15	Upper and lower layers of MT are fixed, tau projection domain is pulled
Residue Phosphorylation	Tau-MT	182 x 39x 33	Upper and lower layers of MT are fixed, tau projection domain is pulled
	Tau Accumulation: 2 tau system	40 x 20 x 15	1ns equilibration
	Tau Accumulation: 3 tau system	40 x 20 x 15	1ns equilibration

	Tau Accumulation: 4 tau system	40 x 20 x 20	1ns equilibration
	Tau Accumulation: 6 tau system	40 x 20 x 20	1ns equilibration

3.3 Results

3.3.1 Domain Focused Phosphorylation

3.3.1.1 Single Tau Unfolding and Stretching

We have performed the tensile tests at high strain rates ($5x10^8$ s^{-1} and $1x10^9$ s^{-1}). The MT binding region atoms are fixed, and first few atoms of the projection domain are pulled at –x direction. The calculated force-displacement and stress-strain graphs are shown in Figure 3.1a. As we have already seen in our previous work, unfolding is followed by stretching of the covalent bonds, therefore we observe two distinct slopes in the graph. The stretching does not begin until the tau is highly unfolded (~200%), and that is followed by a combination of unfolding and stretching in the projection domain. We have calculated the unfolding stiffness from the linear fitting 0% to 175% strain graphs, while the stretching stiffness is obtained from that of 200% to ~268% strain graphs. Figure 3.1b shows the different distinguishable stages of the tensile tests: unfolding and stretching. From our earlier work, we have shown that strain rate greatly affects the unfolding and stretching stiffness in both unfolding and stretching region. However, in the current work, Table 3.3 and Figure 3.1 show that in the unfolding region the phosphorylation alters the stiffness dynamically. The results indicate that both at the unfolding and stretching regions, we have obtained

different slopes for different phosphorylated domain. For phosphorylation in tail, we have obtained smallest slope in the unfolding region (<100MPa). For normal, phosphorylation in MT binding sites and all domains, the stiffness is significantly higher in the stretching region. We can suggest that domain focused phosphorylation can dynamically affect the stiffness of single tau chain while unaffected by external parameters such as intervention of tau-MT interaction, and that we cannot predict a trend of increasing stiffness if we monotonously increase the number of phosphorylated sites by arbitrarily applying phosphorylation. However, we can attempt to predict the change of stiffness due to phosphorylation and strain rate dependency simultaneously, which is out of the scope of this manuscript. The estimated stiffness for both regions, however, are in reasonable range, according to our previous work on the effect of strain rate on tau protein and existent literature, and the randomness of our results strengthens the current hypothesis obtained from the literature that not only phosphorylation is responsible for the stiffness of the tau protein structure, but also other parameters may also be equally important.

Table 3.3: Unfolding stiffness and stretching stiffness of single tau for phosphorylation in different domains

Strain Rate	$5x10^{8}s^{-1}$		$1x10^{9}s^{-1}$	
Phosphorylation Domain	Unfolding Stiffness (MPa)	Stretching Stiffness (MPa)	Unfolding Stiffness (MPa)	Stretching Stiffness (MPa)
Normal	129	549	285	1198
Projection Domain	144	442	227	317
MT Binding Sites	128	520	191	1050

Tail	97	731	179	890
All Domains	113	857	175	962

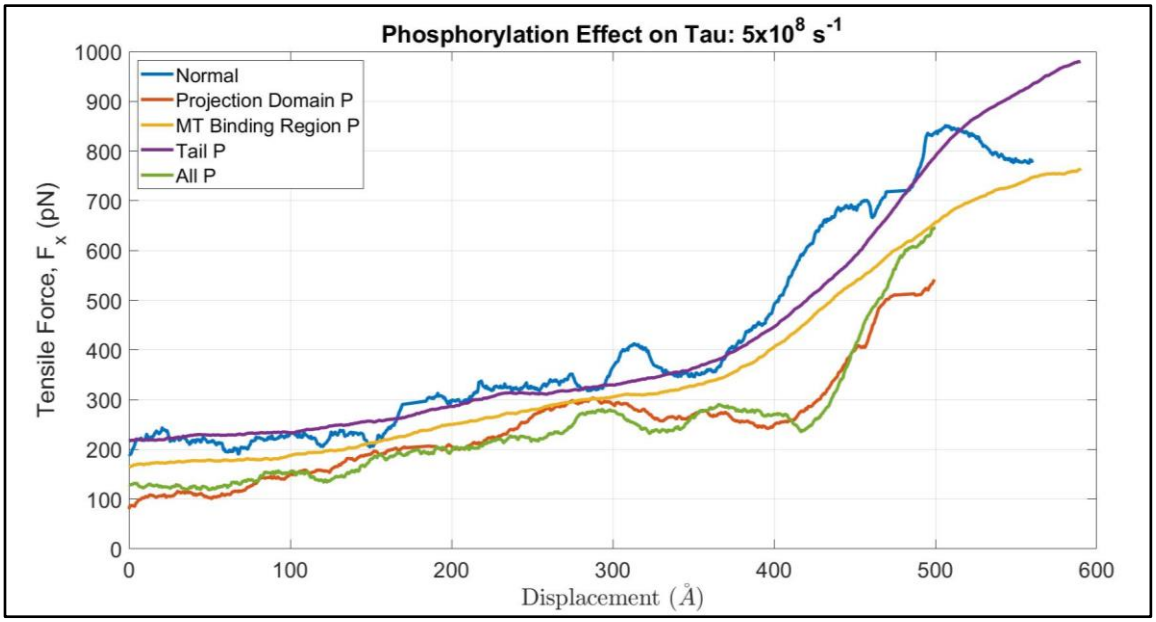

i

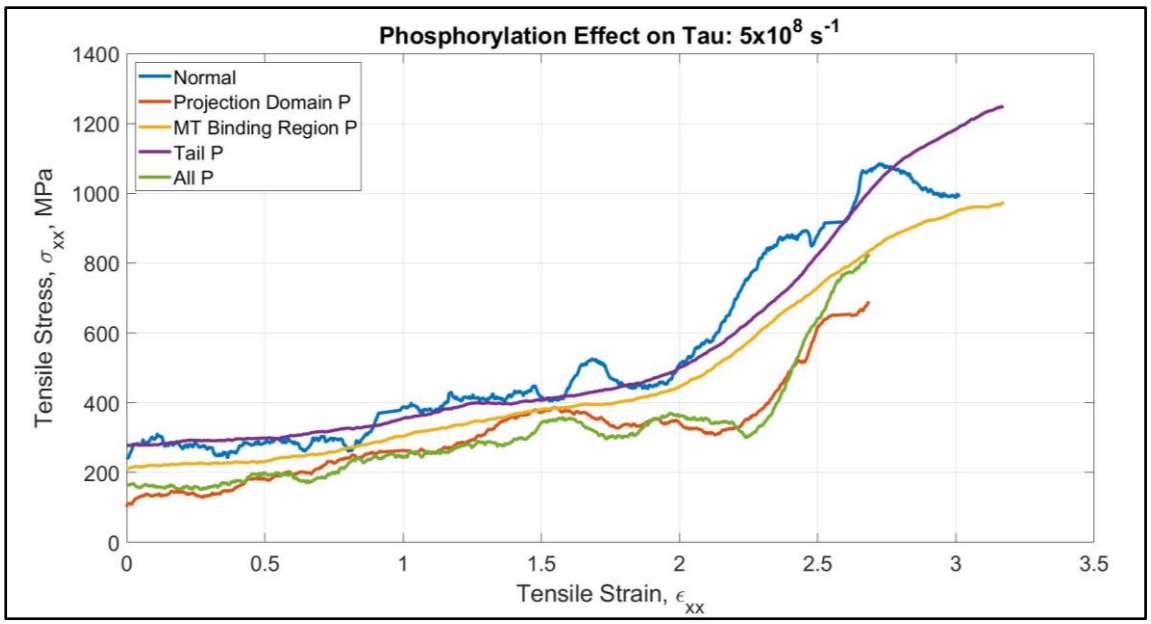
Phosphorylation Effect on Tau: 5x10^8 s^-1
Normal
Projection Domain P
MT Binding Region P
Tail P
All P
Tensile Stress, σxx, MPa
Tensile Strain, εxx
0
200
400
600
800
1000
1200
1400
0
0.5
1
1.5
2
2.5
3
3.5

ii

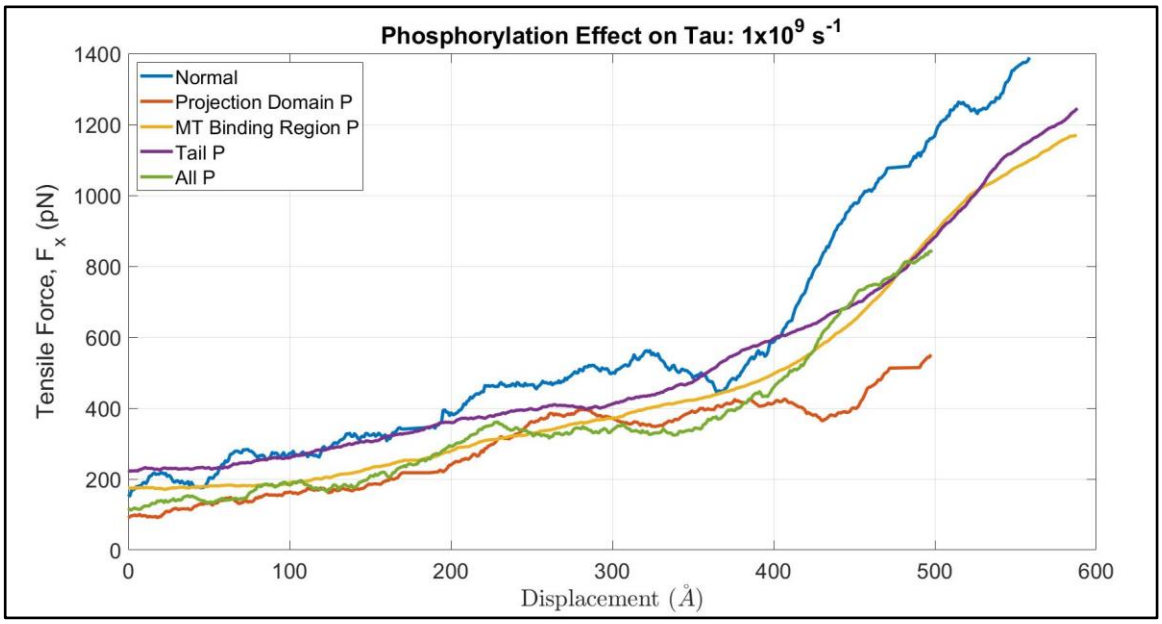
Phosphorylation Effect on Tau: 1x10^9 s^-1
Normal
Projection Domain P
MT Binding Region P
Tail P
All P
Tensile Force, Fx (pN)
Displacement (Å)
0
200
400
600
800
1000
1200
1400
0
100
200
300
400
500
600

iii

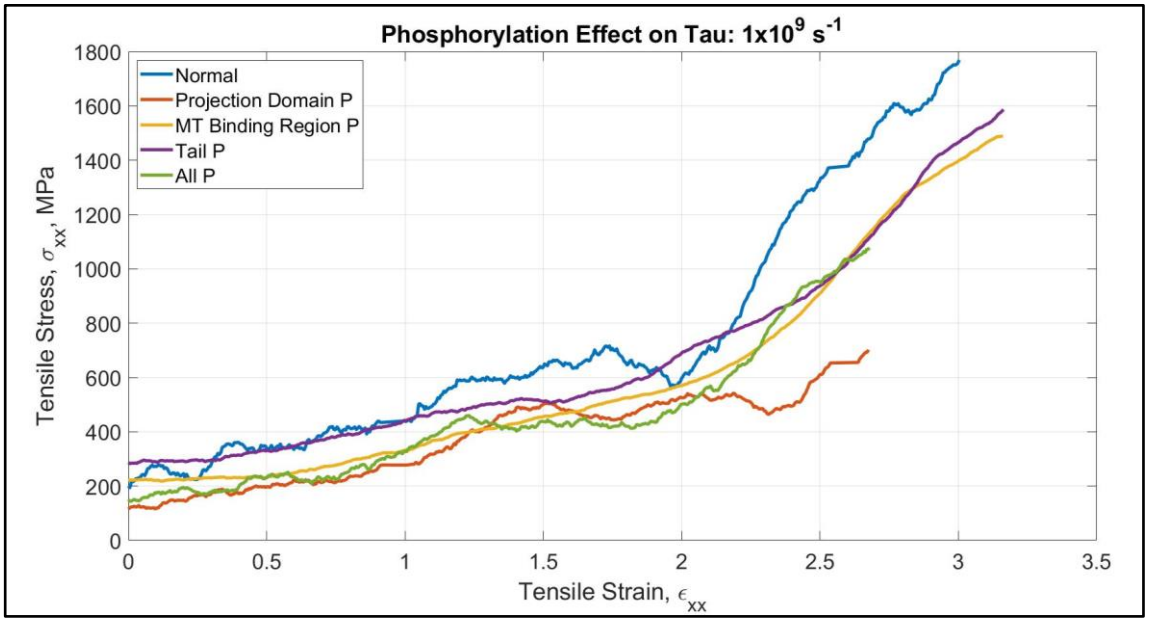

iv

Figure 3.1a: Force vs Displacement and Stress vs strain plot of single tau projection domain. Up to ~175% strain, tau protein keeps unfolding, and after that we see a sharp rise in the slope, suggesting the pure stretching of covalent bonds. We have obtained results for greater than 300% strain for most cases, but only up to ~268% strain is shown for all cases. i-ii) $5x10^{8}s^{-1}$, iii-iv) $1x10^{9}s^{-1}$. Data smoothened by using moving average.

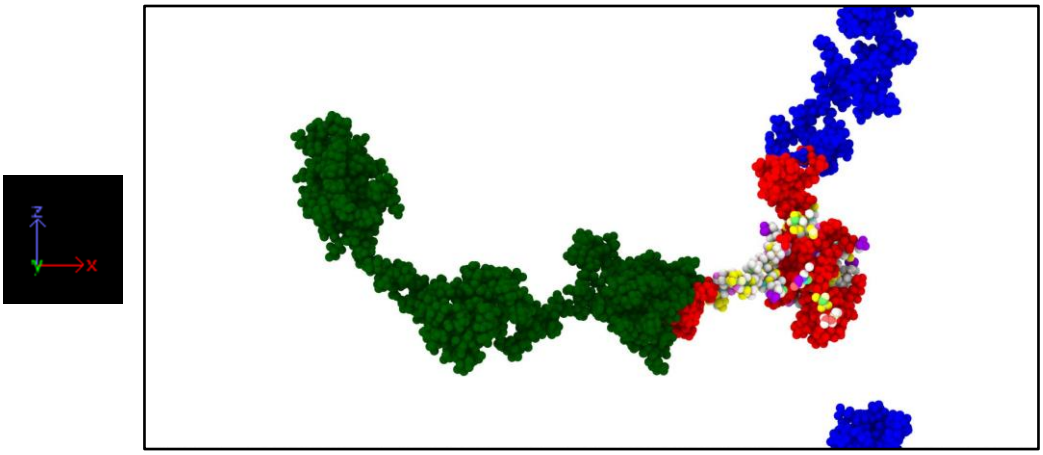

i

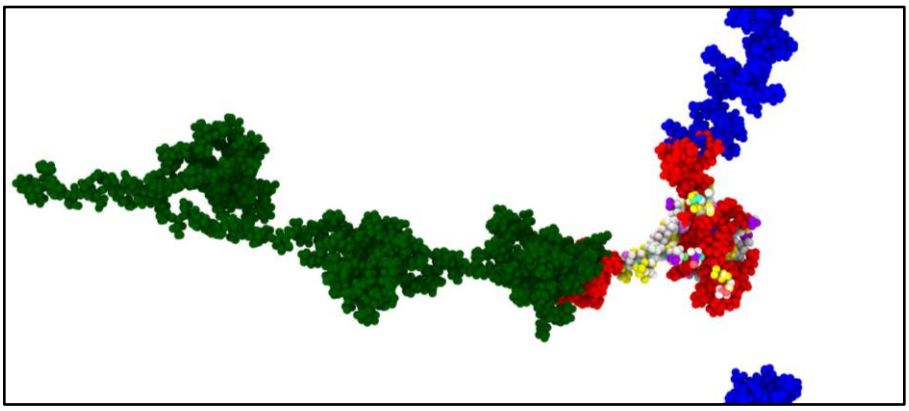

ii

Figure 3.1b: Different stages of the tensile test on single tau (normal phosphorylation, strain rate: $1x10^{9}s^{-1}$). i. Initial single tau structure (strain = 0%), ii. tau protein being unfolded due to pulling at 10^{9} s^{-1} (strain

= 36%). Color legends: green: projection domain, red: MT binding region, blue: N terminus or tail, white: interrepeats between the MT binding regions.

3.3.1.2 Dimerized Tau Separation

We have attempted to observe the developed stress and possible sliding out of tau projection domain at high stretch, and the effect of phosphorylation on this phenomenon. We have fixed the MT binding site of one tau and pulled away the binding site of another tau. The force-displacement and stress-strain graphs (calculation procedure was similar to single tau) for the projection domain of the tau protein that has been pulled along the -x direction, at the strain rate of $2x10^9$ s^{-1} were plotted in Figure 3.2a (ii). Several sub-stages are observed as expected for the strain rate of $2x10^9$ s^{-1} which are shown in Figure 3.2b (we are referring to the protein with fixed MT binding region as protein 1, and the protein being pulled as protein 2): i. Unfolding of protein 2 (up to 163% strain), ii. Stretching of protein 2 (up to 257% strain), iii. Unfolding of protein 1 (up to 334% strain), iv. Stretching of protein 1 (up to 395% strain), v. Disentanglement of the overlapped projection domains of the tau proteins (up to 721% strain), vi. Sliding out or projection domain along with stretching (very fast, occurs at around 722% to 758% strain region), and vii. Separation of proteins (~758% strain). For normal phosphorylation level, we have already observed that strain rate significantly affects the required stretch for separation. However, in this study, the phosphorylation in different domains hardly affected the separation stretch (~750%) except for the case of phosphorylation in all domains (~600%), while unfolding and stretching occur in the similar manner for all cases. We can conclude that although the existent studies suggest that phosphorylation can promote accumulation of taus, it may not be reflected in separated dimerized tau, or domain focused phosphorylation can undermine the effect of phosphorylation on dimerized taus in an unpredictable manner, although the ability of tau for being highly stretched stays unaffected. In the Appendix, Figure A4.1 shows potential energy plots vs time, which suggests that although potential energy level is almost the same for all phosphorylation states, it significantly reduces at separation for all cases.

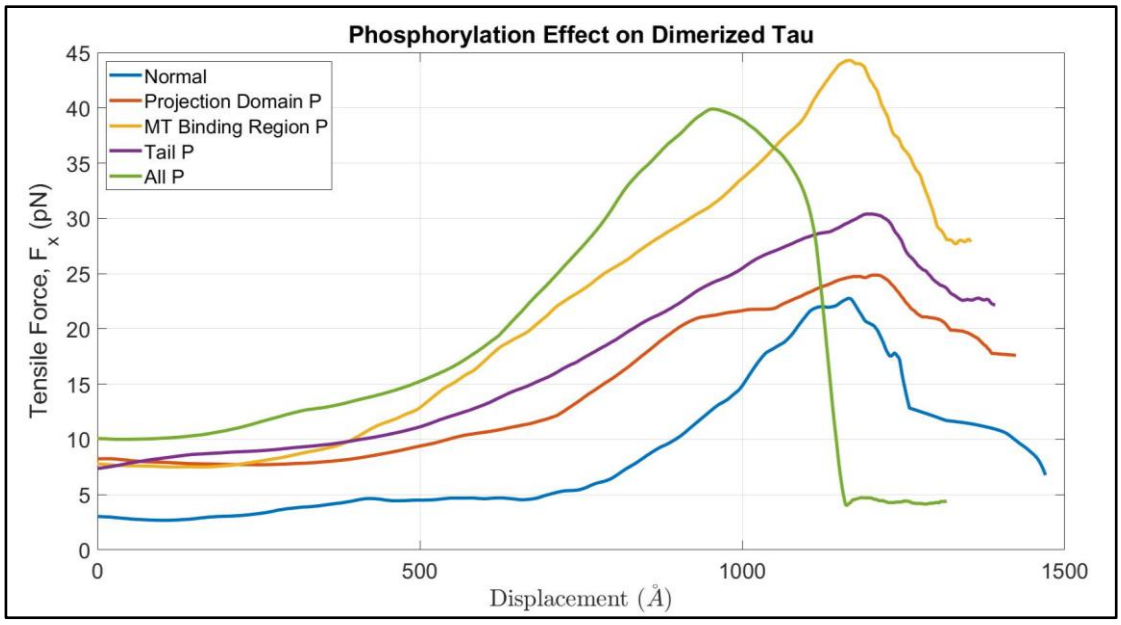
Phosphorylation Effect on Dimerized Tau
Normal
Projection Domain P
MT Binding Region P
Tail P
All P
Tensile Force, F_x (pN)
Displacement (Å)
0
5
10
15
20
25
30
35
40
45
0
500
1000
1500

i

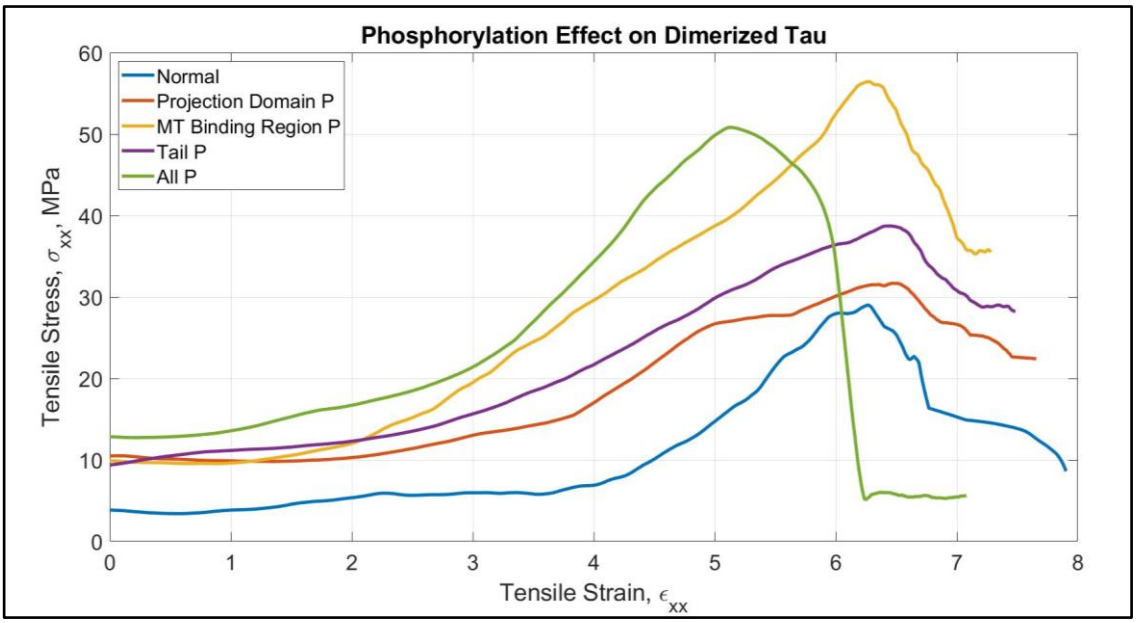
Phosphorylation Effect on Dimerized Tau
Normal
Projection Domain P
MT Binding Region P
Tail P
All P
Tensile Stress, σ_xx, MPa
Tensile Strain, ε_xx
0
10
20
30
40
50
60
0
1
2
3
4
5
6
7
8

ii

Figure 3.2a: i. Force-Displacement and ii. Stress-strain curve of protein 2 projection domain for phosphorylation in different domains (strain rate: $2x10^{9}s^{-1}$). There are several stages observed before complete separation of dimerized tau: such as unfolding of protein 2, stretching of protein 2, unfolding of protein 1, stretching of protein 1, disentanglement of the overlapped projection domains along with stretching and finally, complete separation. Complete separation occurs at almost same strain for all the cases (~750%), except for phosphorylation in all domains simultaneously (~600%). Data smoothened by using moving average.

i

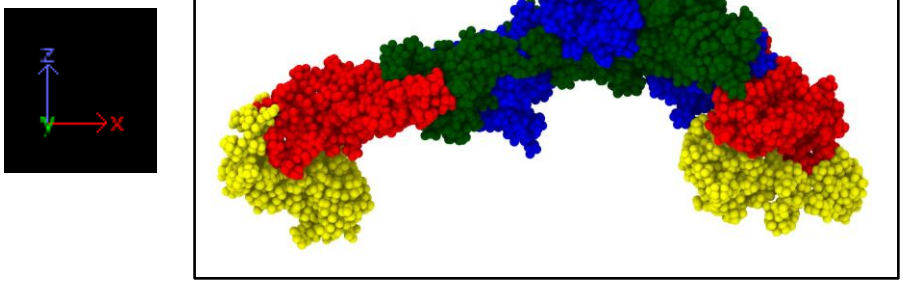

ii

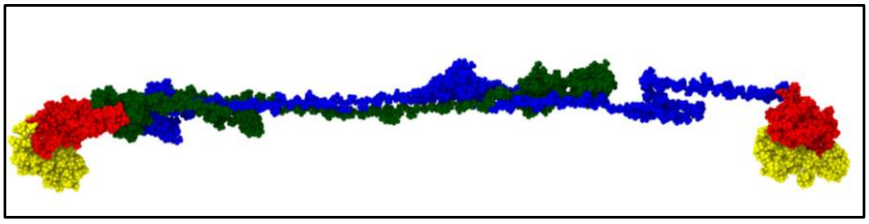

iii

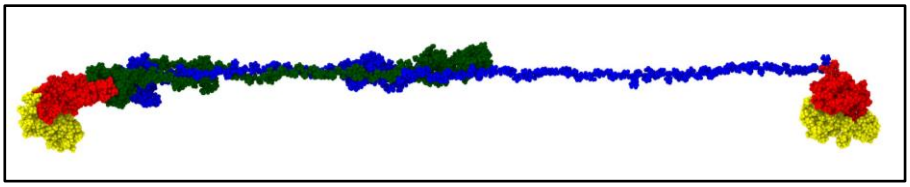

iv

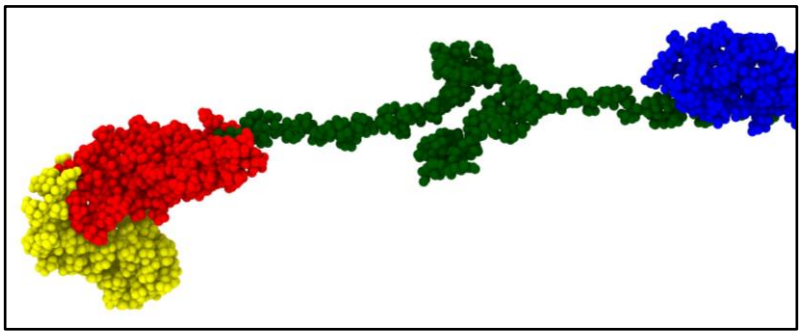

v

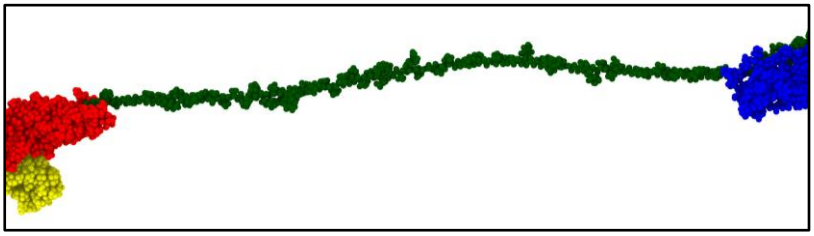

vi

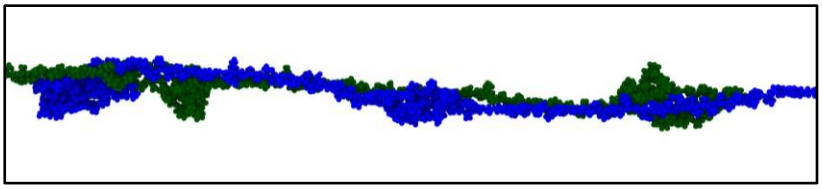

vii

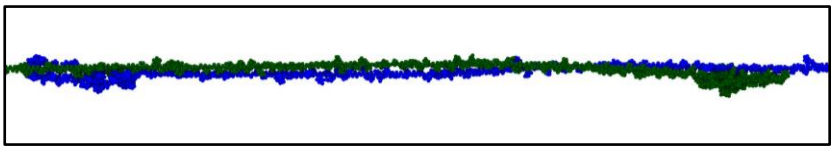

viii

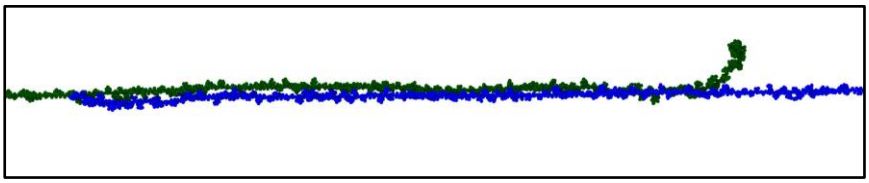

ix

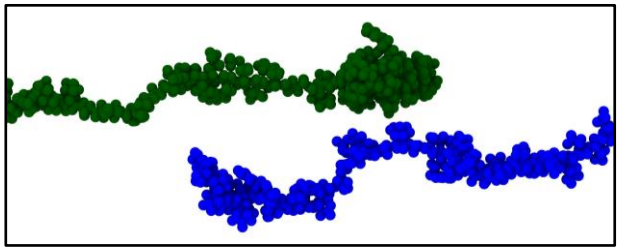

Figure 3.2b: Stages observed during the pull of one protein in the dimerized tau model (normal phosphorylation, strain rate: $2x10^9 s^{-1}$). i. Initial stage (strain: 0%), ii. Unfolding of protein 2 (strain: 135%), iii. Stretching of protein 2 (strain: 177%), iv. Unfolding of protein 1 (strain: 325%), v. stretching of protein 1 (strain: 345%), vi. Disentanglement of the overlapped projection domains of the tau proteins (strain: 430%), vii. Continued disentanglement (strain: 676%), viii. Sliding out of projection domain (strain: 750%), ix. Separation of proteins (strain: 758%). Color legends: Green: Projection domain of protein 2, Blue: projection domain of protein 1, Red: MT binding region (including the interrepeats) for protein 1 and 2, Yellow: N terminal tails of protein 1 and 2.

3.3.1.3 Tau-MT Interaction

In our previous study, we have already shown the tau-MT interaction for normal phosphorylation, and that tau-MT bonding is stronger than MT subunit bonding. In this study, we perform similar tensile tests in high strain rate ($2x10^9$ s^{-1}) for domain focused phosphorylation. We observe different phenomena for phosphorylation at different domains, although the unfolding and stretching due to the pulling force are similar for all cases. The observations are summarized in Table 3.4. For all cases, we have observed expected tau protein unfolding followed by stretching. For normal phosphorylation, we observe vigorous stretching of MT binding site before separation from MT surface at the strain of 1125%. For phosphorylation in projection domain and tail, we observe similar stretching and separation at higher strain (1330%). For phosphorylation in all domains, we observe early separation, at 918%. However, the observation for phosphorylation in MT binding sites is quite different, we see that the MT binding region gets stretched significantly along with the MT tubulin surface, but does not separate, although we have continued the simulation for up to 2000% strain. It is to be noted that we have considered tau as separated from MT when the MT binding region of tau is completely separated from the MT surface. Figure 3.3a(ii) and 3.3b shows the stress-strain graphs and the observed stages in the simulation. In the Appendix, Figure

A4.2 shows the potential energy trend, which shows that potential energy takes a sharp decrease at separation for all cases.

Table 3.4: Observation of tau-MT interaction for phosphorylation at different domains (strain rate: $2x10^9$ s^{-1}).

Phosphorylation	MT Binding Site Separation (Strain, %)
Normal	1125
Projection	1330
MT Binding Site	No (Up to 2000%)
Tail	1330
All	918

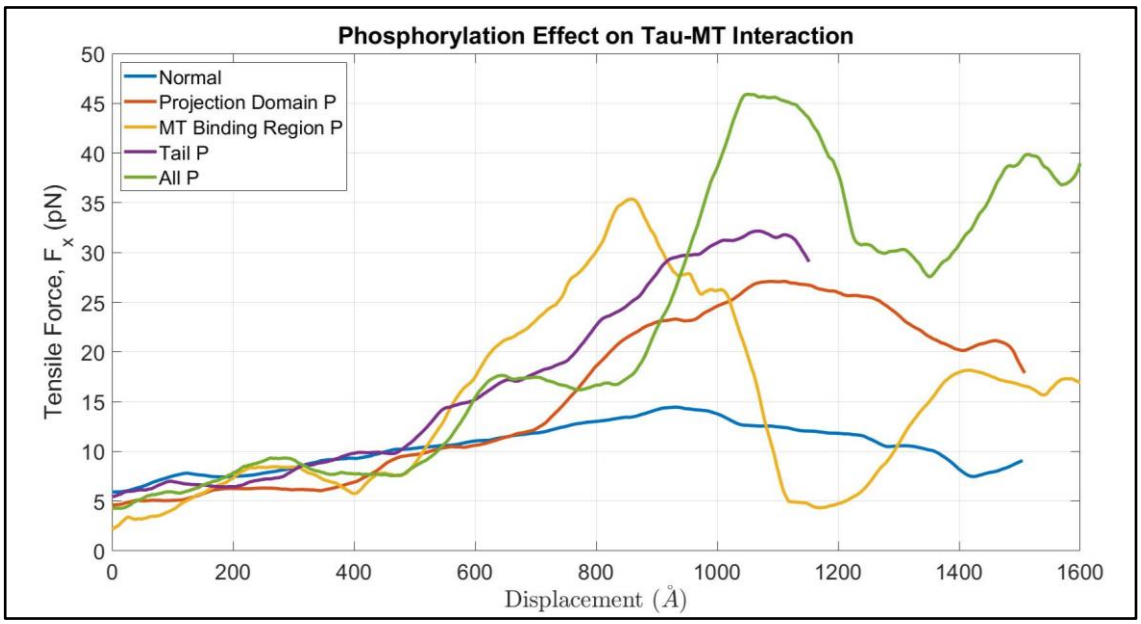
Phosphorylation Effect on Tau-MT Interaction
Normal
Projection Domain P
MT Binding Region P
Tail P
All P
Tensile Force, F_x (pN)
Displacement (Å)
0
5
10
15
20
25
30
35
40
45
50
0
200
400
600
800
1000
1200
1400
1600

i

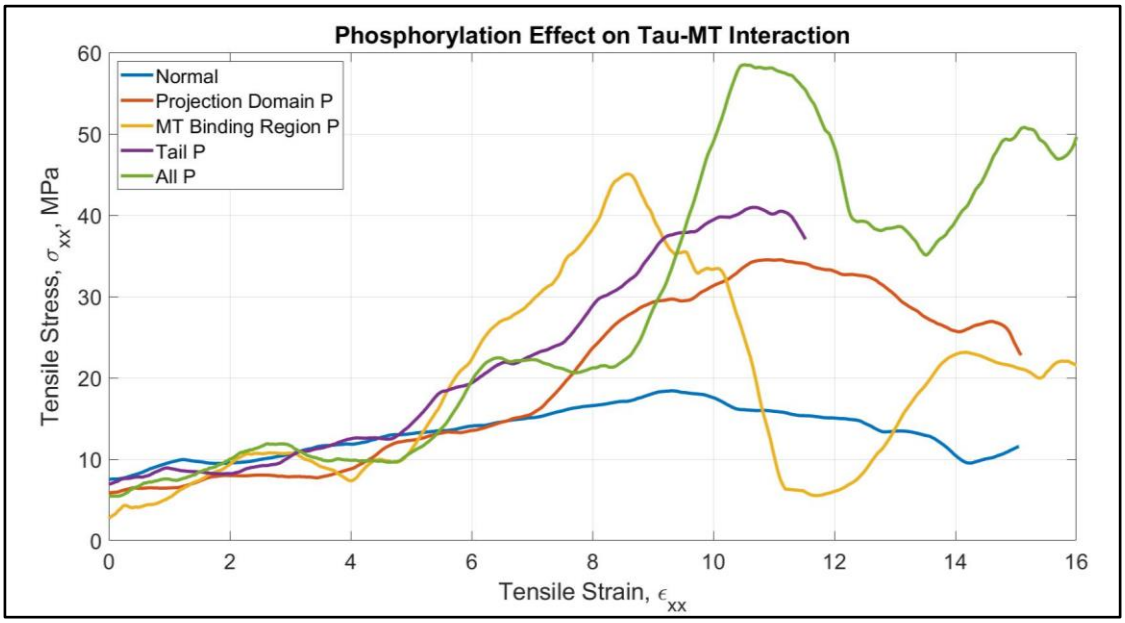
Phosphorylation Effect on Tau-MT Interaction
Normal
Projection Domain P
MT Binding Region P
Tail P
All P
Tensile Stress, σ_xx, MPa
Tensile Strain, ε_xx
0
10
20
30
40
50
60
0
2
4
6
8
10
12
14
16

ii

Figure 3.3a: i. Force-displacement and ii. Stress-vs Strain graph for the projection domain of tau during the pulling from MT (strain rate: $2x10^{9}s^{-1}$). For normal phosphorylation, separation occurs at ~1125% strain. For phosphorylation in projection domain and N-terminus tail, it occurs at ~1330% strain. For phosphorylation in MT binding sites, it does not occur (we have continued the simulation for this case up to 2000%). For phosphorylation in all domains, the separation occurs at ~918%. Data smoothened by using moving average.

i

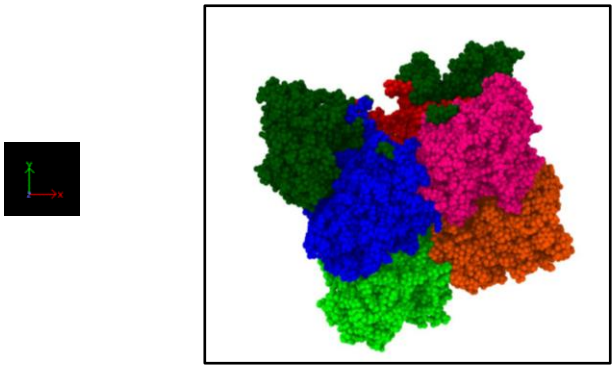

ii

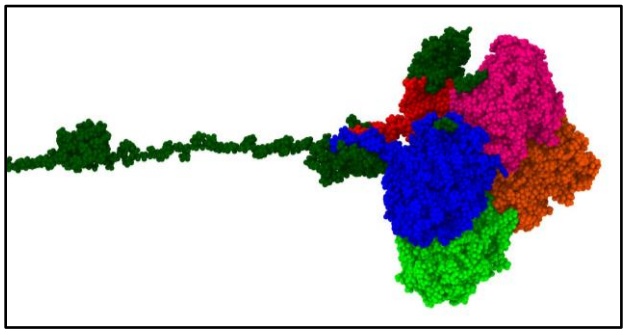

iii

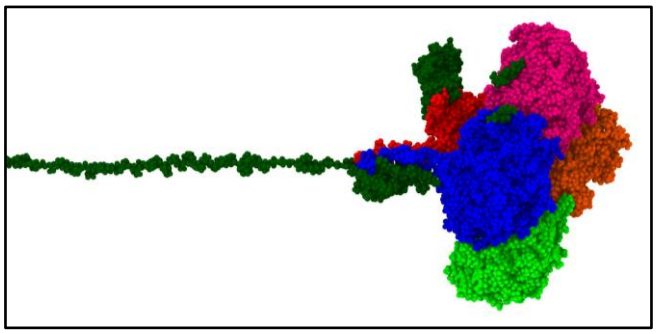

iv

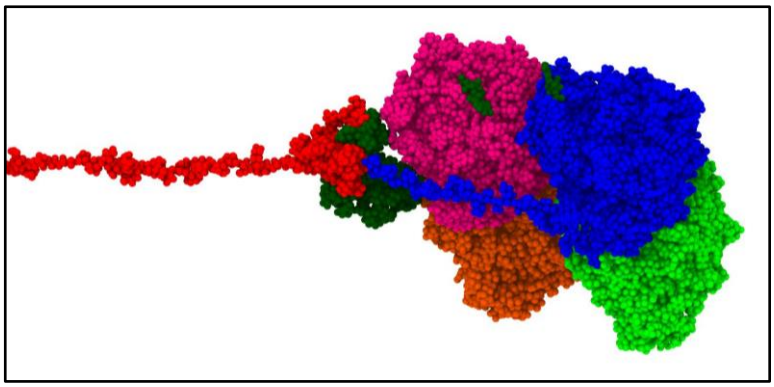

v

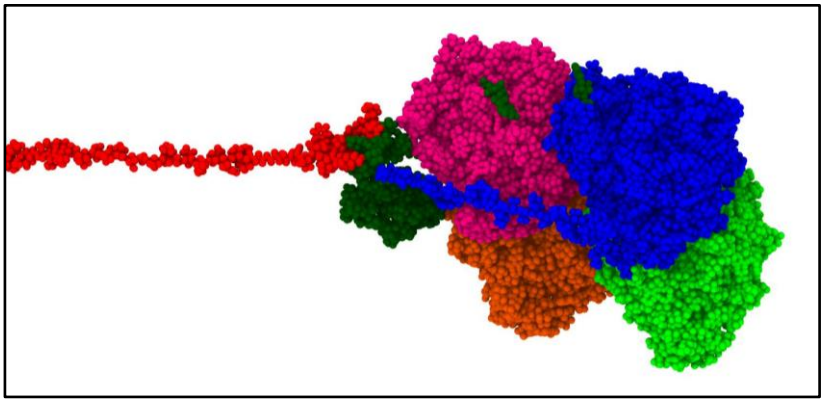

Figure 3.3b: Observation during the pulling of tau along -x direction (normal phosphorylation, strain rate: $2x10^{9}s^{-1}$). i. Initial stage (strain: 0%), ii. Unfolding of tau projection domain (strain: 376%), iii. Stretching of tau projection domain (strain: 640%), iv. Onset of tau MT binding region separation (strain: 1095%), v. Separation of MT binding region from MT surface (strain: 1125%). Color legends: dark green: tau, red: MT binding region of tau (including the interrepeats), orange: α subnit 1, pink: β subnit 1, blue: α subnit 2, light green: β subnit 2, white: GDP and GTP atoms and Mg^{2+} ion.

3.3.2 Residue Focused Phosphorylation

3.3.2.1 Tau-MT Interaction: Normal vs Phosphorylated Tau

The domain focused phosphorylation simulations have shown that we cannot establish a definite trend of the change of mechanical properties according to the phosphorylation at different domains of tau. Furthermore, it is possible that residue focused phosphorylation can provide more insight about the effect of phosphorylation. Therefore, we have performed another set of simulation by attaching one normal and one phosphorylated tau (phosphorylated in seven selected sites) on the same MT surface in order to understand which one is prone to separate earlier under the application of the same strain rate. We have

pulled the tau projection domain at two different strain rates ($10^9 s^{-1}$ and $2x10^9 s^{-1}$). In both cases, we have observed that the phosphorylated tau separates from the MT surface earlier than the normal tau (at ~90% less strain for both cases). The effect of strain rate is important for this study, as we have observed that at lower strain rate the separation occurs at higher strain, that is, high strain rate tends to separate the tau protein from the MT surface earlier, and at lower strain rate, the tau is able to stay attached with the MT surface for 20-40% more strain, depending on the strain rate, which is consistent with the results of our earlier work on tau-MT interaction. The observation is also compatible with earlier studies which suggested that phosphorylation significantly decreases tau-MT bonding (refer to Table 3.1 in the Method section). Additionally, this study further highlights the highly stretchable characteristic of tau and strong tau-MT bond, even at phosphorylated state. Figure 3.4a shows the stress vs strain graph of the tau projection domain for the two strain rates. Figure 3.4b shows the stages of tau-MT interaction in our simulation at the strain rate of $2x10^9 s^{-1}$. Similar to the tau-MT interaction study in the first portion of the manuscript, tau is considered to be separated from MT when the MT binding region is completely separated from MT surface. Figure 3.4a and 3.4b show the force vs displacement and stress vs strain graphs for four sets of simulation, and observable stages up to separation, respectively. In the Appendix, Figure A4.3 shows the potential energy trend for the four sets, which suggests that potential energy decreases significantly at separation, and potential energy is significantly less at phosphorylated state than at normal state. Moreover, they are of close values irrespective of applied strain rate. The observation agrees to previous findings that phosphorylation alone cannot signify the stability of tau-MT system, and even at selectively phosphorylated state, the system can be more stable than at normal state.

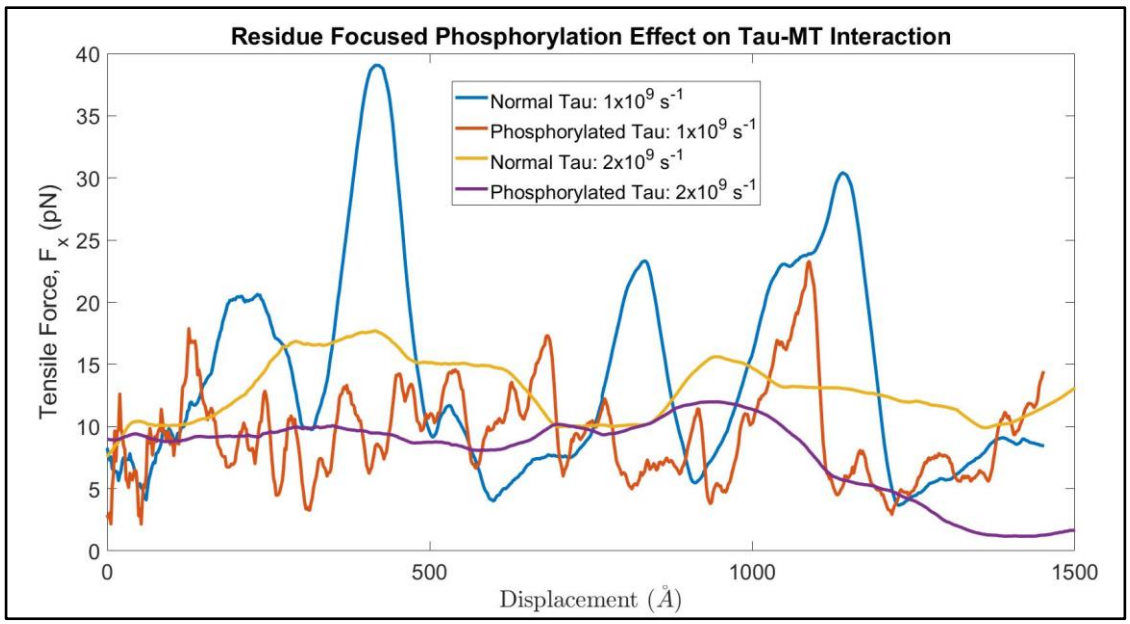
Residue Focused Phosphorylation Effect on Tau-MT Interaction
Normal Tau: 1x10^9 s^-1
Phosphorylated Tau: 1x10^9 s^-1
Normal Tau: 2x10^9 s^-1
Phosphorylated Tau: 2x10^9 s^-1
Tensile Force, F_x (pN)
Displacement (Å)
0
5
10
15
20
25
30
35
40
0
500
1000
1500

i

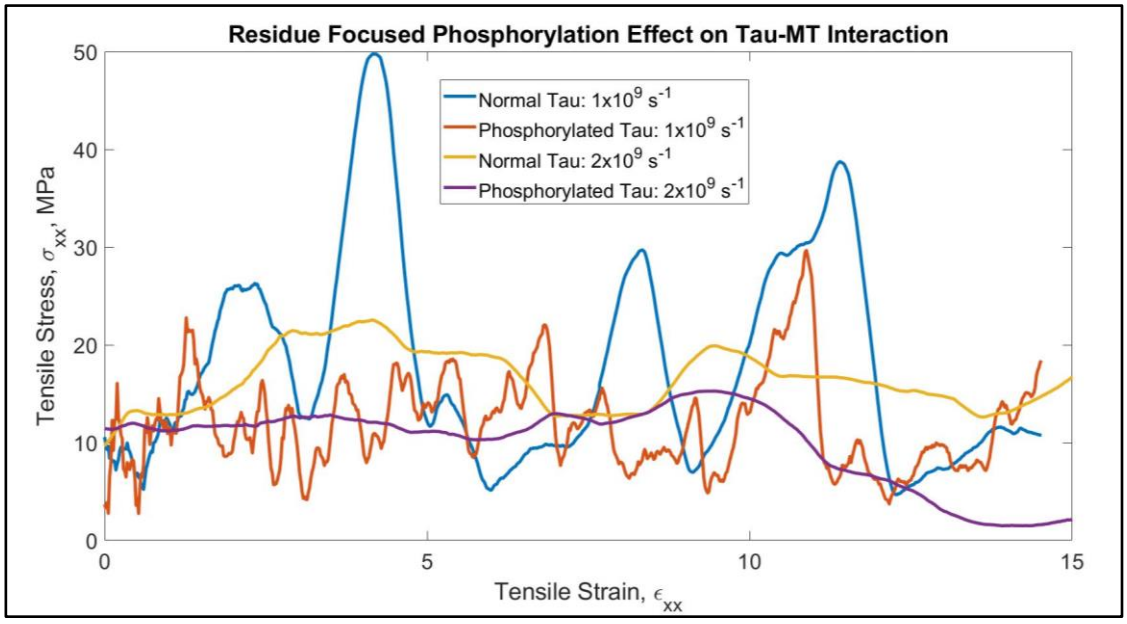
Residue Focused Phosphorylation Effect on Tau-MT Interaction
Normal Tau: 1x10^9 s^-1
Phosphorylated Tau: 1x10^9 s^-1
Normal Tau: 2x10^9 s^-1
Phosphorylated Tau: 2x10^9 s^-1
Tensile Stress, σ_xx, MPa
Tensile Strain, ε_xx
0
10
20
30
40
50
0
5
10
15

ii

Figure 3.4a: i. Force vs Displacement and ii. Stress vs Strain graph for the projection domain of tau during the pulling from MT. At the strain rate of $10^9 s^{-1}$, for normal phosphorylation, separation occurs at ~1193% strain, while for phosphorylated tau, it occurs at ~1100% strain. At the strain rate of $2x10^9 s^{-1}$, for normal phosphorylation, separation occurs at ~1170% strain, while for phosphorylated tau, it occurs at ~1060% strain. The continuous unfolding and stretching patterns are similar for both cases. Data smoothened by using moving average.

i

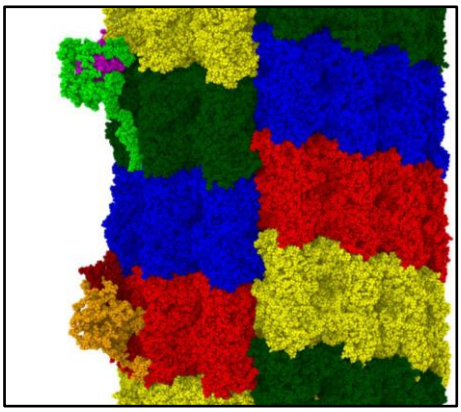

ii

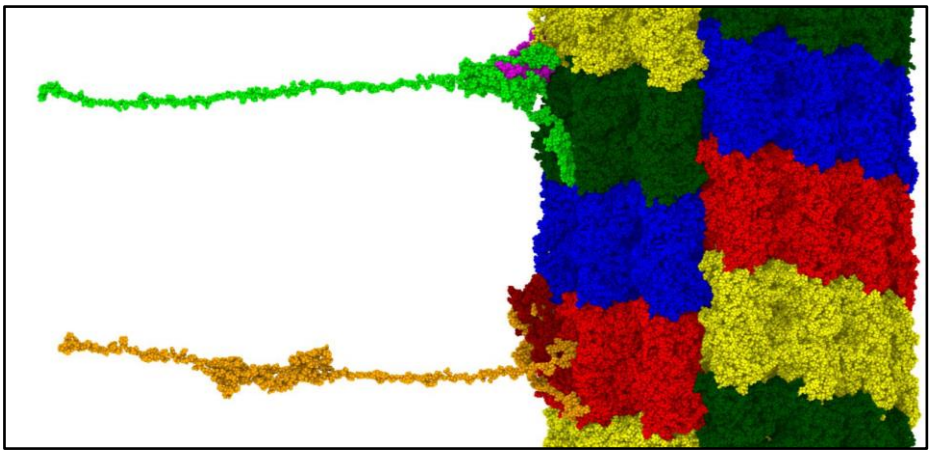

iii

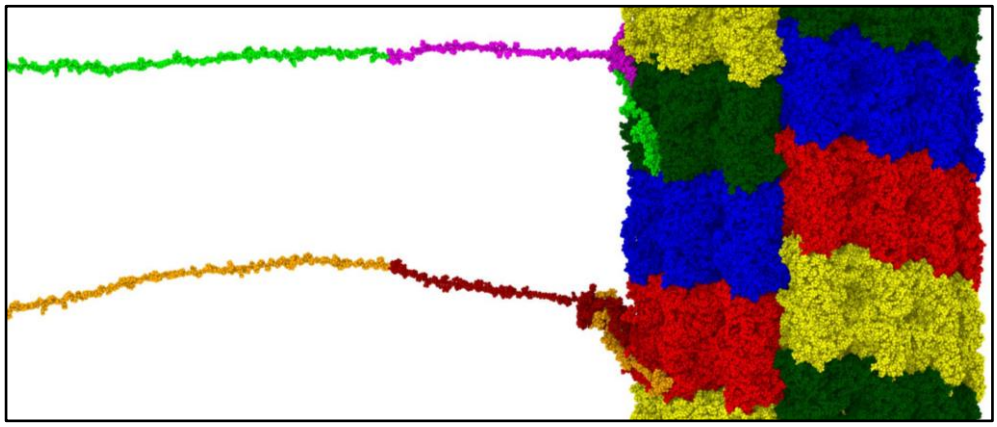

iv

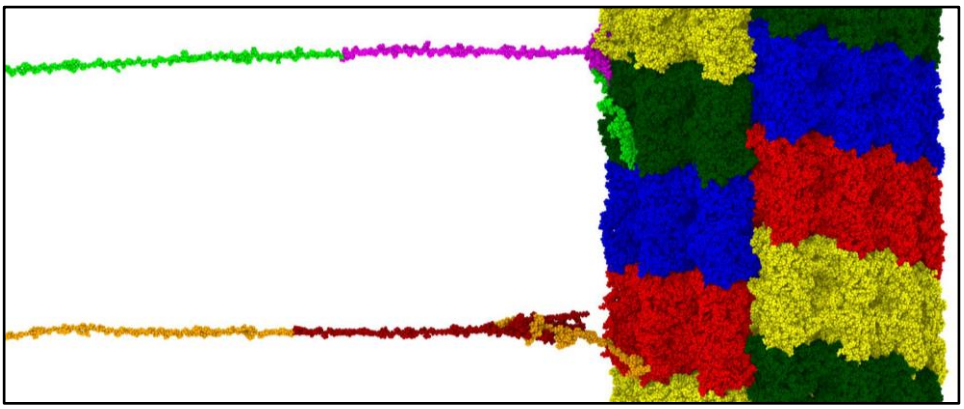

v

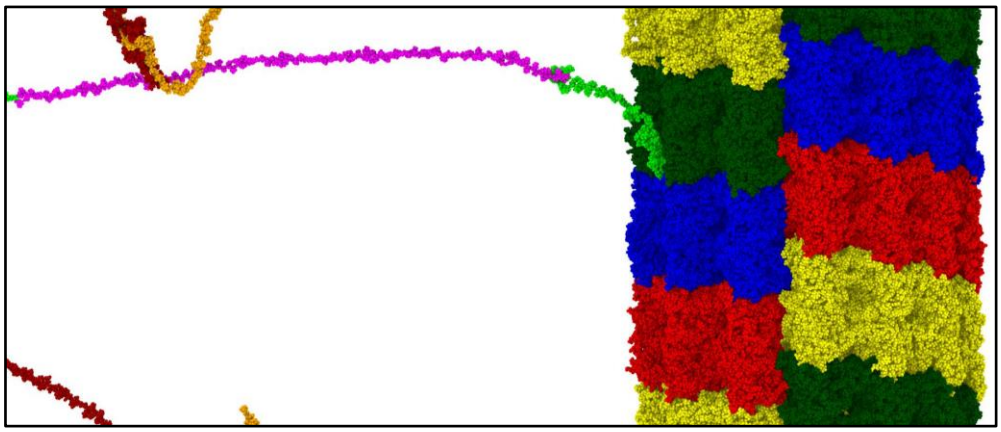

Figure 3.4b: Observation during the pulling of tau in the x direction (normal phosphorylation, strain rate: $2x10^{9}s^{-1}$). i. Initial stage (strain: 0%), ii. Unfolding of tau projection domain (strain: 228%), iii. Stretching of tau projection domain (strain: 932%), iv. MT binding region separation for the phosphorylated tau (strain: 1060%), v. MT binding region separation for normal tau (strain: 1170%). Color legends: Red, blue, green and yellow: repeating helical units of MT, light green: projection domain and tail of normal tau, pink: MT binding region of normal tau (including the interrepeats), orange: projection domain and tail of phosphorylated tau, maroon: MT binding region of phosphorylated tau (including the interrepeats).

3.3.2.2 Tau Accumulation Test

From the existent literature we already know that formation of PHF and tau accumulation are biomarkers of neuropathology, which are highly dependent on phosphorylation. As a part of residue based phosphorylation simulations, we have placed two, three, four, and six tau proteins in the simulation box in presence of explicit water molecules, minimized the potential energy and equilibrated at 310K for 1ns in order to observe possible difference in tau accumulation for normal and phosphorylated cases. Although the potential energy graphs are similar for both normal and phosphorylated cases of all systems (refer to

the Appendix, Figure A4.4-A4.7), we have observed that the normal taus did not accumulate throughout the simulation, while the phosphorylated ones shown distinguishable tendency to decrease the distance between each other. We admit that 1ns is very small timescale for observing total accumulation. Therefore, in order to quantify the decrement of the distances between the tau proteins, we have calculated the relative distance between the mass centers of the projection domains of the tau proteins throughout the simulation, and the differences between the coordinates depict how much they have come closer (or got further away) during the simulation. The calculation is focused on the projection domains of the tau proteins, as dimerization or polymerization occurs in this region, and therefore it is important for us to obtain insight on the accumulation tendency of this region. As a representative system, we have chosen the 3 tau system, and Figure 3.5a shows the snapshots at the beginning, intermediate stage, and end of the simulation for both cases. Figure 3.5b shows the comparison of relative distances in three-dimensional space between the tau proteins in normal and phosphorylated states for all cases. Due to the irregular shape of tau protein, the distances between the overall mass centers do not reflect much on the tau accumulation, but the distances between the mass centers of the projection domains of the tau proteins placed in vicinity of each other do. For example, the projection domain mass center distances in the three dimensional space are approximately 15Å, 20Å and 18Å less for phosphorylated tau proteins than the normal tau proteins for protein 1 to protein 2, protein 2 to protein 3 and protein 3 to protein 1 respectively in the 3 tau system, which essentially suggests the tendency of tau accumulation in phosphorylated state. It is to be mentioned that for 2 and 3 tau systems, the projection domain mass center distances are reported by showing distances for all the combinations. However, for 4 tau system, it is only meaningful to report the distance between the projection domains of protein 1 and protein 4, as the system is created by offsetting protein 1 at a 40Å distance in the z direction, and therefore, protein 1 will tend to interact with the projection domain of the nearest neighbor, which is protein 4. For the same reason, the only insightful way to quantify the decrease of distances at phosphorylated condition is to report the following distances: protein 1 to protein 4, protein 2 to protein 5, and protein 3 to protein 6. Figure 3.5b summarizes the observation that in all systems, residue

phosphorylated proteins show less distance than the normal ones, which suggests greater accumulation tendency.

i

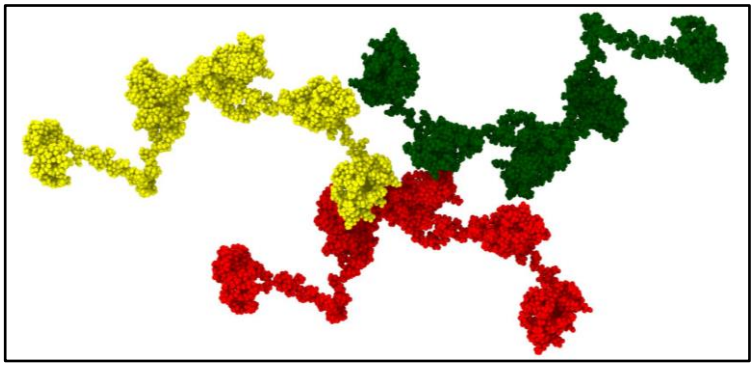

ii

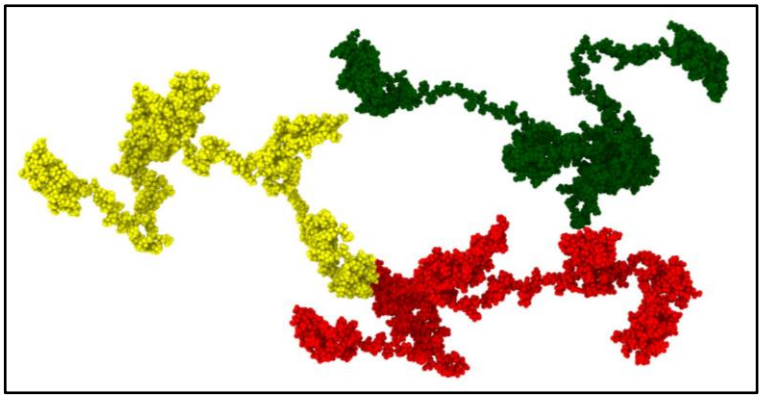

iii

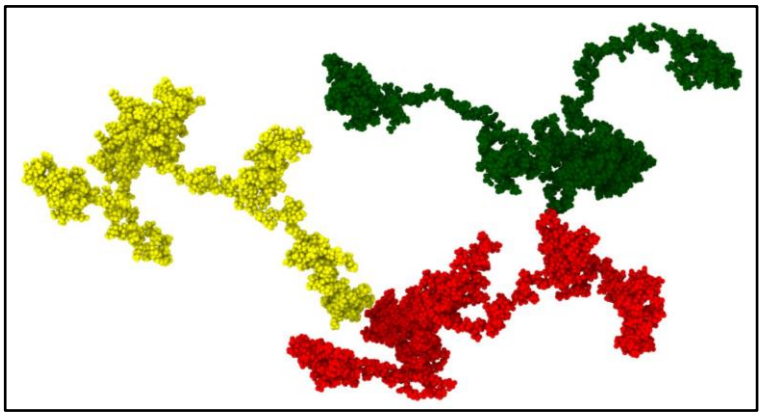

iv

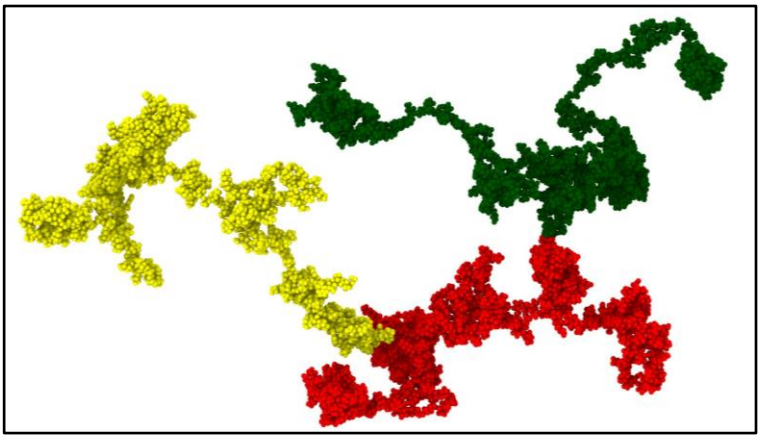

v

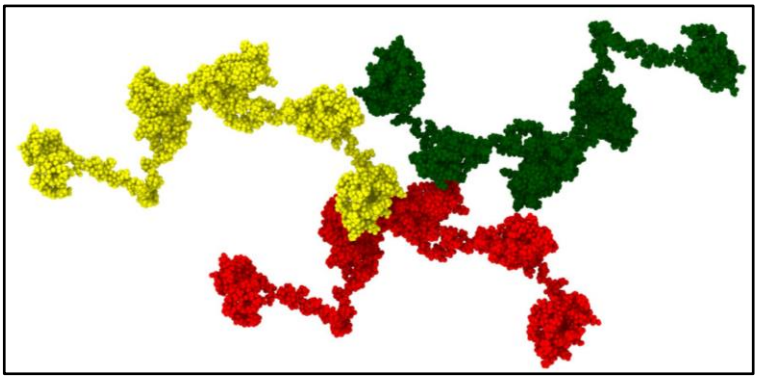

vi

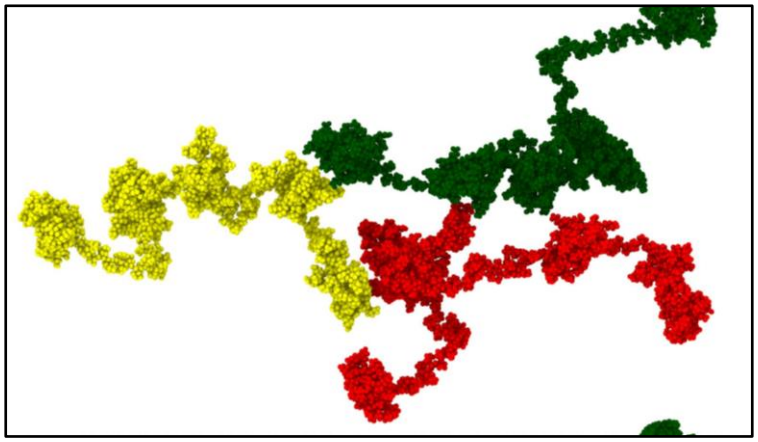

vii

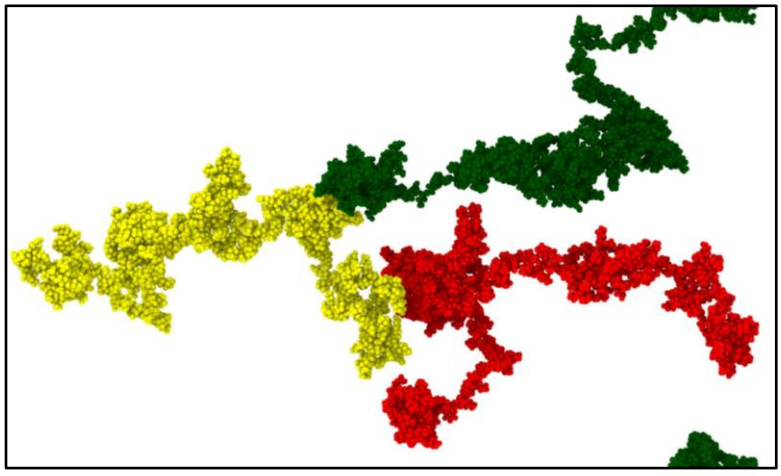

viii

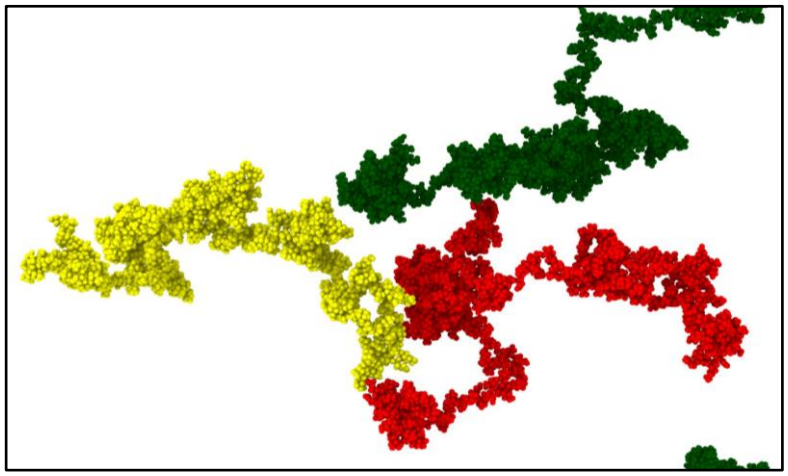

Figure 3.5a: Snapshots at different times during the 1ns NVT equilibration for normal and phosphorylated taus (at 7 sites). For phosphorylated taus, tendency to decrease the distance between the proteins is observed. i. Normal tau: 0ps, ii. Normal tau: 100ps, iii. Normal tau: 500ps, iv. Normal tau: 1ns, v. Phosphorylated tau: 0ps, vi. Phosphorylated tau: 100ps, vii. Phosphorylated tau: 500ps, viii. Phosphorylated tau: 1ns. Color legends: Red: protein 1, Green: protein 2, Yellow: protein 3.

i

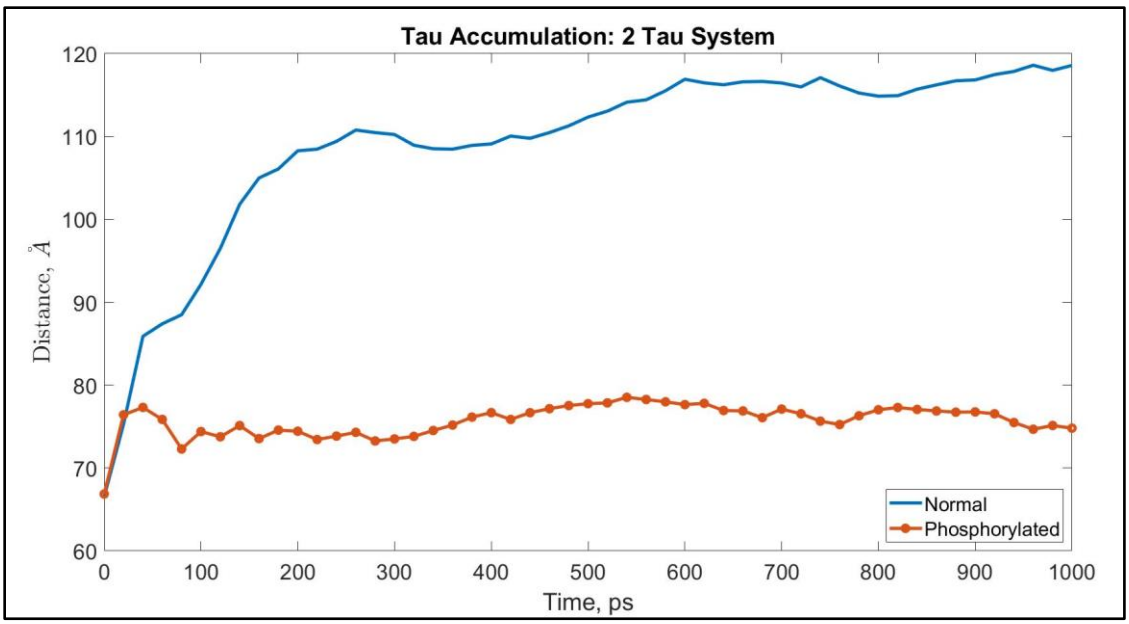
Tau Accumulation: 2 Tau System
Distance, Å
Time, ps
Normal
Phosphorylated

ii

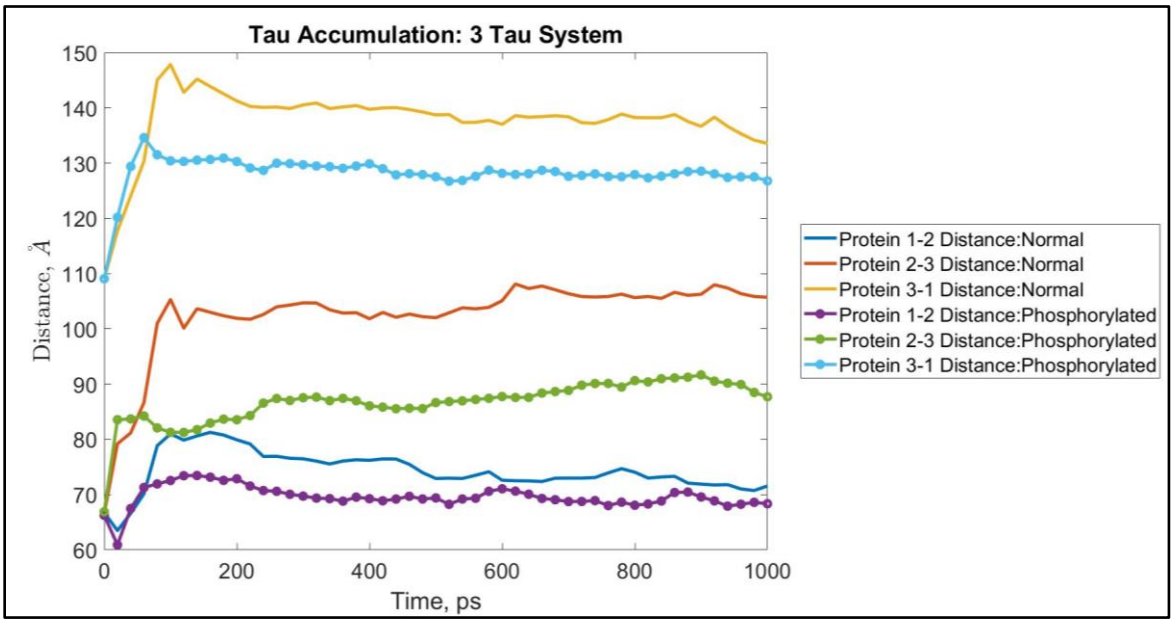
Tau Accumulation: 3 Tau System
Distance, Å
Time, ps
Protein 1-2 Distance:Normal
Protein 2-3 Distance:Normal
Protein 3-1 Distance:Normal
Protein 1-2 Distance:Phosphorylated
Protein 2-3 Distance:Phosphorylated
Protein 3-1 Distance:Phosphorylated

iii

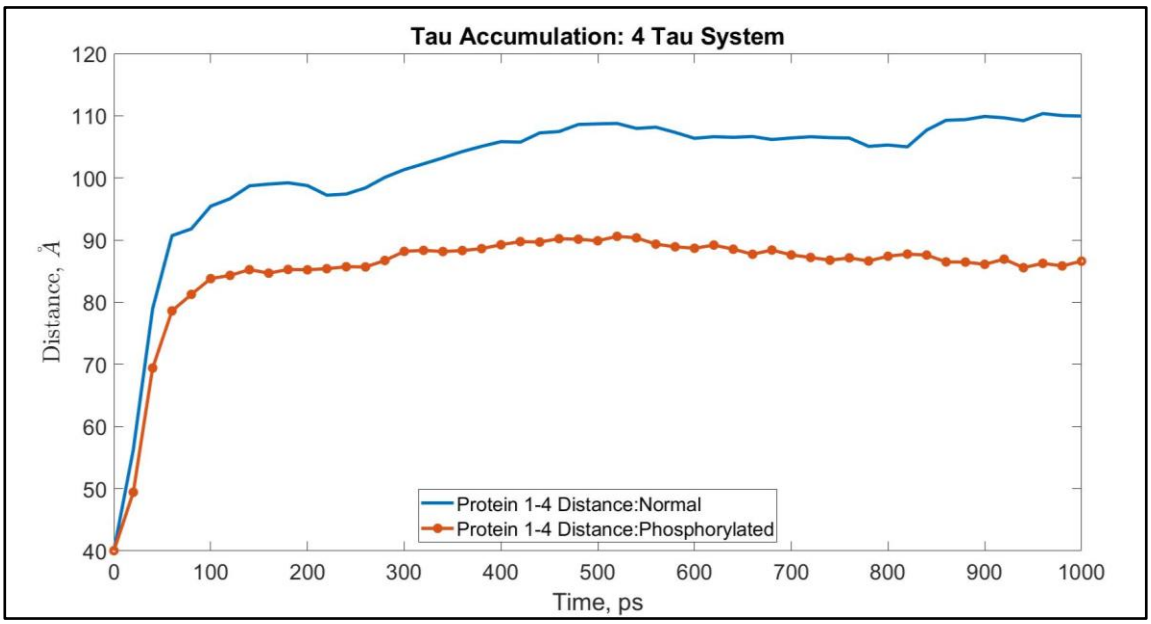
Tau Accumulation: 4 Tau System
Distance, Å
Time, ps
Protein 1-4 Distance:Normal
Protein 1-4 Distance:Phosphorylated

iv

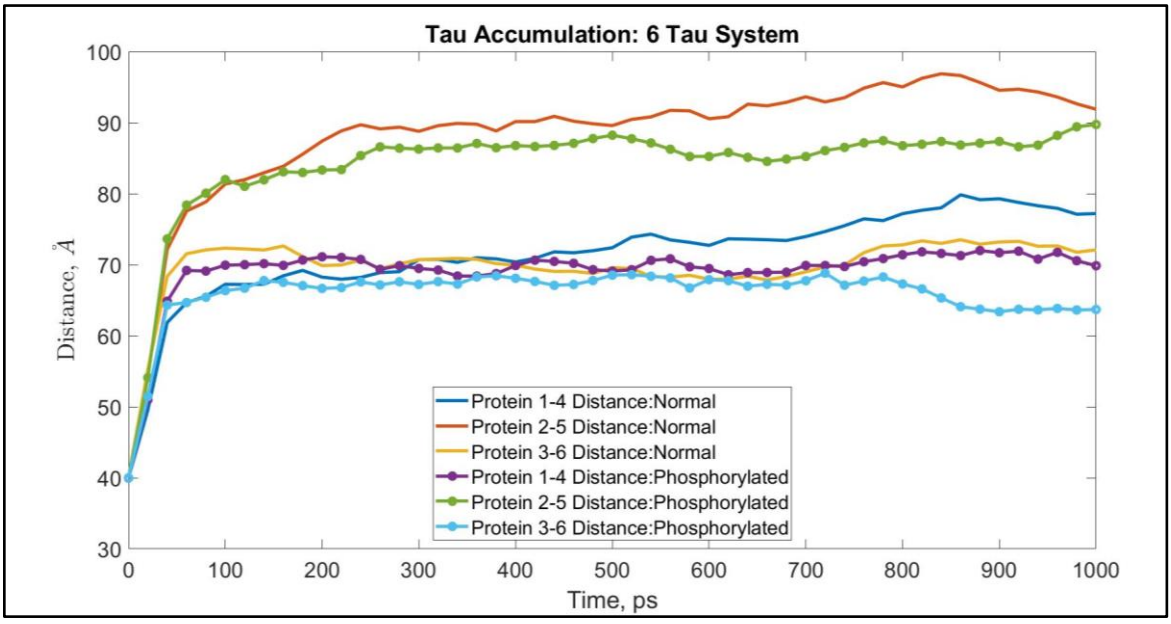
Tau Accumulation: 6 Tau System
Distance, Å
Time, ps
Protein 1-4 Distance:Normal
Protein 2-5 Distance:Normal
Protein 3-6 Distance:Normal
Protein 1-4 Distance:Phosphorylated
Protein 2-5 Distance:Phosphorylated
Protein 3-6 Distance:Phosphorylated

Figure 3.5b: Projection domain mass center distance of the proteins as a function of time. i. 2 tau system, ii. 3 tau system, iii. 4 tau system, iv. 6 tau system.

3.4 Discussion

In this study, we have analyzed the response of tau protein and tau-MT interaction from a mechano-chemical point of view to address a current limitation in the literature manifested by absence of comprehensive study on tau protein mechanical behavior (Khan et al., 2020a). We have performed tensile tests on a predicted structure of tau protein to determine the single tau projection domain stiffness, dimerized tau separation stretch, tau-MT separation stretch, and compared tau accumulation tendency in non-phosphorylated and phosphorylated states in nanosecond time scale. For a disordered protein, the confidence score (C-score) of -0.03 has been assumed as reliable in our simulation. The detail of quantification of the reliability for a protein structure predicted by i-TASSER (Zhang, 2008) is discussed in the supplementary material of this manuscript. It is to be noted that several reference are repeated in this manuscript due to relevance to the mechano-chemical viewpoint, and are discussed in detail in the discussion section on our earlier work on tau protein, which observed tau and tau-MT phenomena from strictly mechanical perspective.

From our extensive literature review, application of high strain rate and the resulting unfolding and stretching alone do not induce any phosphorylation-related symptom or disease in human body, but phosphorylation state significantly manipulates the manner of unfolding, stretching, and tau-MT binding affinity as found by our results. This study is performed to provide a novel insight on simultaneous mechanical loading and phosphorylation effect on tau protein. Existent literature shows that aside from tau protein being a biomarker of TBI, its behavior such as tau-MT affinity, unfolding, etc. strongly depend on the phosphorylation state. Therefore, it is important to discuss the mechanical behavior of tau protein according to domain-phosphorylated and residue-phosphorylated states. In other words, from the TBI

perspective, it is important to obtain insight regarding the extent of injury of a person affected by brain injury due to exposure to blast wave and resulting mechanical loading on axonal cytoskeleton components of neuron. Indeed, a more comprehensive insight is obtained if we incorporate the biochemical effect, as the tau-MT affinity is hypothesized to be significantly dependent upon the phosphorylation state. In a nutshell, this study investigates simultaneous mechanical loading (brain trauma) and biochemical phenomena (domain phosphorylation and residue phosphorylation).

For our simulations, we have utilized CHARMM force field. However, there are several other alternative force field, such as COMPASS (McQuaid et al., 2004), or reactive force field like ReaxFF (Senftle et al., 2016). However, in our case, the main objective is to capture large deformation, which requires large simulation box size. For such large systems associated with significant unfolding and stretching, using ReaxFF is highly expensive. Furthermore, recently published work on microtubules has shown that CHARMM can successfully capture the deformation associated with high strain rate (Wu and Adnan, 2018).

The strain rates that we have applied fall into high to very high range. It is possible to deduct the response of our systems under more realistic strain rate by using Bell's theorem (Buehler and Ackbarow, 2007), which suggests that material behaves as more stiffer when applied strain rate is increased due to logarithmic increment of rupture force of intermolecular bond (Ahmadzadeh et al., 2014). Considering these aspects of this theorem, this could be a possible future direction. However, the range of strain rate we have used is relevant to TBI scenario, especially in the length scale of the simulations we have performed. In reality, moderate level blow on the head may lead to high level tissue deformation, which eventually leads to extreme level of stress and failure in sub-axonal level components, supported by recent finite element method (FEM) studies on axon (Cloots et al., 2011, 2010). These studies show that axonal level anisotropy and cellular level heterogeneity might play instrumental role to determine failure criteria of the components, and injury level. Also, this level of strain rate is justified in the scenario of cavitation bubble collapse or blast wave exposure, which leads to intensely high stress in sub-axonal component (Wu and Adnan, 2018).

Phosphorylation effect on tau protein and its ability to alter mechanical behavior has been hypothesized as an important parameter in cytoskeletal studies, but the causal postulates have been dubious for multiple reasons. Experimental studies have already shown that aggregation can be phosphorylation independent (Goedert et al., 1992) and healthy to disordered conformation is reversible (Biernat et al., 1992). First, due to the dynamic nature of tau-MT interaction scenario, it is postulated that phosphorylation is not the only parameter and a dynamic combination of several biochemical parameters have ability to alter tau behavior (Churcher, 2006; Lindwall and Cole, 1984), and that multiple parameters might play crucial role to invoke a certain single physical or chemical response (Churcher, 2006). Second, healthy versus phosphorylated tau protein vulnerability to instability under mechanical load has not been quantified. Admittedly, quantification from this outlook is difficult because phosphorylation is not only developmentally regulated (Dudek and Johnson, 1995; Goode and Feinstein, 1994), but also dependent on stoichiometry and number of tubulin dimer attached in phosphorylated state, which may invoke less sensitivity to phosphorylation effect (Gustke et al., 1994). The absence of causal relationships between the mechanism of phosphorylation and its effect was the primary motivation of the current study, and essentially the results provide new insight from both perspectives.

In order to avoid overemphasizing on solely phosphorylation effect, the quantification of both domain focused and residue focused phosphorylation must be considered. From that perspective, the healthy versus considerably phosphorylated tau protein response under extreme mechanical load has been documented in this manuscript, where the phosphorylation level from the literature and in this manuscript are comparable. Moreover, MD simulation has proven to be particularly useful in the current study, as we have been able to observe tau protein behavior in realistic environment in nanometer length scale, retaining the atomistic details.

The general observation is negligible to no sensitivity of domain focused phosphorylation to mechanical load, whereas higher level sensitivity of residue focused phosphorylation suggests the importance of targeting specific residues in critical region around MT binding region, and justifies the tendency of kinases

of attacking active sites in the side chains of tau protein filament and interrepeat regions of MT binding sites. From the literature it is already evident that not all phosphorylation sites play equally significant role to determine tau-MT interaction, and therefore, a more comprehensive residue-by-residue phosphorylation effect study would provide more complete insight on the effect of strain rate in presence of posttranslational modification at different domains or residues. However, after comprehensive literature review on this aspects, the author would recommend practicing reservation while selecting phosphorylation sites, as single site phosphorylation can affect the tau-MT affinity, but not strong enough to overlook other effects; and due to possible clustering effects, mutually exclusive combination of phosphorylation sites might be equally strong candidates to alter the mechanical behavior of tau and tau-MT interaction.

Earlier studies have repetitively suggested that residue-focused studies can provide more quantitative insight than the domain-focused ones, and that a representative pathological state of tau would consist of 7-8 phosphorylated sites (Jho et al., 2010; Kenessey and Yen, 1993). Furthermore, from the domain point of view, the projection domain in the vicinity of MT binding region, and the interrepeat domains in the MT binding region are the strongest candidates to alter tau-MT binding affinity. Therefore, the current study can reliably represent the phosphorylation effect from both phosphorylation level and active site location standpoints; and especially the observation from the residue-focused tau-MT interaction results further substantiates the selection of active phosphorylation sites in this region. Our selection of critical phosphorylation sites SER 199, 202, 262, 396, 404, 409, and THR 231) takes the possibility of weakening the cytoskeleton into account, as well as attempts to highlight the effect of phosphorylation effect outside MT binding region, which were not conclusive in the earlier studies (Biernat et al., 1992; Bramblett et al., 1993; Buerger et al., 2002; Haense et al., 2008; Hu et al., 2002; Kenessey and Yen, 1993; Mandelkow and Mandelkow, 1998; Mandelkow et al., 1995; Pickhardt et al., 2005; Santarella et al., 2004; Trinczek et al., 1995).

The response of single tau, dimerized tau, and tau-MT interaction in presence of domain-focused phosphorylation suggested that phosphorylation effect in different domains or multiple domains

simultaneously might be ineffective in presence of extreme mechanical load. On the other hand, residue-focused phosphorylation in tau-MT system and tau accumulation system suggested strong effect of phosphorylation irrespective of mechanical loading, substantiating the relative importance of residues from the perspective of phosphorylation.

Admittedly, the accumulation tendency is likely to be a function of primary conformation also, and therefore, a continuation of this study might consist of a statistical significance of primary conformation of tau protein, and concentration in a given system size to obtain quantitative insight on the aggregation tendency. In order to verify the dependence of multiple tau protein accumulation on the residue phosphorylation state, we have tested four (4) systems with 2, 3, 4, and 6 tau proteins. In all cases, we have observed that phosphorylated tau proteins tend to accumulate more than the normal ones. It is relevant to mention that Between microtubule (MT) bundles, tau protein acts as crosslinks, and they are spaced 20-40nm from each other (Adnan et al., 2018; Ahmadzadeh et al., 2014; Hirokawa et al., 1988; Tang-Schomer et al., 2010). Therefore, for the tensile tests, there is no sample size effect, as one tau protein crosslink does not affect the behavior of another one.

As an intrinsically disordered protein (IDP), the unique responses of tau protein can likely be attributed to its inherent disorder and ever-changing conformation, which might facilitate absorbing strain and extended attachment to MT surface despite extreme strain rate. We consider the scenarios presented as particularly relevant to TBI scenario, as sub-axonal components undergo extreme deformation, and therefore, vulnerable regions would be projection domain of single tau, overlapped projection domains of dimerized tau, and tau-MT interface – as the primary markers in TBI are axonal strain and stretch, and deformation of individual components. Furthermore, the accumulation study is also relevant from TBI perspective, as TBI and similar neurological disorders suggest increased tau aggregation. However, as we have mentioned in our mechanical study on tau, a possible continuation is a quantitative assessment of IDP-substrate bonding in presence of mechanical loading and posttranslational modification to decide whether this enhanced interaction is a common attribute of IDPs, especially microtubule-associated proteins.

Additionally, the current study also substantiates the importance of studying prolin-rich proteins, which are relevant to neurodegenerative diseases. studies (Gladkevich et al., 2007; Sochocka et al., 2019). These proteins are heavily implicated in neurodegenerative diseases and traumatic brain injury, which tau is also involved in. The prolin-rich region (PRR) is a speculative binding site in proteins, so future studies could highlight on protein-protein interactions from biochemical outlook.

Finally, the multiscale modeling aspect of our study can also be a highly potent future direction. In the earlier section of the discussion, we have already substantiated that the extent of injury differs from length scale to length scale, and that mild injury to the head at macroscale may cause significant deformation in tissue level, leading to eventual extreme deformation at axonal level (Cloots et al., 2010). Therefore, the strain-rate dependent behavior of the tau protein (and other axonal cytoskeletal components of neuron) can be used to develop a bottom-up realistic and comprehensive axon model. In this regard, one approach could be determining damage-prone areas of brain by using continuum scale model of highly biofidelic human head (Pearce and Young, 2014), and then incorporate the cellular and axonal level properties to validate the behavior of the model. It is to be noted that multiscale modeling by using combination of MD simulation and finite element method (FEM) has been used in diversified fields of materials science, such as Li-ion battery development, (Mortazavi et al., 2017), graphene composite structure (Mortazavi and Rabczuk, 2015), etc.

3.4 Conclusion

In this study, we have attempted to determine the unfolding and stretching stiffness for single tau, stretching required for dimerized tau and tau-MT interaction models, and find the effect of phosphorylation on different domains of tau on these particular mechanical properties or behaviors. From our simulations, the major findings can be summarized as below:

1. Single tau protein does not show dynamic alteration in unfolding and stretching stiffness due to phosphorylation and stretching stiffness can be 4-7 times higher than the unfolding stiffness.

2. Dimerized tau protein models show that the stretching required to separate the protein forming the dimer is the same for phosphorylation in individual domains (~750%), but is significantly less in case of phosphorylation in all domains (~600%).

3. For tau-MT interaction simulations, it is found that for normal phosphorylation, the tau separation from MT occurs at ~1125% strain, but for phosphorylation in projection domain and N-terminus tail, it occurs at higher strain (~1330%), for phosphorylation in MT binding sites, MT-tau shows the strongest bond that cannot be separated even at the cost of disintegration of MT subunits, and separation takes place earlier for phosphorylation in all domains altogether (~918%).

4. Phosphorylated tau separates earlier from the MT surface than normal tau. However, the separation stretch is different according to the strain rate. At higher strain rate, the normal tau separates at 1170% strain, while phosphorylated one separates at 1060% strain. At lower strain rate, the normal tau and phosphorylated tau separate at 1193% and 1100% strain, respectively.

5. Normal tau and phosphorylated tau show different accumulation tendency. For 1ns NVT equilibration at 310K, randomly placed tau proteins maintain their distance from each other, while the distance decreases significantly for phosphorylated taus.

Although bottom-up modeling of axon requires mechanical characterization of individual neural cytoskeletal components, the physical chemistry perspective is essential due to their relevance in real-life scenario. Therefore, this study has shown the outcome of some unique approaches to depict mechano-chemical behavior of tau protein, where we can observe the effect of both posttranslational modification, and mechanical response under extreme strain rate, which is relevant to TBI; and this particularly facilitates obtaining insight on comparison between the behavior of healthy and pathological tau.

CHAPTER 4

EFFECT OF STRAIN RATE ON NEUROFILAMENTS

4.1 Introduction

4.1.1 NF Structure

NFs are intermediate size filament proteins found in the cytoplasm of neurons, and they build up neural cytoskeleton along with microtubules (MT). NFs consist of five types of proteins: neurofilament light (NF-L), neurofilament medium (NF-M), neurofilament heavy (NF-H), internexin, and peripherin (Hoffman and Lasek, 1975; Yuan et al., 2012b, 2006). The co-assembly of these five types of proteins can be different according to stages of development and nerve cell types. NF expression is directly related to development, as it increases postnatally in neurons that are myelinated (Nixon and Shea, 1992). Aside from their structural role, they can act as cargoes of axonal transport (Hoffman and Lasek, 1975). NF is also important as a biomarker of axonal damage in neurodegenerative diseases, because during axon degeneration, NFs are released into the blood or CSF (Jonsson et al., 2010).

Brain NFs are particularly different from the NFs of the other parts of the body, because they are prone to create a more viscous mixture with MTs (viscosity differing around 1000cP), and microtubule associated proteins (MAPs) act as cross bridges between these two types of proteins, as suggested by the affinity grid electron microscopy study on bovine brains (Aamodt and Williams Jr, 1984a). Accumulation of NFs is a distinctive biomarker of neurological damage or disorders (Perrot and Eyer, 2009; Wang et al., 2012), such as frontotemporal dementia or multiple sclerosis, as suggested by multiple studies (Brureau et al., 2017; Szaro and Strong, 2010). Presence of soluble NFs in cerebrospinal fluid (CSF) or increased NF level have been related to neuronal death or axonal degeneration (Rosengren et al., 1996), and stoichiometry of NF

types differs according to the type of pathology (Kim et al., 2011). Furthermore, NF accumulation in different phosphorylated state is also related to several pathologies (Cifuentes-Diaz et al., 2002).

There have been several hypotheses proposed to elaborate NF structure and behavior including review works (Laser-Azogui et al., 2015; Nixon and Shea, 1992), as NFs contain domains with intrinsic disorder. The structure of an NF contains central alpha-helical region flanked by unstructured N and C termini. General description suggests that the structure contains a globular head (N terminus), a hydrophobic alpha-helical rod domain (Beck et al., 2012) and variable, intrinsically disordered, tail domain (C terminus) differing in length and amino acid composition (Yuan et al., 2012a). The N terminal head domain contains an MT polymerization inhibitory domain that regulates number of MTs in the axon and facilitates forming end to end interaction of heterotrimers to form complete filaments (Kumar et al., 2002), and the rod domains polymerize NF subunits while simultaneously working as a binding site for the myosin (Bocquet et al., 2009). Finally, the C-terminal domains of NFH and NFM form fine lateral extensions that create spacing between NFs, maximizing the space-occupying capability during axon caliber expansion (Rao et al., 2011). The peripheral domains (sidearm projections) have been revealed by different approaches of experimentation, such as rotary shadowing (Hisanaga and Hirokawa, 1988). Conformational properties of interacting NF structure, charge states of the sidearms, etc. have been analyzed in depth in separate studies (Fliegner and Liem, 1991; Stevens and Hoh, 2010). The substructures have also been studied in separate researches earlier (Wen and Wisniewski, 1984), and it is found that the equilibrium structure is determined by ionic strength and pH (Zhulina and Leermakers, 2007a), the effect of pH at physiological ionic strength being noticeable only in the acidic range and more pronounced for a dephosphorylated NF. Moreover, the electrostatic interactions between the charged portions of the structures play a large role on the formation of NF network (Zhulina and Leermakers, 2007b). Sequence based modeling has revealed NF sidearm structure in earlier studies (Chang et al., 2009), and suggested that medium, not extensive, protrusions are critical to define NF spacings and eventually, axonal caliber. In other words, NFM defines the axonal diameter, because even at phosphorylated state, NFHs get stretched but do not unfold fully, staying in the

bounds of the NFM sidearms (Chang et al., 2009). This observation is in conflict of several studies which suggested that NFH has the dominant role in regard of axonal diameter (de Waegh et al., 1992; Hsieh et al., 1994), while agreeing with some experimental results (Elder et al., 1998; Rao et al., 1998). However, the role of NFM phosphorylation should not be overemphasized, because gene replacement technique that produces phosphorylation incompetent alanine showed that there is no significant difference between wild type and phosphorylation incompetent sidearms (Garcia et al., 2009).

There have been several studies to model NF network and interaction, such as sequence-based coarse grained (CG) modeling where phosphorylated state was controlled by assigning appropriate charge to KSP motifs (Chang et al., 2009), Monte Carlo simulation studies (Kim et al., 2011; Kumar et al., 2002) strengthen polymer brush appearance of NF structure, and that phosphorylation state controls the stretching, interaction and conformation of the sidearms. Conformational study performed by molecular dynamics (MD) simulation agrees with the general hypothesis that NF is a polyelectrolyte (NFL is a strong one, while NFM and NFH are weaker) (Stevens and Hoh, 2010).

4.1.2 Modifications in NF structures: Polymerization and Phosphorylation

Polymerization is an important aspect of NFs, where two dimers associate to form a tetramer, which is believed to be the structural unit of NF. The N terminus contains numerous phosphorylation sites, which are important for subunit interactions during filament assembly. The C terminus is intrinsically disordered, which lacks alpha helix or beta sheet. This C terminus domains of NFH and NFM project radially from the filament backbone to form a dense brush border of highly charged and unstructured domains analogous to bristles on a bottle brush, and they have been proposed to define a zone of exclusion around each filament, effectively spacing the filaments apart from their neighbors. These projections maximize the space-filling properties of NF polymers. In mature myelinated axons, NFs can be single most abundant cytoplasmic structure, occupying most of the axonal cross-sectional area. The number and packing density of NFs in an

axonal cross section defines the axonal diameter, which is determined by NF gene expression (Albert, 2017). The side-arms define the packing density, which is affected by phosphorylation, because phosphorylation is thought to increase the extensibility of the sidearms (Eyer and Leterrier, 1988), hence increasing the spacing between the neighboring filaments by the binding of divalent cations between the sidearms of adjacent filaments (Kushkuley et al., 2010, 2009). NF structure and property analyses have obtained conflicting results, because same (and different) group of researchers have found that viscosity of NF-MT mixture is increased as ATP is added, and also highly viscous NF-MT gel can be formed without ATP (Aamodt and Williams Jr, 1984b; Minami and Sakai, 1986; Runge et al., 1981).

Various post-translational modifications take place in NF, including phosphorylation, which is mediated by kinases protein kinase A and C, Cam kinase II etc. (Sihag and Nixon, 1989). Multiple phosphorylation sites have been found in NFs of vertebrate and invertebrate species (Julien and Mushynski, 1982). Phosphorylation state determines the structure and biochemical properties of NF peripheral regions (Carden et al., 1985). Enzymic dephosphorylation caused the NF to lose interconnection, and gelation has been obtained by phosphorylation performed by protein kinase (both in vitro) (Eyer and Leterrier, 1988). The enzymatic phenomenon affects the structural property by altering charged state of the residues, and regulates macroscopic properties, such as orientation and stress response (Malka-Gibor et al., 2017). Phosphorylation in the head domain of NF regulates axonal transport (Yates et al., 2009), inhibits NF assembly, and modulates interaction with other proteins (FRAPPIER et al., 1987; Hashimoto et al., 2000). Sedimentation experiment suggested that 1-2 mol of phosphorylation is sufficient for inducing disassembly, and phosphorylation level greater than that linearly increases disassembled NFL (Hisanaga et al., 1990).

It is proposed that sidearm phosphorylation can regulate such transport in a negative way, because some Lysine-Serine-Proline (KSP) repeats are targeted by cyclin dependent kinase 5 or activator enzyme p35 (CdK5/p35), etc. for phosphorylation (Ackerley et al., 2003; Sharma et al., 1998; Sihag and Nixon, 1989). Serine residues in the KSP repeats are particularly targeted by kinases for phosphorylation in NFH in vivo (Lees et al., 1988). Myelination is hypothesized to have negative effect on phosphorylation, as suggested

by studies on demyelinating mutant Trembler mice (de Waegh et al., 1992). Phosphorylation in the tail domain (mainly due to decreased activities of phosphatases, and increased levels of NF kinases, including Cdk5, ERK1, ERK2, JNKs, etc. (Kaji et al., 2004; Zhu et al., 2001)) causes proteolysis resistance to NFs (Goldstein et al., 1987), and can regulate the interactions between the NF domains themselves and with MTs (Hisanaga et al., 1990; Hisanaga and Hirokawa, 1989; Pant, 1988). Aberrant phosphorylation is a pathological biomarker, because it leads to the accumulation in cell bodies and has been observed in the brains of AD patients and those suffering from other neurodegenerative disorders (Rudrabhatla et al., 2011). Mass spectrometric studies also are compatible with these observations, as they have suggested that AD affected brains have four to eight fold increased phosphorylated KSP repeats than that of control patients (Rudrabhatla et al., 2011). Additionally, O-GlcNAcylation in NF has been observed to reduce phosphorylation (Deng et al., 2008). Some studies, however, have investigated unfolding mechanism of NFs while phosphorylated in specific domains, such as in NF sidearms (SA) by using atomic force microscopy (AFM) (Aranda-Espinoza et al., 2002). The results suggested that SA are larger when phosphorylated and there are four un-foldable domains regardless of phosphorylation state or presence of ATP. Furthermore, phosphorylated SA requires threefold force to unfold than dephosphorylated ones, suggesting a less pliant as well as larger structure when phosphorylated.

Although numerous studies suggested that NF structure and functionalities are affected by phosphorylation and dephosphorylation, there are other studies which conflicted with these observations. For example, rotary shadowing showed that dephosphorylation has not affected the ability of NFs to form cross bridges of the carboxy terminal tail projections in vitro (Hisanaga and Hirokawa, 1989), and recent gene replacement study has shown that NFM KSP repeats do not modify axonal cytoarchitecture (Stevenson et al., 2011).

4.1.3 Other Parameters Affecting NF Network, Structure and Properties

There are several other parameters on which NF network formation and behavior depends because NF-NF interaction and NF to other cytoskeletal component interaction are particularly complex. For example, NF can be separated into bundled ones and separate ones (which are more prone to bind with MTs). NF-NF and NF-MT interaction have found to compete according to the intervention of motor protein kinesin (Kushkuley et al., 2009).

However, one of the most highlighted aspect is the charged nature of the tail domain (the sidearms differ in protein length, net charge and charge distribution (Chang et al., 2009; Herrmann and Aebi, 2004; Janmey et al., 2003)). Although the tail region is mostly negatively charged, there are residues containing positive charge in this region as well. The self-assembly occurs due to the coiled coil interactions along the hydrophobic strips of the alpha-helical region (Beck et al., 2012). Electrostatic analysis shown that due to the polyampholyte nature of the sidearms, there is a handshake (attractive or repulsive) interaction mechanism between the regions of separate NF subunits (tip-tip or tip-body). Additionally, the tail region consists of a nonuniform charge distribution due to amino acid residues that depend on pH control (due to ionizable groups), as well as the level and distribution of phosphorylation sites (Chang et al., 2009). Effect of divalent ions, which can act as effective crosslinkers between adjacent filaments have been emphasized in some studies, and it is hypothesized that multivalent ions screen the repulsive interactions between charged residues on the sidearms leading to their collapsed conformation, and induced a cross-bridge type of interaction between the adjacent filaments (Leterrier and Eyer, 1987). Furthermore, hydrophobic region interactions between adjacent filaments have also been found to reduce the extension of the sidearms (Jayanthi, 2014). Among other parameters, one worth to mention is exposure to neurotoxic aluminum, which induces perikaryal accumulation of phosphorylated NFs by stabilizing cross bridging of the sidearms (Kushkuley et al., 2010). Another one is the proportion of occurrence of NFM and NFH, to which the network has been found remarkably stable by self-consistent field theory (Zhulina and Leermakers, 2010).

4.1.4 NF Properties

Mechanical properties of NF networks have been found to be quite similar to that of semiflexible polymers (Rammensee et al., 2007), the storage modulus of which is highly concentration dependent. The storage modulus increases significantly with aluminum ion (the ion which also incorporates brittleness to NFs). Bovine spinal cord NF study through fluorescence and electron microscopy revealed the properties of the viscous gel formed by NFs (elastic modulus >100Pa and shear moduli increased in a time dependent manner to the level of vimentin i.e. >100Pa, suggesting the importance of the cross-bridges) (Leterrier et al., 1996), which suggested that phosphorylation, dephosphorylation and interaction with other cytoskeletal components (such as actin) are related to the mechanical properties. Nonlinear elasticity has been found in tensile and shear test on intermediate filaments (IF) networks, along with strain stiffening and recovery (Wagner et al., 2007). Linear and nonlinear viscoelastic property study showed that NF network works as a soft solid and exhibits significant strain stiffening above critical strain (30-70%) (Yao et al., 2010). The elasticity is entropic in nature and can be related with cross-linked semiflexible network, mediated by divalent ions.

There are several unanswered questions or areas regarding NFs, such as specification of the regions regulating transport kinetics, mechanics of formation and stabilization of stationary NF network affected by phosphorylation, etc. which require further studies to obtain conclusive insight. In the current study, we have attempted to determine the stiffness of NF isoforms, and their accumulation tendency in normal and phosphorylated state.

4.2 Method

By going through the recent computational approaches on intrinsically disordered proteins (IDPs) or proteins that contain disordered portions in their structures, we have found that recent years have observed significant improvement in computational studies by using predicted structure. Notable examples are electrostatic study (Castro et al., 2019) and aggregation behavior study on tau (Battisti et al., 2012). Similar

to our earlier work on tau protein, the neurofilament structure for NF-Land NF-H are obtained from the i-TASSER predictor software (Zhang, 2008). We have used the model with the C score of 1.04 to 1.06 (the C score is determined based on significance of threading template alignments and the convergence parameters of the structure assembly simulations, the detailed discussion of which is out of scope of this study) which we have assumed satisfactory for a protein containing a significantly disordered structure. We have solvated the obtained structure with TIP3P water using CHARMM-GUI (Jo et al., 2008) solvator and quick-MD simulator modules. Required number of 0.15M KCl ions were added to obtain charge neutralization for explicit solvent simulations. The NF accumulation models were created by using UCSF Chimera (Pettersen et al., 2004), in which we have placed two identical NF isoforms at 20Å offset from each other, and then equilibrated them for 1ns, tracking the distance of the mass center distance between the proteins in normal and phosphorylated state. We have used explicit solvent technique of CHARMM (Best et al., 2012) in LAMMPS (Plimpton, 1995) (pair_style lj/charmm/coul/long) for solvation and equilibration.

With periodic boundary conditions in all three directions, we have equilibrated the structures for all cases (NF-L and NF-H) for 1ns to minimize the potential energy at a targeted temperature of 310K. NF-L and NF-H single filament contained 8486 and 15882 atoms respectively in normal state, and 8526 and 15922 atoms respectively in tail-phosphorylated state. For phosphorylated tests, we have applied phosphorylation in the last available 10 Serine (SER) residues of the structure(s). The LJ potentials are used with inner and outer cutoff of 10Å and 12Å, respectively. Long range coulombic interactions are computed by pppm style, facilitating a particle-particle particle-mesh solver with a 3d mesh.

We have used CHARMM36 (Best et al., 2012; Brooks et al., 2009; MacKerell et al., 1998) potential parameters with appropriate CMAP corrections (Best et al., 2012) for all the simulations. Potentials for GDP and GTP are taken from that of ADP and ATP respectively (Wells and Aksimentiev, 2010). The equilibration was performed in NVT canonical ensemble, with the temperature damping parameter of 100fs.

In the NF tensile tests, we have fixed the head and rod domains and pulled the tail domains at different strain rates (10^8 s^{-1} and 10^9 s^{-1}) along x axis.

The stress-strain plots are obtained by the per-atom stress calculation and summation in LAMMPS. However, as the output is in (pressure x volume) unit, we must divide the obtained stress value by the volume of the protein (or certain portion of the protein). The general formulation used by stress per atom command is $P = (P_{xx}+P_{yy}+P_{zz})/ (3xV)$, where P_{xx}, P_{yy} and P_{zz} is the summation of stress/atom value for all atoms in x, y, and z direction respectively, and V is the summation of volume of the atoms of the protein being considered. The approximated volume was obtained by Voronoi cell approximation, adapted from LAMMPS voro++ package (Rycroft, 2009). The strain is simply obtained by the displacement of the atoms from the initial position. All the tensile tests are performed in NVT ensemble, with 100fs temperature damping parameter. The visualizations of the tensile tests are carried out by OVITO software (Stukowski, 2010).

All the simulations were carried out by the STAMPEDE2 supercomputer of Texas Advanced Computing Center (TACC).

4.3 Results

4.3.1 Effect of Strain Rate on Neurofilaments

We have performed tensile tests at high strain rates on the NF isoforms ($1x10^8$ s^{-1} and $1x10^9$ s^{-1}). The head and rod domain atoms were fixed, and the last few atoms of the tail domain were pulled towards –x direction. The calculated stress-strain graphs are shown in Fig. 4.1. We have assumed that >200% strain of the tail domain is sufficient for determining their unfolding and stretching stiffness. Similar to other cytoskeletal components containing disordered structure portion (such as tau protein), NF tail showed unfolding to a significant extent before going into the stretching region.

The stretching and unfolding, however, are observed simultaneously, unlike the tau protein. The last portion of the tail was under pure stretching, while the portion attached to the rod domain was still unfolding. Most of the isoforms (NF-L and NF-H, each of them in normal and phosphorylated state in the tail region) showed steady increase of the stiffness, although there was no detectable trend of them. For example, in normal NF isoforms, the stiffness is <50 MPa at lower strain rate, while for phosphorylated isoforms it is ~100MPa.

However, the consistency we have found in their behavior is the dependency of the stiffness on the strain rate – that is, NF behaved as a stiffer material under the application of higher strain rate, and it can be ~0.5GPa. Another important aspect is the filament length, which, to our observation, plays an important role to determine the stiffness. Under the application of the same strain rate, the smaller filaments showed higher stiffness than the longer filaments, which is an expected observation. Most of the isoforms showed steady increase over the range of 0%-217% strain. In normal NF-H under both strain rates, the stress-strain response was not steady until they are unfolded to 50%-150% strain. Our hypothesis is that the longer filament length is responsible for this response, as for longer filament, the development of stress (which is calculated in our calculation as an average response of the whole tail domain, and comes from the "xx" component of the pressure tensor measured) requires more unfolding to be considered as a significant amount. It is to be considered that the head and rod domains of the NF structure are conserved, while the tail is the variable part (lengthwise) of the isoforms due to the inherent disorder. In NF-L, the tail portion is comparable in length to the rest of the structure, while in NF-M, it is significantly longer, and in NF-L, it is a few times longer than the rest of the structure, and therefore, bound to show deviation from the behavior observed in case of NF-L. Fig. 4.2 shows different stages of unfolding and stretching of the NF isoforms under different strain rates.

a

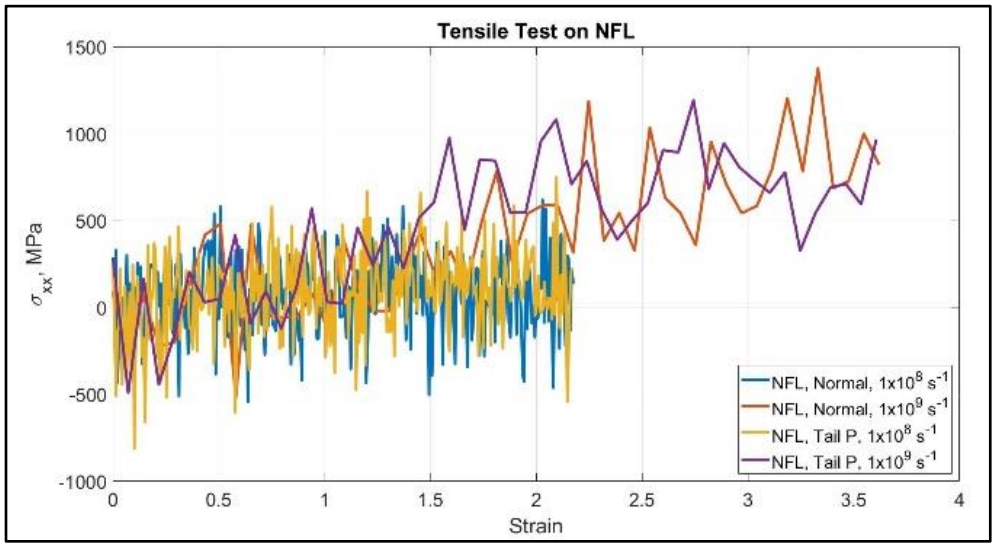

b

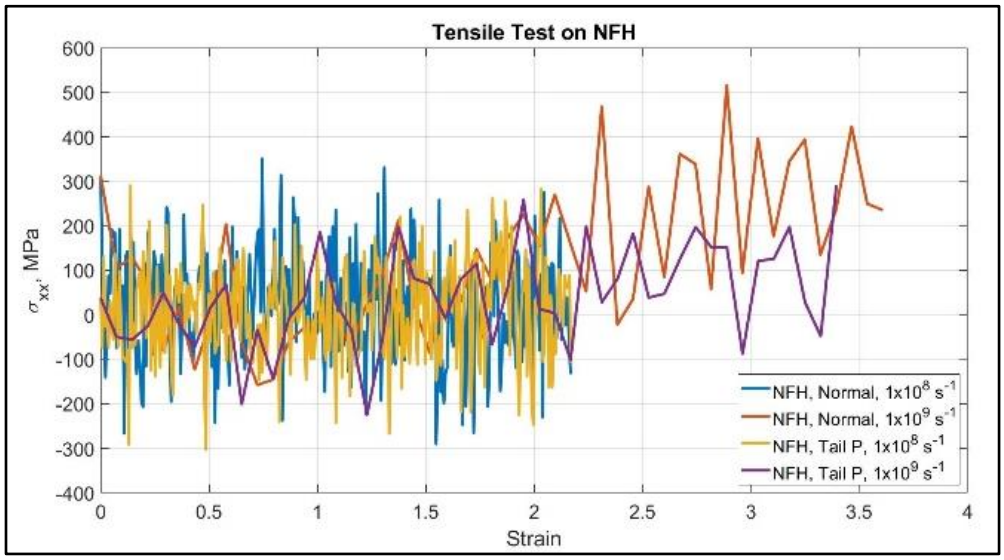

Figure 4.1: Stress-strain graphs at two different strain rates for the pulled tail domain of a. NFL and b. NFH. Throughout the pulling process, we can observe simultaneous unfolding and stretching, and therefore, these two domains cannot be distinguished. However, it is clear that the NF acts as a stiffer material under the application of higher stress, irrespective of phosphorylation state. In order to make a reasonable compromise with the computational cost, we have stopped at ~220% strain for lower strain rate which we

assumed to be sufficient to capture stretched state, while for higher strain rate, we have recorded result till ~360% strain.

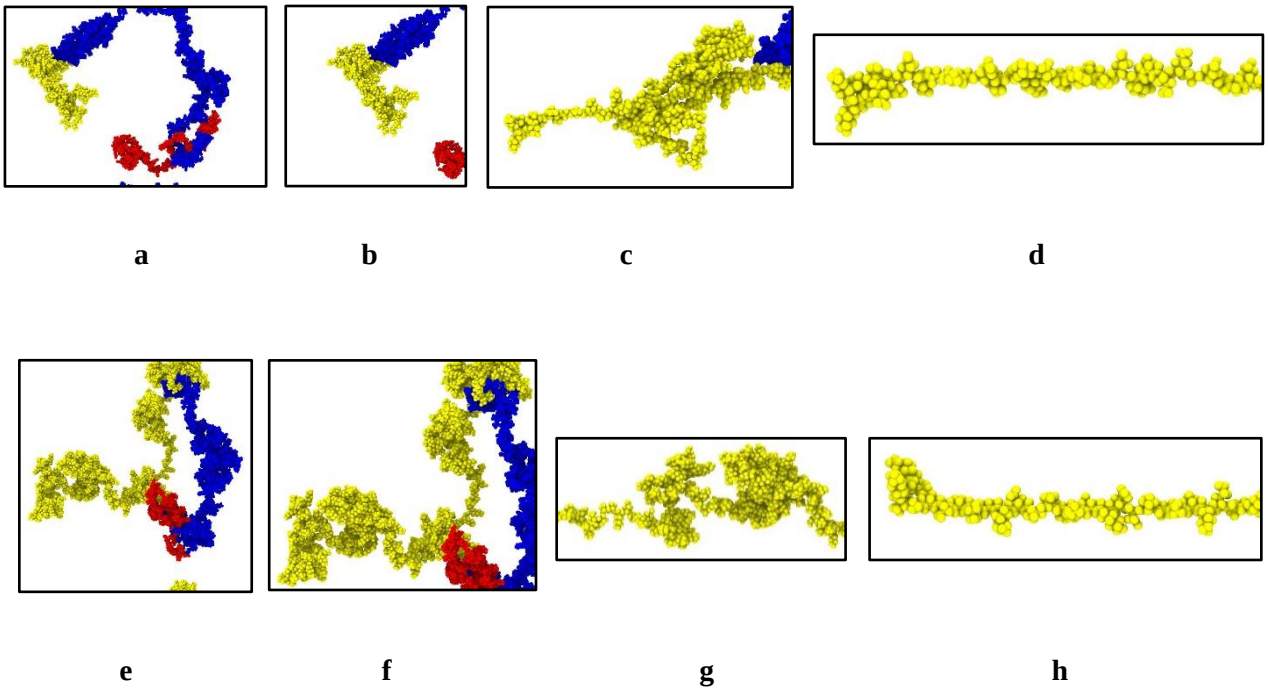

Figure 4.2: Snapshots at different timesteps during the tensile test performed on NFL and NFH (normal phosphorylation, strain rate: $1x10^{9}$ s^{-1}). a. Initial structure of NFL, b. NFL tail region: 0% strain, c. NFL tail region: 180% strain, showing simultaneous unfolding and stretching, d. NFL tail region: 360% strain, showing pure stretching at significant portion of tail region, e. Initial structure of NFH, f. NFH tail region: 0% strain, g. NFH tail region: 160% strain, showing simultaneous unfolding and stretching, h. NFH tail region: 320% strain, showing pure stretching at significant portion of tail region. Color legend: Red: head domain, blue: rod domain, yellow: tail region.

4.3.2 NF Accumulation Test

We have already stated that NF accumulation, at different phosphorylated state has been related to different neuropathology (Cifuentes-Diaz et al., 2002). Therefore, it is important to obtain insight about the effect of phosphorylation on the accumulation of NF isoforms. Although observation of this phenomenon in bulk NF collection would be more realistic, we have made a compromise with the computational cost, and made a representative NF accumulation test model by placing two identical NF isoforms offset by 20Å from each other immersed in a box filled with explicit water molecules. We have minimized the potential energy and equilibrated the structure for 1ns and tracked the distance between the NF filament overall mass center and tail domain mass center. The observation suggests that unlike tau protein, 1ns is very small time to observe considerable distinction between normal and phosphorylated NF accumulation. We have performed the same test for NF-L and NF-H, and found similar mass center-mass center distance in all cases, except the sidearm mass center in NF-L was considerably further in phosphorylated state than in normal state. Our observation suggests two key findings as we have found in our work on tau protein earlier, that is, phosphorylation is not the only key parameter to affect the accumulation tendency of NF filament (as even longer filament of NF-H did not show significant difference in mass center-mass center distance in the accumulation test), and time scale is important to obtain observable distinction between this two cases. In other words, the overall mechano-chemical circumstance is certainly more significant than mere electrostatic interaction between two stand-alone NF filaments. Fig. 4.3 shows potential energy throughout the simulation, Fig. 4.4 shows overall and tail domain mass center-mass center distances of the NF filaments for the different isoforms, and Fig. 4.5 shows the initial, intermediate, and final stage of the accumulation test.

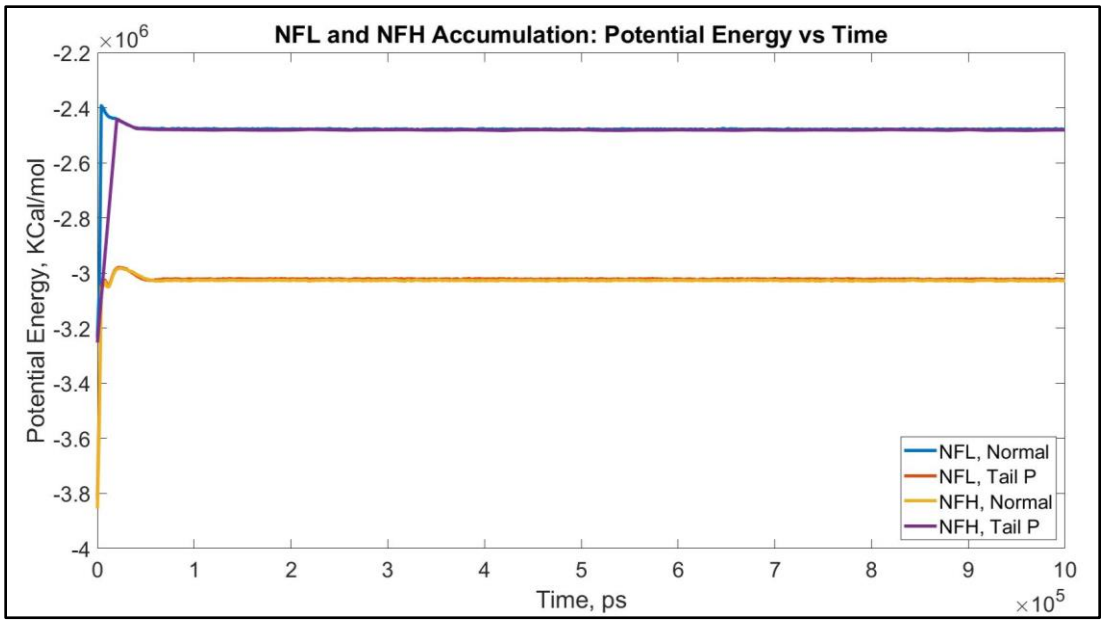

Figure 4.3: Potential energy vs time for NFL and NFH for the entire equilibration time (1ns). After 200ps, the potential energy change over time is negligible for all systems, irrespective of phosphorylation state.

a

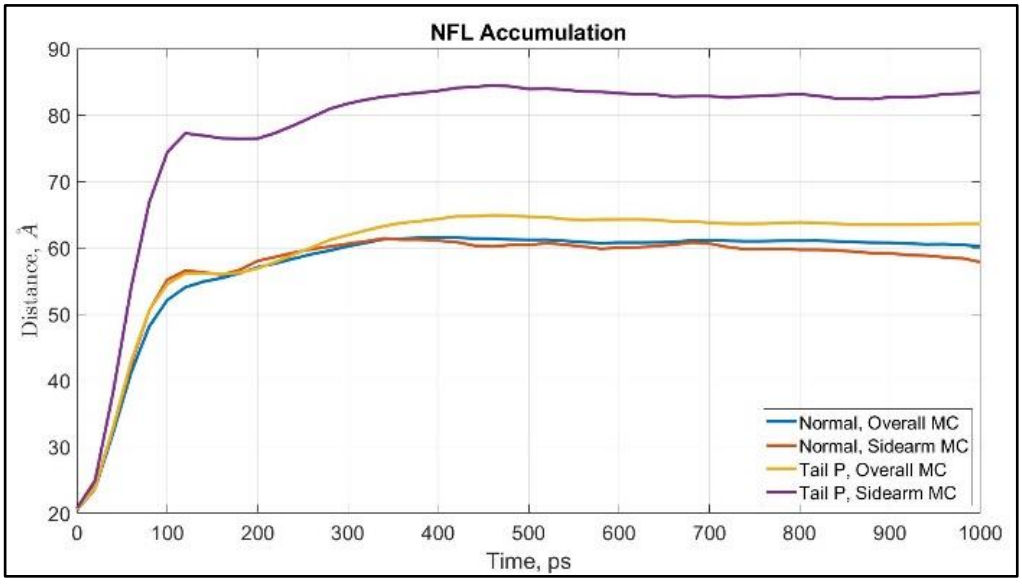

b

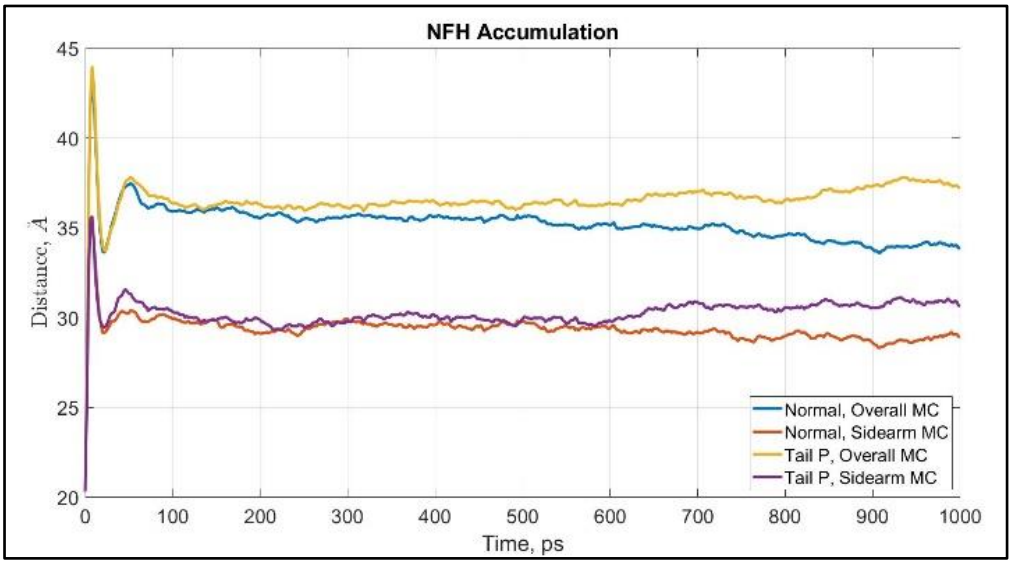

Figure 4.4: Overall mass center distance and sidearm mass center distance for a. NFL, and b. NFH. In both cases, the mass center distance from one protein to the other does not differ significantly, which suggests that unlike tau protein, 1ns is not sufficient to observe possible NF accumulation.

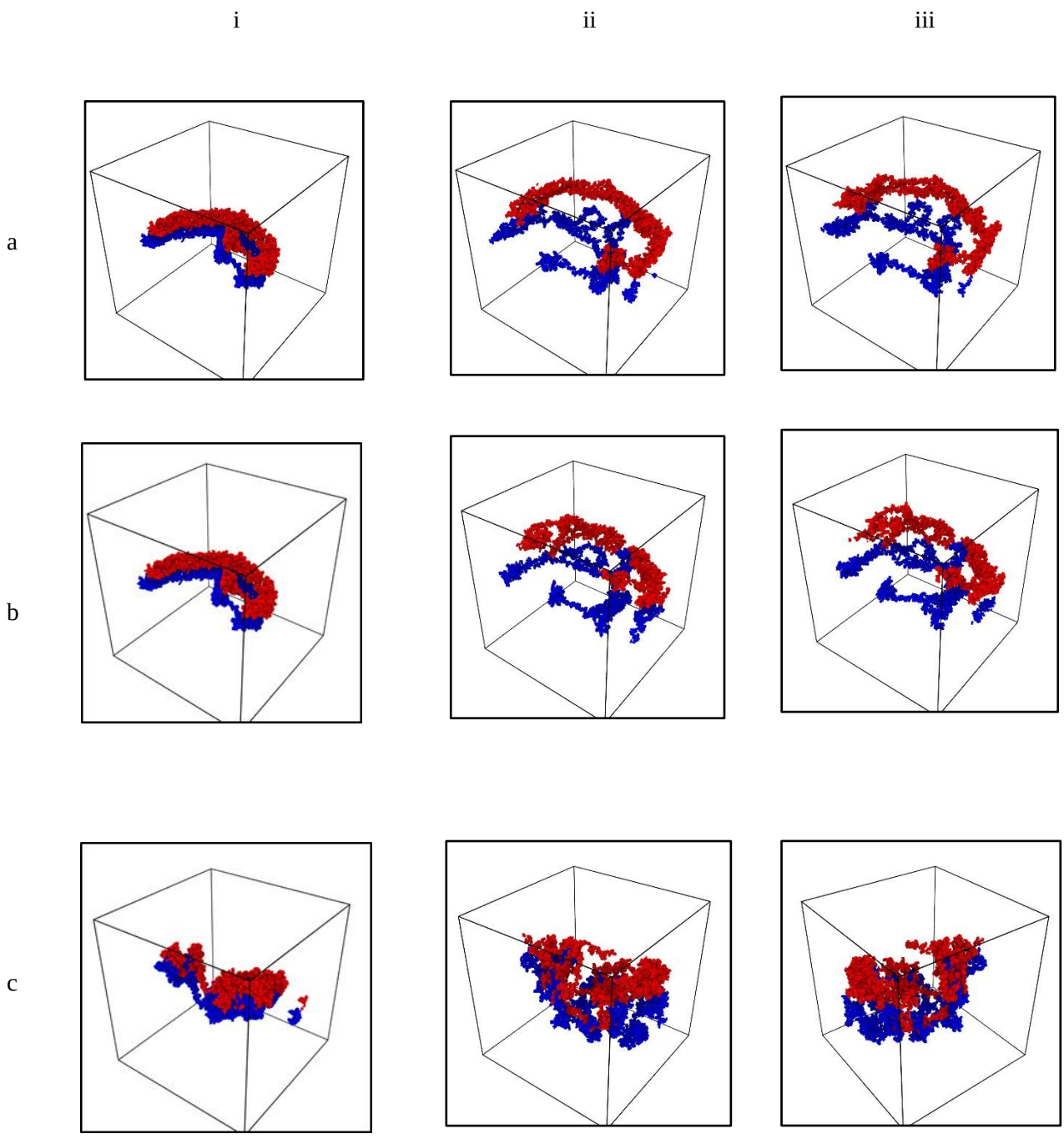
i
ii
iii
a
b
c

d

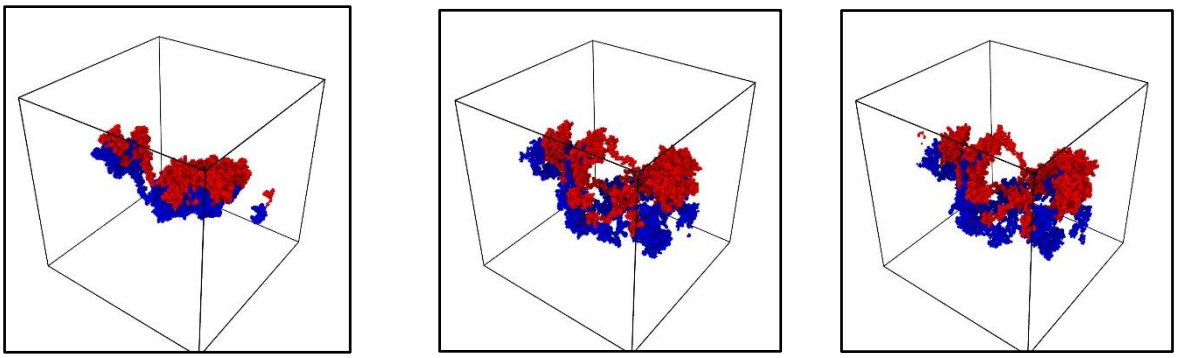

Figure 4.5: Snapshots at different timesteps during the equilibration. a. NFL, normal, b. NFL, tail phosphorylated, c. NFH, normal, d. NFH, tail phosphorylated (for all cases: i. 0ps, ii. 500ps, iii, 1ns). Color legend: Red: First NF, Blue: Second NF. For convenient visualization purpose, water molecules are suppressed. In all cases, we can observe that the protein to protein distance is not changed significantly than the initial distance, irrespective of phosphorylation state, despite their random orientation and absence of any restriction over the periodic boundaries in the box.

4.4 Discussion

The high strain rate behavior of NF is important from the traumatic brain injury (TBI) scenario, and their mechano-chemical behavior under the application of extreme strain and sidearm phosphorylation is important to obtain insight regarding pathological phenomena. Furthermore, their accumulation tendency is also crucial to comprehend their correlation with pathology (Cifuentes-Diaz et al., 2002). It is likely that their highly stretchable attribute is dictated by the intrinsic disorder in the sidearm region (Laser-Azogui et al., 2015).

The NF behavior can also be explained from the potential effect of several parameters, such as conformational properties (Fliegner and Liem, 1991; Stevens and Hoh, 2010)., charged state of sidearms network (Zhulina and Leermakers, 2007b), ionic strength, and pH (Zhulina and Leermakers, 2007a) which

are highly pronounced in the normal (or dephosphorylated) state, and strong NF network formation due to significant interaction between charged network portions. While it is inconclusive from the earlier studies whether the strong interaction in the network level can overcome phosphorylation effect, this study attempts to highlight on this phenomenon.

Studying NF behavior and quantifying their attributes against filament length is also important (Chang et al., 2009; Herrmann and Aebi, 2004; Janmey et al., 2003), as the previous studies were not able to confirm their relative importance from the isoform outlook. While some studies have shown that due to having the largest disordered tail region in structure, NFH can dictate the behavior of overall NF network, conflicting evidence showed that NFH cannot unfold fully in phosphorylated state, and therefore, other isoforms may also play instrumental role to regulate NF network response (Aamodt and Williams Jr, 1984b; Minami and Sakai, 1986; Runge et al., 1981). And in a dynamic environment while there are multiple biochemical parameters such as posttranslational modification and activation of multiple sites due to specific attacks on targeted residues are into play, only phosphorylation in the sidearm region should not be overemphasized, as genetic study showed that wild-type and phosphorylation incompetent sidearms show no remarkable difference (Garcia et al., 2009). Earlier experiments substantiated that phosphorylation effect enhances the extensibility of the sidearms (Eyer and Leterrier, 1988), and therefore, important to dictate the axonal diameter (de Waegh et al., 1992; Hsieh et al., 1994). Multiple studies have further emphasized on the importance of phosphorylation, as it is directly related to altering the charged state of the residues involved, and NF disassembly can be attributed to phosphorylation level.

From specifically sidearm phosphorylation perspective, KSP repeat targeting studies have shown that phosphorylation should regulate the transport in a negative way, and sidearm phosphorylation should induce reduction in interaction (Chang et al., 2009),. Atomic force microscopy (AFM) studies on NF has substantiated the presence of un-foldable regions in the sidearms, which can withstand biochemical effect such as phosphorylation, which explains the behavior of NF filaments in the current study (Aranda-Espinoza et al., 2002). Furthermore, rotary shadowing experiment has also shown that phosphorylation

effect on sidearms cannot be single regulating parameters of such a dynamic phenomenon to define its mechanical characteristics (Hisanaga and Hirokawa, 1988).

Another important parameter is the charge distribution in the sidearm region, which suggests more anomaly in case of longer filament (Chang et al., 2009; Herrmann and Aebi, 2004; Janmey et al., 2003). Sidearm region in NF contains mostly negative, but few positively charged regions, and that decidedly alters the interaction in one-to-one NF interaction scenario. Furthermore, presence of hydrophobic surface on the tail region adds further dynamic aspects while observing the phenomena from biochemical perspective (Beck et al., 2012). While considering NF accumulation, our conclusion is that a combination or mixture of NF-L, NF-M and NF-H will provide comprehensive insight on their aggregation characteristics.

From mechanical perspective, we only know that strain stiffening can occur for NF above critical strain (Wagner et al., 2007; Yao et al., 2010). However, there is not any comparative studies which show the difference between the response of normal versus sidearm phosphorylated NF filament. This study, therefore, provides important insight regarding this scenario, and strengthens the statement that only phosphorylation in a domain cannot fully characterize mechanical behavior for a cytoskeletal component containing intrinsically disordered portion. The increase in extensibility in the sidearm region and the resulting strain stiffening at high strain is substantiating by the increased stress value we have obtained for the phosphorylated NF isoforms. The extreme ability to stretch can also be attributed to inherent disorder which facilitates NF to absorb strain along the length of sidearm, while unfolded region reduces the difference between the stretching characteristics between light and heavy filaments, considering that un-foldable regions are increased while filament length increases; and accumulation characteristic can be attributed to non-uniformly charged portion in the sidearm region.

In short, the parameters that can be attributed to the unique aspects of mechanical behavior of NF are the charged portions, filament length, and intrinsic disorder. Although this study provides critical insight on whether phosphorylation should be held critical with respect to mechanical behavior and NF accumulation, it is difficult to quantify the importance of head-tail proportion in the filament under consideration. If we

juxtapose this study with our earlier works on tau protein from strictly mechanical and mechano-chemical perspectives, we can assert that NF is likely to be slower in aggregation due to longer disordered portion in the structure.

4.5 Conclusion

In this study, the stiffness of the main isoforms of neurofilaments by applying high strain rate relevant to TBI scenario is computationally determined, and significant insight about their aggregation characteristics is obtained. From the MD simulations, the major findings can be summarized as below:

1. NF contains multiple folding at unstretched state, while unfolds to a great extent under the application of strain rate. The unfolding is smoother at smaller filament lengths (smaller isoforms, such as NF-L), while it shows highly unpredictable behavior for larger filament lengths (large isoforms, such as NF-H).
2. The unfolding behavior is highly dynamic, and not only depends on applied strain rate, but also phosphorylation state. The stiffness may differ according to the isoform length, applied strain rate, and phosphorylation state, and may range from a few megapascals to few hundred megapascals.
3. There is no significant difference in the accumulation tendency between normal and phosphorylated NFs even for large filament isoforms, which strengthens the findings of earlier studies suggesting that phosphorylation is not the only factor affecting NF-NF interaction.

The unique aspects of NF mechanical behavior can be attributed to the charged portions, intrinsic disorder in the sidearm, and filament length. This study provides critical information of NF behavior in a realistic environment from the physical chemistry viewpoint and paves the pathway to develop a realistic bottom-up axon model, which requires insight on mechanical behavior of individual neural cytoskeletal components.

CHAPTER 5

VISCOELASTIC PROPERTIES OF TAU PEOTEIN AND NEUROFILAMENTS

5.1 Introduction

Viscoelastic modeling of a material consists of fitting the stress-strain response of that material to an established constitutive correlation. There have been detailed texts which rigorously discuss the methodologies of viscoelasticity for materials (Brinson and Brinson, 2015). The viscoelastic response can be obtained by performing familiar approaches of creep or relaxation tests – according to the nature of the material. If the applied strain causes a time-dependent stress, then the modulus is also a function of time, and thus we calculate the relaxation modulus for the respective material. The deformation mechanism, however, depends on the long-chain polymer characteristics of the material. Determination of viscoelasticity is not just limited to performing relaxation and/or creep test, but also determining the linearity of the material, which is determined by developing isochronous diagrams, i.e. if the relaxation modulus (or creep compliance) is only a function of time and not a function of stress level, then the material is defined as a linear viscoelastic material, otherwise it is called a nonlinear viscoelastic material.

After determining the viscoelastic response, the rest of the modeling consists of fitting the relaxation or creep response to established phenomenological viscoelastic models, such as Kelvin-Voigt or Maxwell models. Without going into details of theoretical discussions on such models, we can mention the feature of Kelvin or Maxwell models that they can increase the parameters by series or parallel addition of the spring or dashpot elements in the constitutive correlation to satisfy our material behavior, which leads to generalized Kelvin or Maxwell model. Their expressions are, in various occasions, convenient to study by expressing them with Prony series expression. Prony series development based on strain rate response have been studied in several independent work, and paved the pathways for further analysis (Chen, 2000;

Tzikang, 2000). However, these linear viscoelastic models may not correspond to the response of all materials undergoing viscoelastic tests, and therefore, we may have to fit with some hyperelastic models, such as Neo-Hookean, Mooney-Rivlin, Ogden, etc. (Kim et al., 2012).

In biomolecules, viscoelastic nature of them has been hypothesized to control their dynamics. For example, viscoelasticity of tau protein, which is an microtubule (MT) associated protein and acts as crosslink between MT fibers – has been found to dictate the reversible sliding and failure of MT, as suggested by experimental and computational works (Ahmadzadeh et al., 2015, 2014; Peter and Mofrad, 2012; van den Bedem and Kuhl, 2015). As an intrinsically disordered protein (IDP), tau has not been studied comprehensively, and when developing viscoelastic models for MTs, crosslink taus are sometimes used with their estimated properties. However, tau protein fragment properties and aspects have been revealed by characterization studies and electron micrography approaches (Wegmann et al., 2011), which have made the estimation of the properties reliable to some extent. However, viscoelasticity of NFs has not yet been characterized in an organized manner, except some experimental insights obtained from NF-MT mixture studies, and their tendency to perform viscous gel – as suggested by electron micrography and other experimental studies (Aamodt and Williams Jr, 1984b; Leterrier and Eyer, 1987; Minami and Sakai, 1986; Runge et al., 1981; Yao et al., 2010). Fitting to any established viscoelastic or hyperelastic model is non-existent for NFs.

The shortcoming in this regard is therefore so evident, that it is necessary to perform viscoelastic modeling for tau and NFs in order to provide required insight for complete axon modeling which incorporate component-level response. This study has undertaken a simplified approach to model stress-strain response of tau protein and neurofilaments (NFs) as viscoelastic material by performing relaxation tests on them after stretching them at different strain rates, and then fitting them with linear viscoelastic model. This study is therefore important to obtain insight on viscoelastic response of two key cytoskeletal components, which will facilitate the development of computational model for axon.

5.2 Method

By going through the recent computational approaches on intrinsically disordered proteins (IDPs), we have found that recent years have observed significant improvement in computational studies by using predicted structure. Notable examples are electrostatic study (Castro et al., 2019) and aggregation behavior study on tau (Battisti et al., 2012). Similar to our earlier work on tau protein and NFs, the NF structures are obtained from the i-TASSER predictor software (Zhang, 2008). We have used the model with the C score of -0.03 for tau protein and 1.06 for NF (the C score is determined based on significance of threading template alignments and the convergence parameters of the structure assembly simulations, the detailed discussion of which is out of scope of this study) which we have assumed satisfactory for a protein containing a significant portion of disordered structure.

We have solvated the obtained structure with TIP3P water using CHARMM-GUI (Jo et al., 2008) solvator and quick-MD simulator modules. Required number of 0.15M KCl ions were added to obtain charge neutralization for explicit solvent simulations. We have used explicit solvent technique of CHARMM (Best et al., 2012) in LAMMPS (Plimpton, 1995) (pair_style lj/charmm/coul/long) for solvation and equilibration.

With periodic boundary conditions in all three directions, we have equilibrated the structures of tau protein and NFL for 1ns to minimize the potential energy at a targeted temperature of 310K. Tau and NFL single filament contained 6424 and 8486 atoms respectively The LJ potentials are used with inner and outer cutoff of 10Å and 12Å, respectively. Long range coulombic interactions are computed by pppm style, facilitating a particle-particle particle-mesh solver with a 3d mesh.

We have used CHARMM36 (Best et al., 2012; Brooks et al., 2009; MacKerell et al., 1998) potential parameters with appropriate CMAP corrections (Best et al., 2012) for all the simulations. The equilibration was performed in NVT canonical ensemble, with the temperature damping parameter of 100fs. For the tau protein, we have fixed the MT binding site atoms and the tail, and pulled the projection domain atoms at two different strain rates (10^8 s^{-1} and 10^9 s^{-1}) using the smd (cvel) command of LAMMPS. In the NF tensile

tests, we have fixed the head and rod domains and pulled the tail domains along -x axis at the same strain rates.

The strain is simply obtained by the displacement of the atoms from the initial position. We have performed the stretch for all filaments for up to 80% strain. However, the smd (cvel) calculations give the force components on the respective filament or filament portion, and we can divide the respective portion with the approximate surface area of the filament to obtain engineering stress component. The approximate diameter of the filament is used as 1.0nm according to the diameter of single strand of tau protein existent in literature (Ruben et al., 1993).

For fitting with 3 parameter viscoelastic model, we have tracked the time dependent modulus, E(t), for each filament, and used it in a simplified MATLAB code to fit to three parameter Maxwell model, using three guessed values of the constitutive equation. The error in the fitting is minimized by using "fminsearch" function of MATLAB (Higham and Higham, 2016), which minimizes the norm of the function generated by the difference of E(t) vs time graph and three parameter function graph obtained from the guessed values. The constitutive equation for the three parameter Maxwell model is shown in Equation 5.1.

$$\mathbf{E(t) = E_1 + E_2 e^{\frac{-t}{\tau}}} \quad \textbf{(5.1)}$$

Where E values are in GPa, and τ is in ps. Therefore, it is sufficient to fit the E(t) vs t graph obtained from the relaxation data to estimated E_1, E_2 and τ values. It is to be mentioned that as per our need, we can extend the equation to fit the result with Maxwell model with more parameters (5, 7, and so on). However, in our case, three parameter fitting was appropriate.

After obtaining the fitted E(t) expression, we can use Alfrey's correspondence principle to obtain shear modulus, G(t) and bulk modulus, K(t) for each case, by using these steps (Brinson and Brinson, 2015):

a. Obtain E(t),
b. Obtain E(s)*, which is the expression of E at the Laplacian domain,

c. Calculate G(s)* and K(s)* using equation 3 and 4 (these are the expression of G and K at the Laplacian domain, respectively,

d. Use inverse Laplace calculation to obtain G(t) and K(t).

As mentioned at step b, the conversion equations for G and K are shown in equations 5.2 and 5.3.

$$\overline{\mathbf{G(s)}^*} = \frac{\overline{\mathbf{E(s)}^*}}{\mathbf{2(1+\overline{\nu(s)}^*)}} \quad \textbf{(5.2)}$$

$$\overline{\mathbf{K(s)}^*} = \frac{\overline{\mathbf{E(s)}^*}}{\mathbf{3(1-2\overline{\nu(s)}^*)}} \quad \textbf{(5.3)}$$

As we know the expression of G and K using the E in the Laplacian domain, we can easily convert them to time domain expressions by using inverse Laplace calculation. And finally, we obtain the Young's modulus, shear modulus, and bulk modulus for the particular filament, at that particular strain rate relaxation experiment. The final expressions for G(t) and K(t) are shown in equations 5.4 and 5.5.

$$\mathbf{G(t) = G_1 + G_2 e^{\frac{-t}{\tau}}} \quad \textbf{(5.4)}$$

$$\mathbf{K(t) = K_1 + K_2 e^{\frac{-t}{\tau}}} \quad \textbf{(5.5)}$$

However, the conversion in equation 5.2 and equation 5.3 requires a Poisson's ratio, and therefore, we have used two scenarios in our calculation: one is for normal, compressible material assumption (Poisson's ratio, ν=0.3), and another is for nearly incompressible material assumption (Poisson's ratio, ν=0.48). Currently we lack the Poisson's ratio calculation in the existent literature, therefore, we had to approach with these two assumed values. However, from microrheological measurements of MT-Actin network study (Pelletier et al., 2009) and orthotropic elastic shell model for MTs (Wang et al., 2006b), we have found that the

Poisson's ratio of such cytoskeletal components are between 0.3 and 0.4. Therefore, our assumption is that the Poisson's ratios we have used in the calculation are reasonable for MT crosslinks (tau proteins) and NFs.

All the tensile tests are performed in NVT ensemble, with 100fs temperature damping parameter. The visualizations of the tensile tests are carried out by OVITO software (Stukowski, 2010). All of the simulations were carried out by the STAMPEDE2 supercomputer of Texas Advanced Computing Center (TACC).

5.3 Results

5.3.1 Viscoelastic Modeling of Tau Protein

In order to perform relaxation test, we have stretched tau protein projection domain up to 80% strain at high strain rates ($1x10^8$/s and $1x10^9$/s). By utilizing the Steered Molecular Dynamics (SMD) feature, we have relaxed the stretched filament for 1ns. This feature facilitates holding the stretched portion at the same coordinates (that is, maintaining the constant strain), and determine the stress relaxation by logging time vs stress data on the stretched portion. The reason to perform relaxation on the projection domain is the same as our earlier studies – as the projection domain is the overlapped portion of tau dimer (Rosenberg et al., 2008) which eventually dictates reversible sliding or failure (instability) of MT structure, studying the response of only the projection domain is sufficient to obtain the stress-strain response. Furthermore, a physical viscoelastic relaxation test typically involves slow strain rate and long period of loading before relaxation, but in our case, the loading strain rates are very high in all cases which means very short duration of loading (Christensen, n.d.; F10gge, 1975). Therefore, we assume that exclusion of the data of the loading stage will not incorporate significant error in viscoelastic modeling.

Fig. 5.1 shows the pre-relaxation stretching, and snapshots of the projection domain conformations at different timesteps during relaxation for tau protein. Fig. 5.2 shows the time dependent modulus trends for the stretched filaments (stretched at two different strain rates). Using the E(t) vs time, we have obtained the expressions of Maxwell viscoelastic model by fitting them with the constitutive equation. The relaxation trend clearly shows that at both strain rates, tau protein acts as 3 parameter solid model. Fig. 5.3 shows the fitting, and Table 5.1 shows the Maxwell parameters.

To obtain complete viscoelastic model, we must determine the shear modulus and bulk modulus. Therefore, we have applied Alfrey's correspondence principle, Laplace transformation, and inverse Laplace transformation to obtain the shear and bulk moduli parameters using two different Poisson's ratios (details are shown in the "Method" section). Fig. 5.4 shows the shear and bulk moduli obtained from the tensile modulus, and Table 5.2 shows the shear and bulk moduli parameters of the fitted curves.

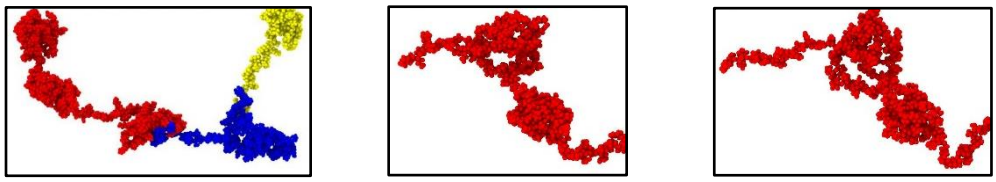

a **b** **c**

Figure 5.1: Pre-relaxation stretching for tau protein ($1x10^8$/s). a. Initial structure (0% strain), b. projection domain at mid-stretch (40% strain), c. projection domain at end of stretch (80% strain). Color legend: Red: projection domain: Blue: MT binding sites and interrepeats, Yellow: tail.

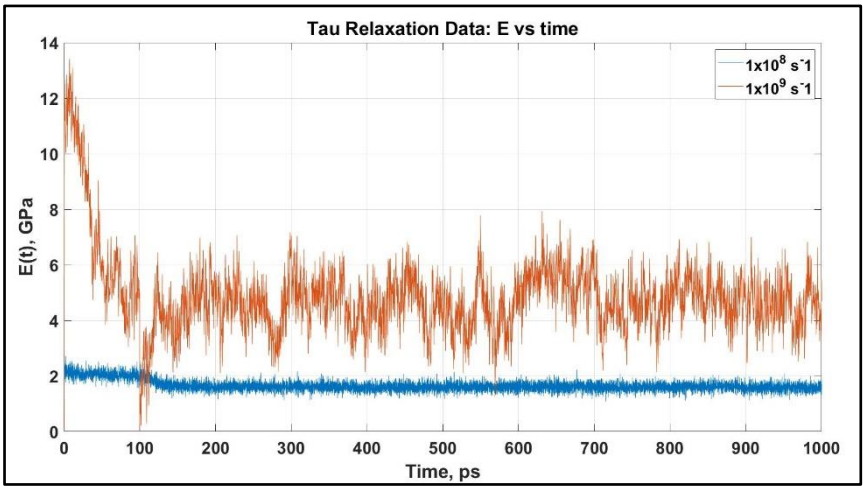

Figure 5.2: Modulus, E(t) vs time for 1ns relaxation test for tau protein which are stretched to 80% at two strain rates. The relaxation curve at two strain rates are distinct for tau protein.

a

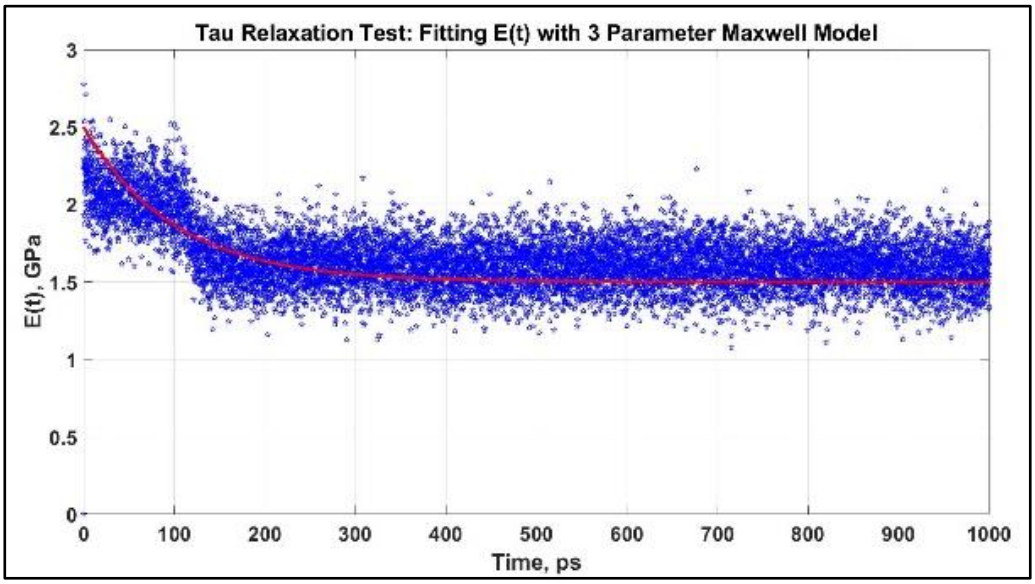

b

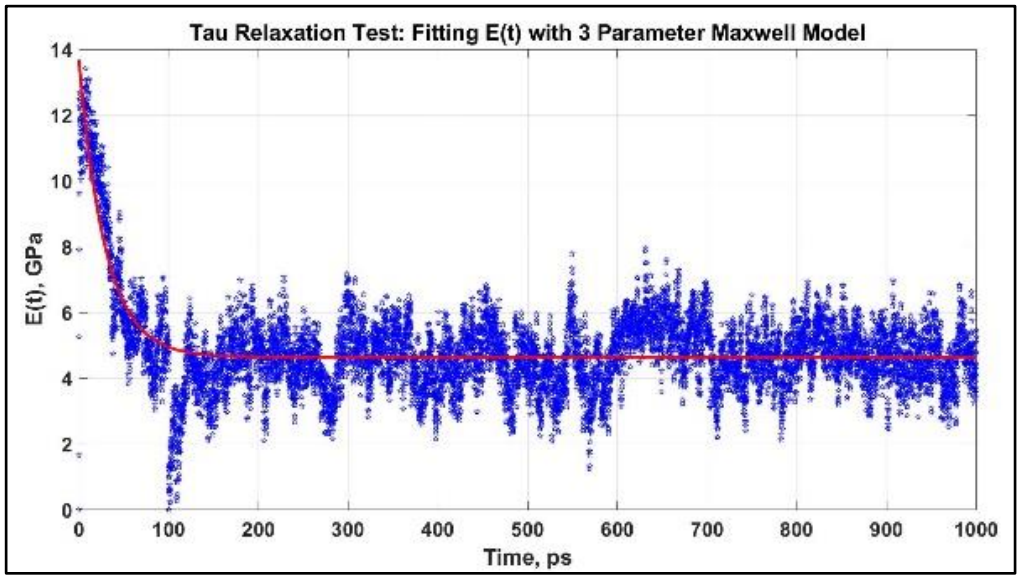

Figure 5.3: Fitting the E(t) vs time curves of tau relaxation test to 3 parameter Maxwell model for initial stretch of 0.8 at two different strain rates. a: $1x10^8$ s^{-1}, b: $1x10^9$ s^{-1}.

Table 5.1: Maxwell Model Parameters from Tau Relaxation Test:

Strain Rate, 1/s	$1x10^8$	$1x10^9$
E_1, GPa	2	3.039
E_2, GPa	1	5.996
τ, ps	100	29.859

a

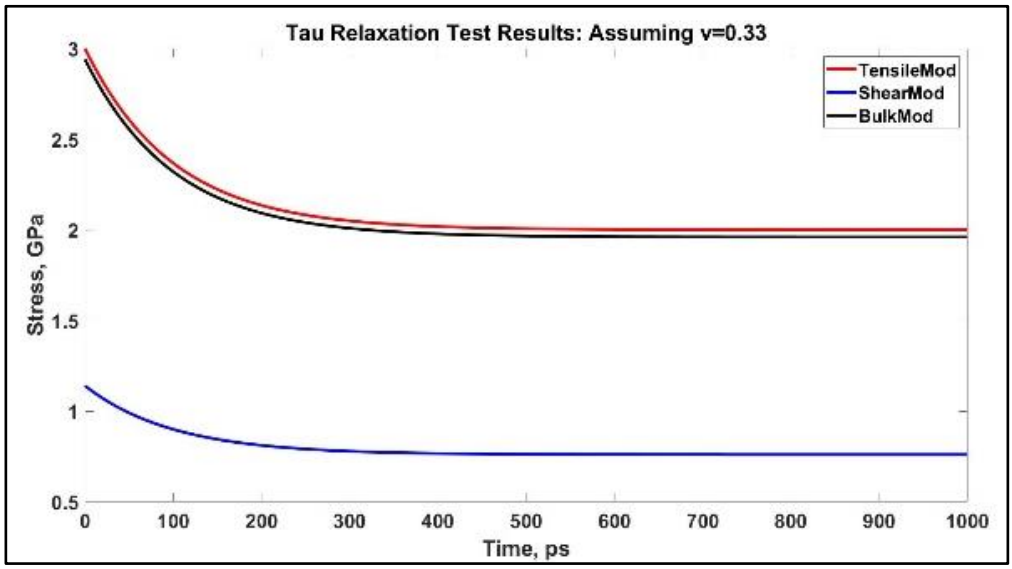
Tau Relaxation Test Results: Assuming v=0.33
TensileMod
ShearMod
BulkMod
Stress, GPa
Time, ps
3
2.5
2
1.5
1
0.5
0
100
200
300
400
500
600
700
800
900
1000

b

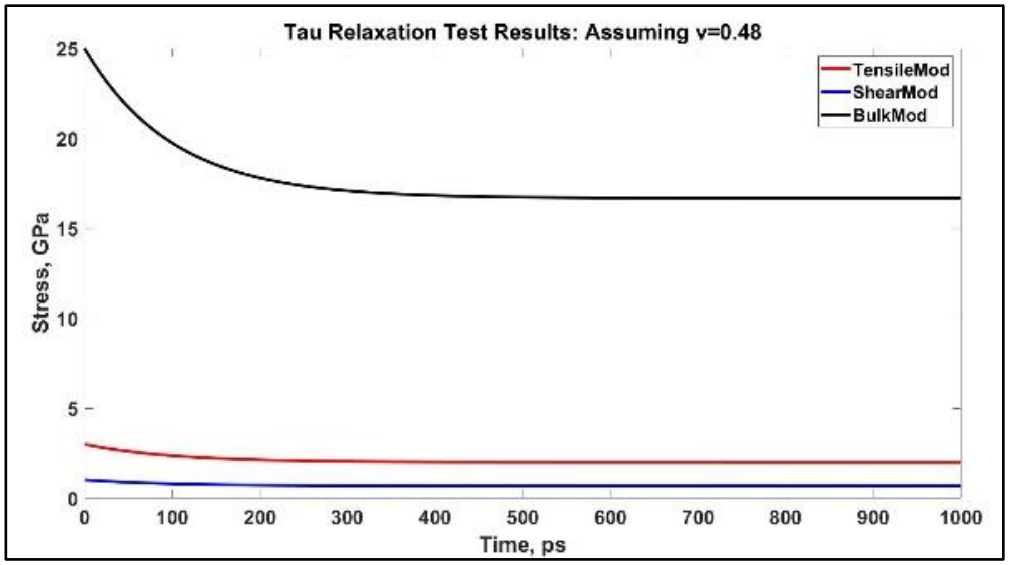
Tau Relaxation Test Results: Assuming v=0.48
TensileMod
ShearMod
BulkMod
Stress, GPa
Time, ps
25
20
15
10
5
0
100
200
300
400
500
600
700
800
900
1000

c

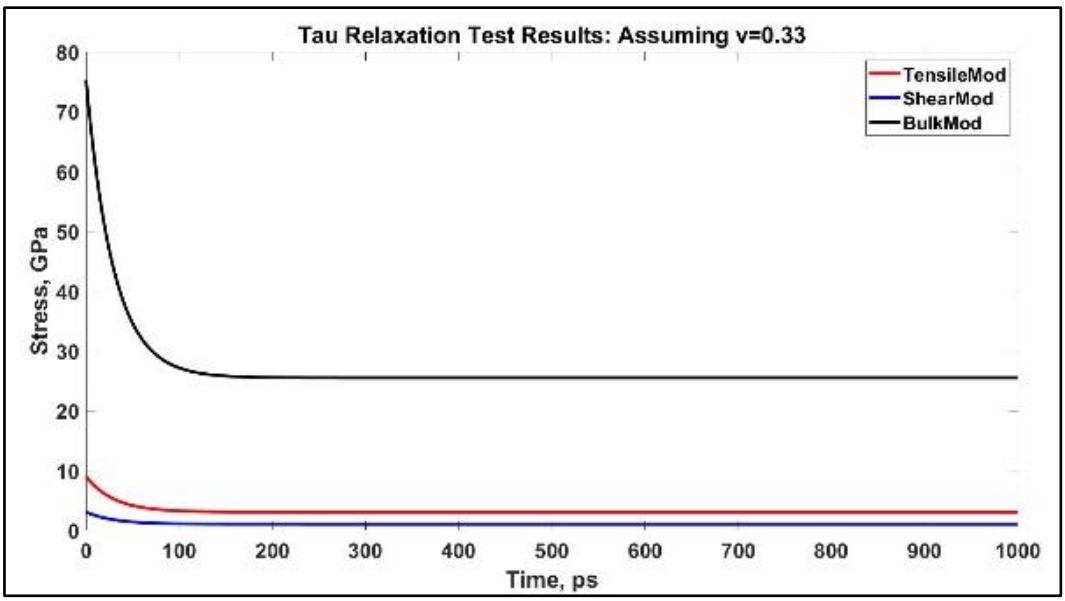
Tau Relaxation Test Results: Assuming v=0.33
TensileMod
ShearMod
BulkMod
Stress, GPa
Time, ps
0
10
20
30
40
50
60
70
80
0
100
200
300
400
500
600
700
800
900
1000

d

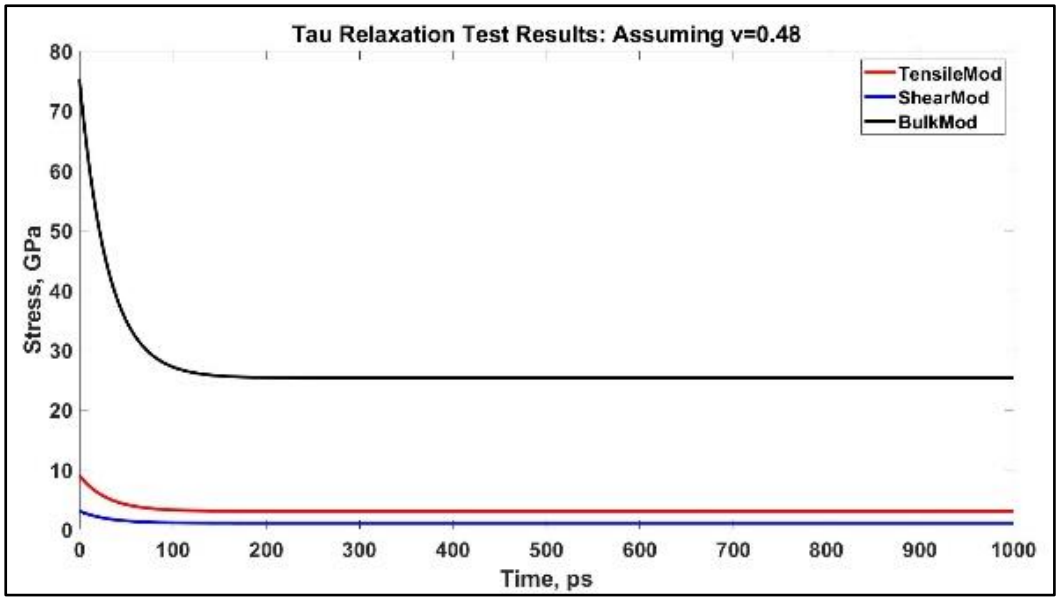
Tau Relaxation Test Results: Assuming v=0.48
TensileMod
ShearMod
BulkMod
Stress, GPa
Time, ps
0
10
20
30
40
50
60
70
80
0
100
200
300
400
500
600
700
800
900
1000

Figure 5.4: Determining G(t) and B(t) from E(t) for two assumed Poisson's ratios. The tau relaxation response is obtained for stretch at two strain rates: $1x10^8$/s and $1x10^9$/s. a and b: $1x10^8$/s, c and d: $1x10^9$/s.

Table 5.2: Maxwell Model Shear Modulus and Bulk Modulus Parameters for Tau (included Heaviside function in the expression is not shown here):

Poisson's Ratio, ν	0.33		0.48	
Strain Rate, 1/s	$1x10^8$	$1x10^9$	$1x10^8$	$1x10^9$
G_1, GPa	0.76	1.155	0.68	1.033
G_2, GPa	0.38	2.278	0.34	2.039
τ (for G), ps	100	30.303	100	30.303
B_1, GPa	1.96	2.978	16.67	25.315
B_2, GPa	0.98	5.876	8.33	49.947
τ (for B), ps	100	30.303	100	30.303

5.3.2 Viscoelastic Modeling of Neurofilaments

We have performed relaxation test on NFL in the same manner as on tau protein described in the previous section. As NF sidearms dictate the sidearm spacing and eventually the axon diameter by orienting themselves as parallel filaments to MTs (Jayanthi, 2014), we have decided to proceed by modeling the

stress-strain response of NF sidearms. The rest of the procedure is the same as tau protein, and it is not repeated in detail here. Fig. 5.5 shows the pre-relaxation stretching, and snapshots of the projection domain conformations at different timesteps during relaxation for NFL. Fig. 5.6 shows the relaxation data (E(t) vs time) for NFL, Fig. 5.7 shows the fitting to Maxwell viscoelastic model, Table 5.3 shows the Maxwell parameters for tensile modulus, Fig. 5.8 shows the shear and bulk moduli obtained for two guessed Poisson's ratio as determined by the similar manner as for tau protein, and finally, Table 5.4 shows the shear and bulk moduli parameters. It is clear that at lower strain rate, NFL acts as standard linear three-parameter solid, while at higher strain rate, it acts as two-parameter solid.

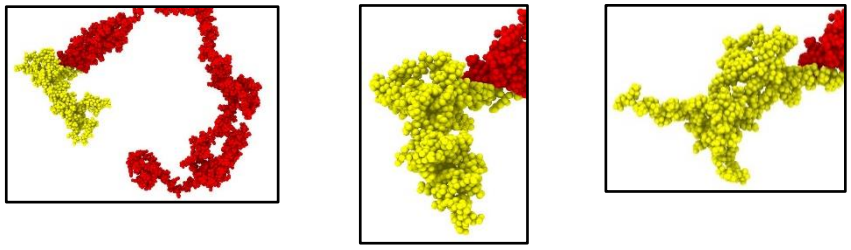

a **b** **c**

Figure 5.5: Pre-relaxation stretching for NFL ($1x10^8$/s). a. Initial structure (0% strain), b. sidearm region at mid-stretch (40% strain), c. sidearm region at end of stretch (80% strain). Color legend: Red: head and rod domain, Yellow: sidearm.

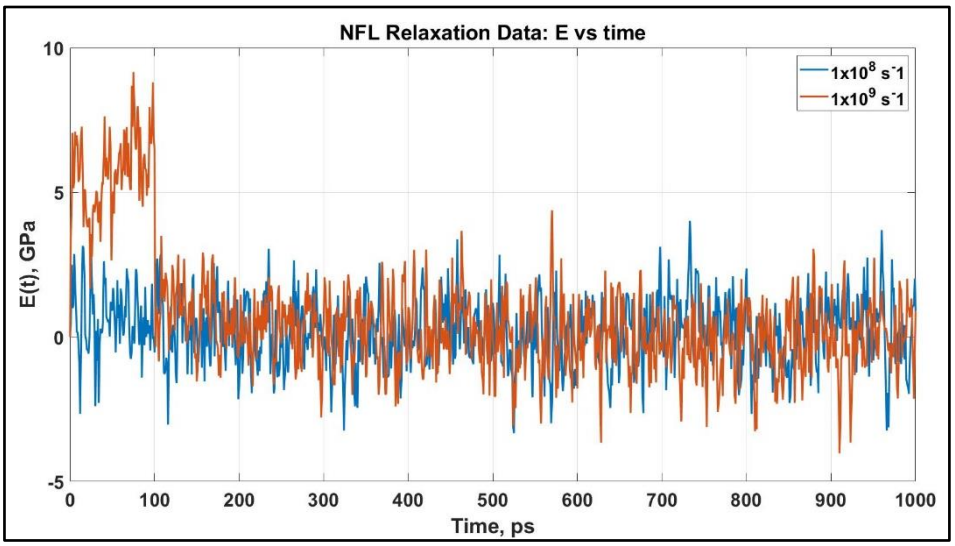

Figure 5.6: Modulus, E(t) vs time for 1ns relaxation test for NFL which are stretched to 80% at two strain rates. The relaxation curve at two strain rates are not significantly distinct for NFL.

a

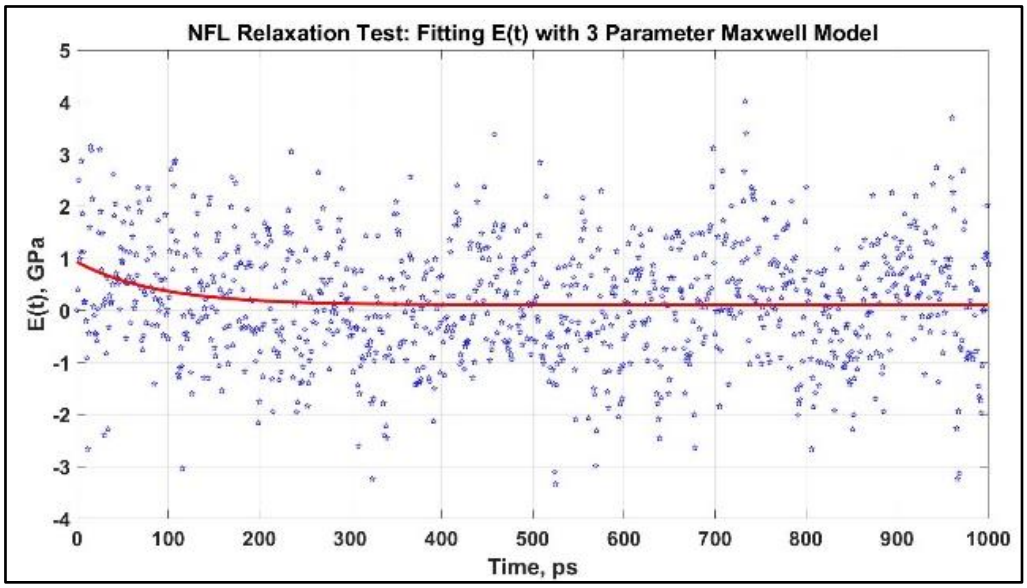

b

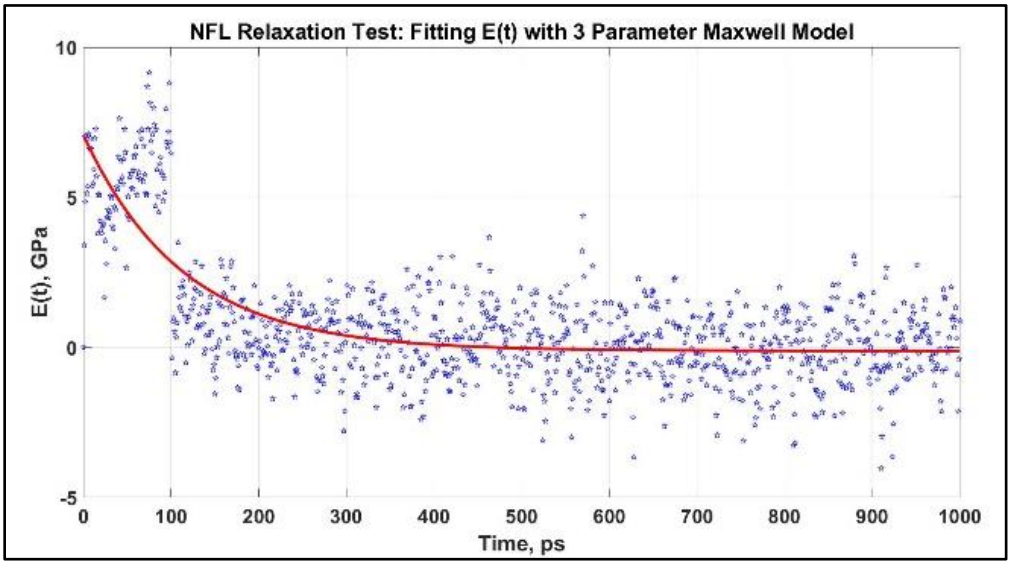

Figure 5.7: Fitting the E(t) vs time curves of NFL relaxation test to 3 parameter Maxwell model for initial stretch of 0.8 at two different strain rates. a: $1x10^8$ s^{-1}, b: $1x10^9$ s^{-1}.

Table 5.3: Maxwell Model Parameters from NFL Relaxation Test:

Strain Rate, 1/s	$1x10^8$	$1x10^9$
E_1, GPa	0.103	0

E_2, GPa	0.827	2
τ, ps	87.866	100

a

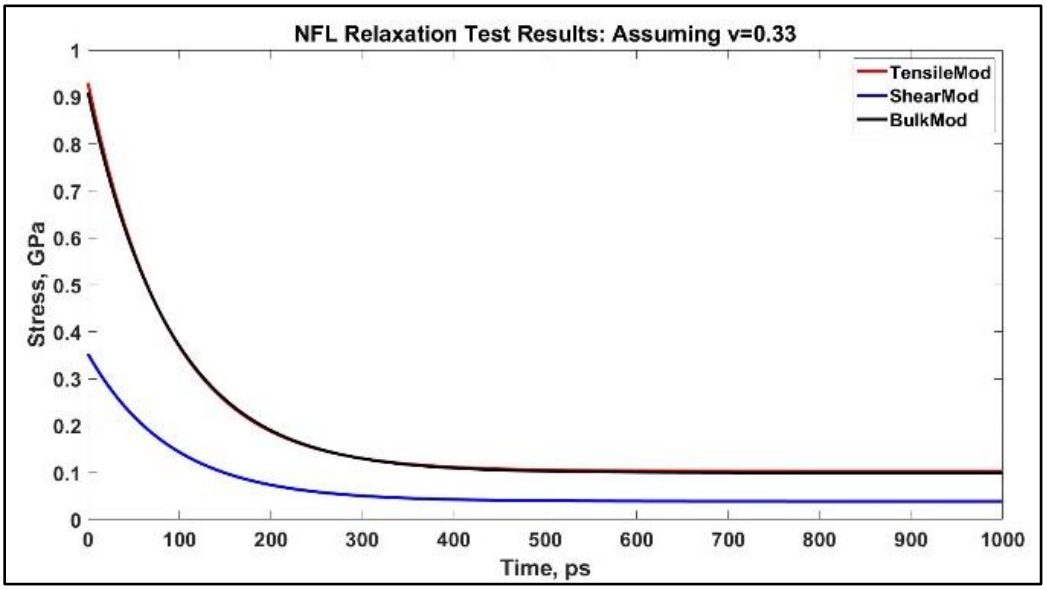

b

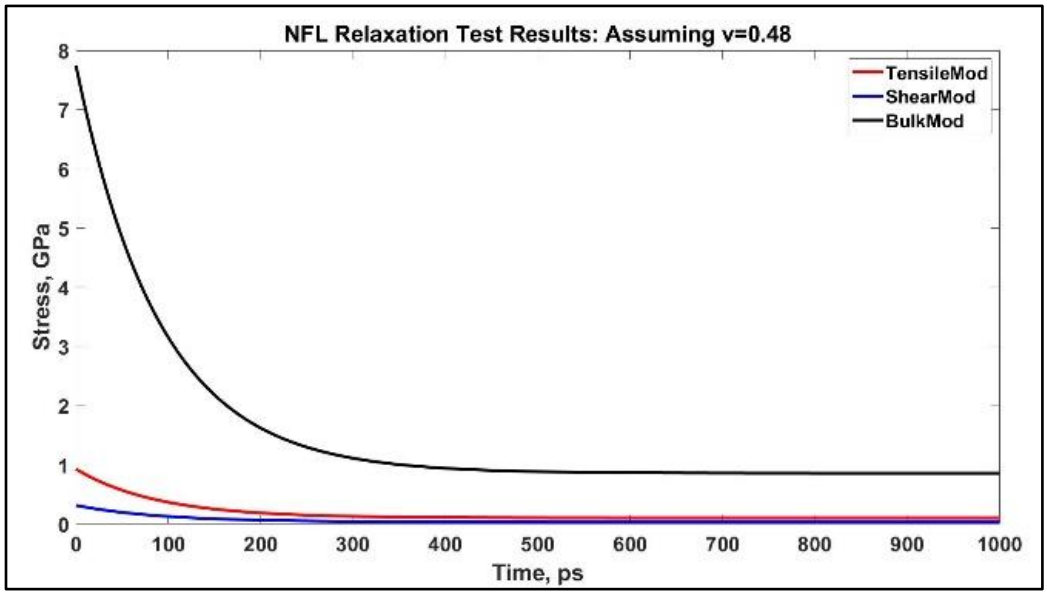

c

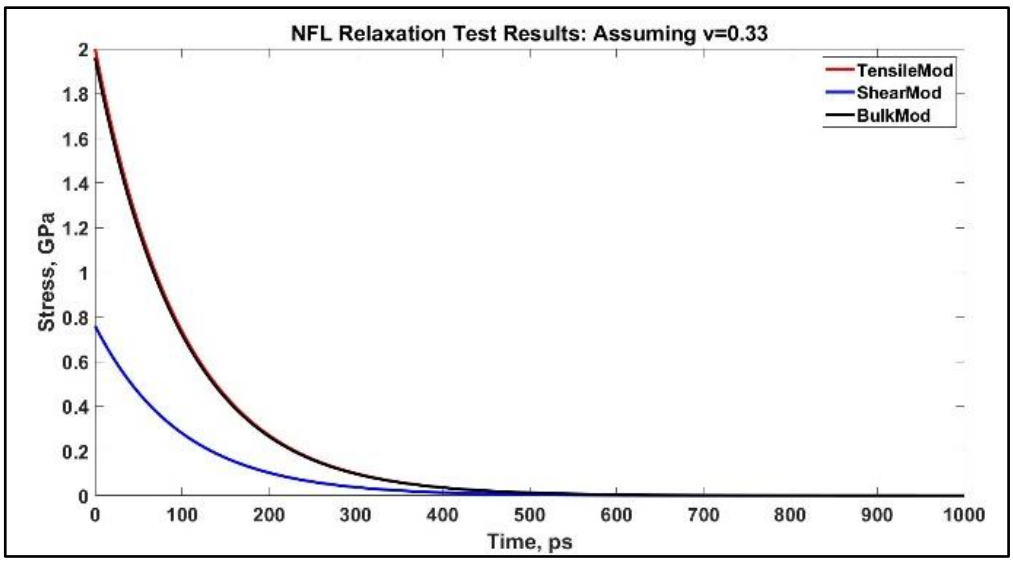

d

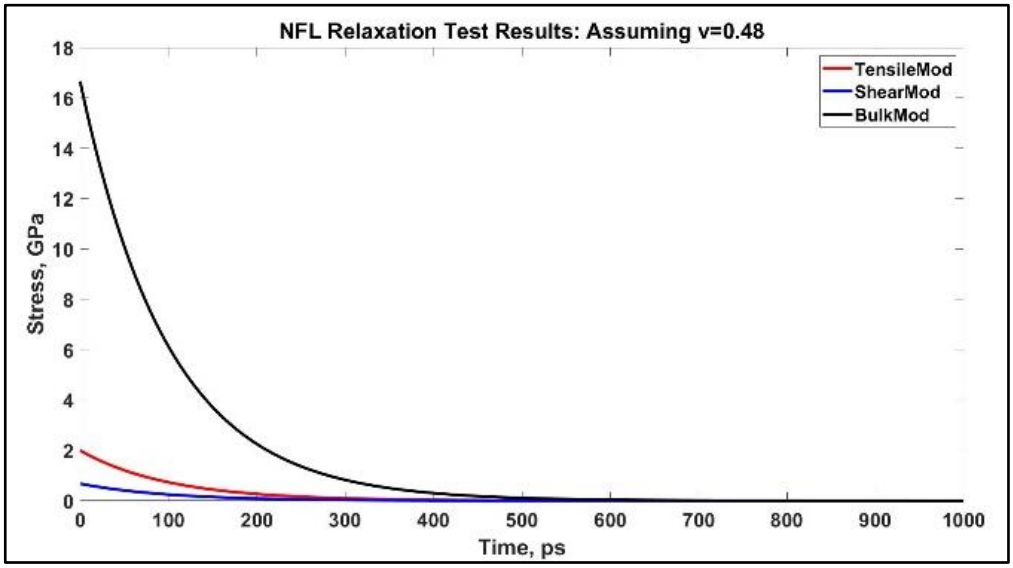

Figure 5.8: Determining G(t) and B(t) from E(t) for two assumed Poisson's ratios. The NFL relaxation response is obtained for two strain rates: $1x10^8$/s and $1x10^9$/s. a and b: $1x10^8$/s, c and d: $1x10^9$/s.

Table 5.4: Maxwell Model Shear Modulus and Bulk Modulus Parameters for NFL (included Heaviside function in the expression is not shown here):

Poisson's Ratio, ν	0.33		0.48	
Strain Rate, 1/s	$1x10^8$	$1x10^9$	$1x10^8$	$1x10^9$
G_1, GPa	0.039	0	0.035	0
G_2, GPa	0.314	0.76	0.281	0.68
τ (for G), ps	90.909	100	90.909	100
B_1, GPa	0.1	0	0.858	0
B_2, GPa	0.81	1.96	6.889	16.66
τ (for B), ps	90.909	100	90.909	100

5.4 Discussion

In this study, we have performed relaxation on projection domain of tau protein and sidearm region of NFL, prior to which high strain rate stretching was performed on them. This high strain rate stretching provides two-fold convenience – it provides us to proceed with the assumption that the loading region response can be ignored without losing significant amount of accuracy in modeling the viscoelastic characteristics (Chen, 2000; Christensen, n.d.; F10gge, 1975), and it facilitates mimicking TBI scenario, where high deformation is observed in sub-axonal components (Wu and Adnan, 2018).

In case of tau protein, we observe that at both strain rates, tau behaves as a three-parameter material. The changes that occur are in the elastic constants which increase, and the relaxation time which decreases significantly. In order to explain that from mechanical perspective, we must consider the filament structure of tau protein projection domain, which consists of both positively charged and negatively charged region including a prolin-rich region. However, the inherent disorder of tau protein dictates its mechanical behavior, as was observed in our previous study on tau protein stretching from strictly mechanical viewpoint. The disordered portion in the flanking region of tau protein enables it to absorb stretching along its entire length in pre-relaxation, and when it is relaxed, its response proceeds towards stiffer region, increasing the magnitude of elastic constants, and decreasing the relaxation time.

As opposed to tau protein, NF contains several un-foldable regions, which cannot contribute to the stretching during the pre-relaxation. Therefore, we observe that when we increase the strain rate, the elastic portion becomes weaker, and the viscous time constant is not allowed to change significantly. This unique behavior can be attributed to a combination of high strain rate, as well as the disordered portion in the sidearm region and presence of un-foldable regions.

Lastly, in order to obtain a more comprehensive insight on the viscoelastic behavior of tau protein and NF, two approaches can be taken. First, quantification of the response under slower and faster strain rate, without going into the failure region. Second, observing the viscoelastic response from a physical chemistry point of view by including effects like posttranslational modification as phosphorylation, as this phenomenon has been hypothesized to dictate functionality of tau protein and NF. In near future, we intend to address these two aspects. This study provides particular insight on the time-dependent behavior of the most vulnerable regions of two neural cytoskeletal components in TBI scenario.

5.5 Conclusion

In this study, we have attempted to develop simplified Prony series viscoelastic formulation models for tau protein and NFs using MD simulation. The projection domain of tau protein and sidearm region of NFL are stretched at high strain rate, which are relevant to TBI scenario.

From our simulations, the major findings can be summarized as below:

1. Relaxation test on tau protein at two strain rates shows that at 80% strain, their relaxation response can be fitted with 3-parameter Maxwell model.
2. Similar model is adequate to fit relaxation response of NFs at two strain rates. However, at lower strain rate, NFL acts as 3-parameter solid, but at higher strain rate, it corresponds to a 2-parameter solid.
3. Relaxation response of such cytoskeletal components can be attributed to stretching time and stretched state at relaxation.
4. Similar scheme can be extended to other filamentous subcellular structures, and SMD simulation can be a particularly useful tool to perform viscoelastic computations on such biomolecules.

As this study provides critical insight on time-dependent response for two important neural cytoskeletal components, it facilitates paving the pathway for an all-component-inclusive realistic bottom-up computational model for axon. In other words, this study will play instrumental role in enhancement of existing axon models which account for viscoelastic response of the cytoskeletal components and predicting sub-axonal behavior in extreme strain rate condition, which will provide significant contribution in TBI research.

CHAPTER 6

MECHANICAL BEHAVIOR OF ACTIN-SPECTRIN SKELETON IN AXON

6.1 Introduction

6.1.1 Relevance of Actin, Spectrin, and Periodic Actin-Spectrin Lattice

There are three (3) major axonal cytoskeletal components in neuron: microtubules (MT) (Avila, 1990) crosslinked with tau proteins (Lee et al., 1989; Rosenberg et al., 2008), neurofilaments (NF) (Janmey et al., 2003), and microfilaments (MF) (Ouyang et al., 2013). Among these, MFs in axon are comprised of globular or G-actin, which eventually form filamentous or F-actin. However, these three components do not comprehensively define the axonal structure, as recent seminal super-resolution microscopy study has shown that axonal diameter is determined by periodic arrays of actin ring formed by short F-actin filaments (Xu et al., 2013). Furthermore, spectrin, which is structurally and functionally important component of axonal cytoskeleton, forms heterodimers and eventually, tetramers – which generate a lattice by connecting the periodic actin rings (Zhang et al., 2013). Furthermore, the spectrin is connected to the membrane due to facilitation by other membrane associated proteins – such as adducin which caps one end of F-actin and promotes actin-spectrin bond (Leite et al., 2016; Naydenov and Ivanov, 2011), ankyrin which binds spectrin to membrane (Zhang et al., 2013), etc. The overall mechanical behavior of axon and extent of mechanical support to the cytoskeleton are determined by significant contribution of actin-spectrin network. Therefore, mechanical behavior of i) lone F-actin, ii) lone spectrin, and iii) actin-spectrin interaction are required to be determined – which will eventually facilitate the development of a bottom-up, realistic, all-component inclusive computational model of axon. This study attempts to explore the three aspects mentioned above. A thorough literature review is required to comprehend the current understanding and approaches in the field of mechanical behavior of actin and spectrin, and substantiation of the periodicity of actin-spectrin

network in the axonal cytoskeleton – which is presented here. In a nutshell, this section presents relevant studies regarding actin, spectrin, and actin-spectrin skeleton.

6.1.2 Insights on Actin, Spectrin, and Periodic Actin-Spectrin Network

6.1.2.1 Actin: Structure, Mechanical Insight, and Computational Approaches

6.1.2.1.1 Actin Structure

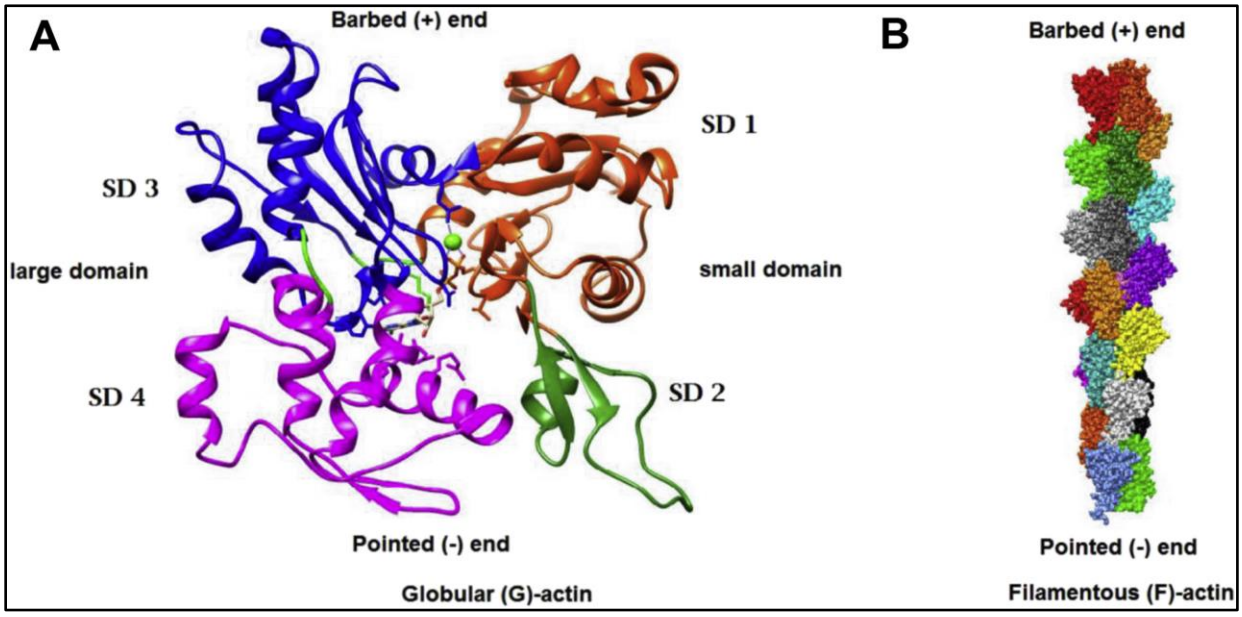

Figure 6.1: Different domains of G-actin (left), and F-actin formed by polymerization of G-actin (right). The F-actin contributes significantly to the stability of axonal cytoskeleton. Ref.: (Kumar and Mansson, 2017)

Actin, being one of the most conserved biological structures found in nature has been explored in numerous experimental and computational ways. Although actin has diversified functionality, interaction with cell

membrane is one of the most significant attributes of this cytoskeletal component. Actins can be related to several neuropathological disorders and other pathologies. For example, cancer-affected cytoskeleton properties depend on actin filaments to microtubule content (Pachenari et al., 2014). Also, AFM experiment shows that affecting MTs reduces stiffness of axons greatly, while in case of affecting MFs the effect is not that severe (Ouyang et al., 2013).

F-actins contain right handed double helices of actin monomer with around $18nm^2$ cross sectional area and several micrometers of length (Deriu et al., 2012b). Its structure is asymmetric, its monomer is ~6nm long, and the pitch of double helix is ~72nm. Within the double helix, monomers bind to each other through noncovalent interactions (longitudinal bonds between monomers in each helical strand and diagonal bonds between adjacent monomers in opposite helical strands) (Erickson, 1989; Howard, 2001). The monomeric subunit (G-actin) has four subdomains, of which, subdomain 2 (the D loop) folds into α-helix in ADP bound state, but has no definite secondary structure in ATP bound state (Graceffa and Dominguez, 2003; Otterbein et al., 2001). X-ray diffraction experiments show that globular to stable, flat, fibrous actin transition can occur by rotation of two major domains by around 20 degrees (Oda et al., 2009). It is believed that actin configurations cannot be correlated to a particular nucleotide state, rather they are differ in two loops: β hairpin loop containing Ser-14 and sensor loop with the methylated His-73 (Dominguez and Holmes, 2011). Electron microscopy shows different structural states of actin, especially the subunit 2 can be disordered in the way of connecting to the C terminus of a subunit above it, and therefore, it should be studied as an ensemble of different structures (Galkin et al., 2010). Cryo-EM technology has facilitated direct visualization of secondary structure of actin (Fujii et al., 2010). Immunofluoroscence has also been applied for examining actin network structure (Lazarides, 1975). Actin networks and bundles should be studied along with the properties of individual filaments, as they show the holistic characteristics of the cytoskeletal component. Purified actins assemble into uniform mass of long filaments, while in presence of macrophage actin binding proteins they assemble into straight, short filaments with parallel branching network

(Niederman et al., 1983). Divalent cation binding sites induce F-actin polymerization (Splettstoesser et al., 2011).

Actin filaments are crosslinked by actin binding proteins (ABP) such as filamin, and depending on its concentration, a single type of ABP can induce different actin microstructure (Schmoller et al., 2009). F-actin, being crosslinked by bundling proteins such as actinin, can assemble into frequently branching 3D network (Pelletier et al., 2003).

6.1.2.1.2 Mechanical Properties of Actin

Mechanical properties, especially the persistence length of actin filament have been studied in earlier works (Isambert et al., 1995; Tsuda et al., 1996). The persistence length with all subunits in ATP state (F-ATP) is ~17μm, although it can vary to a large extent. ATP bound, unfolded actin persistence length has been found to be twice of ADP bound, folded D-loop contained actins (Chu and Voth, 2005). Further studies revealed that unfolding of the D-loop increases persistence length regardless of the state of bound nucleotide (Oda et al., 2009; Pfaendtner et al., 2010b). Separate studies have proposed possible mechanism of ATP hydrolysis in actin (Akola and Jones, 2006; Vorobiev et al., 2003). Mechanics of F-actin cytoskeleton is dictated by diverse mechanical dynamics of F-actin networks and bundles, and it has been reviewed thoroughly (Stricker et al., 2010).

Due to having helical structure, bending and twisting of F-actin have significant effects, especially on short ones (Enrique et al., 2010). From that perspective, chemical, and mechanical properties of actin should be studied separately. Mechanical behaviors of actin monomers and filament are studied by molecular dynamics (MD) simulations which, however, cannot capture filament-scale, biologically relevant phenomena. Therefore, an alternative has been CG modeling (Chu and Voth, 2006; Deriu et al., 2012b). There are several theories regarding behaviors of F-actin, such as elastic rod buckling theory and filament severing by cofilin theory (Berro et al., 2007; McCullough et al., 2011), while some models have examined

mechanics and chemistry interplay (Asakura et al., 1963). Yogurtcu et al (Yogurtcu et al., 2012) proposed an intermediate scale model (which does not consider internal conformational complexity of actin, but include possible conformational changes due to ATP hydrolysis) found that actin filaments are mechanically stiff under stretch, but easily deformable by bending. The chemical state of actin monomers can change, and rate of ATP conversion depends on the overall elastic energy of the filament. For filament length much longer than the helical actin pitch (>1μm), the filament mechanically deforms as a semiflexible rod. It is also found that F-actin easily buckles under compressive deformation (Chu and Voth, 2006).

Earlier works have found that ATP bound actin filaments have higher bending and torsional rigidities than ADP bound filaments (Isambert et al., 1995; McCullough et al., 2011; Rebello and Ludescher, 1998). Coarse grain MD simulations validated the findings about the properties (Fan et al., 2012). From the force-extension experiment in CG, Chu et al (Chu and Voth, 2006) found the stretching stiffness of F-ATP actin and F-ADP actin as 37pn/nm and 31pn/nm, respectively.

Effect of tensile force on actin filaments has also been studied earlier (Matsushita et al., 2011), and it is shown that tensile force causes decrement of twist angle, leading to increased extensional and torsional stiffness. According to earlier works, torsional rigidity per unit length of actin filament ranges from $2.3 \times 10^{-27}\ Nm^2$ to $8 \times 10^{-26}\ Nm^2$ (Matsushita et al., 2012, 2010; Tsuda et al., 1996), and that extension-torsion coupling is important to comprehend the mechanical behavior of actin. Furthermore, role of ABPs (which incorporate conformational changes in the structure of actin) on mechanical properties of actin has been investigated by steered molecular dynamics (SMD) simulations (Kim et al., 2016). Cofilactin (cofilin bound with each actin monomer) is found to be more flexible than a pure actin filament, especially actin filament with partially bound cofilin (refer to Figure 6.2). The severing mechanism of cofilin on actin filaments is described in some studies, and found that mechanism of cofilin activity is promoting stress concentrations in junctions of filaments, which is similar to grain boundary fracture of crystalline materials or shear transformation of colloidal materials (De La Cruz, 2009). Regulatory severing protein (cofilin) has been found to increase bending and twisting compliance of actin in some atomistic and continuum models

(Schramm et al., 2017), because buckled cofilactin (actin decorated with cofilin) stores elastic energy between the bare and cofilin-decorated segments, accelerating severing. Experimentally determined Young's Modulus of actin is reported to be 400MPa-2.5GPa (ben-Avraham and Tirion, 1995; Higuchi et al., 1995b; Huxley et al., 1994b; Kojima et al., 1994b; Wakabayashi et al., 1994b), to which the MD simulation results of Kim et al (Kim et al., 2016) and Matsushita et al (Matsushita et al., 2011) match closely. Torsional stiffness value obtained from MD simulation performed by Matsushita et al (Matsushita et al., 2010) also agreed with the experimental values, assuming that difference can occur depending on the initial conformational state.

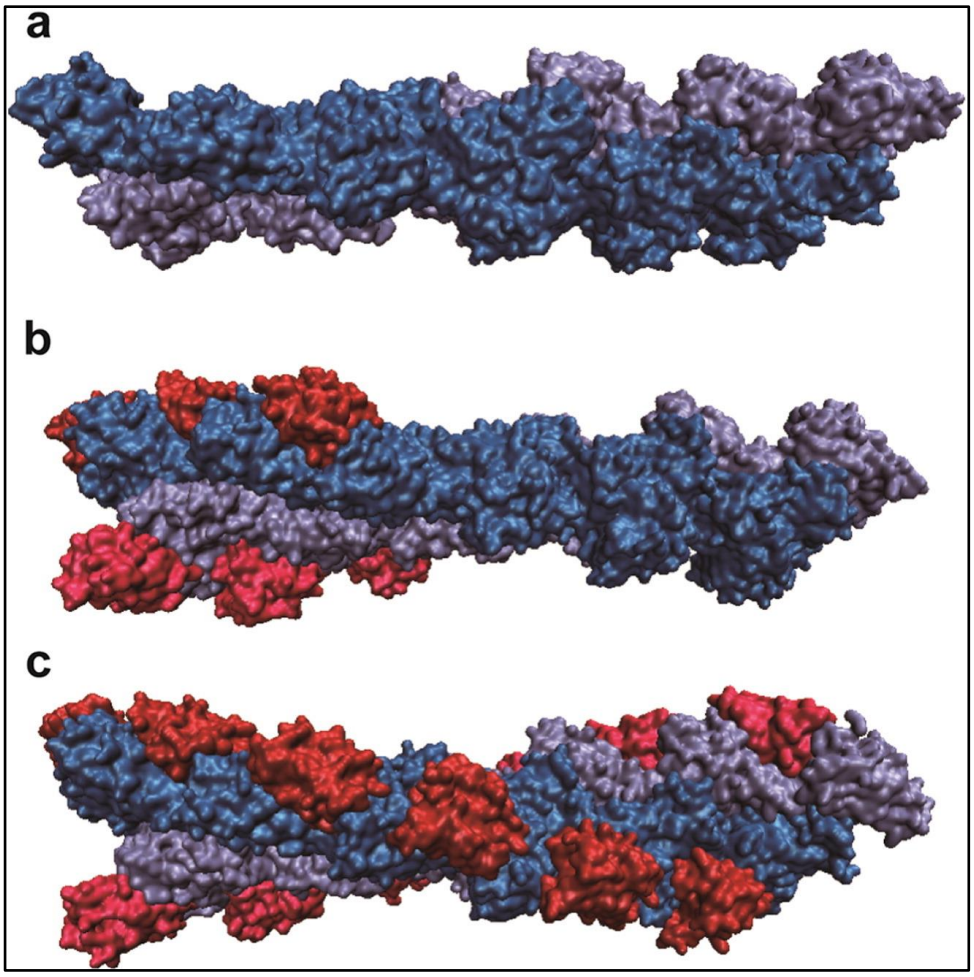

Figure 6.2: Actin filament decoration with cofilin, leading to formation of cofilactin, which facilitated determining enhanced flexibility obtained by cofilactin, investigated by steered molecular dynamics (SMD)

approach. The model is prepared from protein data bank (PDB) code 3JOS. a) Actin without cofilin, b) actin decorated by 6 cofilin, c) actin decorated with 12 cofilin. Ref: (Kim et al., 2016).

Different conformation of F actin has been studied separately, which we have already mentioned (Oda et al., 2009). Viscoelastic response of actin network has been studied in different works (Lieleg et al., 2009; Schmoller et al., 2009) and it is found that the response depends on cross-linker off rate, binding energy or characteristic bond length of individual actin/ABP interactions (Schmoller et al., 2009). The response of the network is a combination of elasticity of the network and force-induced cross-linker unbinding and rebinding (Gurmessa et al., 2017). Both oscillatory and shear type experiments showed viscoelastic nature for filamentous and nonfilamentous actins (Sato et al., 1985). Viscoelastic behavior of actin network has been studied by modeling single filament, cross-linking and incorporating Maxwell properties in FEM, and validated by large strain experiments (Unterberger et al., 2013b).

Cross-linking dynamics has been strongly related to mechanical properties of actin (Xu et al., 1998b). Rate of deformation also affects the difference between the stiffness of pure actin and actinin - at higher deformation rate, actinin is found to be stiffer than pure actin (Sato et al., 1987). Actin, when associated with cross-linking proteins, act as around 40 times stiffer than pure actin under high deformation rate, although the difference becomes indistinguishable under small deformation rate (Sato et al., 1987), which is justified by multiple rearranging of cross-link hypothesis.

Range of obtained rheological parameters of actin, such as shear modulus and storage modulus from different experiments have been investigated as the reported values differ from 0.01Pa to tens of Pa, and it is concluded that mechanical properties depend on initial length of filament as well as preparation, polymerization condition and storage methodology (Janmey et al., 1994; Xu et al., 1998a). It is also found in a study we have already mentioned that stiffness of 1μm long actin is higher in case of association with tropomyosin (Kojima et al., 1994b).

Actin-actin bond breaking force is also measured in some studies, and they showed that turning of filaments greatly reduce the required force (Tsuda et al., 1996). In separate studies, strain dependent behavior of actin networks has been investigated to show that at high strain the elasticity ceases to be linear (Gardel et al., 2004).

6.1.2.1.3 Computational Aspects of Actin Modeling

Computationally, there have been numerous approaches to model and characterize actin. For example, atomistic studies on MFs have used Oda (Oda et al., 2009) or Holmes (Dominguez and Holmes, 2011) model. Due to the nanometer length scale, multiscale approaches have also been proven effective from modeling perspective (Li et al., 2013). The structure, network, and stiffness properties have been determined by multiple studies. However, recently published review study, after performing a comprehensive literature exploration has concluded that the stiffness of microfilaments i.e. actins can vary significantly, from a few hundred megapascals to 2.5 gigapascals (Khan et al., 2020a). Atomistic and CG studies have facilitated obtaining significant insight regarding mechanical behavior of actin including the effect of actin-severing protein (T Kim et al., 2009), effect of crosslinking (Claessens et al., 2006), and dynamic attributes (Deriu et al., 2012b). Aside from the stiffness and strictly mechanical insights, computational studies have also provided with critical information regarding mechanochemical attributes (Zheng et al., 2007), deformation criteria (Yogurtcu et al., 2012), persistence length (Fan et al., 2012), torsional mechanism (Fan et al., 2012), viscoelastic characteristics (Unterberger et al., 2013b), etc. In this study, however, the results will be limited to mechanical behavior of actin under extreme strain rate to mimic TBI scenario.

Specifically from the modeling perspective, there have been numerous MD, coarse grained MD, FEM and continuum scale models on actin, and it is relevant to mention the aspects of some studies we have already cited in the earlier seciton. Fully atomistic models by fitting known structures of G actin has been proposed

earlier (Fujii et al., 2010; Oda et al., 2009; Splettstoesser et al., 2011). Some MD simulation studies have attempted to capture global structure as well as internal stereochemistry of actin (Splettstoesser et al., 2011). Coarse-graining from fully atomistic simulations further revealed holistic properties of F-actin (Deriu et al., 2012b). Actin network properties has also been studied by continuum models, which highly emphasize cross-linking proteins (Holzapfel et al., 2014; Unterberger et al., 2013b). Oda model and Holmes model have been used extensively by others in MD simulations to further investigate F actin network structure and properties (Pfaendtner et al., 2010b).

6.1.2.2 Spectrin: Structure and Mechanical Insight

6.1.2.2.1 Structure of Spectrin

As a significant axonal cytoskeletal component and a member of F-actin crosslinking superfamily, the functionality, structure, and attributes of spectrin have been explored in detail (Zhang et al., 2013). Structurally, spectrin forms α-spectrin and β-spectrin heterodimers (Kusunoki et al., 2004) which lead to tetramers (Harper et al., 2010), eventually forming a hexagonal lattice when combined with periodic actin rings. Among the two α and five β isoforms, the α-II (genetic encoding: SPTAN1) and β-II (genetic encoding: SPTBN1) are the most relevant ones for axonal spectrins. It is worthy to mention that due to being part of heterodimer, α and β shares only 30% similarity in structure. Furthermore, they have distinct function in axonal pathfinding (Hülsmeier et al., 2007). The role of spectrin is recognized in maintaining axon stability and mechanical properties (Baines, 2009; Grum et al., 1999). Lack of spectrin has been marked as a source of axon instability, even breaking (Hammarlund et al., 2007).

Recently proposed medium resolution zipper model of spectrin dimerization shows that α20-21 and β1-2 repeats create a dimer initation site and close the dimer by utilizing electrostatic interaction. At the junction between α20-21 and β1-2 repeats, there are the actin binding domain, adducin binding spot, and Ca^{2+} binding EF hand. The determination of building blocks of spectrin i.e. α and β subunits have been performed

experimentally in the early 80's, mostly by using gel-filtration and ion-exchange chromatography, which laid out the groundwork of membrane associated actin-spectrin cytoskeleton (Burns et al., 1983; CALVERT et al., 1980). However, the function of spectrin was observed from biochemical perspective by incorporating phosphorylation and resulting change in association or dissociation from membrane which leads to specific stability states of the cytoskeleton, instead of response to mechanical loading perspective. It is to be mentioned that the actin-binding domain in spectrin subunits has also been determined in early chromatography researches (FRAPPIER et al., 1992, 1987) and later green fluorescence microscopy (Nestor et al., 2011), which led to quantification of specific domains and repeat regions later, even for non-erythroid spectrins (Moon and McMahon, 1990; Nagase et al., 1997). Additionally, the ~180nm periodicity of spectrin, which is consistent with the periodicity of axon rings placed ~180nm interval along the length of axon has been established by recent nanoscopy studies – which provide concluding evidence that indeed axonal cytoskeleton contains periodic lattice of actin-spectrin network (D'Este et al., 2015), while the exact details of the structure will be dependent on appropriate imaging method.

6.1.2.2.2 Limited Mechanical and Modeling Insight on Spectrin

Most of the published work on spectrin properties investigate erythroid spectrin and actin-spectrin biochemical interaction (Smith et al., 2018). For example, shear response of spectrin in red-blood cell is attributed to head-to-head association of spectrin heterodimers (An et al., 2002), large deformation and elastic response of erythroid spectrin (Dao et al., 2006), network level elasticity in erythrocytes (Hoore et al., 2018), etc. These studies provided excellent validation of continuum models of red blood cells by providing reliable length scale relationships. The extent of progress in erythrocyte related modeling which incorporates properties of spectrin are diverse and advanced in literature due to advancements in optical

tweezer experiment methodologies and atomic force microscopy (AFM), while the literature lacks insight regarding axonal cytoskeletal modeling of spectrin (Li et al., 2010, 2005).

As a biological material, the failure behavior of spectrin can be explained from biochemical perspective, catalytic induction states, and associated viewpoints (Witek and Fung, 2013). However, forced unfolding research studies are particularly relevant to the current work, as they provide insight regarding extensibility of multi-domain proteins such as spectrin (refer to Figure 6.3). One example is forced unfolding of tandem spectrin repeats at low forces performed by AFM, which has suggested that tandem unfolding differs significantly from single unfolding (Law et al., 2003). In comparison, single molecule force spectroscopy (SMFS) has demonstrated single unfolding of spectrin specifically, which showed that single spectrin unfolding occurs in a stepwise fashion when susceptible to stretching, substantiating the presence of multiple intermediate repeat region in the structure (Lenne et al., 2000). Also, AFM study has quantified that force required to unfold spectrin repeats ranges between 25-35pN (Rief et al., 1999). In addition, biochemical analyses of spectrin folding and unfolding mechanism have attributed different folding mechanism to interchain binding aspects (Viel, 1999), different kinetic characteristics (Scott et al., 2004), and existence of critical extension (Zhu and Asaro, 2008).

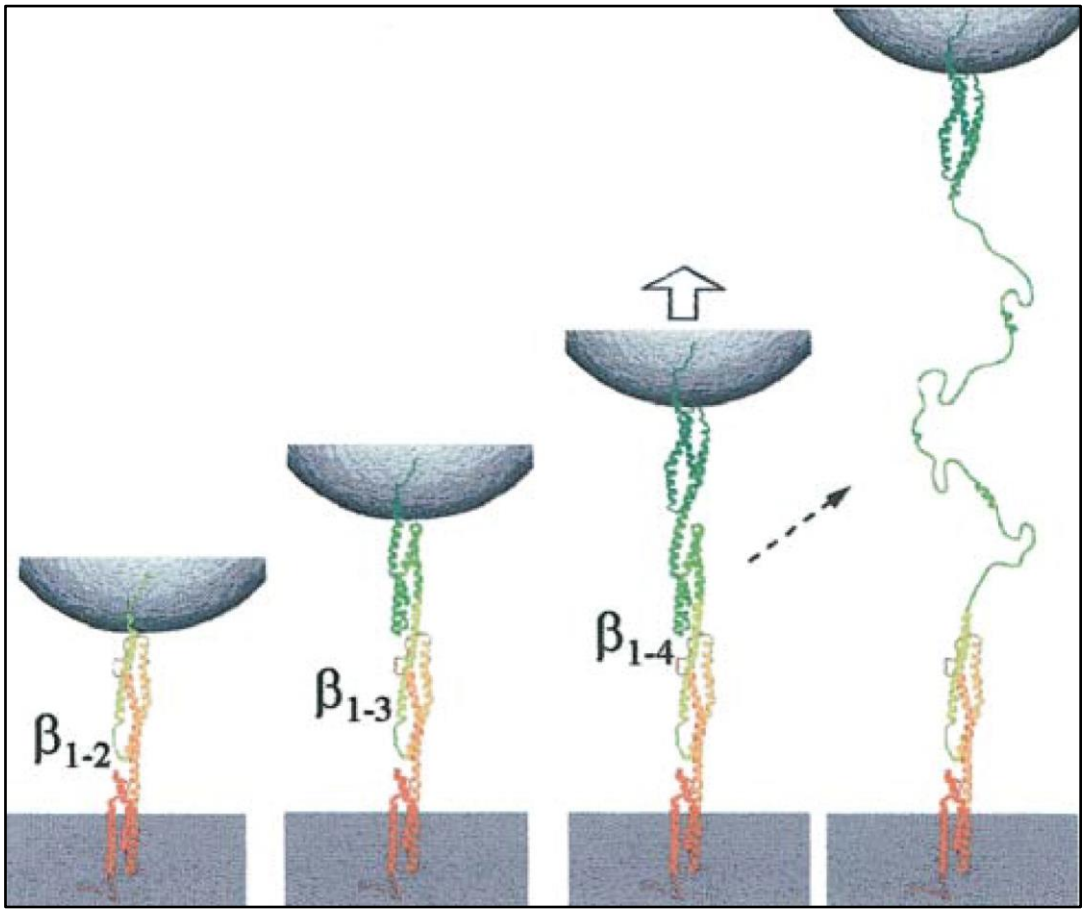

Figure 6.3: Depiction of forced unfolding of spectrin tandem repeats as found by atomic force microscopy (AFM). Ref: (Law et al., 2003).

Additionally, steered molecular dynamics (SMD) studies on human erythroid and chicken brain spectrin have examined forced unfolding of multiple repeat spectrin suggesting that α-helical linker can be ruptured if susceptible to forced unfolding, the propagation of which may lead to destabilization of the tertiary structure (Paramore and Voth, 2006). Moreover, the same group has investigated the rupture criteria of spectrin specifically by implementing non-equilibrium MD simulation, which has shown that force-extension response changes significantly at ~0.4nm extension, and spectrin behavior can make a transition

from elastic to viscous material as suggested by force-extension curves (Paramore et al., 2006). Formation of stable intermediate unfolded structures has been substantiated by similar MD simulation works on spectrin (Altmann et al., 2002; Ortiz et al., 2005).

Furthermore, theoretical modeling of spectrin network in axonal cytoskeleton has led to insights regarding the extension and fluctuation characteristics, which suggested that spectrins, within the periodicity of axons, can fluctuate in-sync. This study substantiated that a spectrin network can be considered as a slender structure which can be coarse-grained (Lai and Cao, 2014).

Lastly, among other mechanical properties of spectrin, the frequency dependence of shear response has been measured by multiple lumped resonating viscoelastometer, which suggested that spectrin dimer can extend at a specific ionic strength (Sandvold et al., 1989). Moreover, viscoelastic and mechanochemical characteristics of spectrin gel have also been determined, but only for erythrocytic ones (Stokke et al., 1986, 1985). The limitation in the literature is therefore evident that the stiffness and mechanical response data are almost limited to erythrocyte related studies (Svetina et al., 2016).

6.1.2.3 Periodic Actin-Spectrin Skeleton: Role in Axon and Strain Rate Dependent Scenario

The periodic actin-spectrin cytoskeleton structure as well as the difference between cytoskeleton structure in dendrites, synapse, axon initial segment, and axonal cytoskeleton have been substantiated only after 2010s by dint of super-resolution microscopy and fluorescence nanoscopy (Barabas et al., 2017; Han et al., 2017; Huang et al., 2017; Koskinen and Hotulainen, 2014; Sidenstein et al., 2016; Xu et al., 2013). The significant advancement in the microscopy front is understood by recent review work and remodeling study on periodic actin-spectrin network (Unsain et al., 2018b, 2018a). Specifically for axonal cytoskeleton, the periodicity is stated to be formed at the early stages of development and extends from proximal to distal end of axon (Zhong et al., 2014). It is to be mentioned that the periodicity of cytoskeleton is found in

different types of cells and across species (He et al., 2016) and even axonal actin structure may differ from rings to waves and trails (Roy, 2016) – but in this section, the discussion is limited to axonal cytoskeleton.

Specifically, the periodic structure of actin is found in axon, axon initial segment, and neck of dendritic spines – which differs than the structure of actin found in dendrites changing the conformation as one moves forward along the length of dendrites (Abouelezz, 2020; Bär et al., 2016). In this regard, earlier experimentations have investigated spectrin-actin gel elasticity as a function of protein concentration, which proposed actin fiber network crosslinked by spectrin networks at regular intervals (Schanus et al., 1985). The role of actin-spectrin network in maintaining axon diameter and MT stability have also been well-established by multiple studies including recent ones (Costa et al., 2018; Leite et al., 2016; Leite and Sousa, 2016; Qu et al., 2017).

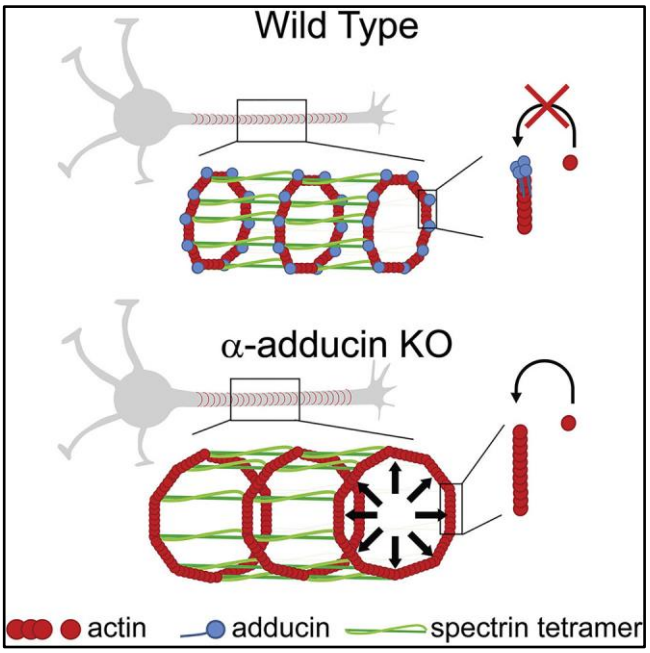

Figure 6.4: Representation of actin-spectrin network, which provides stability to axonal cytoskeleton in cooperation with other proteins such as adducin. Ref: (Leite et al., 2016).

Spectrin-actin interaction and associated alteration of cytoskeleton (even axon degeneration) have been found to be manipulated by numerous biochemical agents and phenomena, such as effect of dematin (Koshino et al., 2012), tropic deprivation (TD) (Wang et al., 2019), etc. Furthermore, continuous remodeling of neural cytoskeleton has been attributed to neural growth, which is dictated by actin-MT and actin-spectrin interaction (Coles and Bradke, 2015). However, studies focusing on spectrin-actin interaction or alteration of the interface between them due to mechanical loading is scarce in literature. Among the few recent studies relevant to actin-spectrin cytoskeleton, one has attributed the tension-buffering shock absorber mechanism of the cytoskeleton (especially reversible unfolding of the repeat domains of the spectrin tetramers) to the ability of axon to stretch significantly by performing stretching experiment on chicken dorsal root ganglion in a customized force apparatus (Dubey et al., 2020). In relevance, red blood cell (RBC) coarse grain modeling has revealed that spectrin contributes to shear stress at lower shear strain, but lipid membrane also contributes at higher strain rates (Li and Lykotrafitis, 2012).

In short, current literature lacks insight in mechanical behavior of spectrin and actin-spectrin interaction, although most of the mechanical properties of actin are existent. However, recent studies on cytoskeletal components have focused on applicable strain rate on different cytoskeletal component to imitate TBI scenario by undertaking computational approaches such as microtubules and tau proteins (Khan et al., 2020b; Wu and Adnan, 2018) which can be extended to other axonal cytoskeleatal components to provide novel insights regarding the specific mechanical behavior of such cytoskeletal components at extreme strain rate. However, to achieve these objectives, different customized approaches are expected, such as atomistic based continuum modeling, coarse-graining, adopting comprehensive multiscale maneuver (Adnan et al., 2018), etc. Optimistically, the possible future directions mentioned above will play an instrumental role in developing a bottom-up axon model focusing on TBI scenario and contribute to the existent computational axon models.

6.1.3 Summary of the Literature Review on Actin, Spectrin, and Periodic Actin-Spectrin Cytoskeleton

In this section, current advancements in the analysis of structure and mechanical behavior of actin, spectrin, and periodic actin-spectrin cytoskeleton. As biological materials, relevant literature from biochemical perspective are also represented.

The major findings can be summarized as below:

1. Actin: Mechanical insights are mostly present.
2. Spectrin: Little mechanical insight is present, but mostly for erythroid spectrin, not axonal ones.
3. Actin-Spectrin Network: Little mechanical insight is present.

Especially, the current literature fails to cover the high strain rate response of actin-spectrin network. However, the limitations in (b) and (c) can certainly be attributed to lack of advanced imaging techniques and customized mechanical experimentation as well as modeling. However, over the next few years, it can be hoped that the current limitations will be overcome to a significant extent – as structural insights will be more substantiated and microscopy methodologies will be advanced further. Due to the nanometer length scale, molecular dynamics and associated computational approaches will also serve valuable complementary purpose.

Table 6.1 summarizes the finding in this study focusing on mechanical insight – substantiating that there is sufficient literature focusing on actin behavior, but not spectrin and actin-spectrin cytoskeleton.

Table 6.1: Actin, Spectrin, and Actin-Spectrin Network: Mechanical Behavior Insight

Axonal Cytoskeletal Component	Mechanical Property or Attribute Investigated	Reference
Actin	Persistence length	(Chu and Voth, 2005; Isambert et al., 1995; Tsuda et al., 1996)
	Unfolding and stretching characteristics	(Oda et al., 2009; Pfaendtner et al., 2010b)
	Mechanics of F-actin bundles	(Stricker et al., 2010)
	Bending and torsional rigidity and stiffness, twisting	(Enrique et al., 2010; Fan et al., 2012; Isambert et al., 1995; Matsushita et al., 2010; Rebello and Ludescher, 1998)
	Severing mechanism and response to tensile loading	(Berro et al., 2007; Chu and Voth, 2006; De La Cruz, 2009; Kim et al., 2016; T Kim et al., 2009; Matsushita et al., 2011; McCullough et al., 2011; Schramm et al., 2017)
	Mechanics + chemistry aspects	(Asakura et al., 1963)
	Young's modulus	(ben-Avraham and Tirion, 1995; Higuchi et al., 1995a; Huxley et al., 1994b; Khan et al., 2020a; Kim et al., 2016; Kojima et al., 1994b; Matsushita et al., 2011; Wakabayashi et al., 1994b)
	Viscoelastic behavior	(Gurmessa et al., 2017; Lieleg et al., 2009; Sato et al., 1985; Schmoller et al., 2009; Unterberger et al., 2013b)
	Cross-linking dynamics	(Sato et al., 1987; Xu et al., 1998b)

	Rheological parameters (such as storage and lost modulus) at filament and network level	(Janmey et al., 1994; Kojima et al., 1994a; Xu et al., 1998a)
	Actin-actin bond	(Tsuda et al., 1996)
	Strain-rate dependent behavior	(Gardel et al., 2004)
Spectrin	Shear response	(An et al., 2002; Smith et al., 2018)
	Elastic response	(Dao et al., 2006; Hoore et al., 2018)
	Biochemical failure	(Witek and Fung, 2013)
	Forced unfolding mechanism	(Altmann et al., 2002; Law et al., 2003; Lenne et al., 2000; Ortiz et al., 2005; Paramore and Voth, 2006; Rief et al., 1999; Scott et al., 2004; Viel, 1999; Zhu and Asaro, 2008)
Actin-Spectrin Network	Contribution of reversible unfolding of spectrin at low strain rate	(Dubey et al., 2020; Li and Lykotrafitis, 2012)

Therefore, it is evident that more mechanical studies are required focusing on spectrin and actin-spectrin network, which can be achieved by computational approaches as depicted by molecular level studies on other axonal cytoskeletal components (Khan et al., 2020b; Wu and Adnan, 2018). Keeping these aspects in consideration, this study attempts to provide novel insights regarding the specific mechanical behavior of such cytoskeletal components at extreme strain rate – which will play an instrumental role in developing a bottom-up axon model focusing on TBI scenario and contribute to the existent computational axon models.

6.2 Method

The required PDB file and FASTA sequence for actin and spectrin structures are obtained from RCSB and Uniprot protein data banks, and then simulation-compliant models are built based on the predicted obtained from the i-TASSER predictor software (Zhang, 2008). The reason of proceeding with i-TASSER predicted structure is its reliability quantified by CASP and recent successful implementation of predicted structure in MD simulations (Battisti and Tenenbaum, 2012; Castro et al., 2019; Khan et al., 2020b).

The PDB files are converted into LAMMPS (Plimpton, 1995) readable data files with OPLS force field (Jorgensen et al., 1996) for simulation. The simulation box is filled with explicit water molecules, for which MARTINI force field (Marrink et al., 2007) is used for van der Waals interaction parameters. Required NaCl ions were added to obtain charge neutralization for explicit solvent simulations.

With periodic boundary conditions in all three directions, the protein structures solvated in water are equilibrated for 200ps to minimize the potential energy at a targeted temperature of 310K. The LJ potentials are used with inner and outer cutoff of 10Å and 12Å, respectively. Long range coulombic interactions are computed by pppm style, facilitating a particle-particle particle-mesh solver with a 3d mesh. The equilibration was performed in NVT canonical ensemble, with the temperature damping parameter of 100fs (for the first 100ps), and then in NPT isobaric ensemble, with target pressure of 1 bar (for another 100ps). After the structures are well equilibrated as ensured by flat potential energy of the system vs time graphs, the uniaxial tensile tests are performed by pulling the residues along the length axis, towards the opposite direction, at the strain rates of 10^8 s^{-1} and 10^9 s^{-1} which are relevant to TBI scenario despite being high strain rates (Wu and Adnan, 2018). It is assumed that ~10% of strain is sufficient to obtain the stiffness data. Table 6.2 summarizes the box size of the systems and the specific tensile test schemes.

6.2.1 Tensile Test on 6-actin and 12-actin Models

To determine mechanical property of actin, 6-actin and 12-actin models are utilized. Both models are built from existent literature. The 6-actin model is obtained from "actin filament pointed end" structure found by electron microscopy deposited with PDB ID 2Y83 (Narita et al., 2011), while the 12-actin model is obtained from the cryo-EM structure of actin deposited with PDB ID 3G37 (Murakami et al., 2010). The objective of tensile test is to observe strain rate dependence and difference between the stretching mechanism between short and long F-actin filaments.

6.2.2 Tensile Test on α-spectrin and β-spectrin

For α-spectrin and β-spectrin, the models are built from Uniprot structures – for non-erythrocytic α-spectrin (gene: SPTAN1) (Moon and McMahon, 1990) and β-spectrin (SPTBN2) (Nagase et al., 1997) structures. These sources facilitate specification of domains and repeat regions, which is utilized in the modeling and tensile tests. The tensile test scheme is similar to that of actin. The simulation-compliant versions are created by using the last seven (7) repeats and the EF hand regions for α-spectrin, while the first seven (7) repeats and the actin binding domain are used for β-spectrin. According to the comprehensive review study on spectrin (Zhang et al., 2013), 19-20 repeats in α-spectrin and 1-2 repeats in β-spectrin are sufficient for actin-spectrin modeling, and therefore, it is ensured that these repeats are included in the standalone spectrin models. The specification of the residue numbers of both spectrin isoforms are provided in Table 1. Aside from obtaining the mechanical property, another objective of the tensile test on standalone spectrin is to observe the unfolding mechanism.

6.2.3 Determination of Actin-Spectrin Interaction

For actin-spectrin interaction model, two β-spectrin filaments (a smaller version with the actin-binding domain and the first two repeats) (Zhang et al., 2013) are attached to the 12-actin surface, and then pulled at the opposite directions. The objective of applying two different strain rates is to observe the strain rate

dependence and possible separation mechanism. This ensures that possible TBI scenarios are covered where either of the axonal cytoskeletal components might be susceptible to stretching.

6.2.4 Stress-Strain Calculation and Tensile Test Schemes

Calculation of the stress and strain are similar to recently published MD work on axonal cytoskeletal component of neuron (Khan et al., 2020b). The stress-strain plots are obtained by the per-atom stress calculation and summation in LAMMPS. However, as the output is in (pressure x volume) unit, the obtained stress value must be divided by the volume of the protein (or certain portion of the protein). The general formulation used by stress per atom command is $P = (P_{xx}+P_{yy}+P_{zz})/ (3xV)$, where P_{xx}, P_{yy} and P_{zz} are the summations of stress/atom values for all atoms in x, y, and z direction respectively, and V is the summation of volume of the atoms of the protein being considered. The approximated volume was obtained by Voronoi cell approximation, adapted from LAMMPS voro++ package (Rycroft, 2009). The strain is simply obtained by the displacement of the atoms from the initial position. All the tensile tests are performed in NVT ensemble, with 100fs temperature damping parameter.

The visualizations of the tests are carried out by OVITO software (Stukowski, 2010). All the simulations were carried out by the STAMPEDE2 and Lonestar supercomputers of Texas Advanced Computing Center (TACC).

Table 6.2: Simulation setup for tensile tests on actin, spectrin, and actin-spectrin models

System	Box Size Approximation (nm x nm x nm)	Number of protein atoms	Number of atoms in the system	Boundary Condition or Loading Scheme for Tensile Test

	[Note: biggest dimension is always in the length (or pulling) direction]		(approx. in millions)	(all are performed for strain rates $1x10^{8}s^{-1}$ and $1x10^{9}s^{-1}$)
6 Actin	13 x 13 x 48.5	35202	0.75	First 100 and last 100 residues are pulled towards the opposite direction
12 Actin	17 x 17 x 63.5	70548	1.6	First 100 and last 100 residues are pulled towards the opposite direction
α-Spectrin	68.5 x 12 x 12	13034	0.9	Left-most repeat region is pulled towards -x direction, right-most repeat region and EF regions are pulled towards +x direction
β-Spectrin	68 x 12 x 12	15342	0.9	Left-most repeat region and actin-binding region are pulled towards -x direction, right-most repeat region is pulled towards +x direction
Actin-Spectrin	58 x 11 x 38.5	87702	2.2	The outermost 50 residues of the two β-Spectrins attached to the 12-

				actin surface are pulled towards the opposite directions

6.3 Results

6.3.1 Mechanical Property of Actin

For 6-actin and 12-actin systems, uniaxial tensile tests are performed at two strain rates, $10^8 s^{-1}$ and $10^9 s^{-1}$. Figure 6.5-6.7 show the stress-strain response and tensile test snapshots for the 6-actin system, while Figure 6.8-6.10 show the same for the 12-actin system. It is observed that both 6-actin and 12-actin behave as stiffer material at higher strain rate. However, the stretching stiffness is in the range found in the literature, even at such high strain rate.

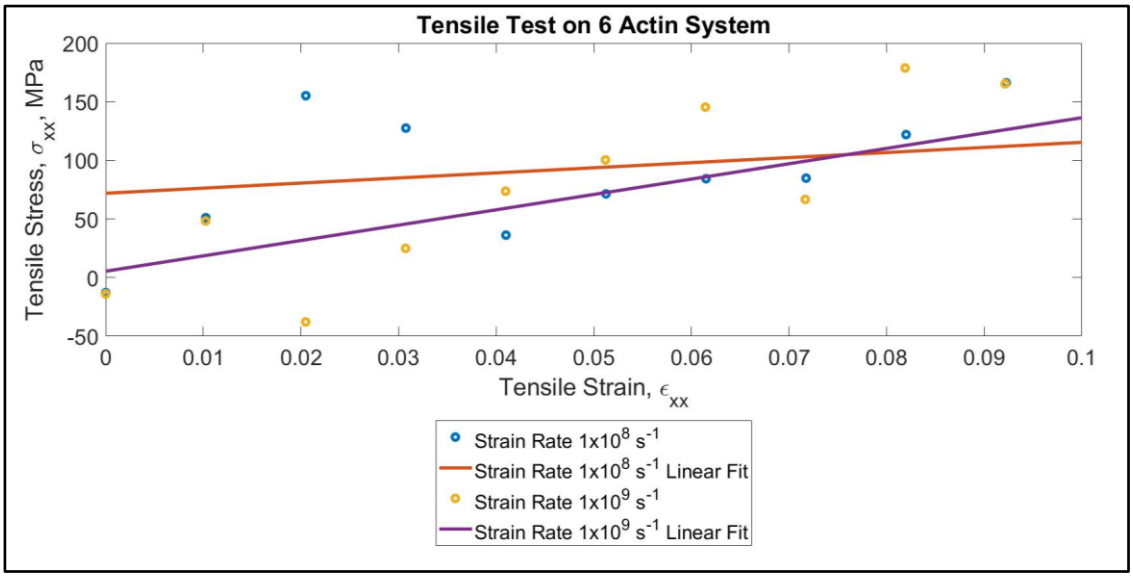

Figure 6.5: Stress-strain response of 6 actin system for two strain rates.

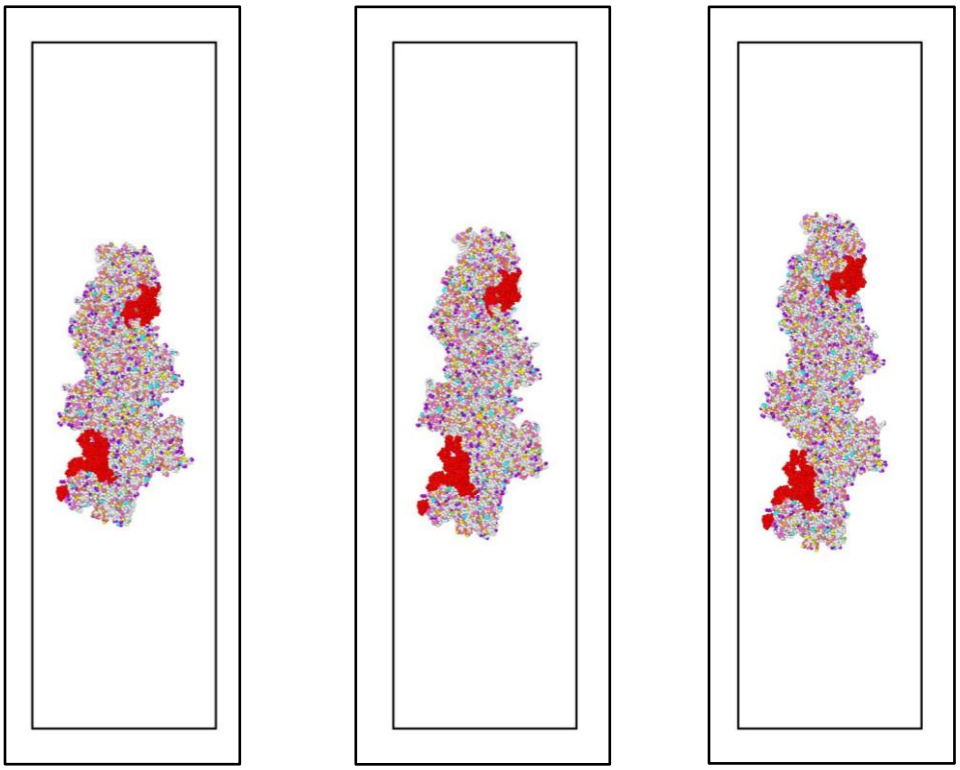

a b c

Figure 6.6: Snapshots of tensile test on 6-actin system at strain rate $1x10^{8}s^{-1}$. Strain: a) 0%, b) 5%, c) 10%. The atoms being pulled are shown in red color. For the rest, the default coloring of OVITO software is retained.

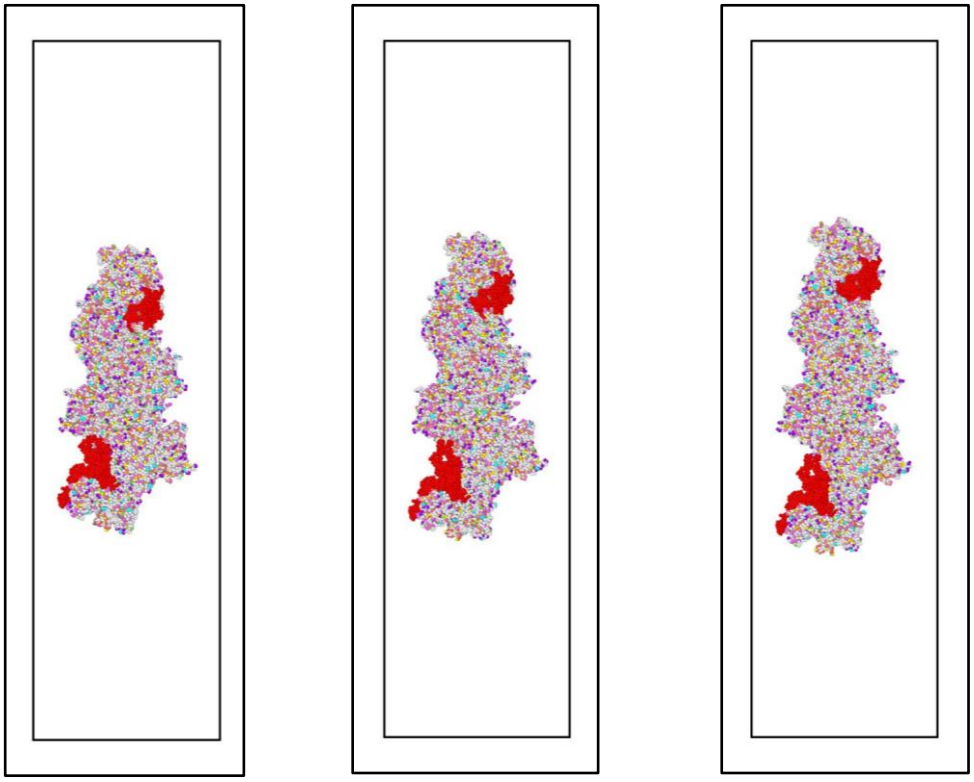

a b c

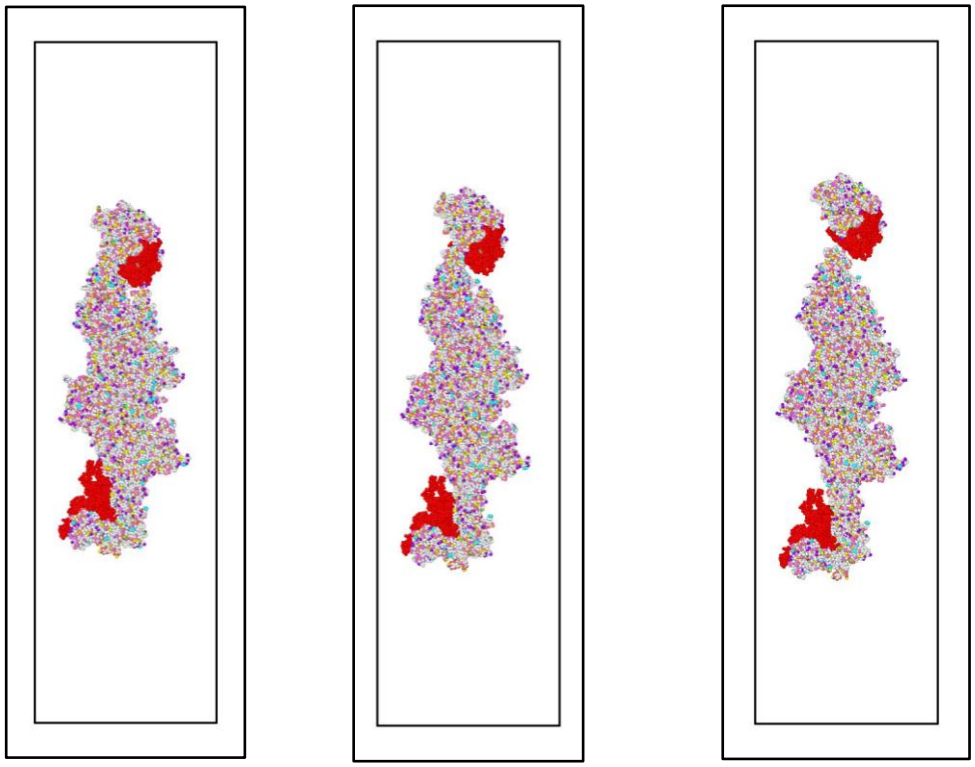

d e f

Figure 6.7: Snapshots of tensile test on 6-actin system at strain rate $1x10^{9}s^{-1}$. Strain: a) 0%, b) 10%, c) 20%, d) 30%, e) 40%, f)50%. The onset of failure is found at ~30% strain, where for complete failure (fragmentation of the main filament) occurs at ~50%. The atoms being pulled are shown in red color. For the rest, the default coloring of OVITO software is retained.

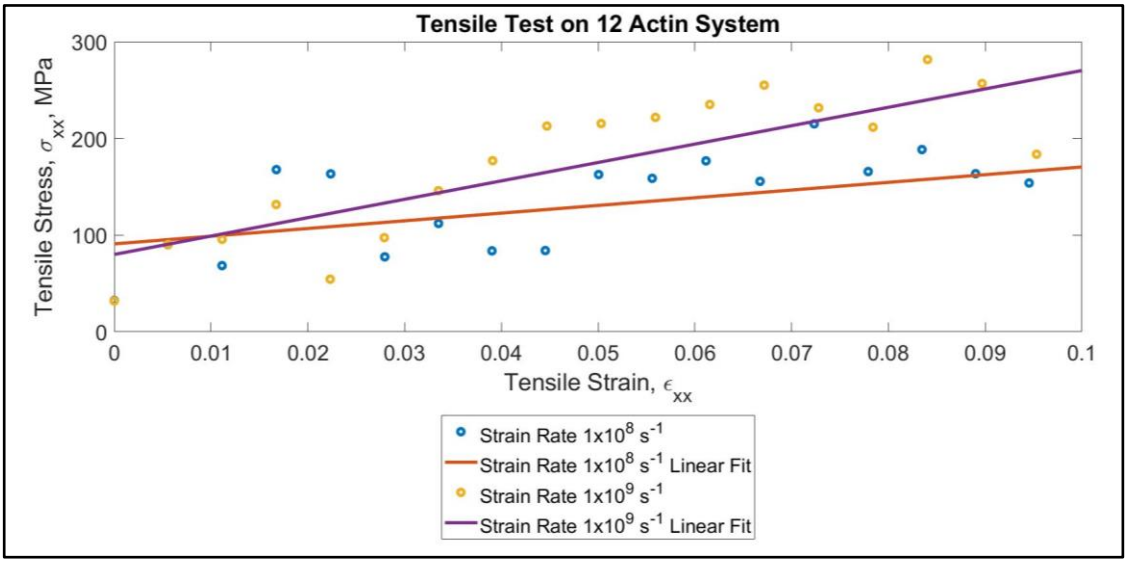

Figure 6.8: Stress-strain response of 12 actin system for two strain rates.

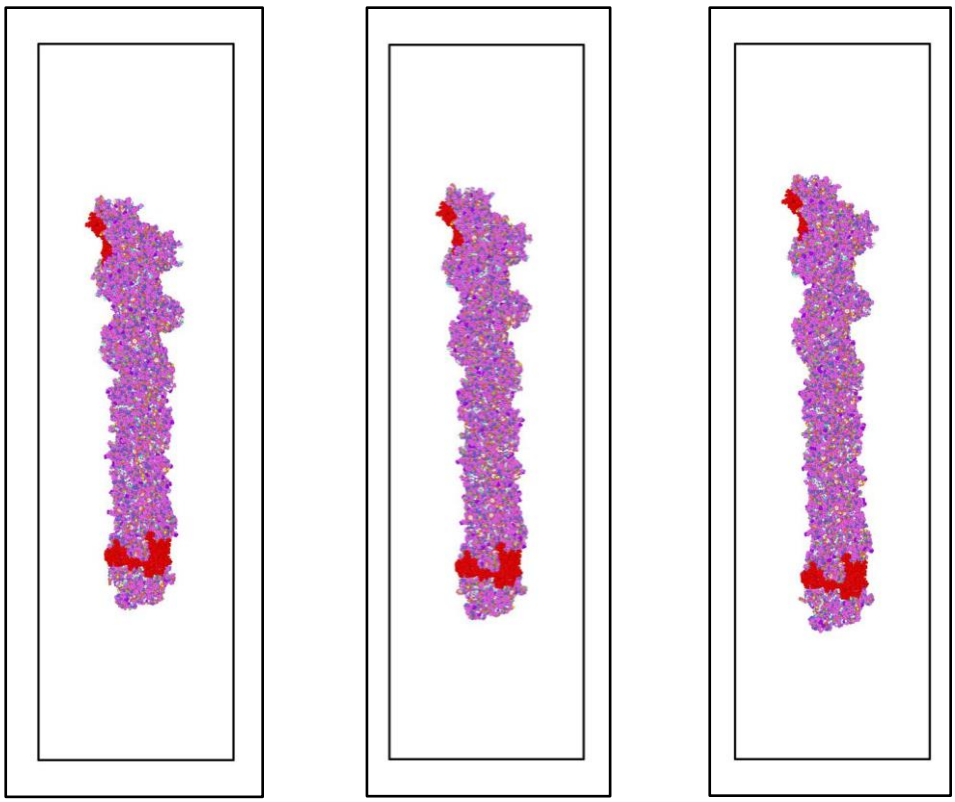

a b c

Figure 6.9: Snapshots of tensile test on 12-actin system at strain rate $1x10^{8}s^{-1}$. Strain: a) 0%, b) 5%, c) 10%. The atoms being pulled are shown in red color. For the rest, the default coloring of OVITO software is retained.

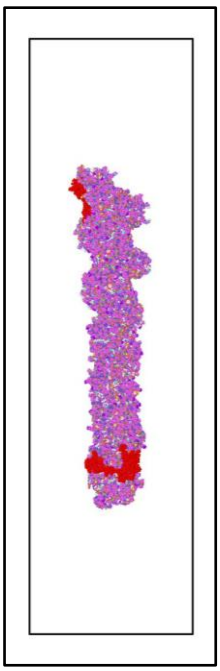

a

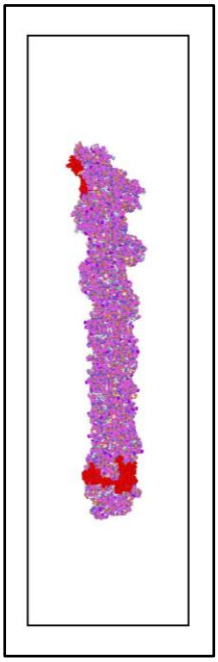

b

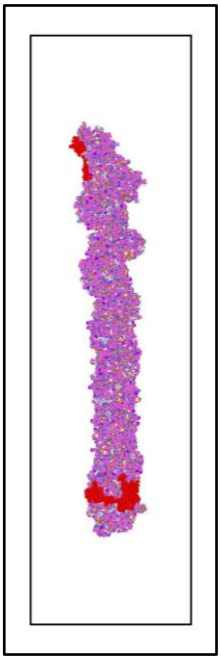

c

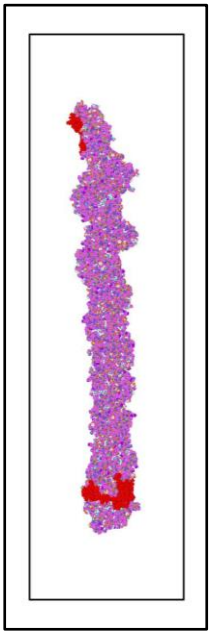

d

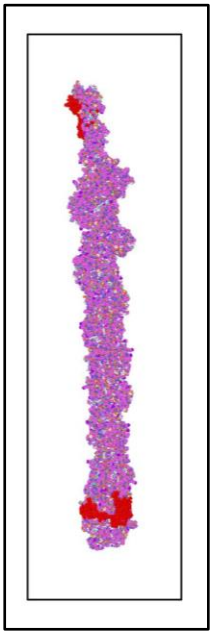

e

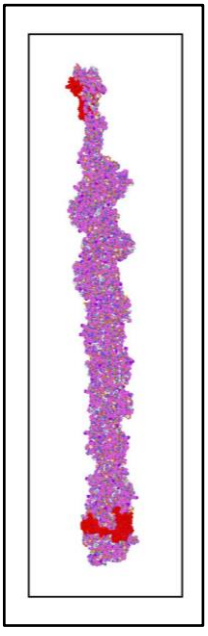

f

Figure 6.10: Snapshots of tensile test on 12-actin system at strain rate $1x10^{9}s^{-1}$. Strain: a) 0%, b) 10%, c) 20%, d) 30%, e) 40%, f)50%. This longer filament does not show failure by fragmentation, rather it shows increased stretchability. The atoms being pulled are shown in red color. For the rest, the default coloring of OVITO software is retained.

6.3.2 Mechanical Property of Spectrin

For α-spectrin and β-spectrin systems, uniaxial tensile tests are performed at two strain rates, $10^{8}s^{-1}$ and $10^{9}s^{-1}$. Figure 6.11-6.13 show the stress-strain response and tensile test snapshots for the α-spectrin system, while Figure 6.14-6.16 show the same for the β-actin system. It is observed that spectrin also behaves as stiffer material when susceptible to higher strain rate. However, the extent of dependence on the strain rate is relatively lower, as spectrin goes through unfolding stage of the interrepeat domains unlike actins (which manifest stretching of the F-actin filaments even at low strain due to strong bond between G-actins in the filament) as depicted by the snapshots.

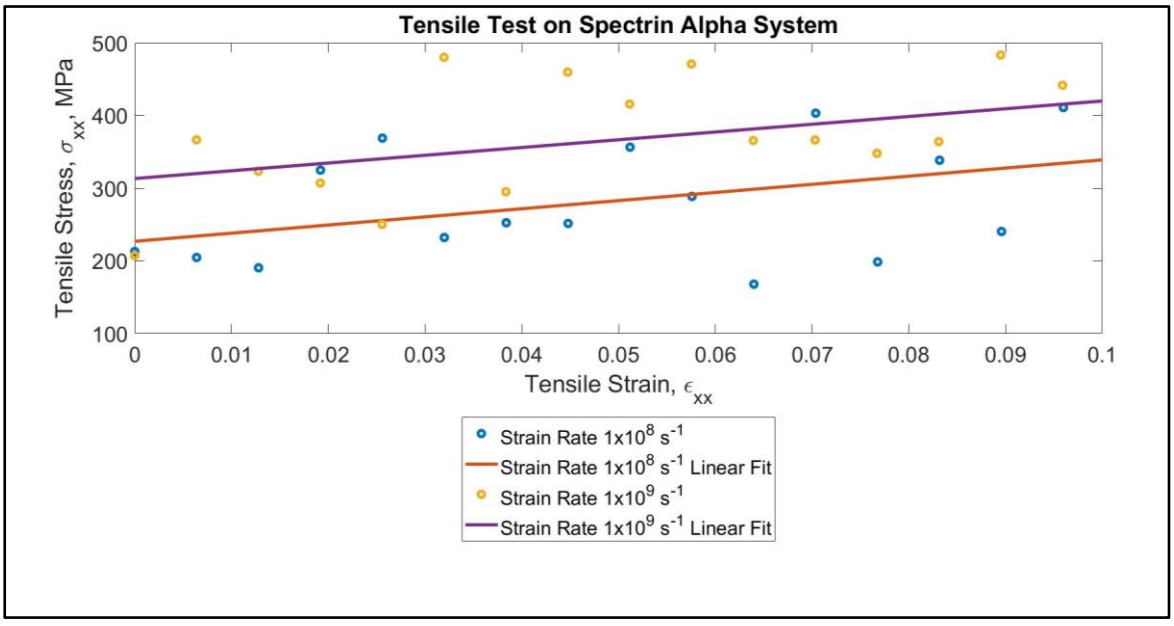

Figure 6.11: Stress-strain response of α-spectrin system for two strain rates.

a

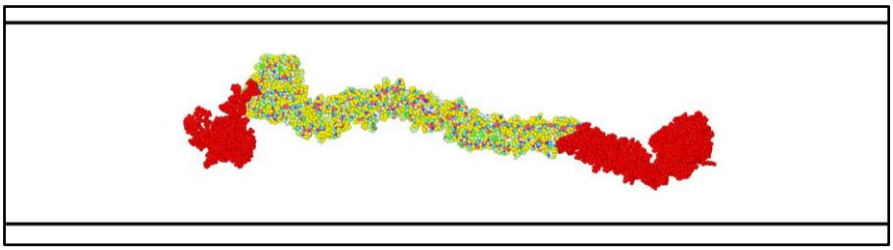

b

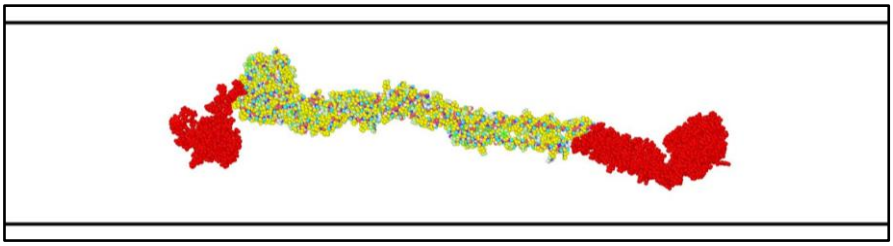

c

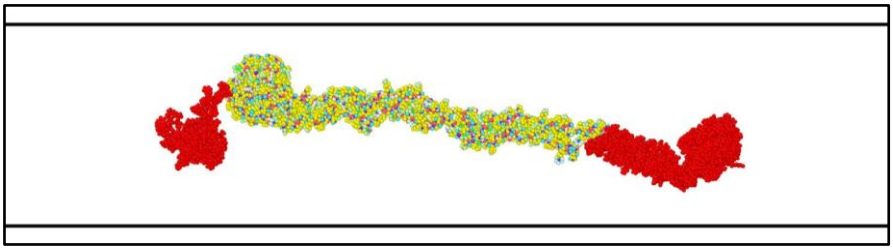

Figure 6.12: Snapshots of tensile test on α-spectrin system at strain rate $1x10^{8}s^{-1}$. Strain: a) 0%, b) 5%, c) 10%. The atoms being pulled are shown in red color. For the rest, the default coloring of OVITO software is retained.

a

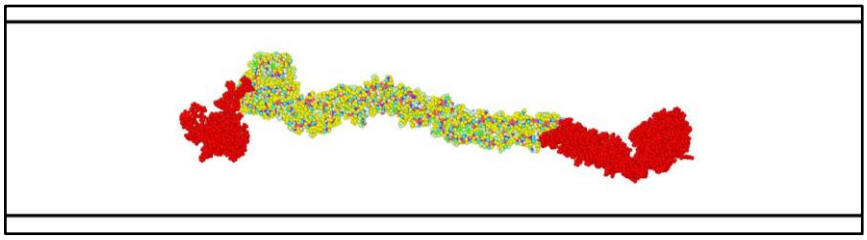

b

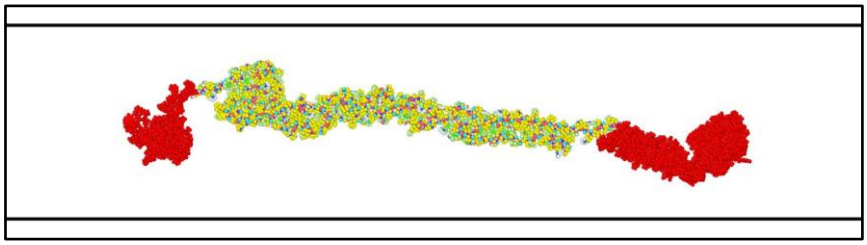

c

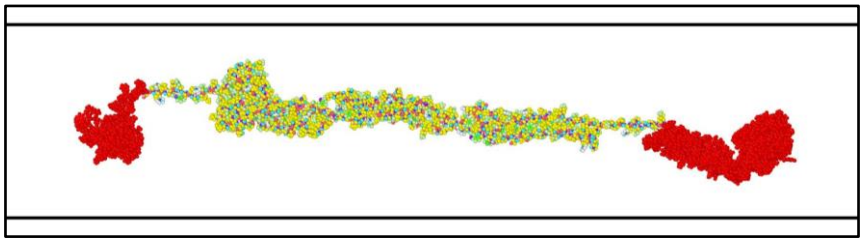

d

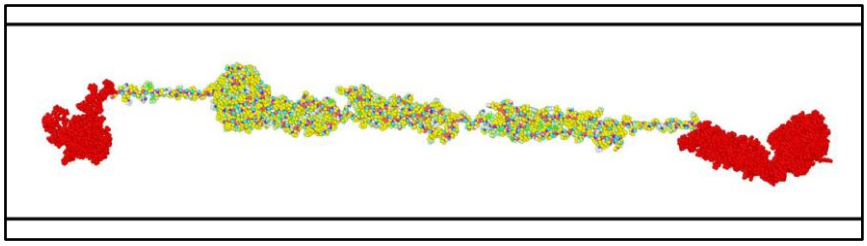

Figure 6.13: Snapshots of tensile test on α-spectrin system at strain rate $1x10^{9}s^{-1}$. Strain: a) 0%, b) 20%, c) 40%, d) 60%. The unfolding of the inter-repeat domains are manifested strongly at high strain rate. The atoms being pulled are shown in red color. For the rest, the default coloring of OVITO software is retained.

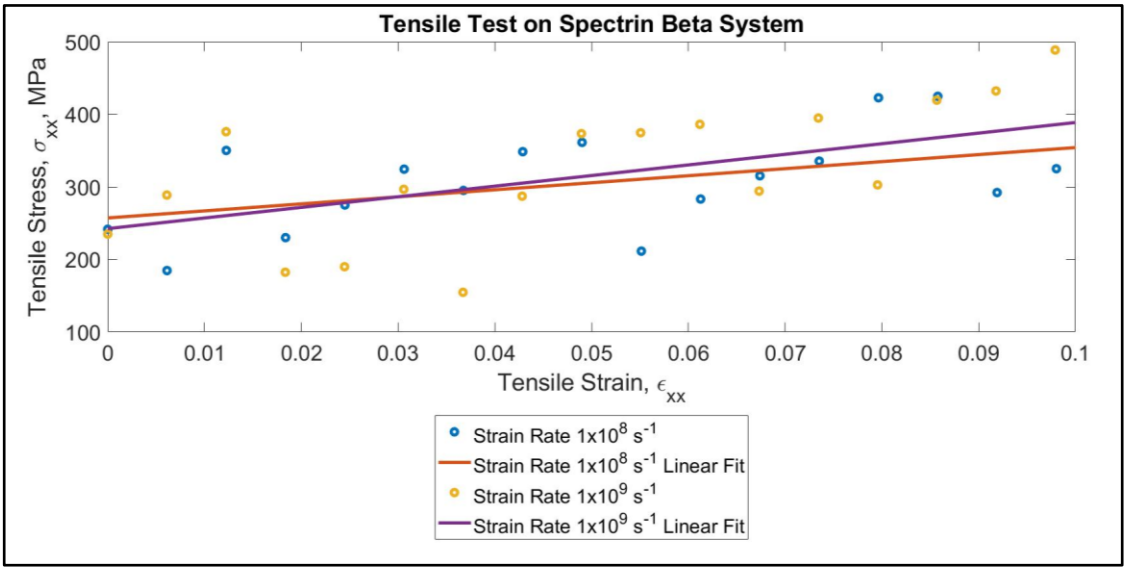

Figure 6.14: Stress-strain response of β-spectrin system for two strain rates.

a

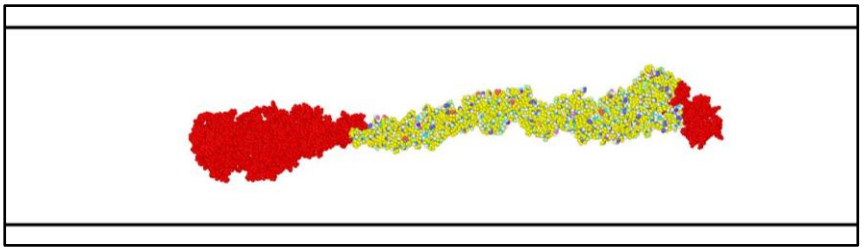

b

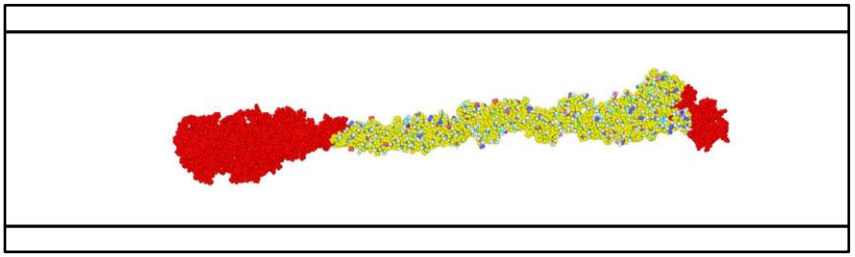

c

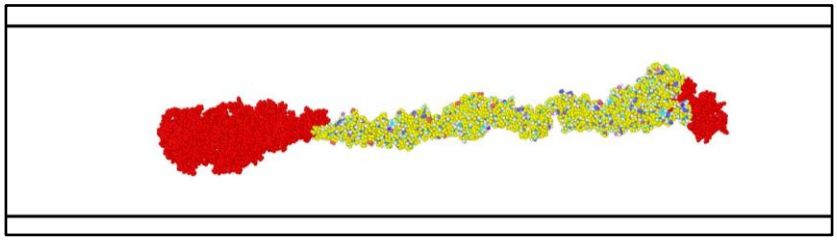

Figure 6.15: Snapshots of tensile test on β-spectrin system at strain rate $1x10^{8}s^{-1}$. Strain: a) 0%, b) 5%, c) 10%. The atoms being pulled are shown in red color. For the rest, the default coloring of OVITO software is retained.

a

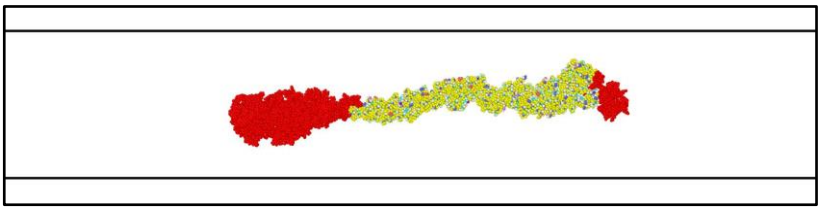

b

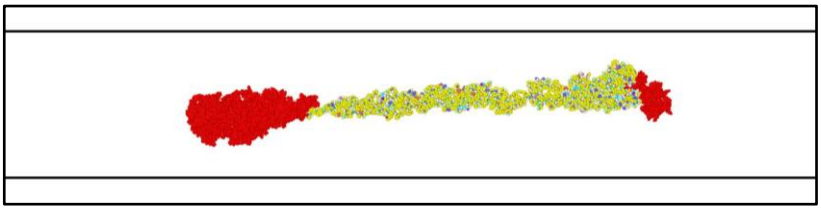

c

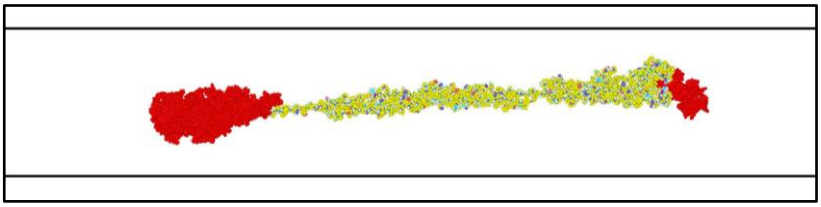

d

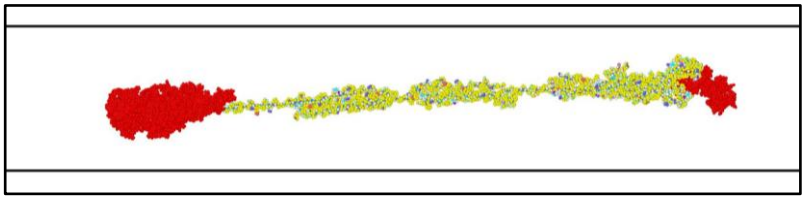

Figure 6.16: Snapshots of tensile test on β-spectrin system at strain rate $1x10^{9}s^{-1}$. Strain: a) 0%, b) 20%, c) 40%, d) 60%. The unfolding of the inter-repeat domains is manifested strongly at high strain rate. The atoms being pulled are shown in red color. For the rest, the default coloring of OVITO software is retained.

Table 6.3 summarizes the stiffness result based on the linear fit of 10% strain vs stress data of actin and spectrin models.

Table 6.3: Stiffness summary from the tensile tests on actin and spectrin models.

Model	Stiffness (MPa)	
	$1x10^{8}s^{-1}$	$1x10^{9}s^{-1}$
12-actin	919	2054
6-actin	852	1816
Spectrin-α	973	2107
Spectrin-β	1120	1067

6.3.3 Actin-Spectrin Interaction

For actin-spectrin systems, tensile tests are performed at two strain rates, $10^8 s^{-1}$ and $10^9 s^{-1}$ by attaching two β-spectrin to the surface of a 12-actin system, and then pulled away towards the opposite directions. Figure 6.17 and 6.18 show the tensile test snapshots for the system for $10^8 s^{-1}$ and $10^9 s^{-1}$, respectively. It is depicted that not only the separation differs according to the applied strain rate, but also the failure mechanism. At lower strain rate, the prone-to-failure region is the actin-spectrin interface, while at higher strain rate, it is the inter-repeat regions of spectrin.

a

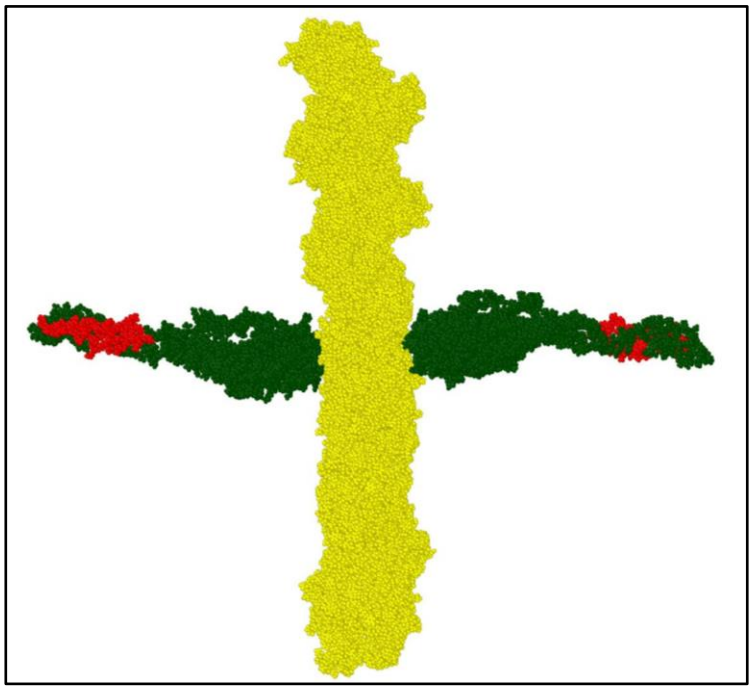

b

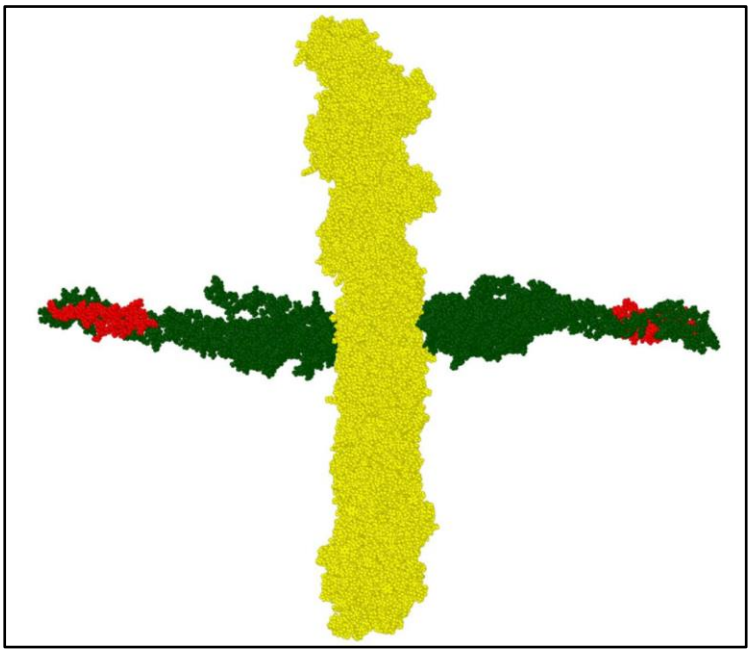

c

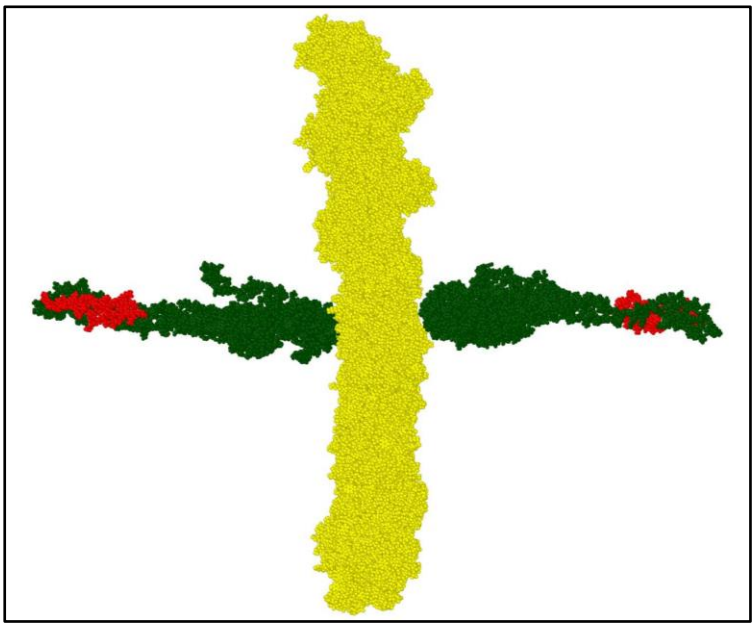

d

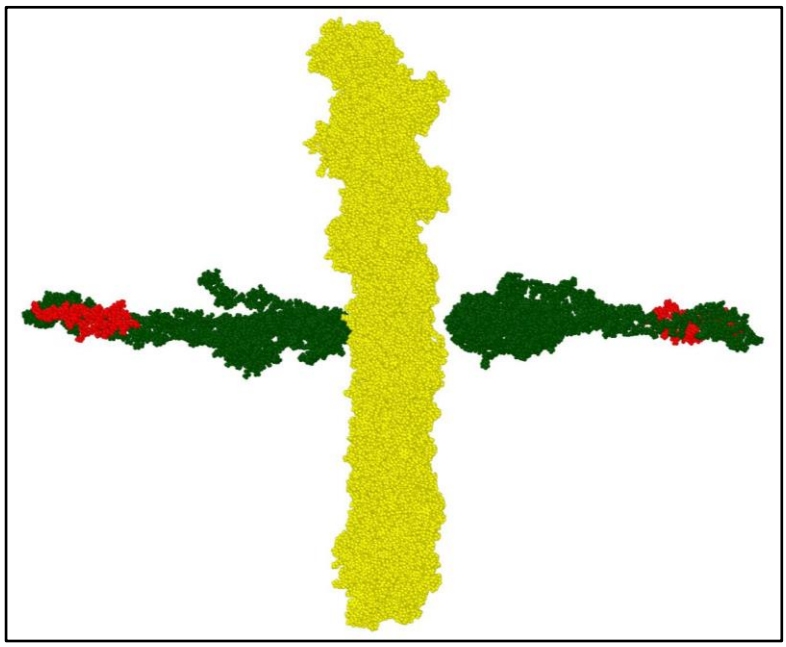

Figure 6.17: Actin-spectrin interaction at strain rate $1x10^{8}s^{-1}$. a) 0%: initial, b) 6%: stretching of β-spectrin, c) 12.5%: onset of separation, d) 18.75%: complete separation. Legend: Yellow: 12-actin, Green: β-spectrin, Red: atoms being pulled.

a

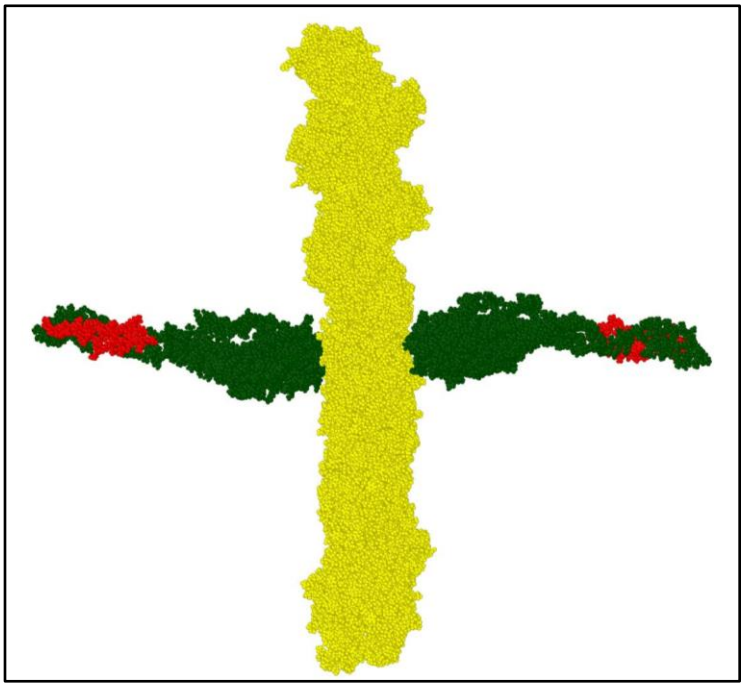

b

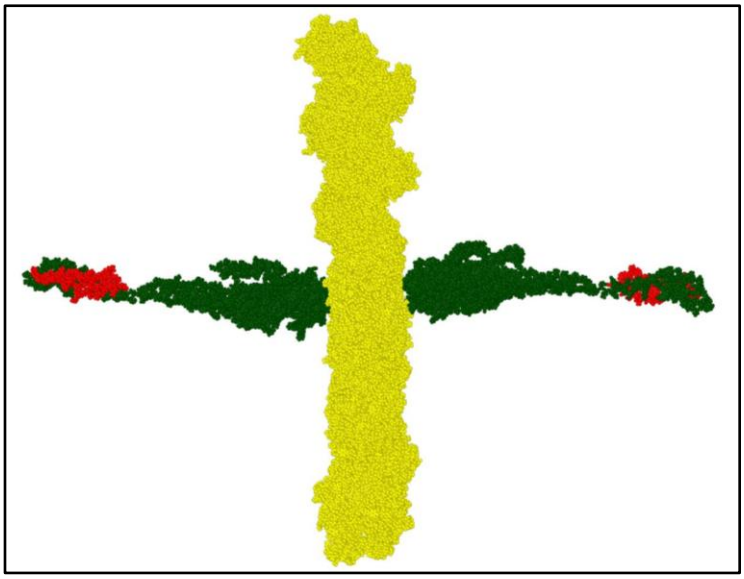

c

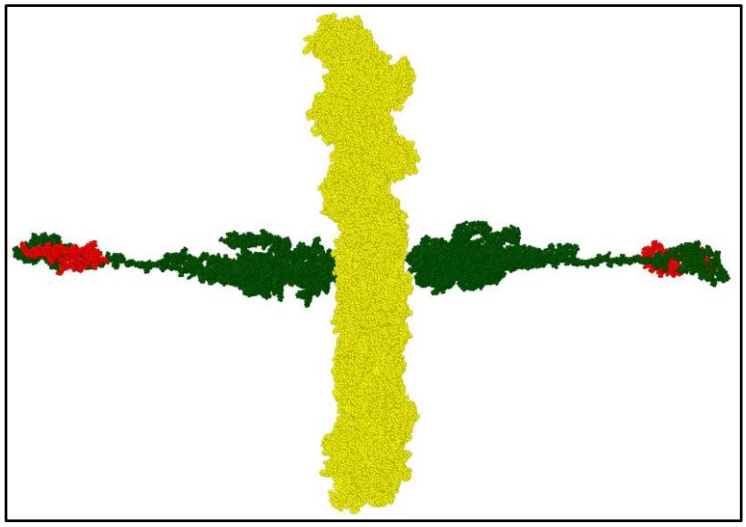

d

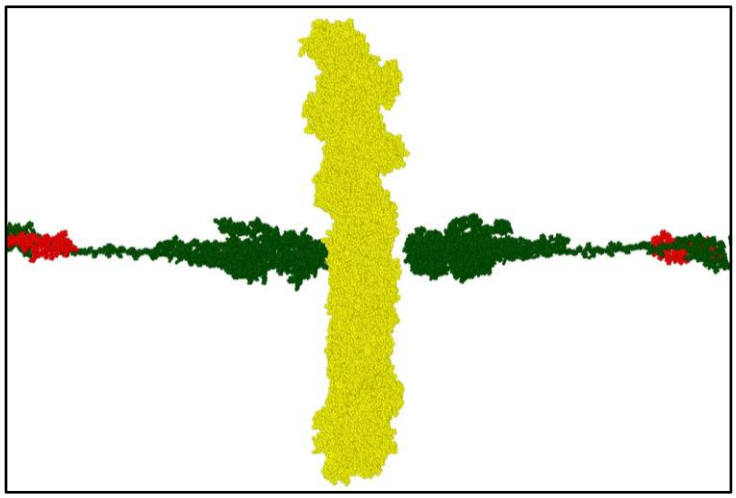

Figure 6.18: Actin-spectrin interaction at strain rate $1x10^{9}s^{-1}$. a) 0%: initial, b) 23.5%: stretching and unfolding of β-spectrin, c) 42.3%: onset of separation, d) 58.75%: complete separation. Legend: Yellow: 12-actin, Green: β-spectrin, Red: atoms being pulled.

6.4 Discussion

The tensile tests performed in this study provides novel insights on mechanical behavior of actin, spectrin, and actin-spectrin cytoskeleton in axon. However, as a computational study, some common issues must be addressed – such as selection of force field, application of strain rate, and using predicted structure for protein.

First, selection of appropriate force field is vital for realistic representation of a biophysical scenario. In this study, OPLS force field is used for simulations, as it is specifically fine-tuned for protein simulation (Kaminski et al., 2001; Robertson et al., 2015). Recently it is found that non-reactive force field such as CHARMM can successfully capture high deformation phenomena for cytoskeletal components of neuron (Khan et al., 2020b; Wu and Adnan, 2018). As a benchmark test, the tensile test on α-spectrin is performed for both CHARMM and OPLS force fields, which shows comparable results as depicted in the Appendix A5.

Second, the strain rates used in this study for the tensile tests fall into "extreme" range for axonal cytoskeletal components. However, recent computational study on such components has found such range of strain rates as relevant to blast-induced TBI scenario (Wu and Adnan, 2018).

And third, proceeding with predicted structure obtained from the FASTA sequence available in the protein data bank (PDB) is justified due to increased application and successful implementation in the recent years (Battisti et al., 2012; Battisti and Tenenbaum, 2012; Castro et al., 2019; Khan et al., 2020b).

In the following sub-sections, the specific aspects of the obtained results, their impact, and future directions are discussed.

6.4.1 Mechanical Behavior of Actin in TBI Scenario

Studies that explored the failure mechanism of actin have emphasized the effect of actin-severing proteins, such as cofilin (Berro et al., 2007; McCullough et al., 2011). While it is admitted that both biochemical and mechanical aspects should be considered for determining mechanical behavior of actin at high strain rate, it can be argued that effect of mechanical loading (applied tension on the protein in this study) will be most significant at extreme strain rate scenario, which is shown in recent studies on other axonal cytoskeletal components of neuron (Khan et al., 2020b; Wu and Adnan, 2018). Furthermore, from the results of both 6-actin and 12-actin systems it is substantiated that actin behaves as a stiffer material at higher strain rate. Increase of extensional and torsional stiffness is established in the literature (Matsushita et al., 2011), which is in harmony with the finding of the current study. Therefore, from the perspective of extensional stiffness, it can be asserted that mechanical behavior of actin is maintained throughout a large range of tensile loading. The only difference between the 6-actin and 12-actin system is the failure mechanism. For 6-actin or shorter system, actin tends to fail along the junction of G-actin to G-actin. Similar type of failure is also observed for MTs at extreme strain rate, which fails along the line of the tubulin junction when susceptible to tensile loading (Wu and Adnan, 2018). As there is mainly electrostatic and van der Waals bond i.e. non-bonded interactions between G-actins, it is expected that these bonds will be broken before the covalent bonds within the G-actin atoms. However, for longer system (12-actin), the pulled region is substantially smaller than the overall filament length, and therefore, the tensile load can be carried along the length of the whole filament – leading to high stretchability. The range of stiffness is, however, coherent with recent review work (Khan et al., 2020a), which suggests that at high strain rate, actin stiffness will be at the high end of the range proposed (400MPa-2.5GPa) (ben-Avraham and Tirion, 1995; Higuchi et al., 1995b; Huxley et al., 1994b; Kim et al., 2016; Kojima et al., 1994b; Matsushita et al., 2011; Wakabayashi et al., 1994b).

6.4.2 Mechanical Behavior of Spectrin in TBI Scenario

Similar to that of actin, the mechanical behavior of spectrin can also be explained from the biochemical perspective (Witek and Fung, 2013). Earlier atomic force microscopy (AFM) studies on spectrin tandem repeats and single spectrin have established that susceptibility to tensile loading leads to unfolding and stretching, which is impressively close to the observation in the current study (Altmann et al., 2002; Law et al., 2003; Lenne et al., 2000). Furthermore, the high stretchability can be attributed to the initial "folded" state of the repeat regions and the inter-repeat regions, which get unfolded due to applied high strain rate. Although the force required to unfold spectrin has been found to be small (Rief et al., 1999), it can be asserted that due to having multiple un-foldable regions throughout the structure, axonal spectrin can have high stretchability. However, the multiple fold is attributed to the mechanical strength of the spectrin filament, and unfolding leads to vulnerability to failure. It is discussed in recent studies that axonal cytoskeletal components provide mechanical stretchability due to their inherent capacity to stretch even more than 100% of their initial length (Dubey et al., 2020), and therefore, it can be assumed that this capacity is originated from the ability of membrane-associated proteins in axon which contain folded regions i.e. spectrins. Therefore, the results on spectrin not only substantiates the structural and mechanical insight in the current literature, but also provides indirect causation of the ability of axon to stretch significantly.

6.4.3 Actin-Spectrin Interaction in TBI Scenario

As there is little insight present in the current literature regarding actin-spectrin network (Dubey et al., 2020), from the actin-spectrin models in the current study it is substantiated that even at high strain rate, actin-spectrin lattice can provide substantial mechanical support. Also, two different manners of failure can be observed according to the applied strain rates. At lower strain rate, there is significant stretch in spectrin,

but the primary failure-prone region is the actin-spectrin interface. However, the scenario is different at higher strain rate, as the tensile loading gets less amount of time to be propagated through the spectrin filament and manifested at the interface region. Therefore, it is observed that the more damage-prone area is the inter-repeat regions of spectrin – same observation obtained in standalone spectrin tensile tests performed in this study. In other words, at a single TBI scenario, there could be occurrence of different failure along the periodic actin-spectrin lattice: such as separation of spectrin from actin surface, substantial spectrin unfolding, or both. In any case, the result is disorientation of the axonal cytoskeleton of neuron, regarding which this study provides a novel, strictly mechanical insight from TBI perspective. However, for more comprehensive insight, length-dependent tests could also be performed as the F-actin models in this study. For this purpose, different number of repeats might be implemented in the actin-spectrin models. Optimistically, the near future works will be considering coarse-grained models to accommodate longer filament lengths and multiscale approach to obtain lattice-level mechanical response.

6.5 Conclusion

In this study, mechanical behavior of actin, spectrin, and actin-spectrin interaction at high strain rate are determined. The major findings can be summarized as below:

1. Actin: Both short and long F-actin filaments show stiffer characteristics at higher strain rate. Short filament tends to fail at the G-actin to G-actin junction, while long filament shows increased stretchability.

2. Spectrin: Both α-spectrin and β-spectrin show high stretchability. Unfolding of inter-repeat regions is strongly manifested at higher strain rate.

3. Actin-spectrin: Failure occurs at actin-spectrin interface at lower strain rate, while significant unfolding of spectrin occurs at higher strain rate.

This study not only substantiates recent findings on periodic axonal structure of cytoskeleton, but also provides novel insights regarding the mechanical behavior and interaction. Therefore, this study will provide pathway for bottom-up axon modeling, contribute to refinement of existent computational axon models, and invoke further research focusing TBI scenario.

CHAPTER 7

SUMMARY AND FUTURE STUDIES

7.1 Summary

We have completed five (5) computational studies on tau protein and NFs, which cover their strain rate dependent mechanical behavior, phosphorylation effect, and viscoelastic modeling of them. The following points summarize the findings of the studies, and the parameters or aspects we have determined:

1. Effect of strain rate on single tau, dimerized tau, and tau-MT interface interaction have been determined. Here we have shown the strain rate dependent unfolding and stretching phenomena, that differs based on strain rate on single tau, separation stretch required in the dimerized tau, and separation stretch required to detach tau protein from MT surface, including the comparative strength of tau-tau and tau-MT bond, and potential energy aspect of such phenomena.

2. Domain focused and residue focused phosphorylation in tau have been shown. This study addresses the behavior of tau according to the phosphorylated state, and attempts to find out the effect of this post-translational modification on single tau unfolding and stretch, dimerized tau separation, tau separation from tubulin surface and MT surface, and tau accumulation tendency. We can argue that in the first and second studies have successfully given crucial insights on rate dependent aspects of tau, and structural and chemical response of this cytoskeletal component.

3. Strain rate dependent tests on the sidearms of NF isoforms have been performed, and their unfolding and stretching behavior, including NF accumulation have been observed. This study, although independent, takes a similar approach as we have taken on tau protein, and gives crucial insights on rate dependent aspects of NF.

4. Tau and NF behavior have been characterized by fitting their relaxation data to established viscoelastic model. This study practically completes our understanding on tau and NF behavior under the application of high strain rate mechanical loading.

5. Mechanical properties of actin and spectrin have been determined, along with the actin-spectrin separation stretch. This study justifies several mechanical insights present in the literature, and provides novel insight at periodic axonal cytoskeleton lattice level from the damage-prone region perspective.

Based on the five (5) studies, we assert that the existent axon models can be enhanced, the FEM models can be improved, and a holistic computational axon model can be developed.

7.2 Implementation of the MD Studies

There are axon models in literature which do not include all the required cytoskeletal components. For example, the viscoelastic shear lag model which focuses on the elasticity of MTs and viscoelasticity of tau, developed by Ahmadzadeh et al(Ahmadzadeh et al., 2014). In the previous chapter, we have elaborated on tau protein and NFs, determining their deformation nature and rate dependent responses. Therefore, the existent model can be enhanced by using our study results. The tentative enhanced model might include polymerized, or at least dimerized tau protein interaction with MT. Fig. 7.1 Clarifies the limitations of the existent model.

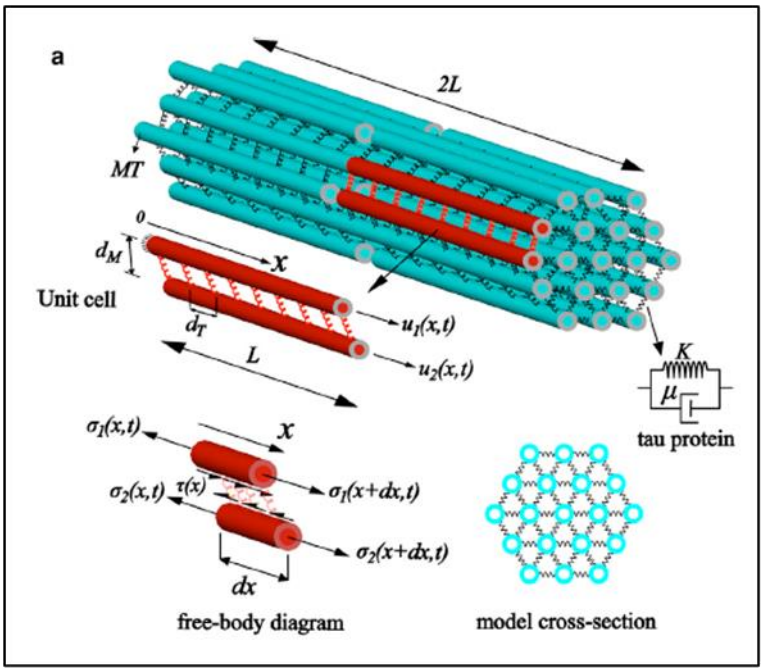

Figure 7.1: The viscoelastic shear lag model, in which MT is considered as elastic, while tau protein as viscoelastic. In this model, MF and NF are absent, which can be enhanced by using the MD simulation study results on tau and NF, and literature results on MF.

Furthermore, FEM axon model has been also developed, which require the elastic and viscoelastic material properties of MT crosslinks i.e. tau proteins (Hasan et al, 2020, Multiscale Mechanics and Physics Laboratory, University of Texas at Arlington). Moreover, inclusion of MFs and NFs are also important in order to attain comprehensive axon model. Admittedly, MT controls majority of the property and behavior of axon, but the individual component response, and interaction aspects as well as properties are highly important under the application of impact loading and high strain. Hence our studies will be instrumental to complete the FEM axon models. Fig. 7.2 shows ANSYS snapshot of the FEM axon model under construction, which incorporates tau protein, but here NF and MF are absent.

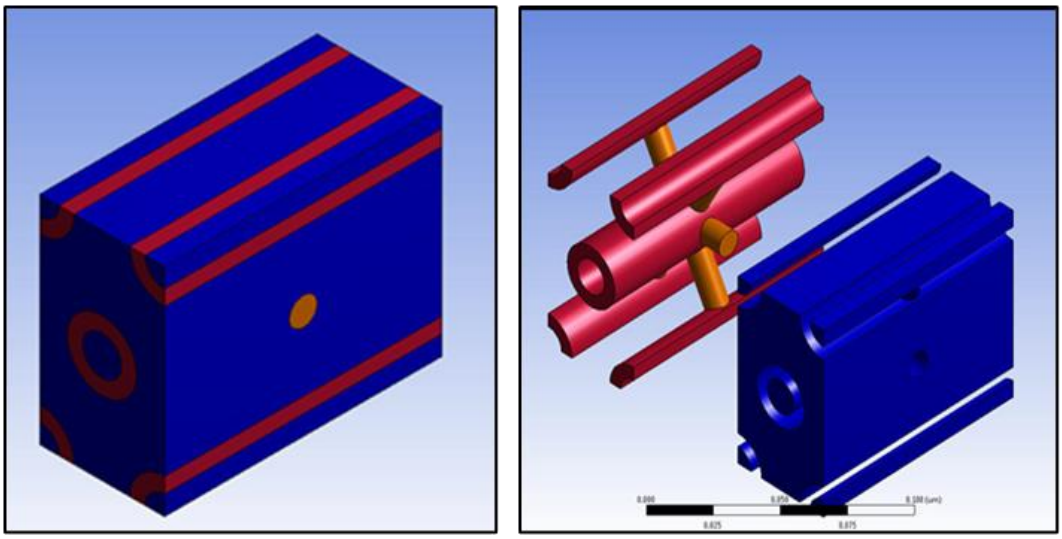

a **b**

Figure 7.2: FEM axon model under construction, which includes MT and tau protein absorbed in axoplasm. a. MT and tau protein are absorbed in axoplasm, b. MT-tau structure shown separately from axoplasm.

In short, our studies facilitate developing a realistic and comprehensive computational bottom-up axon model, which will consist all major cytoskeletal components – MT, tau, NF, and MF.

7.3 Future Direction

One of the promising aspects of our completed studies is the length-scale transition. By dint of the molecular dynamics simulations on tau proteins and neurofilaments, and approaches to obtain insight regarding the mechanical behavior of axonal cytoskeleton, we can conduct meaningful experiments and computational studies, especially location-focused impact or deformation studies to determine the damage-prone areas. More specifically, our possible next step will be linking up the bottom-up approach of axon modeling and top-down approach of macroscale impact tests on head models, which will validate substantial amount of data originated by our effort. However, the direction will be dependent upon our access to and interpretation

of highly biofidelic head model and insightful FEM simulations to determine the regions most susceptible to damage due to developed stress and strain. One example is the deformation test of cerebral cortex model of Simpleware software, which was converted to a coarse-grained FEM model and simulated in ABAQUS for observing deformation and stress responses (Fig. 7.3). The preliminary test shows that the highly susceptible areas for damage are the gyri and sulci regions (rises and falls or wavy shaped regions), and therefore, a meaningful bottom-up step will be to model a small area of one of those regions. Furthermore, a highly sophisticated area will probably consist of the effect of the supporting cells of brain, namely glial cells. In association with implementation of high-resolution and high frame rate cameras, we will be able to determine the deformation of damage-prone regions experimentally and validate our computational model, too.

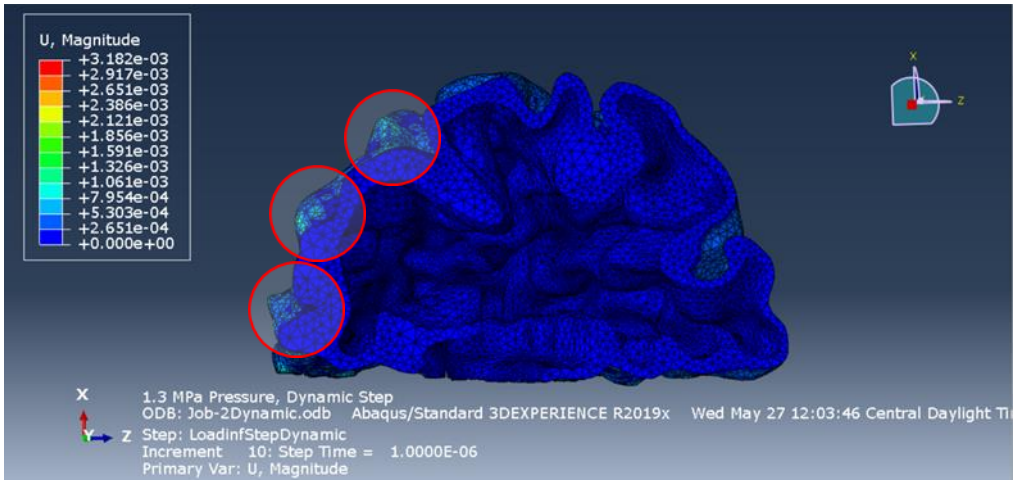

a

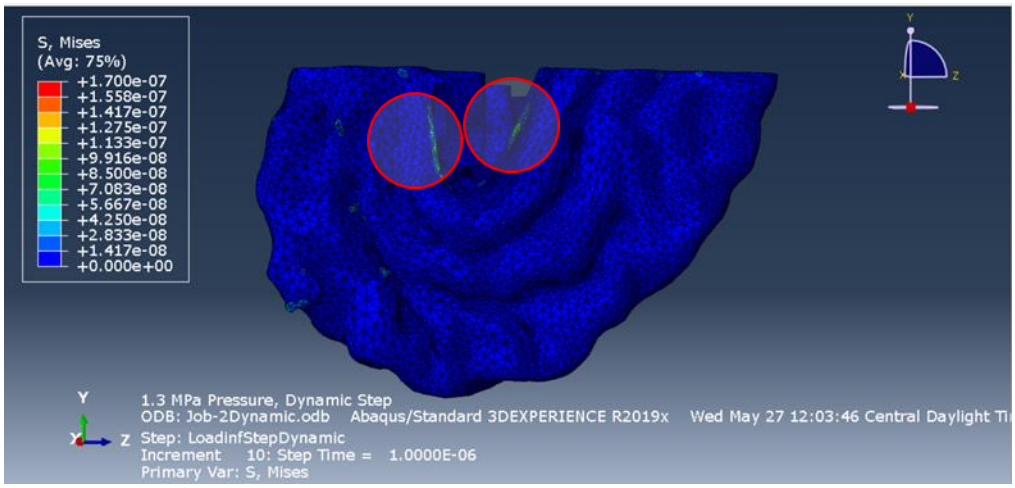

b

Figure 7.3: Determination of damage-prone areas in an FEM model of cerebral cortex (Source: Simpleware software pre-built models obtained from the laboratory of Dr. Jun Liao, Department of Mechanical and Aerospace Engineering, The University of Texas at Arlington. The meshing is coarse, 88000 elements, and exposed to an instantaneous loading. Deformation and stress values are calculated by ABAQUS). a) Deformation, b) von Mises stress developed. The red circles depict that the damage-prone areas are the gyri and sulci.

APPENDIX

APPENDIX 1

PREDICTED STRUCTURE OF TAU PROTEIN

A1.1 i-TASSER Methodology

In the manuscript, we have studied the single tau, dimerized tau, and tau-MT interaction. The structure of tau protein which is an intrinsically disordered protein (IDP) is obtained by using predictor software i-TASSER (Zhang, 2008). i-TASSER uses a hierarchical protein structure modeling approach based on the secondary-structure enhanced Profile-Profile threading Alignment (PPA) (Cozzetto et al., 2007) and the iterative implementation of the Threading ASSEmbly Refinement (TASSER) program (Wu and Zhang, 2007). In order to address the problem of predicting 3D structures of proteins in structural biology and completely automate the system by computer algorithm while admitting the importance of intervention of human expert, i-TASSER has set a methodology to obtain reliable predicted structure for protein with appropriate quantification of the quality of the models. Due to the reliability of its predicted structure, i-TASSER has been ranked as the best method in the server section of the 7th CASP (Critical Assessment of Structure Prediction) experiment (Zhang and Skolnick, 2004a).

The scoring function (C-score) of this software, is based on the relative clustering structural density and the consensus significance score of multiple threading templates. In order to validate the reliability of the scoring system, the developer group of the software has performed a large benchmark test on 800 non-homologous single domain random proteins, which demonstrates a strong correlation between the C-score and the TM-score (a structural similarity measurement with values in [0, 1]) of the first models with a correlation coefficient of 0.91. Using a C-score cutoff > -1.5 for the models of correct topology, both false positive and false negative rates are below 0.1. Combining C-score and protein length, the accuracy of the I-TASSER models can be predicted with an average error of 0.08 for TM-score and 2 Å for RMSD.

Although we have cited the paper which describes the quantitative measure i-TASSER takes to ensure the model reliability, we are briefly discussing the C-score and TM-score here for relevance.

The C-score is defined as:

$$\mathbf{C-score} = \ln\left(\frac{\mathbf{M}}{\mathbf{M_{total}}} \times \frac{1}{\langle \mathbf{RMSD} \rangle} \times \frac{\prod_{i=1}^{4} \mathbf{Z(i)}}{\prod_{i=1}^{4} \mathbf{Z_0(i)}}\right) \quad \textbf{(A1.1)}$$

where M is the multiplicity of structures in the SPICKER cluster (Zhang and Skolnick, 2004b); M_{tot} is the total number of the i-TASSER structure decoys used in the clustering; ⟨RMSD⟩ is the average RMSD of the decoys to the cluster centroid; Z(i) is the highest Z_{score} (the energy to mean in the unit of standard deviation) of the templates by the i^{th} PPA threading program and $Z_0(i)$ is a program-specified Z-score cutoff for distinguishing between good and bad templates. The first two factors of the equation accounts for the degree of structure convergence of the SPICKER cluster, while the third factor accounts for the quality of the threading alignments. The logarithm is taken to ensure the even adjustment of the distribution of the C-score. The previous definition of C-score proved the strong correlation between the C-score and the reliability of the predicted models (Zhang and Skolnick, 2004a), while the definition of C-score is slightly different due to the normalization of Z-score, which extends the scope of the definition to the cases where different threading algorithms might be used to predict the same template. Furthermore, it accounts for the consensus of the alignment confidence of multiple threading programs.

The second scoring function, the TM-score (Zhang and Skolnick, 2004c) is defined as:

$$\mathbf{TM-score} = \frac{1}{\mathbf{L}} \sum_{i=1}^{\mathbf{L}} \frac{1}{1 + \frac{\mathbf{d_i}^2}{\mathbf{d_0}^2}} \quad \textbf{(A1.2)}$$

where d_i is the distance of the i^{th} pair of residues between two structures after an optimal superposition, $\mathbf{d_0 = 1.24\sqrt[3]{L - 15} - 1.8}$, and L is the protein length. TM-score stays in [0, 1] with higher values indicating better models. Statistically, a TM-score ≤ 0.17 corresponds to a similarity between two randomly selected structures from the PDB library; a TM-score > 0.5 corresponds approximately to two structures of the similar topology. One advantage of the TM-score is that the meaning of the TM-score cutoffs is independent of the size of proteins.

A1.2 Predicted Structure of Tau Protein from i-TASSER:

After submitting the tau protein amino acid sequence to i-TASSER queue, we have obtained 5 predicted "pdb format" models as output. For each target, i-TASSER simulations generate a large ensemble of structural conformations, called decoys. To select the final models, i-TASSER uses the SPICKER program to cluster all the decoys based on the pair-wise structure similarity and reports up to five models which corresponds to the five largest structure clusters. The confidence of each model is quantitatively measured by C-score that is calculated based on the significance of threading template alignments and the convergence parameters of the structure assembly simulations. C-score is typically in the range of [-5, 2], where a C-score of a higher value signifies a model with a higher confidence and vice-versa. TM-score and RMSD are estimated based on C-score and protein length following the correlation observed between these qualities.

According to i-TASSER policy, they report C-score for all the five models but provide TM-score and RMSD values for only the first one (the most reliable model in most cases, because of the usage of the biggest cluster for the first model). Fig. A1.1 shows the five models they have reported.

The first model is used for our simulation, which has the C-score of -0.03, estimated TM-score = 0.71±0.12, and estimated RMSD = 7.1±4.2Å. As it is at the very reliable end of the C-score, and the TM score is far higher than >0.5 which ensures a good topology, we have proceeded with the reported structure. We already

know that tau protein is an intrinsically disordered protein (IDP), and there can be multiple stable conformations. However, by strictly following the reliability parameters defined by i-TASSER, we can proceed with the first predicted model.

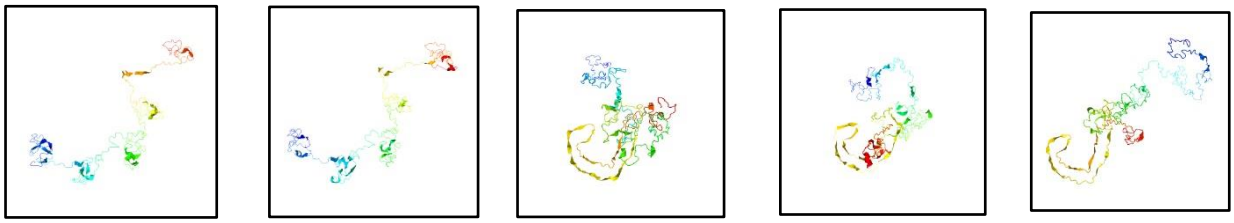

a **b** **c** **d** **e**

Figure A1.1: Predicted tau protein structure models from i-TASSER. a. Model 1: C-score = -0.03, estimated TM-score = 0.71±0.12, and estimated RMSD = 7.1±4.2Å (used for our simulations), b. Model 2: C-score = -0.03, c. Model 3: C-score = -3.57, d. Model 4: C-score = -3.14, e. Model 5: C-score = -3.91. The color coding is blue to read, meaning from C-terminal to N-terminal.

A1.3 Limitations of the Prediction of Tau, which is an IDP:

The authors of this manuscript are completely aware that it is intuitive to question the reliability of the predicted structure of an IDP. However, to pave the pathway to characterize the material properties of tau protein, we must compromise between the available experimental repertoire and the convenience that the computational approaches provide. Experimentally, the research groups have tended to determine the 3D structure of tau protein of only diseased tau proteins by dint of cryo-EM procedures, which facilitated the development of structure and availability of diseased tau protein in the Protein Data Bank (PDB). It has been possible to obtain the filamentous structure of tau protein for chronic traumatic encephalopathy (CTE) (Falcon et al., 2019), pick's disease (Falcon et al., 2018), or Alzheimer's disease (AD) (Fitzpatrick et al., 2017) affected tau protein, which are in general formed by the result of abundance of hyperphosphorylation

sites, or repeated impact on the head leading to neuropathology. From the experimental data in the literature, the filamentous structure, paired helical filaments (PHF), or neurofibrillary tangles (NFT) are only formed in diseased tau protein and/or their aggregates. To find the mechanical properties, we must proceed with normal (healthy) tau protein structure, which is not yet experimentally determined. Even the partial structures of diseased tau proteins are made available in the PDB very recently (Falcon et al., 2019; Seidler et al., 2018) (in the years of 2019-2020, prior to which our study begun, and we have continued to review the literature to cope up with the very recent advancement of protein structure determination).

Therefore, our computational approach has addressed certain aspects of tau protein that have not yet been addressed by any experimental means to date, according to the best knowledge of the authors. Furthermore, we have justified the reliability of the predicted structure in this supplementary material. The limitation of this work is that due to computational constraint, other conformations of tau protein which are competitively reliable from the perspective of C-score and TM-score have not been statistically explored. However, we plan to address this issue as well in the continuing study. We admit that there are certain unanswered areas in the study of tau protein which are not revealed by experimental means conclusively to date (such as the mechanism of phosphorylation in altering the properties of tau protein, which we plan to address in our continuing study), and based on the recent molecular level tau studies, we can proceed with our representative structure of tau, which can be suggested as “one possible conformation which is stable with reliable mark of confidence”. In the main manuscript, we have cited some relevant tau studies which have used i-TASSER predicted structure.

APPENDIX 2

MD SIMULATION: EXPLICIT VS IMPLICIT SOLVENT

A2.1 Difference Between Explicit and Implicit Solvation

A molecular dynamics simulation can be carried out in two ways – with explicit solvation or implicit solvation. In explicit solvation, the simulation box is filled with explicit water molecules, whereas in case of implicit solvation, the interaction between the molecule of concern and implicit water molecules is defined analytically. The definitions of such interactions have been defined by establishment of a handful of models e.g. models which consider mean potential force (Kleinjung and Fraternali, 2014), or models which consider distance-dependent electrostatic interaction (Chen et al., 2008). Aside from the established importance of explicit water molecule solvation which is closer to the realistic physical phenomenon, it is relevant to discuss the validity and reliability of using implicit solvation technique. A direct study comparing the effect of the solvent molecule type on the mechanical behavior of tau protein is not currently available in the literature. However, this supplementary material is an attempt to explain the expected difference between the two types of simulations.

In the studies, explicit solvation has been used for single tau simulations, but implicit solvation was used for dimerized tau and tau-MT simulations due to the bigger box size involved. Using implicit solvent techniques in some of the simulations consisted adjustment of coulombic terms by modifying 1/r terms to $1/r^2$. The advantages for this method are two-fold, such as:

1. Ability to ignore Ewald sum or potential mean force type interaction,
2. Accommodating large deformation associated with the applied high strain rate.

While these provide certain level of conveniences while simulating mechanical response of the respective axonal cytoskeletal components of neuron at high stretch, the solvent-molecule surface charged layer interactions are being ignored. Keeping these in consideration, differences can be expected in the calculated stress values, because:

1. The initial length of the proteins in the two systems will not be equal,
2. In explicit system, the tau protein will be stretched against resistance of solvent molecule interaction,
3. Incremental stretch will expose more charged (Chau et al., 1998; SERRANO et al., 1985; Silber et al., 2004) and hydrophobic surface (Rosenberg et al., 2008) of the flanking (projection) domain of tau protein in case of explicit system, unlike in implicit system,
4. Solvent accessible surface area will continuously change as the protein unfolds and moves in the box during equilibration and tensile test. Note that the projection domain and the tail domain are not constrained in space,
5. Irrespective of the box orientation and filament orientation, the length scale of tau protein will be always significantly smaller than the box size due to the inherent disordered portion (Rosenberg et al., 2008) of tau protein structure, and therefore, explicit water molecule interaction cannot be ignored.

Considering the abovementioned differences, it is expected that the stress development will be significantly higher in case of tau protein stretching in explicit solvent than that in implicit solvent, meaning implicit solvation will undercalculate the development of stress.

Now, as a direct comparison between the explicit and implicit equilibration and tensile tests that are performed to obtain an insight regarding the difference in stress-strain relation and the energy terms, a comparison test is also performed for single tau (the methodology is the same as Chapter 2). The comparison test equilibrates two systems with the same initial structure of tau protein, equilibrates in the same condition,

and then performs tensile test at $1x10^{8}s^{-1}$ strain rate up to 80% strain of the projection domain. The objective is to compare the structural and energetical differences that occur during the comparison test.

The equilibration and tensile test are completed in two steps:

1. Equilibration for 100ps at 1fs timestep to equilibrate the system adequately,
2. Performing the tensile test by fixing the MT binding region and pulling the projection domain towards the -x direction up to 80% strain.

It is to be noted that in the implicit solvation, the system contains only 6424 atoms of the protein, while for the explicit solvation, it contains 410197 atoms in total. The appropriate density of water is maintained automatically by CHARMM-GUI.

Below, the steps will be detailed with appropriate data analysis and snapshots.

A2.2 Equilibration and Tensile Test Comparison

Step 1: Equilibration for 100ps with 1fs timestep

Figure A2.1 shows the comparison between potential energy graphs in the explicit and implicit system. Figure A2.2 shows the Snapshots of the initial, intermediate, and final snapshot of the protein structure.

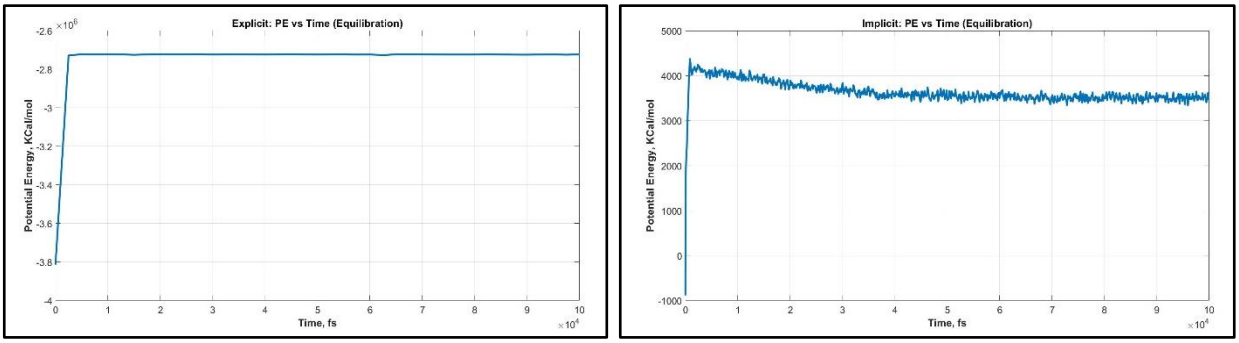

a b

Figure A2.1: Equilibration: Potential energy vs time for a) explicit solvation, b) implicit solvation. Both systems are well-equilibrated, as both the graphs show that potential energy changes negligibly over time.

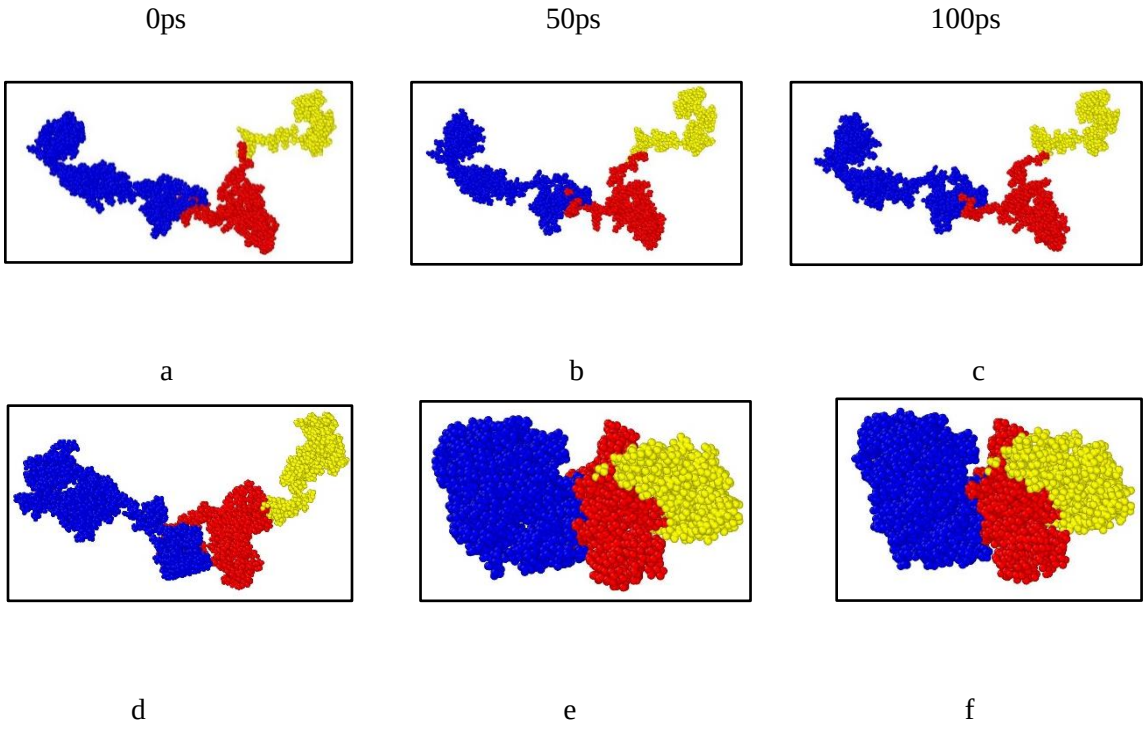

Figure A2.2: Equilibration: Structural snapshot of the tau protein for a-c) explicit solvation, d-f) implicit solvation at left: 0ps, middle: 50ps, right: 100ps. Legend: Blue: projection domain, Red: MT binding sites including interrepeats, Yellow: tail.

As Figure A2.2 depicts, the major structural difference occurs over this 100ps equilibration. Due to the continuous interaction with explicit water molecules, the projection domain retains its expanded structure (expands ~2Å by the end of the 100ps equilibration, meaning no unfolding or significant structural change occurs) for explicit solvation, while due to continuous interaction between the positively and negatively charged region, the projection domain shrinks on itself, or "tightens" the existent folds. At the end of the 100ps equilibration, the length of the projection domain (determined by the difference of the highest and

lowest x coordinate of atom in the projection domain) becomes significantly smaller, ~39Å, which is ~57.6% shrinkage. This leads to a significant difference of the initial length for the tensile test.

Step 2: Performing the tensile test by fixing the MT binding region and pulling the projection domain towards the -x direction up to 80% strain

Figure A2.3 shows the comparison between stress vs strain in the explicit and implicit system. Finally, Figure A2.5 shows the Snapshots of the protein structure at every 8% incremental strain for insight of unfolding phenomenon.

Explicit Implicit

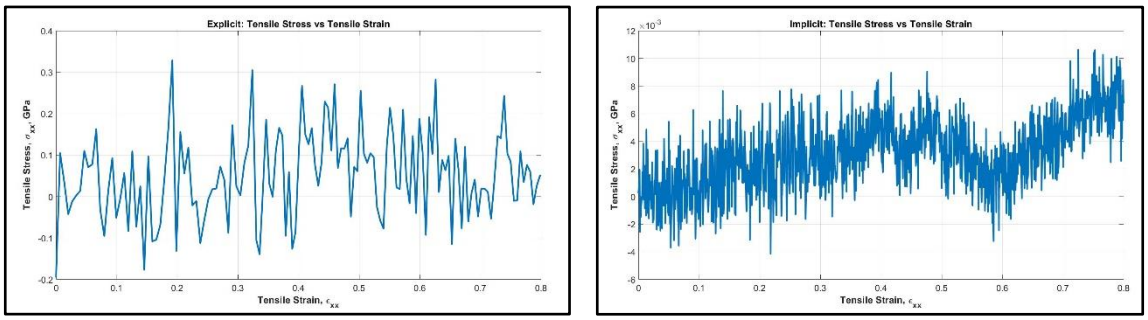

a b

Figure A2.3: Tensile test: Stress vs strain for a: explicit system and b: implicit system.

From the PDB file cartoon representation (Figure A2.4) it is evident that there are three major tertiary folded regions in the projection domain: 1) Residue 1-80 containing one α-helix in between, 2) Residue 87-160

containing another α-helix in between, and c) Residue 187-242. For convenience, these regions will be called as regions A, B, and C afterwards in this section.

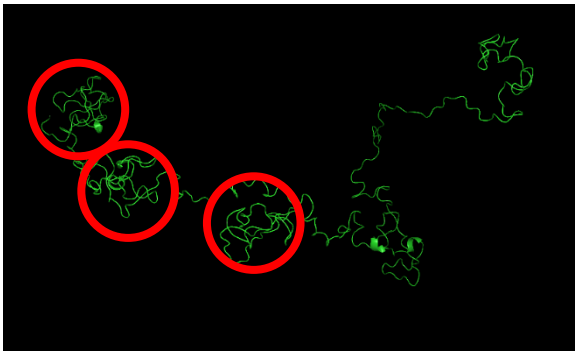

Figure A2.4: Cartoon representation of the PDB file of the initial structure. Regions A, B, and C are marked by red circles. Visualization by PyMol (DeLano, 2002).

While the tension is applied towards the -x direction, simultaneous unfolding begins to take place in these three regions. It is important to verify that both the systems with explicit and implicit solvation can capture similar trend of unfolding. Furthermore, the intermediary portions in between the regions A, B, C will be also unfolded or stretched, and these are to be considered as well. However, the folding situation is significantly different in case of implicit system, as the whole protein is shrunk on itself. To make a direct comparison, the gradual evolution of the equivalent portions will be tabulated.

	Explicit	Implicit
0%	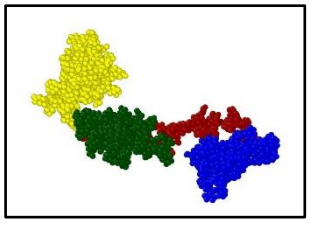	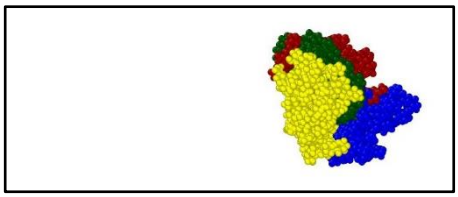

8%

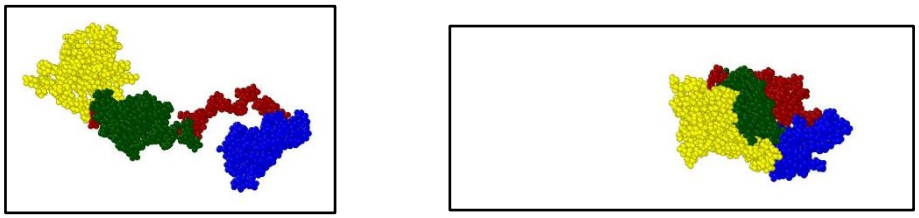

16%

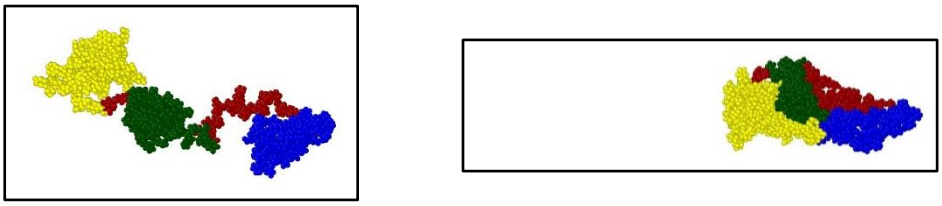

24%

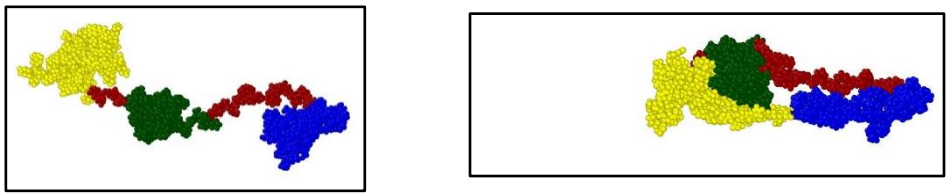

32%

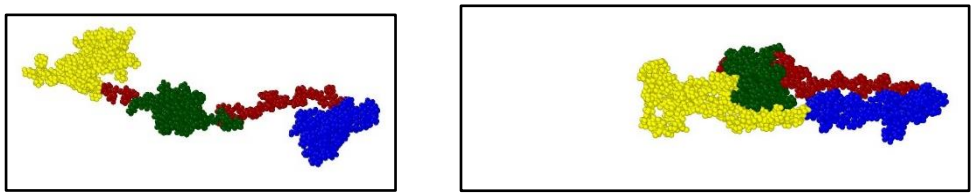

40%

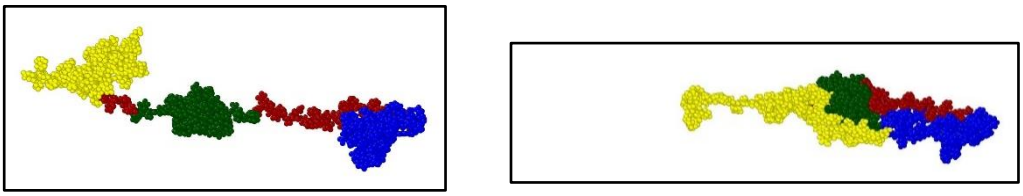

48%

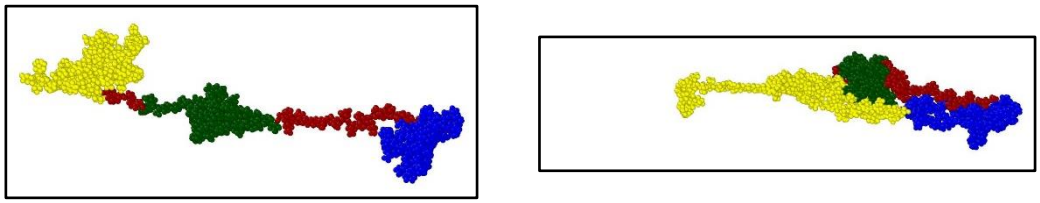

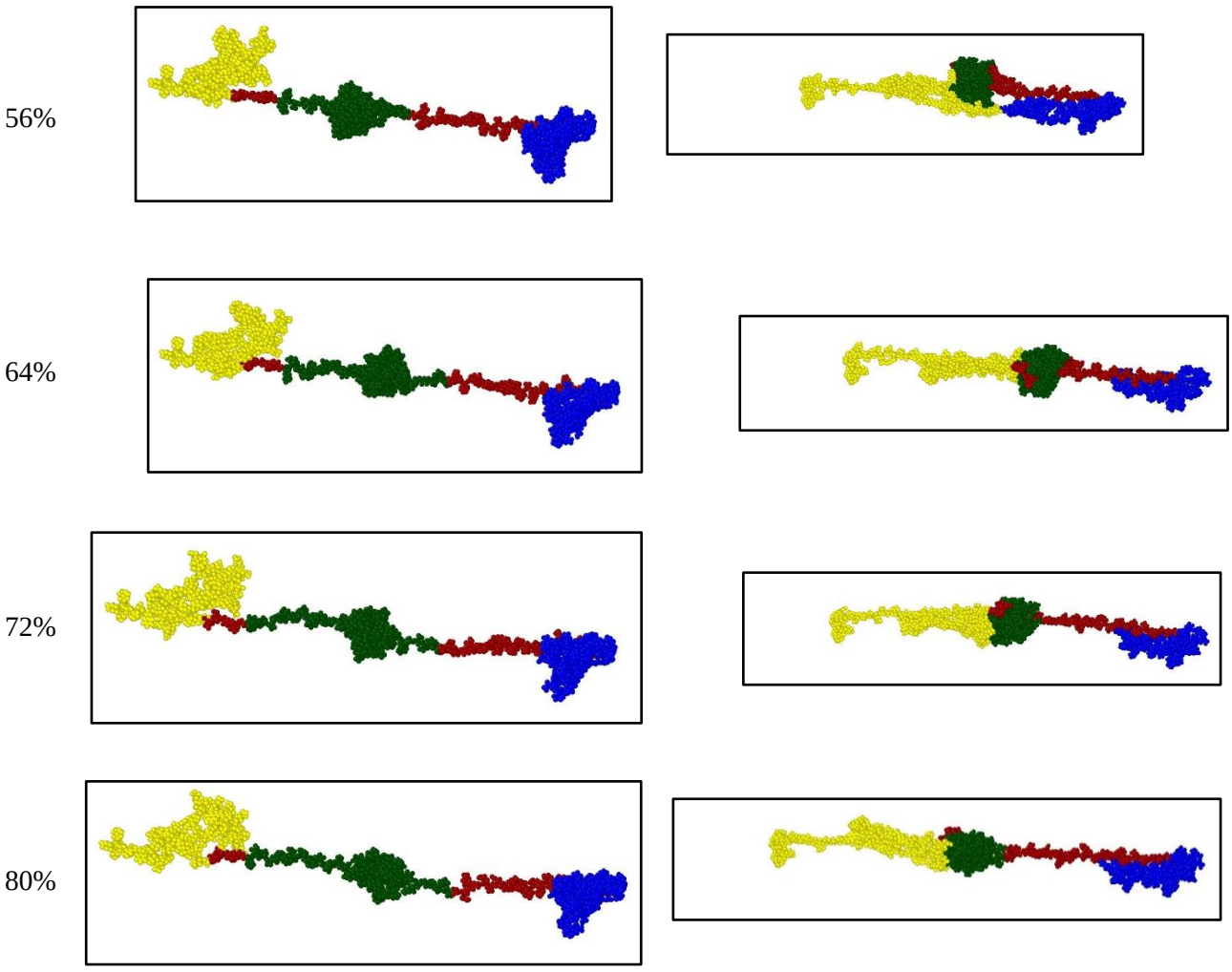

Figure A2.5: Tensile test: Structural snapshot of the tau protein for Left: explicit solvation, Right: implicit solvation. For the convenience of visualization, only the projection domain is shown. Legend: Yellow: First major fold, Green: second major fold, Blue: third major fold, Maroon: intermediary region between the major folded regions.

Now, Table A2.1 below summarizes the unfolding phenomena that take place for explicit and implicit solvation.

Table A2.1: Gradual Progression of Unfolding of Single Tau

Strain	Observation: Explicit	Observation: Implicit
0%	Initial	Initial
8%	A: initialization of unfolding, B: unfolding in multiple places, C: initialization of unfolding, Between A and B: straightening, Between B and C: straightening.	A: initialization of unfolding, B: initialization of unfolding, C: initialization of unfolding, Between A and B: initialization of unfolding, Between B and C: initialization of unfolding.
16%	A: visible unfolding, B: continued unfolding in multiple places, C: initialization of unfolding, Between A and B: visible unfolding, Between B and C: visible unfolding.	A: initialization of unfolding, B: initialization of unfolding, C: initialization of unfolding, Between A and B: initialization of unfolding, Between B and C: visible unfolding.
24%	A: visible unfolding, B: visible unfolding, C: initialization of unfolding, Between A and B: visible unfolding, Between B and C: visible unfolding.	A: visible unfolding, B: initialization of unfolding, C: initialization of unfolding, Between A and B: initialization of unfolding, Between B and C: significant unfolding.
32%	A: visible unfolding, B: visible unfolding, C: initialization of unfolding, Between A and B: significant unfolding, Between B and C: significant unfolding.	A: significant unfolding, B: initialization of unfolding, C: significant unfolding, Between A and B: initialization of unfolding, Between B and C: significant unfolding.
40%	A: significant unfolding, B: significant unfolding, C: visible unfolding,	A: significant unfolding, B: visible unfolding, C: visible unfolding,

	Between A and B: significant unfolding, Between B and C: significant unfolding.	Between A and B: visible unfolding, Between B and C: significant unfolding.
48%	A: significant unfolding, B: significant unfolding, C: significant unfolding, Between A and B: significant unfolding, Between B and C: significant unfolding.	A: significant unfolding, B: visible unfolding, C: visible unfolding, Between A and B: visible unfolding, Between B and C: significant unfolding.
56%	A: significant unfolding, B: significant unfolding, C: significant unfolding, Between A and B: significant unfolding, Between B and C: significant unfolding.	A: significant unfolding, B: significant unfolding, C: significant unfolding, Between A and B: visible unfolding, Between B and C: significant unfolding.
64%	A: significant unfolding, B: significant unfolding, C: significant unfolding, Between A and B: significant unfolding, Between B and C: significant unfolding.	A: significant unfolding, B: significant unfolding, C: significant unfolding, Between A and B: significant unfolding, Between B and C: significant unfolding.
72%	A: significant unfolding, B: significant unfolding, C: significant unfolding, Between A and B: significant unfolding, Between B and C: significant unfolding.	A: significant unfolding, B: significant unfolding, C: significant unfolding, Between A and B: significant unfolding, Between B and C: significant unfolding.
80%	A: significant unfolding, B: significant unfolding, C: significant unfolding,	A: significant unfolding, B: significant unfolding, C: significant unfolding,

	Between A and B: significant unfolding, Between B and C: significant unfolding.	Between A and B: significant unfolding, Between B and C: significant unfolding.

From Table A2.1 it is evident that the unfolding mechanism differs between the explicit and implicit system for up to 56% strain which can be attributed to the difference in the initial structure. For explicit system, the A, B, and C regions are well-separated from each other by the intermediary region. However, for implicit system, the A, B, and C are not well-separated due to the shrinkage of the projection domain. It takes up to 56% strain to unfold and get separated from each other for the regions. This is expected because it is already substantiated that during equilibration the projection domain faces shrinkage of ~57.2% of its length. After that, it can be observed that all the A, B, and C regions as well as intermediary regions reach "significant unfolding" state for both explicit and implicit system. This structural evolution analysis depicts that both systems predict the similar mechanical behavior after their orientations become similar after a certain stretch (~56%).

The only issue remaining is the difference between the stress-strain values in the systems with explicit vs implicit solvation. This discrepancy can be resolved if it is considered that in implicit system, the solvent-surface charged layer interaction is absent. However, the internal stress component can be obtained from the surface force. If it is considered that the tau protein single strand radius is approximately 0.5nm (Ruben et al., 1993), then the area on which the surface force is acting can be calculated. The area multiplied by the surface tension will be equal to the surface force at static equilibrium. Therefore, we can write,

$$F = 2\pi r\gamma = -\sigma_x(\pi r^2), \text{or } \sigma_x = -\frac{2\gamma}{r} \quad \textbf{(A2.1)}$$

Now, despite having significant charge difference along the filament length, the tau protein surface interacts with weakly hydrophilic MT surface, and therefore, the surface tension of tau protein surface can be approximated with that of water, which is 0.072N/m at 310K. Putting this value in the above equation,

it can be calculated that σ_x=-288MPa, which is ignored in the implicit solvation system. After adding this amount of stress with the stress values calculated for the implicit system and then plotting with the explicit system values, it can be observed that the stress values are remarkably close (Figure A2.6). The slight difference can certainly be attributed to the difference of conformation of the projection domain. Therefore, it can be concluded that if the surface force is included to the calculation, both explicit and implicit systems will show nearly the same stress-strain relation.

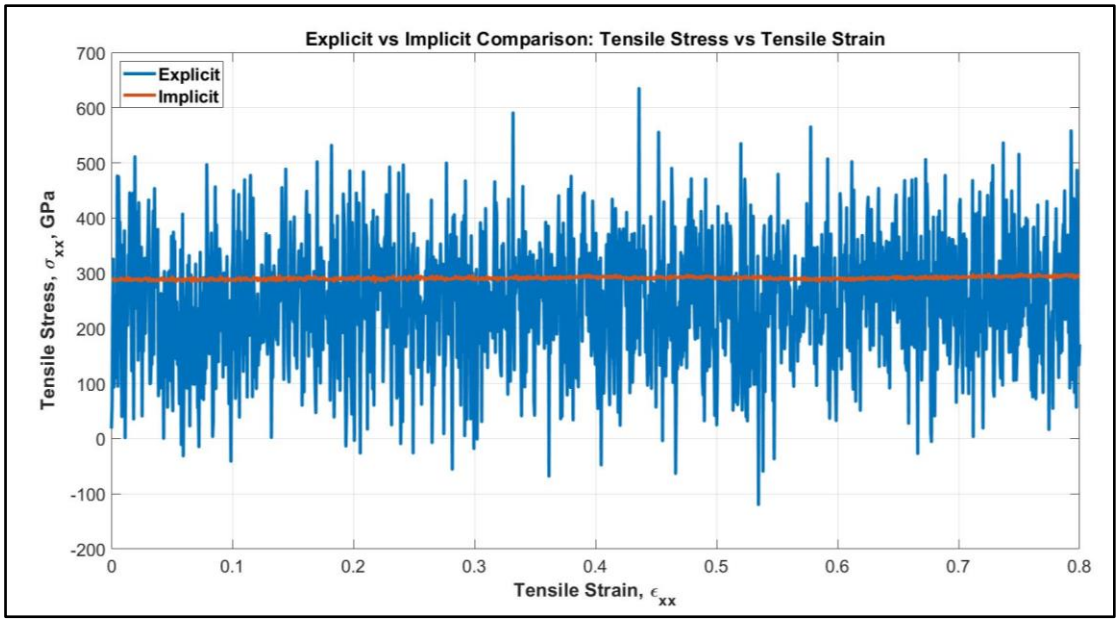

Figure A2.6: Comparison between the explicit and implicit system stress-strain relation after considering the correction originated from calculating the surface force.

Therefore, despite the constraints that must be dealt with in molecular dynamics simulation, the implicit simulations for single tau protein, dimerized tau protein, and tau-MT interaction system are providing important insight regarding the behavior of tau protein from strictly mechanical viewpoint which is relevant from traumatic brain injury (TBI) perspective, and the first of its kind. The difference between the explicit

and implicit system behaviors can be compensated by including the surface force to the calculation. To the best knowledge of the authors, this work has particularly shed light on strain-rate dependent behavior of tau protein in polymerized state, and highlighted different damage mechanisms in sub-axonal level, which were not explored entirely in earlier studies.

APPENDIX 3

i-TASSER Predicted Models: Reliability of Independently Predicted Structures

When an amino acid sequence is submitted to i-TASSER server, it produces five (5) models with reliability score at descending order. It is relevant to determine to test the stability of independently predicted models under the same equilibration and tensile condition to determine whether a particular model with a particular reliability score is representative. We have, therefore, compared the potential energy vs time for equilibration of two models of single tau protein (Model 1 and Model 2, both with C-score of -0.03). Later, we have carried out tensile test to find out whether the two models show similar trend of tensile stress vs strain (up to 80% strain, at applied strain rate = $1x10^{9}s^{-1}$). If in both cases they show similar values, we can be sure that the C-score is reliable, and that independently predicted structures with similar C-score are similar, both with respect to stability and mechanical behavior. Fig. A3.1 and A3.2 depict our finding. The methodology is the same as Chapter 2.

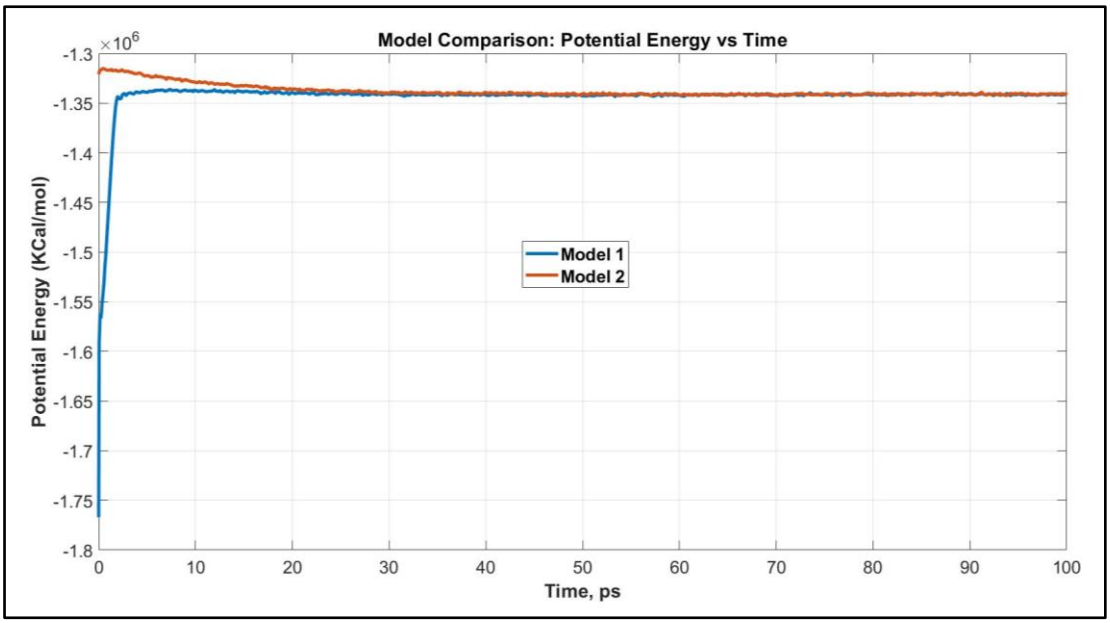

Figure A3.1: Potential energy vs time for two models. We find that potential energy for both models converge towards similar value over time.

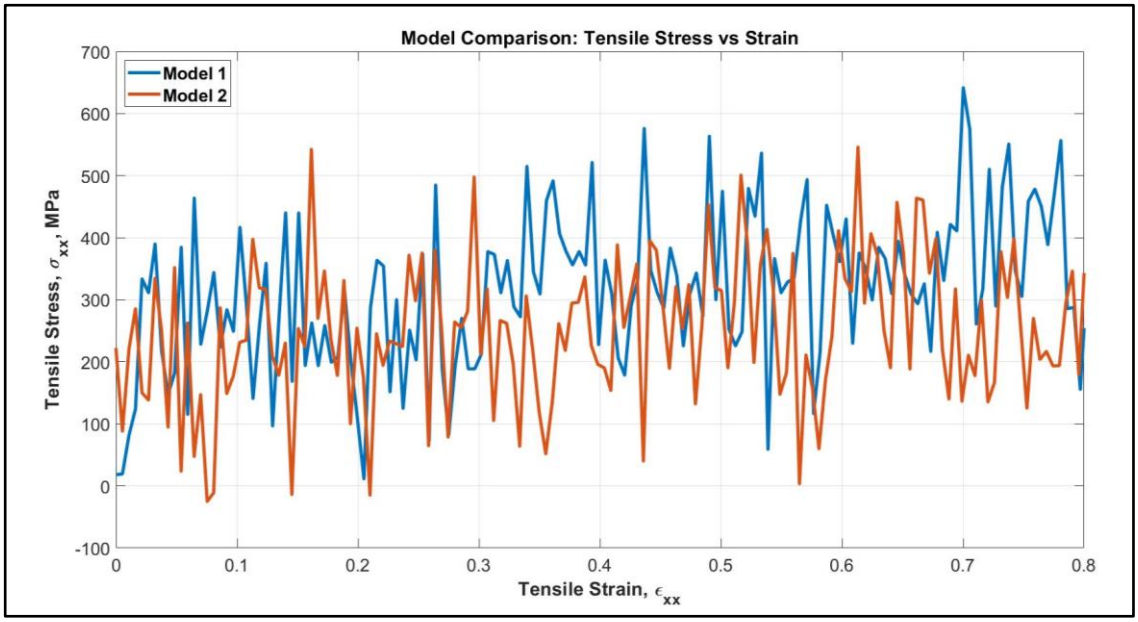

Figure A3.2: Tensile stress vs strain for two models. We find that they show similar trend after initial discrepancies. The slight variation can be attributed to unconstrained movement in the space. Linear fit shows that for up to 80% strain, the unfolding stiffness for Model 1 is ~227MPa, while for Model 2 is ~126MPa, which are very comparable.

From Fig. A3.1 and Fig. A3.2, it is evident that two independently predicted models of single tau protein show similar stability and mechanical behavior, which strengthens the reliability of the C-score of our predicted model, and justifies using the model with highest C-score in our studies.

APPENDIX 4

Potential Energy vs Time Graphs for Phosphorylation Effect on Tau

We have plotted potential energy vs time for the dimerized tau, tau-MT, and tau accumulation test for both normal and phosphorylated systems. For dimerized tau and tau-MT systems, these curves are plotted to determine whether any energetical artifacts generate due to the separation of tau from tau or tau from MT surface. In the accumulation test, we plot potential energy vs time to ensure that both systems are well equilibrated. In this appendix, the potential energy vs time graphs are presented.

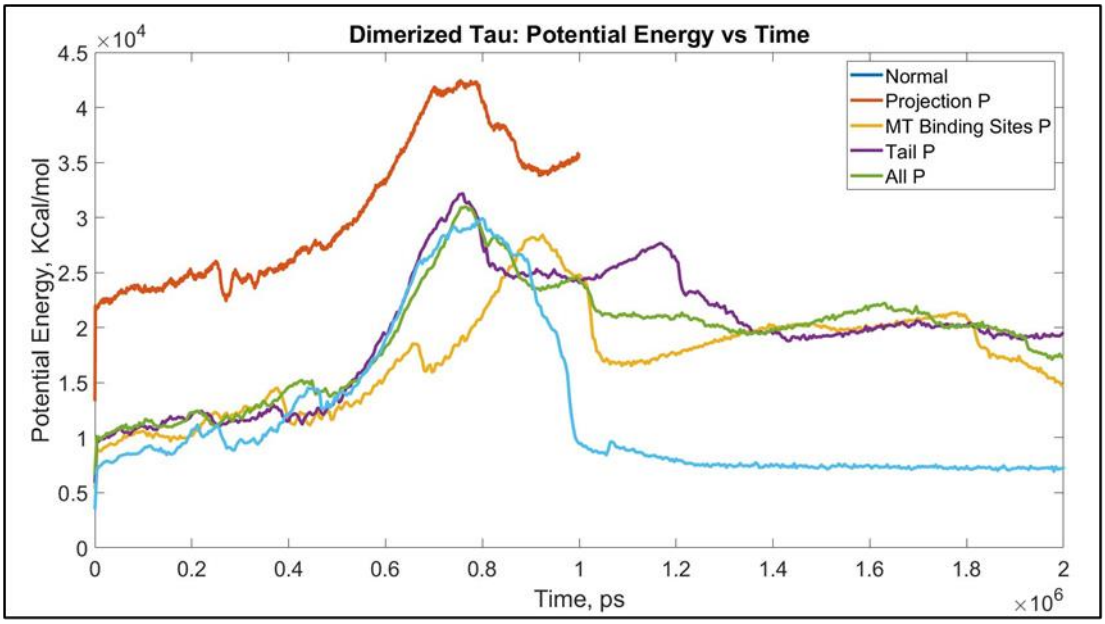

Figure A4.1: Dimerized tau: potential energy vs time for the domain phosphorylated systems.

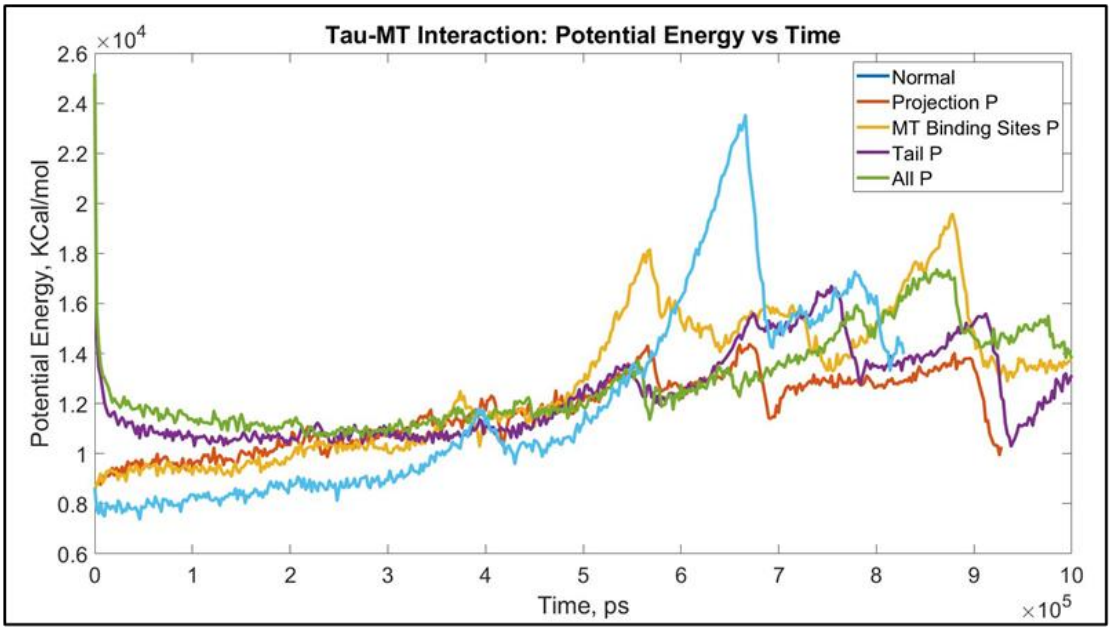

Figure A4.2: Tau-MT interaction: potential energy vs time for the domain phosphorylated systems.

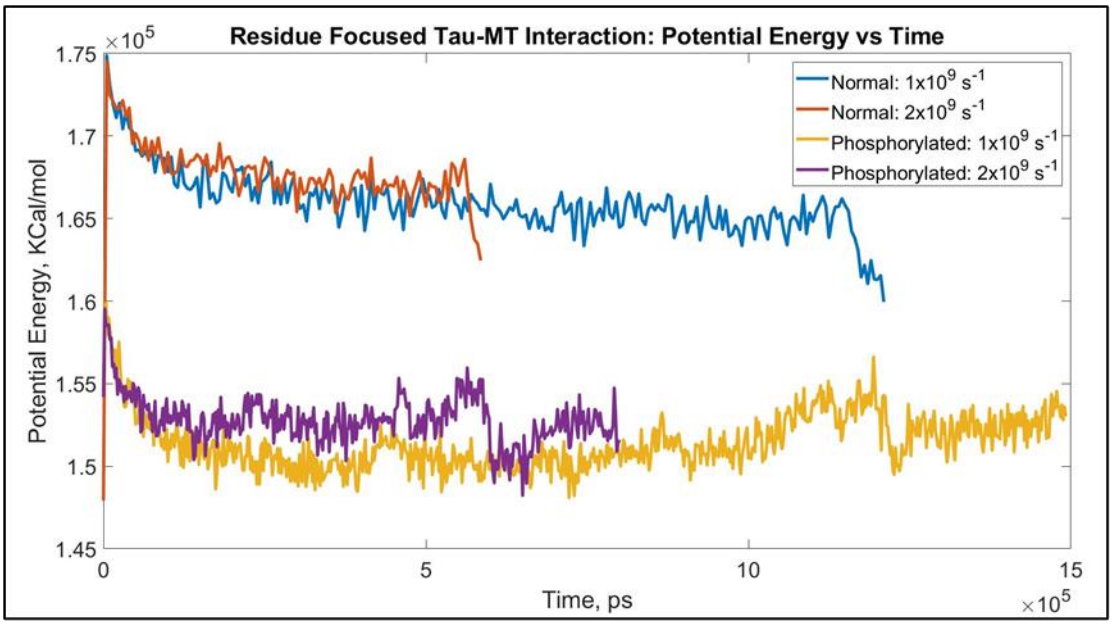

Figure A4.3: Tau-MT interaction: potential energy vs time for the residue phosphorylated systems.

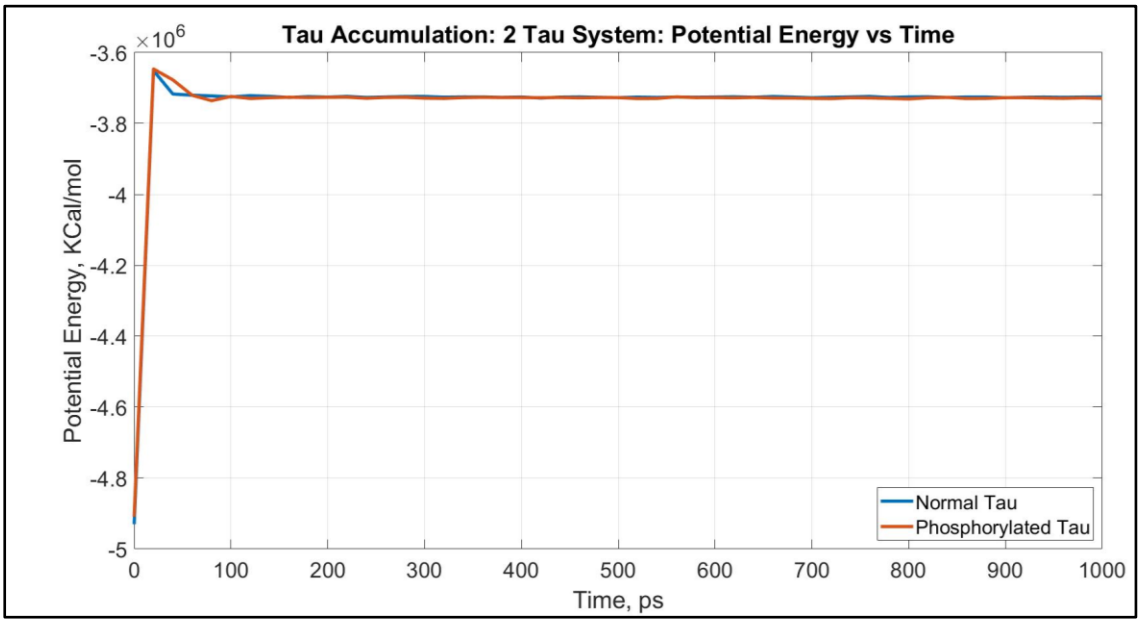

Figure A4.4: Tau accumulation test: 2 tau system: potential energy vs time during the 1ns equilibration.

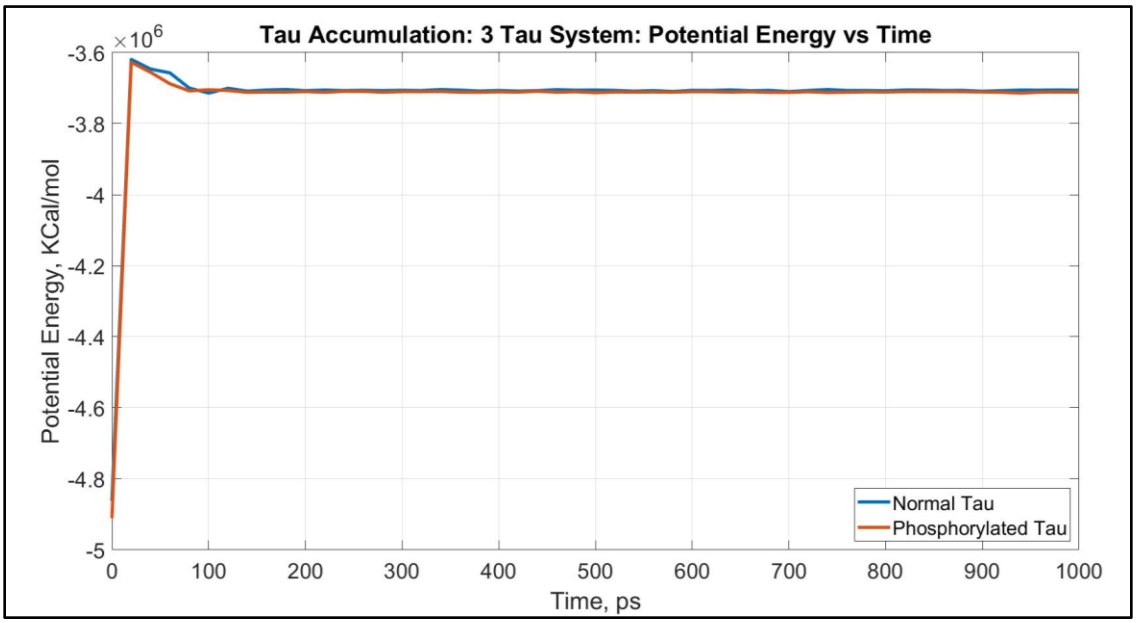

Figure A4.5: Tau accumulation test: 3 tau system: potential energy vs time during the 1ns equilibration.

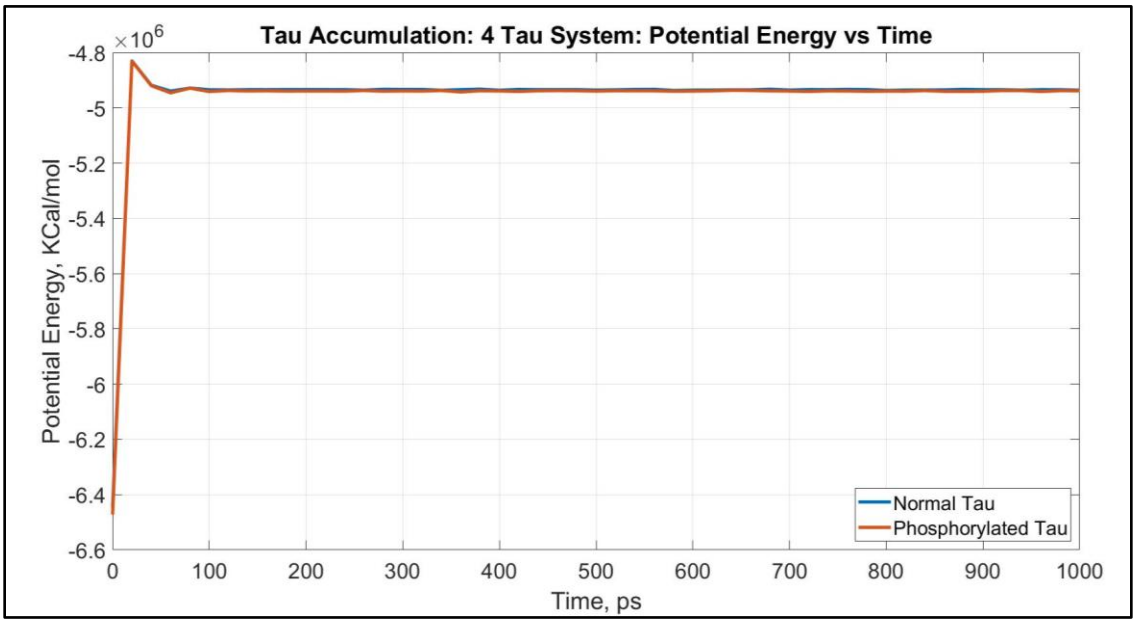

Figure A4.6: Tau accumulation test: 4 tau system: potential energy vs time during the 1ns NVT equilibration.

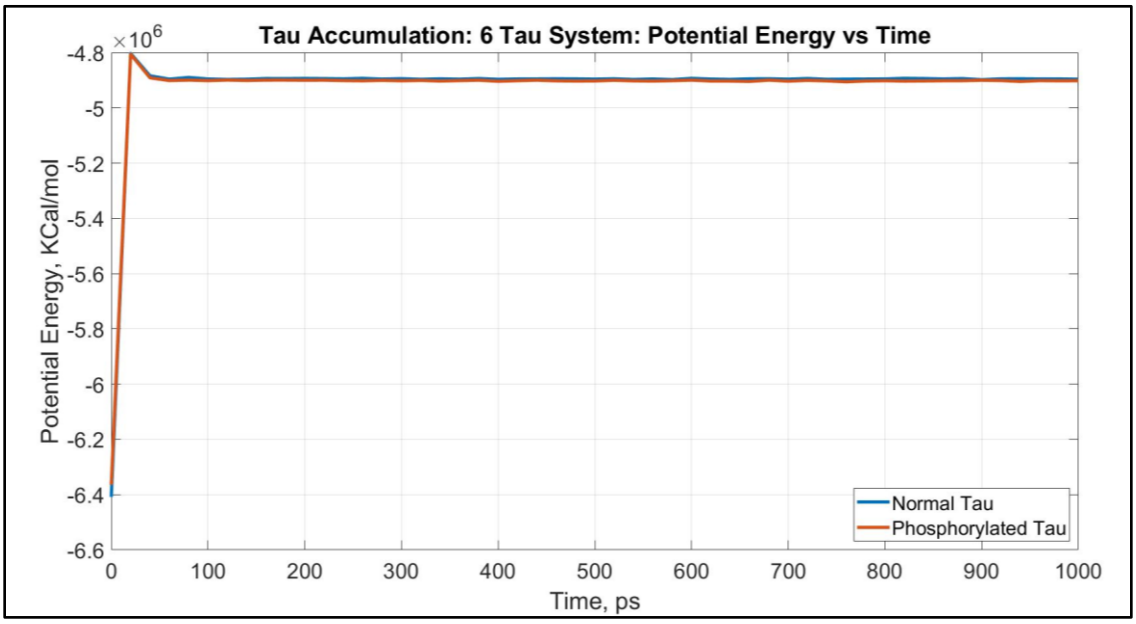

Figure A4.7: Tau accumulation test: 6 tau system: potential energy vs time during the 1ns NVT equilibration.

APPENDIX 5

Comparison Between CHARMM and OPLS Results: Tensile Test on α-Spectrin

To compare CHARMM with respect to OPLS, two identical models are created for α-spectrin, and the tensile test is performed at strain rate $1x10^{8}s^{-1}$ as per the "Method" section in this manuscript. Figure A5.1 shows the stress-strain response for both force fields, which depicts that both force fields similar results. Furthermore, Figure A5.2 shows that both CHARMM and OPLS shows similar manner of unfolding in α-spectrin. Considering these findings, it can be concluded that both force fields are equally eligible candidates for such simulations.

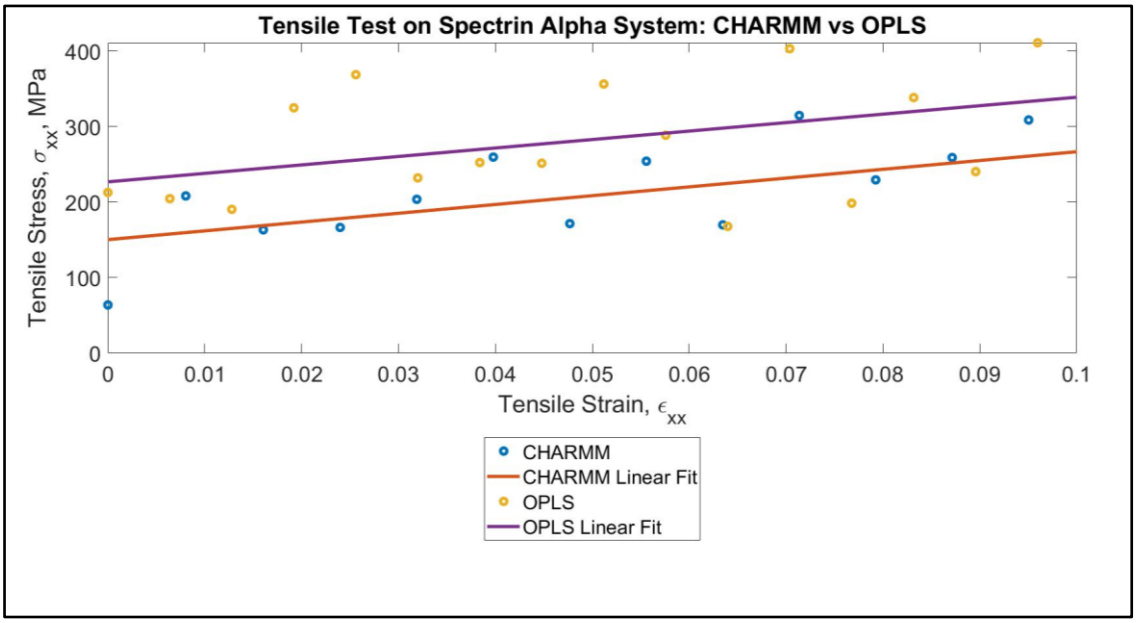

Figure A5.1: Comparison between CHARMM and OPLS tensile test results for α-spectrin. For CHARMM, the stiffness is 1164MPa, while for OPLS, it is 1120MPa.

0%

5%

10%

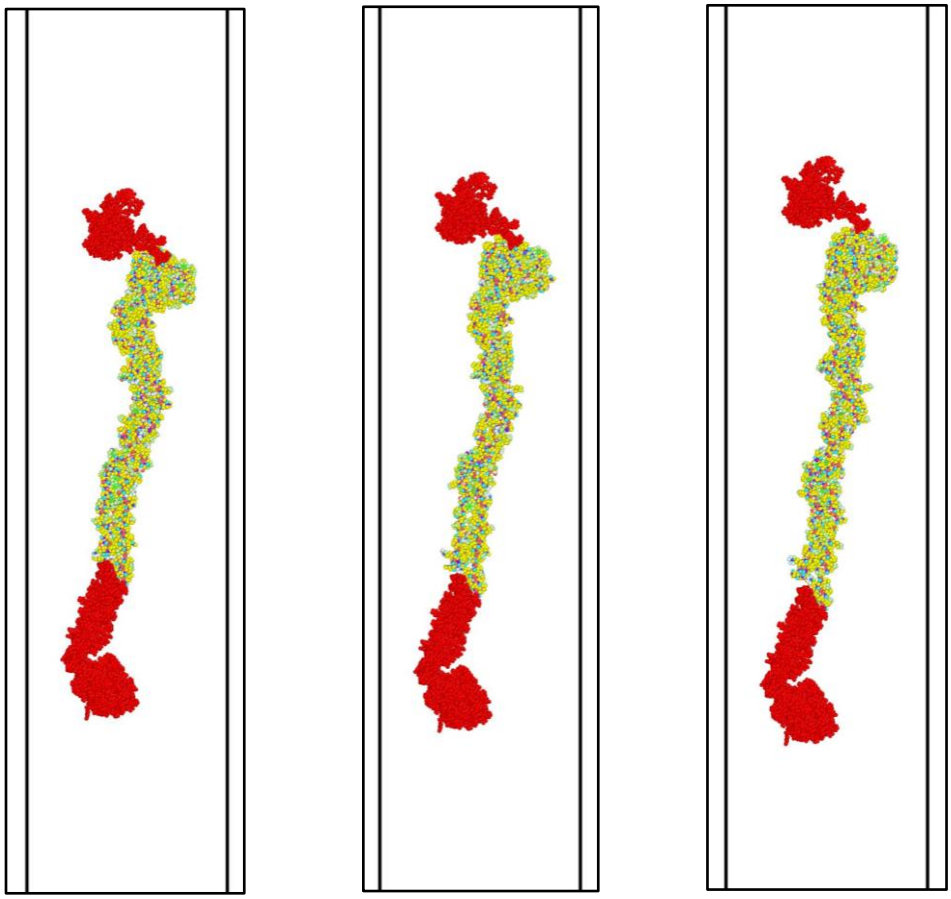

a

b

c

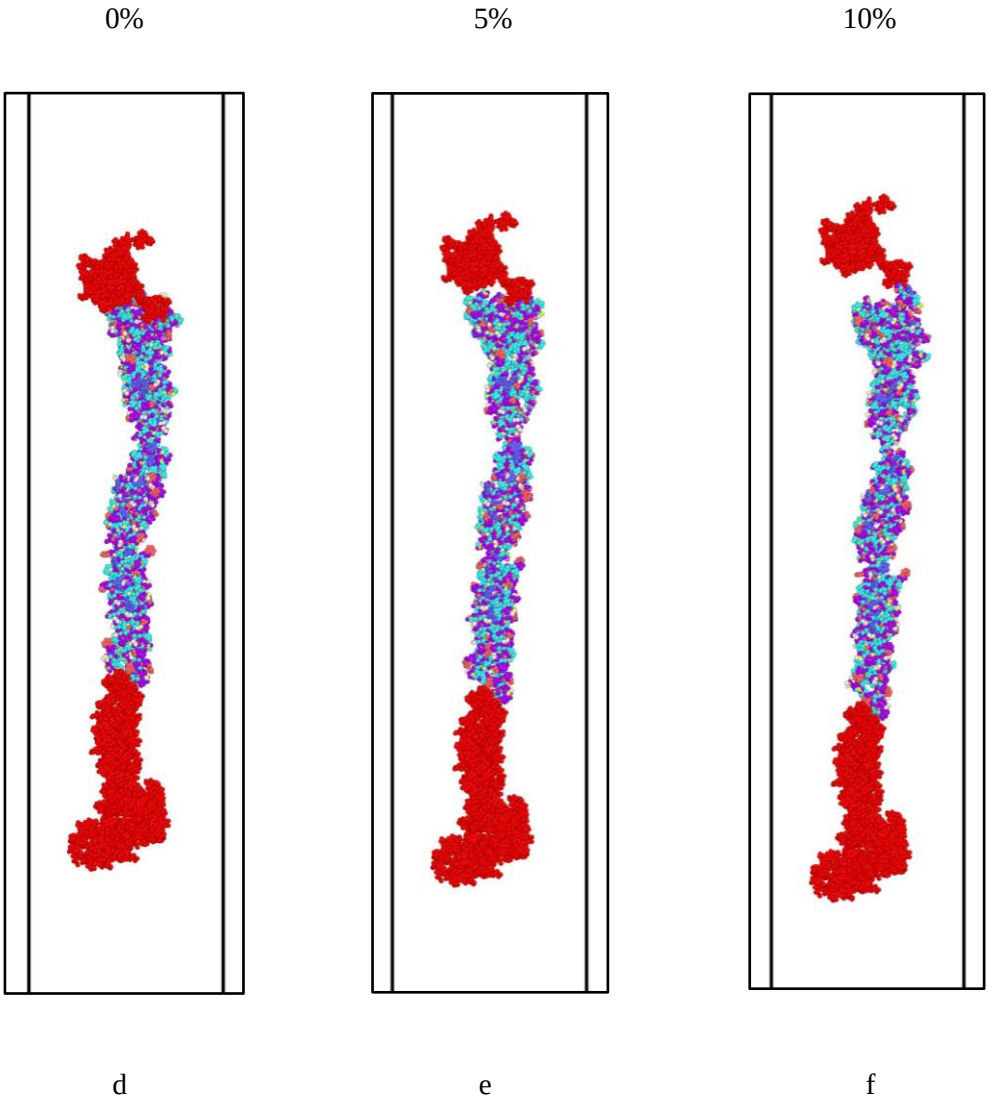

Figure A5.2: Tensile test snapshots at 0%, 5%, and 10% strain for α-spectrin created by a-c) OPLS, d-f) CHARMM. Atoms being pulled are shown in red color. For the rest, the default coloring by OVITO is retained.

REFERENCES

REFERENCES

Aamodt, E.J., Williams Jr, R.C., 1984a. Microtubule-associated proteins connect microtubules and neurofilaments in vitro. Biochemistry 23, 6023–6031.

Aamodt, E.J., Williams Jr, R.C., 1984b. Association of microtubules and neurofilaments in vitro is not mediated by ATP. Biochemistry 23, 6031–6035.

Abouelezz, A., 2020. The Structure and Dynamics of the Actin Cytoskeleton in the Axon Initial Segment. Diss. Sch. Dr. ad Sanit. Investig. Univ. Hels.

Ackerley, S., Thornhill, P., Grierson, A.J., Brownlees, J., Anderton, B.H., Leigh, P.N., Shaw, C.E., Miller, C.C.J., 2003. Neurofilament heavy chain side arm phosphorylation regulates axonal transport of neurofilaments. J. Cell Biol. 161, 489–495.

Adiga, S.P., Brenner, D.W., 2010. Molecular Basis for Neurofilament Heavy Chain Side Arm Structure Modulation by Phosphorylation. J. Phys. Chem. C 114, 5410–5416. https://doi.org/10.1021/jp905671u

Adnan, A., Qidwai, S., Bagchi, A., 2018. On the atomistic-based continuum viscoelastic constitutive relations for axonal microtubules. J. Mech. Behav. Biomed. Mater. 86, 375–389.

ADNAN, A., QIDWAI, S., BAGCHI, A., 2015. Viscoelastic Response of Microtubule—Tau Proteins Assembly During Axonal Stretch: Combined Atomistic and Continuum Predictions, in: American Society of Composites-30th Technical Conference.

Ahmadzadeh, H., Smith, D.H., Shenoy, V.B., 2015. Mechanical effects of dynamic binding between tau proteins on microtubules during axonal injury. Biophys. J. 109, 2328–2337.

Ahmadzadeh, H., Smith, D.H., Shenoy, V.B., 2014. Viscoelasticity of Tau Proteins Leads to Strain Rate-Dependent Breaking of Microtubules during Axonal Stretch Injury: Predictions from a Mathematical Model. Biophys. J. 106, 1123–1133. https://doi.org/https://doi.org/10.1016/j.bpj.2014.01.024

Akola, J., Jones, R.O., 2006. Density functional calculations of ATP systems. 2. ATP hydrolysis at the active site of actin. J. Phys. Chem. B 110, 8121–8129.

Al-Bassam, J., Ozer, R.S., Safer, D., Halpain, S., Milligan, R.A., 2002. MAP2 and tau bind longitudinally along the outer ridges of microtubule protofilaments. J. Cell Biol. 157, 1187–1196.

Albert, M.P., 2017. Cell biology. Cell 7.

Alonso, A. del C., Mederlyova, A., Novak, M., Grundke-Iqbal, I., Iqbal, K., 2004. Promotion of hyperphosphorylation by frontotemporal dementia tau mutations. J. Biol. Chem. 279, 34873–34881.

Altmann, S.M., Grünberg, R.G., Lenne, P.-F., Ylänne, J., Raae, A., Herbert, K., Saraste, M., Nilges, M., Hörber, J.K.H., 2002. Pathways and intermediates in forced unfolding of spectrin repeats. Structure 10, 1085–1096.

An, L., Gao, Y., 2010. Mechanics behavior of microtubules based on nonlocal anisotropic shell theory. IOP Conf. Ser. Mater. Sci. Eng. 10, 12181. https://doi.org/10.1088/1757-899x/10/1/012181

An, X., Lecomte, M.C., Chasis, J.A., Mohandas, N., Gratzer, W., 2002. Shear-response of the spectrin dimer-tetramer equilibrium in the red blood cell membrane. J. Biol. Chem. 277, 31796–31800.

Aranda-Espinoza, H., Carl, P., Leterrier, J.-F., Janmey, P., Discher, D.E., 2002. Domain unfolding in neurofilament sidearms: effects of phosphorylation and ATP. FEBS Lett. 531, 397–401.

Asakura, S., Taniguchi, M., Oosawa, F., 1963. Mechano-chemical behaviour of F-actin. J. Mol. Biol. 7, 55–69.

Avila, J., 1990. Microtubule dynamics. FASEB J. 4, 3284–3290. https://doi.org/10.1096/fasebj.4.15.2253844

Baines, A.J., 2009. Evolution of spectrin function in cytoskeletal and membrane networks. Biochem. Soc. Trans. 37, 796–803.

Ballatore, C., Lee, V.M.-Y., Trojanowski, J.Q., 2007. Tau-mediated neurodegeneration in Alzheimer's disease and related disorders. Nat. Rev. Neurosci. 8, 663.

Bär, J., Kobler, O., Van Bommel, B., Mikhaylova, M., 2016. Periodic F-actin structures shape the neck of dendritic spines. Sci. Rep. 6, 1–9.

Barabas, F.M., Masullo, L.A., Bordenave, M.D., Giusti, S.A., Unsain, N., Refojo, D., Cáceres, A., Stefani, F.D., 2017. Automated quantification of protein periodic nanostructures in fluorescence nanoscopy images: abundance and regularity of neuronal spectrin membrane-associated skeleton. Sci. Rep. 7, 1–10.

Barreto, S., Clausen, C.H., Perrault, C.M., Fletcher, D.A., Lacroix, D., 2013. A multi-structural single cell model of force-induced interactions of cytoskeletal components. Biomaterials 34, 6119–6126.

Bathe, M., Heussinger, C., Claessens, M.M.A.E., Bausch, A.R., Frey, E., 2008. Cytoskeletal Bundle Mechanics. Biophys. J. 94, 2955–2964. https://doi.org/https://doi.org/10.1529/biophysj.107.119743

Battisti, A., Ciasca, G., Grottesi, A., Bianconi, A., Tenenbaum, A., 2012. Temporary secondary structures in tau, an intrinsically disordered protein. Mol. Simul. 38, 525–533.

Battisti, A., Tenenbaum, A., 2012. Molecular dynamics simulation of intrinsically disordered proteins. Mol. Simul. 38, 139–143.

Baudier, J., Cole, R.D., 1987. Phosphorylation of tau proteins to a state like that in Alzheimer's brain is catalyzed by a calcium/calmodulin-dependent kinase and modulated by phospholipids. J. Biol. Chem. 262, 17577–17583.

Beck, R., Deek, J., Safinya, C.R., 2012. Structures and interactions in 'bottlebrush'neurofilaments: the role of charged disordered proteins in forming hydrogel networks.

Becker, J.S., Przybylski, M., 2007. Studies of structure and phosphorylation of tau protein using high resolution mass spectrometry. J. Anal. At. Spectrom. 22, 761–765.

ben-Avraham, D., Tirion, M.M., 1995. Dynamic and elastic properties of F-actin: a normal-modes analysis. Biophys. J. 68, 1231–1245. https://doi.org/https://doi.org/10.1016/S0006-3495(95)80299-7

Berro, J., Michelot, A., Blanchoin, L., Kovar, D.R., Martiel, J.-L., 2007. Attachment conditions control actin filament buckling and the production of forces. Biophys. J. 92, 2546–2558.

Best, R.B., Zhu, X., Shim, J., Lopes, P.E.M., Mittal, J., Feig, M., MacKerell, A.D., 2012. Optimization of the Additive CHARMM All-Atom Protein Force Field Targeting Improved Sampling of the Backbone ϕ, ψ and Side-Chain $\chi 1$ and $\chi 2$ Dihedral Angles. J. Chem. Theory Comput. 8, 3257–3273. https://doi.org/10.1021/ct300400x

Biernat, J., Gustke, N., Drewes, G., Mandelkow, E., 1993. Phosphorylation of Ser262 strongly reduces binding of tau to microtubules: distinction between PHF-like immunoreactivity and microtubule binding. Neuron 11, 153–163.

Biernat, J., Mandelkow, E.M., Schröter, C., Lichtenberg-Kraag, B., Steiner, B., Berling, B., Meyer, H., Mercken, M., Vandermeeren, A., Goedert, M., 1992. The switch of tau protein to an Alzheimer-like state includes the phosphorylation of two serine-proline motifs upstream of the microtubule binding region. EMBO J. 11, 1593–1597.

Billingsley, M.L., Kincaid, R.L., 1997. Regulated phosphorylation and dephosphorylation of tau protein: effects on microtubule interaction, intracellular trafficking and neurodegeneration. Biochem. J. 323, 577–591.

Bocquet, A., Berges, R., Frank, R., Robert, P., Peterson, A.C., Eyer, J., 2009. Neurofilaments bind tubulin

and modulate its polymerization. J. Neurosci. 29, 11043–11054.

Bramblett, G.T., Goedert, M., Jakes, R., Merrick, S.E., Trojanowski, J.Q., Lee, V.M.Y., 1993. Abnormal tau phosphorylation at Ser396 in Alzheimer's disease recapitulates development and contributes to reduced microtubule binding. Neuron 10, 1089–1099.

Brandt, R., Lee, G., 1993. Functional organization of microtubule-associated protein tau. Identification of regions which affect microtubule growth, nucleation, and bundle formation in vitro. J. Biol. Chem. 268, 3414–3419.

Brinson, H.F., Brinson, L.C., 2015. Polymer engineering science and viscoelasticity. Springer.

Brooks, B.R., Brooks III, C.L., Mackerell Jr., A.D., Nilsson, L., Petrella, R.J., Roux, B., Won, Y., Archontis, G., Bartels, C., Boresch, S., Caflisch, A., Caves, L., Cui, Q., Dinner, A.R., Feig, M., Fischer, S., Gao, J., Hodoscek, M., Im, W., Kuczera, K., Lazaridis, T., Ma, J., Ovchinnikov, V., Paci, E., Pastor, R.W., Post, C.B., Pu, J.Z., Schaefer, M., Tidor, B., Venable, R.M., Woodcock, H.L., Wu, X., Yang, W., York, D.M., Karplus, M., 2009. CHARMM: The biomolecular simulation program. J. Comput. Chem. 30, 1545–1614. https://doi.org/10.1002/jcc.21287

Brureau, A., Blanchard-Bregeon, V., Pech, C., Hamon, S., Chaillou, P., Guillemot, J.-C., Barneoud, P., Bertrand, P., Pradier, L., Rooney, T., 2017. NF-L in cerebrospinal fluid and serum is a biomarker of neuronal damage in an inducible mouse model of neurodegeneration. Neurobiol. Dis. 104, 73–84.

Buck, M., Bouguet-Bonnet, S., Pastor, R.W., MacKerell, A.D., 2006. Importance of the CMAP Correction to the CHARMM22 Protein Force Field: Dynamics of Hen Lysozyme. Biophys. J. 90, L36–L38. https://doi.org/https://doi.org/10.1529/biophysj.105.078154

Buée, L., Bussière, T., Buée-Scherrer, V., Delacourte, A., Hof, P.R., 2000. Tau protein isoforms, phosphorylation and role in neurodegenerative disorders. Brain Res. Rev. 33, 95–130.

Buehler, M.J., Ackbarow, T., 2007. Fracture mechanics of protein materials. Mater. Today 10, 46–58.

Buerger, K., Zinkowski, R., Teipel, S.J., Tapiola, T., Arai, H., Blennow, K., Andreasen, N., Hofmann-Kiefer, K., DeBernardis, J., Kerkman, D., 2002. Differential diagnosis of Alzheimer disease with cerebrospinal fluid levels of tau protein phosphorylated at threonine 231. Arch. Neurol. 59, 1267–1272.

Burns, N.R., Ohanian, V., Gratzer, W.B., 1983. Properties of brain spectrin (fodrin). FEBS Lett. 153, 165–168.

CALVERT, R., BENNETT, P., GRATZER, W., 1980. Properties and structural role of the subunits of human spectrin. Eur. J. Biochem. 107, 355–361.

Carden, M.J., Schlaepfer, W.W., Lee, V.M., 1985. The structure, biochemical properties, and immunogenicity of neurofilament peripheral regions are determined by phosphorylation state. J. Biol. Chem. 260, 9805–9817.

Carpenter, E.J., Huzil, J.T., Ludueña, R.F., Tuszynski, J.A., 2006. Homology modeling of tubulin: influence predictions for microtubule's biophysical properties. Eur. Biophys. J. 36, 35–43. https://doi.org/10.1007/s00249-006-0088-0

Castro, T.G., Munteanu, F.-D., Cavaco-Paulo, A., 2019. Electrostatics of tau protein by molecular dynamics. Biomolecules 9, 116.

Chandran, P.L., Mofrad, M.R.K., 2009. Rods-on-string idealization captures semiflexible filament dynamics. Phys. Rev. E 79, 11906. https://doi.org/10.1103/PhysRevE.79.011906

Chang, R., Kwak, Y., Gebremichael, Y., 2009. Structural properties of neurofilament sidearms: sequence-based modeling of neurofilament architecture. J. Mol. Biol. 391, 648–660.

Chau, M.-F., Radeke, M.J., de Inés, C., Barasoain, I., Kohlstaedt, L.A., Feinstein, S.C., 1998. The microtubule-associated protein tau cross-links to two distinct sites on each α and β tubulin monomer via separate domains. Biochemistry 37, 17692–17703.

Chen, J., Brooks III, C.L., Khandogin, J., 2008. Recent advances in implicit solvent-based methods for biomolecular simulations. Curr. Opin. Struct. Biol. 18, 140–148.

Chen, J., Kanai, Y., Cowan, N.J., Hirokawa, N., 1992. Projection domains of MAP2 and tau determine spacings between microtubules in dendrites and axons. Nature 360, 674–677. https://doi.org/10.1038/360674a0

Chen, T., 2000. Determining a prony series for a viscoelastic material from time strain data. US Army Res. Lab. May 1–26.

Christensen, R.M., n.d. Theory of viscoelasticity: an introduction. 1982.

Chu, J.-W., Voth, G.A., 2006. Coarse-grained modeling of the actin filament derived from atomistic-scale simulations. Biophys. J. 90, 1572–1582.

Chu, J.-W., Voth, G.A., 2005. Allostery of actin filaments: molecular dynamics simulations and coarse-grained analysis. Proc. Natl. Acad. Sci. 102, 13111–13116.

Chung, R.S., Staal, J.A., McCormack, G.H., Dickson, T.C., Cozens, M.A., Chuckowree, J.A., Quilty, M.C., Vickers, J.C., 2005. Mild axonal stretch injury in vitro induces a progressive series of neurofilament alterations ultimately leading to delayed axotomy. J. Neurotrauma 22, 1081–1091.

Churcher, I., 2006. Tau therapeutic strategies for the treatment of Alzheimer's disease. Curr. Top. Med. Chem. 6, 579–595.

Cifuentes-Diaz, C., Nicole, S., Velasco, M.E., Borra-Cebrian, C., Panozzo, C., Frugier, T., Millet, G., Roblot, N., Joshi, V., Melki, J., 2002. Neurofilament accumulation at the motor endplate and lack of axonal sprouting in a spinal muscular atrophy mouse model. Hum. Mol. Genet. 11, 1439–1447. https://doi.org/10.1093/hmg/11.12.1439

Civalek, Ö., Demir, C., 2016. A simple mathematical model of microtubules surrounded by an elastic matrix by nonlocal finite element method. Appl. Math. Comput. 289, 335–352.

Civalek, Ö., Demir, Ç., 2011. Bending analysis of microtubules using nonlocal Euler–Bernoulli beam theory. Appl. Math. Model. 35, 2053–2067. https://doi.org/https://doi.org/10.1016/j.apm.2010.11.004

Claessens, M.M.A.E., Bathe, M., Frey, E., Bausch, A.R., 2006. Actin-binding proteins sensitively mediate F-actin bundle stiffness. Nat. Mater. 5, 748–753. https://doi.org/10.1038/nmat1718

Cleveland, D.W., Hwo, S.-Y., Kirschner, M.W., 1977. Physical and chemical properties of purified tau factor and the role of tau in microtubule assembly. J. Mol. Biol. 116, 227–247.

Cloots, R.J.H., Van Dommelen, J.A.W., Kleiven, S., Geers, M.G.D., 2010. Traumatic brain injury at multiple length scales: relating diffuse axonal injury to discrete axonal impairment, in: Proceedings of IRCOBI Conference. pp. 119–130.

Cloots, R.J.H., Van Dommelen, J.A.W., Nyberg, T., Kleiven, S., Geers, M.G.D., 2011. Micromechanics of diffuse axonal injury: influence of axonal orientation and anisotropy. Biomech. Model. Mechanobiol. 10, 413–422.

Coles, C.H., Bradke, F., 2015. Coordinating neuronal actin–microtubule dynamics. Curr. Biol. 25, R677–R691.

Costa, A.R., Pinto-Costa, R., Sousa, S.C., Sousa, M.M., 2018. The regulation of axon diameter: from axonal circumferential contractility to activity-dependent axon swelling. Front. Mol. Neurosci. 11, 319.

Cozzetto, D., Kryshtafovych, A., Ceriani, M., Tramontano, A., 2007. Assessment of predictions in the model quality assessment category. Proteins Struct. Funct. Bioinforma. 69, 175–183.

D'Este, E., Kamin, D., Göttfert, F., El-Hady, A., Hell, S.W., 2015. STED Nanoscopy Reveals the Ubiquity of Subcortical Cytoskeleton Periodicity in Living Neurons. Cell Rep. 10, 1246–1251. https://doi.org/https://doi.org/10.1016/j.celrep.2015.02.007

Dalhaimer, P., Pollard, T.D., Nolen, B.J., 2008. Nucleotide-Mediated Conformational Changes of Monomeric Actin and Arp3 Studied by Molecular Dynamics Simulations. J. Mol. Biol. 376, 166–183. https://doi.org/https://doi.org/10.1016/j.jmb.2007.11.068

Damm, W., Frontera, A., Tirado–Rives, J., Jorgensen, W.L., 1997. OPLS all-atom force field for carbohydrates. J. Comput. Chem. 18, 1955–1970.

Dao, M., Li, J., Suresh, S., 2006. Molecularly based analysis of deformation of spectrin network and human erythrocyte. Mater. Sci. Eng. C 26, 1232–1244.

De La Cruz, E.M., 2009. How cofilin severs an actin filament. Biophys. Rev. 1, 51–59. https://doi.org/10.1007/s12551-009-0008-5

de Pablo, P.J., Schaap, I.A.T., MacKintosh, F.C., Schmidt, C.F., 2003. Deformation and Collapse of Microtubules on the Nanometer Scale. Phys. Rev. Lett. 91, 98101. https://doi.org/10.1103/PhysRevLett.91.098101

de Rooij, R., Kuhl, E., 2018. Microtubule Polymerization and Cross-Link Dynamics Explain Axonal Stiffness and Damage. Biophys. J. 114, 201–212. https://doi.org/https://doi.org/10.1016/j.bpj.2017.11.010

de Waegh, S.M., Lee, V.M.-Y., Brady, S.T., 1992. Local modulation of neurofilament phosphorylation, axonal caliber, and slow axonal transport by myelinating Schwann cells. Cell 68, 451–463.

DeLano, W.L., 2002. PyMOL.

Demir, Ç., Civalek, Ö., 2013. Torsional and longitudinal frequency and wave response of microtubules based on the nonlocal continuum and nonlocal discrete models. Appl. Math. Model. 37, 9355–9367. https://doi.org/https://doi.org/10.1016/j.apm.2013.04.050

Deng, Y., Li, B., Liu, F., Iqbal, K., Grundke-Iqbal, I., Brandt, R., Gong, C.-X., 2008. Regulation between O-GlcNAcylation and phosphorylation of neurofilament-M and their dysregulation in Alzheimer

disease. FASEB J. 22, 138–145.

Deriu, M.A., Bidone, T.C., Grasso, G., Acquaviva, A., Morbiducci, U., 2012a. Multiscale modeling of microtubules and actin filaments. IFAC Proc. Vol. 45, 1023–1028.

Deriu, M.A., Enemark, S., Soncini, M., Montevecchi, F.M., Redaelli, A., 2007. Tubulin: from atomistic structure to supramolecular mechanical properties. J. Mater. Sci. 42, 8864–8872. https://doi.org/10.1007/s10853-007-1784-6

Deriu, M.A., Shkurti, A., Paciello, G., Bidone, T.C., Morbiducci, U., Ficarra, E., Audenino, A., Acquaviva, A., 2012b. Multiscale modeling of cellular actin filaments: From atomistic molecular to coarse-grained dynamics. Proteins Struct. Funct. Bioinforma. 80, 1598–1609.

Deriu, M.A., Soncini, M., Orsi, M., Patel, M., Essex, J.W., Montevecchi, F.M., Redaelli, A., 2010. Anisotropic elastic network modeling of entire microtubules. Biophys. J. 99, 2190–2199.

Dima, R.I., Joshi, H., 2008. Probing the origin of tubulin rigidity with molecular simulations. Proc. Natl. Acad. Sci. 105, 15743 LP – 15748. https://doi.org/10.1073/pnas.0806113105

Ding, Y., Xu, Z., 2011. Mechanics of Microtubules from a Coarse-Grained Model. Bionanoscience 1, 173–182. https://doi.org/10.1007/s12668-011-0027-0

Dominguez, R., Holmes, K.C., 2011. Actin structure and function. Annu. Rev. Biophys. 40, 169–186.

Dubey, S., Bhembre, N., Bodas, S., Veer, S., Ghose, A., Callan-Jones, A., Pullarkat, P., 2020. The axonal actin-spectrin lattice acts as a tension buffering shock absorber. Elife 9, e51772.

Dudek, S.M., Johnson, G.V.W., 1995. Postnatal changes in serine/threonine protein phosphatases and their association with the microtubules. Dev. brain Res. 90, 54–61.

Dułak, D., Gadzała, M., Banach, M., Ptak, M., Wiśniowski, Z., Konieczny, L., Roterman, I., 2018. Filamentous aggregates of tau proteins fulfil standard amyloid criteria provided by the fuzzy oil

drop (FOD) model. Int. J. Mol. Sci. 19, 2910.

Ekiert, M., Mlyniec, A., Uhl, T., 2015. The influence of degradation on the viscosity and molecular mass of poly (lactide acid) biopolymer. Diagnostyka 16, 63–70.

Elder, G.A., Friedrich, V.L., Bosco, P., Kang, C., Gourov, A., Tu, P.-H., Lee, V.M.-Y., Lazzarini, R.A., 1998. Absence of the mid-sized neurofilament subunit decreases axonal calibers, levels of light neurofilament (NF-L), and neurofilament content. J. Cell Biol. 141, 727–739.

Enemark, S., Deriu, M.A., Soncini, M., Redaelli, A., 2008. Mechanical model of the tubulin dimer based on molecular dynamics simulations. J. Biomech. Eng. 130, 41008.

Enrique, M., Roland, J., McCullough, B.R., Blanchoin, L., Martiel, J.-L., 2010. Origin of twist-bend coupling in actin filaments. Biophys. J. 99, 1852–1860.

Erickson, H.P., 1989. Co-operativity in protein-protein association: The structure and stability of the actin filament. J. Mol. Biol. 206, 465–474.

Eyer, J., Leterrier, J.-F., 1988. Influence of the phosphorylation state of neurofilament proteins on the interactions between purified filaments in vitro. Biochem. J. 252, 655–660.

F10gge, W., 1975. Viscoelasticity. Blaisdell Publ. Co., Massachusetts.

Falcon, B., Zhang, W., Murzin, A.G., Murshudov, G., Garringer, H.J., Vidal, R., Crowther, R.A., Ghetti, B., Scheres, S.H.W., Goedert, M., 2018. Structures of filaments from Pick's disease reveal a novel tau protein fold. Nature 561, 137–140.

Falcon, B., Zivanov, J., Zhang, W., Murzin, A.G., Garringer, H.J., Vidal, R., Crowther, R.A., Newell, K.L., Ghetti, B., Goedert, M., 2019. Novel tau filament fold in chronic traumatic encephalopathy encloses hydrophobic molecules. Nature 568, 420–423.

Fan, J., Saunders, M.G., Voth, G.A., 2012. Coarse-graining provides insights on the essential nature of

heterogeneity in actin filaments. Biophys. J. 103, 1334–1342.

Feng, S., Liang, H., 2012. A coarse grain model of microtubules. Theor. Appl. Mech. Lett. 2, 14006.

Ferrer, I., Gomez-Isla, T., Puig, B., Freixes, M., Ribe, E., Dalfo, E., Avila, J., 2005. Current advances on different kinases involved in tau phosphorylation, and implications in Alzheimer's disease and tauopathies. Curr. Alzheimer Res. 2, 3–18.

Fichou, Y., Heyden, M., Zaccai, G., Weik, M., Tobias, D.J., 2015. Molecular dynamics simulations of a powder model of the intrinsically disordered protein Tau. J. Phys. Chem. B 119, 12580–12589.

Fitzpatrick, A.W.P., Falcon, B., He, S., Murzin, A.G., Murshudov, G., Garringer, H.J., Crowther, R.A., Ghetti, B., Goedert, M., Scheres, S.H.W., 2017. Cryo-EM structures of tau filaments from Alzheimer's disease. Nature 547, 185.

Fliegner, K.H., Liem, R.K.H., 1991. Cellular and molecular biology of neuronal intermediate filaments, in: International Review of Cytology. Elsevier, pp. 109–167.

FRAPPIER, T., DERANCOURT, J., PRADEL, L., 1992. Actin and neurofilament binding domain of brain spectrin β subunit. Eur. J. Biochem. 205, 85–91.

FRAPPIER, T., REGNOUF, F., PRADEL, L.A., 1987. Binding of brain spectrin to the 70-kDa neurofilament subunit protein. Eur. J. Biochem. 169, 651–657.

Fujii, T., Iwane, A.H., Yanagida, T., Namba, K., 2010. Direct visualization of secondary structures of F-actin by electron cryomicroscopy. Nature 467, 724.

Galkin, V.E., Orlova, A., Schröder, G.F., Egelman, E.H., 2010. Structural polymorphism in F-actin. Nat. Struct. Mol. Biol. 17, 1318.

Gao, Y., Wang, J., Gao, H., 2010. Persistence length of microtubules based on a continuum anisotropic shell model. J. Comput. Theor. Nanosci. 7, 1227–1237.

Garcia, M.L., Rao, M. V, Fujimoto, J., Garcia, V.B., Shah, S.B., Crum, J., Gotow, T., Uchiyama, Y., Ellisman, M., Calcutt, N.A., 2009. Phosphorylation of highly conserved neurofilament medium KSP repeats is not required for myelin-dependent radial axonal growth. J. Neurosci. 29, 1277–1284.

Gardel, M.L., Shin, J.H., MacKintosh, F.C., Mahadevan, L., Matsudaira, P., Weitz, D.A., 2004. Elastic Behavior of Cross-Linked and Bundled Actin Networks. Science (80-.). 304, 1301 LP – 1305. https://doi.org/10.1126/science.1095087

Garver, T.D., Lehman, R.A.W., Billingsley, M.L., 1996. Microtubule assembly competence analysis of freshly-biopsied human tau, dephosphorylated tau, and Alzheimer tau. J. Neurosci. Res. 44, 12–20. https://doi.org/10.1002/(SICI)1097-4547(19960401)44:1<12::AID-JNR2>3.0.CO;2-L

Gebremichael, Y., Chu, J.-W., Voth, G.A., 2008. Intrinsic Bending and Structural Rearrangement of Tubulin Dimer: Molecular Dynamics Simulations and Coarse-Grained Analysis. Biophys. J. 95, 2487–2499. https://doi.org/https://doi.org/10.1529/biophysj.108.129072

Gittes, F., Mickey, B., Nettleton, J., Howard, J., 1993. Flexural rigidity of microtubules and actin filaments measured from thermal fluctuations in shape. J. Cell Biol. 120, 923–934.

Gladkevich, A., Bosker, F., Korf, J., Yenkoyan, K., Vahradyan, H., Aghajanov, M., 2007. Proline-rich polypeptides in Alzheimer's disease and neurodegenerative disorders—Therapeutic potential or a mirage? Prog. Neuro-Psychopharmacology Biol. Psychiatry 31, 1347–1355.

Goedert, M., Jakes, R., Crowther, R.A., Six, J., Lübke, U., Vandermeeren, M., Cras, P., Trojanowski, J.Q., Lee, V.M., 1993. The abnormal phosphorylation of tau protein at Ser-202 in Alzheimer disease recapitulates phosphorylation during development. Proc. Natl. Acad. Sci. 90, 5066–5070.

Goedert, M., Jakes, R., Spillantini, M.G., Hasegawa, M., Smith, M.J., Crowther, R.A., 1996. Assembly of microtubule-associated protein tau into Alzheimer-like filaments induced by sulphated glycosaminoglycans. Nature 383, 550–553.

Goedert, M., Spillantini, M.G., Cairns, N.J., Crowther, R.A., 1992. Tau proteins of Alzheimer paired helical filaments: abnormal phosphorylation of all six brain isoforms. Neuron 8, 159–168.

Goedert, M., Spillantini, M.G., Jakes, R., Rutherford, D., Crowther, R.A., 1989. Multiple isoforms of human microtubule-associated protein tau: sequences and localization in neurofibrillary tangles of Alzheimer's disease. Neuron 3, 519–526.

Goldstein, M.E., Sternberger, N.H., Sternberger, L.A., 1987. Phosphorylation protects neurofilaments against proteolysis. J. Neuroimmunol. 14, 149–160.

Goode, B.L., Denis, P.E., Panda, D., Radeke, M.J., Miller, H.P., Wilson, L., Feinstein, S.C., 1997. Functional interactions between the proline-rich and repeat regions of tau enhance microtubule binding and assembly. Mol. Biol. Cell 8, 353–365. https://doi.org/10.1091/mbc.8.2.353

Goode, B.L., Feinstein, S.C., 1994. Identification of a novel microtubule binding and assembly domain in the developmentally regulated inter-repeat region of tau. J. Cell Biol. 124, 769 LP – 782. https://doi.org/10.1083/jcb.124.5.769

Götz, J., Probst, A., Spillantini, M.G., Schäfer, T., Jakes, R., Bürki, K., Goedert, M., 1995. Somatodendritic localization and hyperphosphorylation of tau protein in transgenic mice expressing the longest human brain tau isoform. EMBO J. 14, 1304–1313.

Graceffa, P., Dominguez, R., 2003. Crystal Structure of Monomeric Actin in the ATP State STRUCTURAL BASIS OF NUCLEOTIDE-DEPENDENT ACTIN DYNAMICS. J. Biol. Chem. 278, 34172–34180.

Grafmüller, A., Voth, G.A., 2011. Intrinsic Bending of Microtubule Protofilaments. Structure 19, 409–417. https://doi.org/https://doi.org/10.1016/j.str.2010.12.020

Grum, V.L., Li, D., MacDonald, R.I., Mondragón, A., 1999. Structures of two repeats of spectrin suggest models of flexibility. Cell 98, 523–535.

Grundke-Iqbal, I., Iqbal, K., Tung, Y.-C., Quinlan, M., Wisniewski, H.M., Binder, L.I., 1986. Abnormal phosphorylation of the microtubule-associated protein tau (tau) in Alzheimer cytoskeletal pathology. Proc. Natl. Acad. Sci. 83, 4913–4917.

Gu, B., Mai, Y.-W., Ru, C.Q., 2009. Mechanics of microtubules modeled as orthotropic elastic shells with transverse shearing. Acta Mech. 207, 195–209.

Gurmessa, B., Ricketts, S., Robertson-Anderson, R.M., 2017. Nonlinear Actin Deformations Lead to Network Stiffening, Yielding, and Nonuniform Stress Propagation. Biophys. J. 113, 1540–1550. https://doi.org/https://doi.org/10.1016/j.bpj.2017.01.012

Gustke, N., Trinczek, B., Biernat, J., Mandelkow, E.-M., Mandelkow, E., 1994. Domains of tau protein and interactions with microtubules. Biochemistry 33, 9511–9522.

Haense, C., Buerger, K., Kalbe, E., Drzezga, A., Teipel, S.J., Markiewicz, P., Herholz, K., Heiss, W.-D., Hampel, H., 2008. CSF total and phosphorylated tau protein, regional glucose metabolism and dementia severity in Alzheimer's disease. Eur. J. Neurol. 15, 1155–1162.

Hammarlund, M., Jorgensen, E.M., Bastiani, M.J., 2007. Axons break in animals lacking β-spectrin. J. Cell Biol. 176, 269–275.

Han, B., Zhou, R., Xia, C., Zhuang, X., 2017. Structural organization of the actin-spectrin–based membrane skeleton in dendrites and soma of neurons. Proc. Natl. Acad. Sci. 114, E6678–E6685.

Hanger, D.P., Anderton, B.H., Noble, W., 2009. Tau phosphorylation: the therapeutic challenge for neurodegenerative disease. Trends Mol. Med. 15, 112–119.

Harper, S.L., Li, D., Maksimova, Y., Gallagher, P.G., Speicher, D.W., 2010. A fused α-β "mini-spectrin" mimics the intact erythrocyte spectrin head-to-head tetramer. J. Biol. Chem. 285, 11003–11012.

Hashimoto, R., Nakamura, Y., Komai, S., Kashiwagi, Y., Tamura, K., Goto, T., Aimoto, S., Kaibuchi, K., Shiosaka, S., Takeda, M., 2000. Site-specific phosphorylation of neurofilament-L is mediated by

calcium/calmodulin-dependent protein kinase II in the apical dendrites during long-term potentiation. J. Neurochem. 75, 373–382.

Hawkins, B.E., Krishnamurthy, S., Castillo-Carranza, D.L., Sengupta, U., Prough, D.S., Jackson, G.R., DeWitt, D.S., Kayed, R., 2013. Rapid accumulation of endogenous tau oligomers in a rat model of traumatic brain injury possible link between traumatic brain injury and sporadic tauopathies. J. Biol. Chem. 288, 17042–17050.

Hawkins, T., Mirigian, M., Yasar, M.S., Ross, J.L., 2010. Mechanics of microtubules. J. Biomech. 43, 23–30.

He, J., Zhou, R., Wu, Z., Carrasco, M.A., Kurshan, P.T., Farley, J.E., Simon, D.J., Wang, G., Han, B., Hao, J., 2016. Prevalent presence of periodic actin–spectrin-based membrane skeleton in a broad range of neuronal cell types and animal species. Proc. Natl. Acad. Sci. 113, 6029–6034.

Hemmat, M., Castle, B.T., Odde, D.J., 2018. Microtubule dynamics: moving toward a multi-scale approach. Curr. Opin. Cell Biol. 50, 8–13. https://doi.org/https://doi.org/10.1016/j.ceb.2017.12.013

Herrmann, H., Aebi, U., 2004. Intermediate filaments: molecular structure, assembly mechanism, and integration into functionally distinct intracellular scaffolds. Annu. Rev. Biochem. 73, 749–789.

Higham, D.J., Higham, N.J., 2016. MATLAB guide. SIAM.

Higuchi, H., Yanagida, T., Goldman, Y.E., 1995a. Compliance of thin filaments in skinned fibers of rabbit skeletal muscle. Biophys. J. 69, 1000–1010. https://doi.org/https://doi.org/10.1016/S0006-3495(95)79975-1

Higuchi, H., Yanagida, T., Goldman, Y.E., 1995b. Compliance of thin filaments in skinned fibers of rabbit skeletal muscle. Biophys. J. 69, 1000–1010. https://doi.org/https://doi.org/10.1016/S0006-3495(95)79975-1

Hirokawa, N., Shiomura, Y., Okabe, S., 1988. Tau proteins: the molecular structure and mode of binding

on microtubules. J. Cell Biol. 107, 1449–1459.

Hisanaga, S., Gonda, Y., Inagaki, M., Ikai, A., Hirokawa, N., 1990. Effects of phosphorylation of the neurofilament L protein on filamentous structures. Cell Regul. 1, 237–248.

Hisanaga, S., Hirokawa, N., 1989. The effects of dephosphorylation on the structure of the projections of neurofilament. J. Neurosci. 9, 959–966.

Hisanaga, S., Hirokawa, N., 1988. Structure of the peripheral domains of neurofilaments revealed by low angle rotary shadowing. J. Mol. Biol. 202, 297–305.

Hoffman, P.N., Lasek, R.J., 1975. The slow component of axonal transport. Identification of major structural polypeptides of the axon and their generality among mammalian neurons. J. Cell Biol. 66, 351–366.

Holzapfel, G.A., Unterberger, M.J., Ogden, R.W., 2014. An affine continuum mechanical model for cross-linked F-actin networks with compliant linker proteins. J. Mech. Behav. Biomed. Mater. 38, 78–90. https://doi.org/https://doi.org/10.1016/j.jmbbm.2014.05.014

Hoore, M., Yaya, F., Podgorski, T., Wagner, C., Gompper, G., Fedosov, D.A., 2018. Effect of spectrin network elasticity on the shapes of erythrocyte doublets. Soft Matter 14, 6278–6289.

Howard, J., 2001. Mechanics of motor proteins and the cytoskeleton.

Hsieh, S.-T., Crawford, T.O., Griffin, J.W., 1994. Neurofilament distribution and organization in the myelinated axons of the peripheral nervous system. Brain Res. 642, 316–326.

Hu, Y.Y., He, S.S., Wang, X., Duan, Q.H., Grundke-Iqbal, I., Iqbal, K., Wang, J., 2002. Levels of nonphosphorylated and phosphorylated tau in cerebrospinal fluid of Alzheimer's disease patients: an ultrasensitive bienzyme-substrate-recycle enzyme-linked immunosorbent assay. Am. J. Pathol. 160, 1269–1278.

Huang, C.Y.-M., Zhang, C., Ho, T.S.-Y., Oses-Prieto, J., Burlingame, A.L., Lalonde, J., Noebels, J.L., Leterrier, C., Rasband, M.N., 2017. αII spectrin forms a periodic cytoskeleton at the axon initial segment and is required for nervous system function. J. Neurosci. 37, 11311–11322.

Hülsmeier, J., Pielage, J., Rickert, C., Technau, G.M., Klämbt, C., Stork, T., 2007. Distinct functions of α-Spectrin and β-Spectrin during axonal pathfinding. Development 134, 713–722.

Huxley, H.E., Stewart, A., Sosa, H., Irving, T., 1994a. X-ray diffraction measurements of the extensibility of actin and myosin filaments in contracting muscle. Biophys. J. 67, 2411–2421. https://doi.org/https://doi.org/10.1016/S0006-3495(94)80728-3

Huxley, H.E., Stewart, A., Sosa, H., Irving, T., 1994b. X-ray diffraction measurements of the extensibility of actin and myosin filaments in contracting muscle. Biophys. J. 67, 2411–2421. https://doi.org/https://doi.org/10.1016/S0006-3495(94)80728-3

Iqbal, K., Grundke-Iqbal, I., Smith, A.J., George, L., Tung, Y.-C., Zaidi, T., 1989. Identification and localization of a tau peptide to paired helical filaments of Alzheimer disease. Proc. Natl. Acad. Sci. 86, 5646–5650.

Isambert, H., Venier, P., Maggs, A.C., Fattoum, A., Kassab, R., Pantaloni, D., Carlier, M.-F., 1995. Flexibility of actin filaments derived from thermal fluctuations. Effect of bound nucleotide, phalloidin, and muscle regulatory proteins. J. Biol. Chem. 270, 11437–11444.

Isralewitz, B., Gao, M., Schulten, K., 2001. Steered molecular dynamics and mechanical functions of proteins. Curr. Opin. Struct. Biol. 11, 224–230.

Janmey, P.A., Hvidt, S., Käs, J., Lerche, D., Maggs, A., Sackmann, E., Schliwa, M., Stossel, T.P., 1994. The mechanical properties of actin gels. Elastic modulus and filament motions. J. Biol. Chem. 269, 32503–32513.

Janmey, P.A., Leterrier, J.-F., Herrmann, H., 2003. Assembly and structure of neurofilaments. Curr. Opin.

Colloid Interface Sci. 8, 40–47.

Jayanthi, L., 2014. Computational Investigation On The Structural Properties Of Neurofilaments And Their Sidearms.

Jayanthi, L., Stevenson, W., Kwak, Y., Chang, R., Gebremichael, Y., 2013. Conformational properties of interacting neurofilaments: Monte Carlo simulations of cylindrically grafted apposing neurofilament brushes. J. Biol. Phys. 39, 343–362.

Jeon, J., Alexander, N.R., Weaver, A.M., Cummings, P.T., 2008. Protrusion of a Virtual Model Lamellipodium by Actin Polymerization: A Coarse-Grained Langevin Dynamics Model. J. Stat. Phys. 133, 79. https://doi.org/10.1007/s10955-008-9600-5

Jho, Y.S., Zhulina, E.B., Kim, M.-W., Pincus, P.A., 2010. Monte carlo simulations of tau proteins: effect of phosphorylation. Biophys. J. 99, 2387–2397.

Ji, X.-Y., Feng, X.-Q., 2011. Coarse-grained mechanochemical model for simulating the dynamic behavior of microtubules. Phys. Rev. E 84, 31933.

Jiang, H., Jiang, L., Posner, J.D., Vogt, B.D., 2008. Atomistic-based continuum constitutive relation for microtubules: elastic modulus prediction. Comput. Mech. 42, 607–618.

Jo, S., Kim, T., Iyer, V.G., Im, W., 2008. CHARMM-GUI: A web-based graphical user interface for CHARMM. J. Comput. Chem. 29, 1859–1865. https://doi.org/10.1002/jcc.20945

Jonsson, M., Zetterberg, H., Van Straaten, E., Lind, K., Syversen, S., Edman, Å., Blennow, K., Rosengren, L., Pantoni, L., Inzitari, D., 2010. Cerebrospinal fluid biomarkers of white matter lesions–cross-sectional results from the LADIS study. Eur. J. Neurol. 17, 377–382.

Jorda, J., Xue, B., Uversky, V.N., Kajava, A. V, 2010. Protein tandem repeats–the more perfect, the less structured. FEBS J. 277, 2673–2682.

Jorgensen, W.L., Maxwell, D.S., Tirado-Rives, J., 1996. Development and Testing of the OPLS All-Atom Force Field on Conformational Energetics and Properties of Organic Liquids. J. Am. Chem. Soc. 118, 11225–11236. https://doi.org/10.1021/ja9621760

Julien, J.P., Mushynski, W.E., 1982. Multiple phosphorylation sites in mammalian neurofilament polypeptides. J. Biol. Chem. 257, 10467–10470.

Kadavath, H., Jaremko, M., Jaremko, Ł., Biernat, J., Mandelkow, E., Zweckstetter, M., 2015. Folding of the tau protein on microtubules. Angew. Chemie Int. Ed. 54, 10347–10351.

Kaji, T., Boland, B., Odrljin, T., Mohan, P., Basavarajappa, B.S., Peterhoff, C., Cataldo, A., Rudnicki, A., Amin, N., Li, B.S., 2004. Calpain mediates calcium-induced activation of the erk1, 2 MAPK pathway and cytoskeletal phosphorylation in neurons: relevance to Alzheimer's disease. Am. J. Pathol. 165, 795–805.

Kaminski, G.A., Friesner, R.A., Tirado-Rives, J., Jorgensen, W.L., 2001. Evaluation and Reparametrization of the OPLS-AA Force Field for Proteins via Comparison with Accurate Quantum Chemical Calculations on Peptides. J. Phys. Chem. B 105, 6474–6487. https://doi.org/10.1021/jp003919d

Kandimalla, R.J.L., Prabhakar, S., Wani, W.Y., Kaushal, A., Gupta, N., Sharma, D.R., Grover, V.K., Bhardwaj, N., Jain, K., Gill, K.D., 2013. CSF p-Tau levels in the prediction of Alzheimer's disease. Biol. Open 2, 1119–1124.

Kasas, S, Cibert, C., Kis, A., De Los Rios, P., Riederer, B.M., Forró, L., Dietler, G., Catsicas, S., 2004. Oscillation modes of microtubules. Biol. Cell 96, 697–700. https://doi.org/https://doi.org/10.1016/j.biolcel.2004.09.002

Kasas, Sandor, Kis, A., Riederer, B.M., Forró, L., Dietler, G., Catsicas, S., 2004. Mechanical Properties of Microtubules Explored Using the Finite Elements Method. ChemPhysChem 5, 252–257.

https://doi.org/10.1002/cphc.200300799

Kelley, L.A., Mezulis, S., Yates, C.M., Wass, M.N., Sternberg, M.J.E., 2015. The Phyre2 web portal for protein modeling, prediction and analysis. Nat. Protoc. 10, 845.

Kenessey, A., Yen, S.-H.C., 1993. The extent of phosphorylation of fetal tau is comparable to that of PHF-tau from Alzheimer paired helical filaments. Brain Res. 629, 40–46.

Kerssemakers, J.W.J., Laura Munteanu, E., Laan, L., Noetzel, T.L., Janson, M.E., Dogterom, M., 2006. Assembly dynamics of microtubules at molecular resolution. Nature 442, 709–712. https://doi.org/10.1038/nature04928

Khan, M.I., Hasan, F., Al Mahmud, K.A.H., Adnan, A., 2020a. Recent Computational Approaches on Mechanical Behavior of Axonal Cytoskeletal Components of Neuron: A Brief Review. Multiscale Sci. Eng. 1–15.

Khan, M.I., Hasan, F., Hasan Al Mahmud, K.A., Adnan, A., 2020b. Domain focused and residue focused phosphorylation effect on tau protein: A molecular dynamics simulation study. J. Mech. Behav. Biomed. Mater. 104149. https://doi.org/https://doi.org/10.1016/j.jmbbm.2020.104149

Khatoon, S., Grundke-Iqbal, I., Iqbal, K., 1994. Levels of normal and abnormally phosphorylated tau in different cellular and regional compartments of Alzheimer disease and control brains. FEBS Lett. 351, 80–84.

Kim, B., Lee, S.B., Lee, J., Cho, S., Park, H., Yeom, S., Park, S.H., 2012. A comparison among Neo-Hookean model, Mooney-Rivlin model, and Ogden model for chloroprene rubber. Int. J. Precis. Eng. Manuf. 13, 759–764.

Kim, J.I., Kwon, J., Baek, I., Na, S., 2016. Steered molecular dynamics analysis of the role of cofilin in increasing the flexibility of actin filaments. Biophys. Chem. 218, 27–35. https://doi.org/https://doi.org/10.1016/j.bpc.2016.08.002

Kim, J.I., Kwon, J., Baek, I., Park, H.S., Na, S., 2015. Cofilin reduces the mechanical properties of actin filaments: approach with coarse-grained methods. Phys. Chem. Chem. Phys. 17, 8148–8158. https://doi.org/10.1039/C4CP06100D

Kim, S., Chang, R., Teunissen, C., Gebremichael, Y., Petzold, A., 2011. Neurofilament stoichiometry simulations during neurodegeneration suggest a remarkable self-sufficient and stable in vivo protein structure. J. Neurol. Sci. 307, 132–138.

Kim, T, Hwang, W., Kamm, R.D., 2009. Computational Analysis of a Cross-linked Actin-like Network. Exp. Mech. 49, 91–104. https://doi.org/10.1007/s11340-007-9091-3

Kim, Taeyoon, Hwang, W., Lee, H., Kamm, R.D., 2009. Computational Analysis of Viscoelastic Properties of Crosslinked Actin Networks. PLOS Comput. Biol. 5, e1000439.

Kis, A., Kasas, S., Babić, B., Kulik, A.J., Benoît, W., Briggs, G.A.D., Schönenberger, C., Catsicas, S., Forró, L., 2002. Nanomechanics of Microtubules. Phys. Rev. Lett. 89, 248101. https://doi.org/10.1103/PhysRevLett.89.248101

Kleinjung, J., Fraternali, F., 2014. Design and application of implicit solvent models in biomolecular simulations. Curr. Opin. Struct. Biol. 25, 126–134.

Kojima, H., Ishijima, A., Yanagida, T., 1994a. Direct measurement of stiffness of single actin filaments with and without tropomyosin by in vitro nanomanipulation. Proc. Natl. Acad. Sci. 91, 12962 LP – 12966. https://doi.org/10.1073/pnas.91.26.12962

Kojima, H., Ishijima, A., Yanagida, T., 1994b. Direct measurement of stiffness of single actin filaments with and without tropomyosin by in vitro nanomanipulation. Proc. Natl. Acad. Sci. 91, 12962 LP – 12966. https://doi.org/10.1073/pnas.91.26.12962

Kolarova, M., García-Sierra, F., Bartos, A., Ricny, J., Ripova, D., 2012. Structure and pathology of tau protein in Alzheimer disease. Int. J. Alzheimer's Dis. 2012.

Köpke, E., Tung, Y.-C., Shaikh, S., Alonso, A. del C., Iqbal, K., Grundke-Iqbal, I., 1993. Microtubule-associated protein tau. Abnormal phosphorylation of a non-paired helical filament pool in Alzheimer disease. J. Biol. Chem. 268, 24374–24384.

Koshino, I., Mohandas, N., Takakuwa, Y., 2012. Identification of a novel role for dematin in regulating red cell membrane function by modulating spectrin-actin interaction. J. Biol. Chem. 287, 35244–35250.

Koskinen, M., Hotulainen, P., 2014. Measuring F-actin properties in dendritic spines . Front. Neuroanat. .

Kumar, S., Mansson, A., 2017. Covalent and non-covalent chemical engineering of actin for biotechnological applications. Biotechnol. Adv. 35, 867–888.

Kumar, S., Yin, X., Trapp, B.D., Hoh, J.H., Paulaitis, M.E., 2002. Relating interactions between neurofilaments to the structure of axonal neurofilament distributions through polymer brush models. Biophys. J. 82, 2360–2372.

Kushkuley, J., Chan, W.K.H., Lee, S., Eyer, J., Leterrier, J.-F., Letournel, F., Shea, T.B., 2009. Neurofilament cross-bridging competes with kinesin-dependent association of neurofilaments with microtubules. J. Cell Sci. 122, 3579–3586.

Kushkuley, J., Metkar, S., Chan, W.K.H., Lee, S., Shea, T.B., 2010. Aluminum induces neurofilament aggregation by stabilizing cross-bridging of phosphorylated c-terminal sidearms. Brain Res. 1322, 118–123.

Kusunoki, H., Minasov, G., MacDonald, R.I., Mondragón, A., 2004. Independent movement, dimerization and stability of tandem repeats of chicken brain α-spectrin. J. Mol. Biol. 344, 495–511.

Lai, L., Cao, J., 2014. Spectrins in axonal cytoskeletons: dynamics revealed by extensions and fluctuations. J. Chem. Phys. 141, 07B601_1.

Laser-Azogui, A., Kornreich, M., Malka-Gibor, E., Beck, R., 2015. Neurofilament assembly and function during neuronal development. Curr. Opin. Cell Biol. 32, 92–101.

Law, R., Carl, P., Harper, S., Dalhaimer, P., Speicher, D.W., Discher, D.E., 2003. Cooperativity in forced unfolding of tandem spectrin repeats. Biophys. J. 84, 533–544.

Lazarides, E., 1975. Immunofluorescence studies on the structure of actin filaments in tissue culture cells. J. Histochem. Cytochem. 23, 507–528.

Lazarus, C., Soheilypour, M., Mofrad, M.R.K., 2015. Torsional behavior of axonal microtubule bundles. Biophys. J. 109, 231–239.

Lee, G., Neve, R.L., Kosik, K.S., 1989. The microtubule binding domain of tau protein. Neuron 2, 1615–1624. https://doi.org/https://doi.org/10.1016/0896-6273(89)90050-0

Lee, J., Kim, S., Chang, R., Jayanthi, L., Gebremichael, Y., 2013. Effects of molecular model, ionic strength, divalent ions, and hydrophobic interaction on human neurofilament conformation. J. Chem. Phys. 138, 01B604.

Lee, J.Y., Iverson, T.M., Dima, R.I., 2011. Molecular Investigations into the Mechanics of Actin in Different Nucleotide States. J. Phys. Chem. B 115, 186–195. https://doi.org/10.1021/jp108249g

Lees, J.F., Shneidman, P.S., Skuntz, S.F., Carden, M.J., Lazzarini, R.A., 1988. The structure and organization of the human heavy neurofilament subunit (NF-H) and the gene encoding it. EMBO J. 7, 1947–1955.

Leite, S.C., Sampaio, P., Sousa, V.F., Nogueira-Rodrigues, J., Pinto-Costa, R., Peters, L.L., Brites, P., Sousa, M.M., 2016. The actin-binding protein α-adducin is required for maintaining axon diameter. Cell Rep. 15, 490–498.

Leite, S.C., Sousa, M.M., 2016. The neuronal and actin commitment: Why do neurons need rings? Cytoskeleton 73, 424–434.

Lenne, P.-F., Raae, A.J., Altmann, S.M., Saraste, M., Hörber, J.K.H., 2000. States and transitions during forced unfolding of a single spectrin repeat. FEBS Lett. 476, 124–128.

Leterrier, J.-F., Eyer, J., 1987. Properties of highly viscous gels formed by neurofilaments in vitro. A possible consequence of a specific inter-filament cross-bridging. Biochem. J. 245, 93–101.

Leterrier, J.F., Käs, J., Hartwig, J., Vegners, R., Janmey, P.A., 1996. Mechanical effects of neurofilament cross-bridges modulation by phosphorylation, lipids, and interactions with f-actin. J. Biol. Chem. 271, 15687–15694.

Li, C., Ru, C.Q., Mioduchowski, A., 2006. Torsion of the central pair microtubules in eukaryotic flagella due to bending-driven lateral buckling. Biochem. Biophys. Res. Commun. 351, 159–164. https://doi.org/https://doi.org/10.1016/j.bbrc.2006.10.019

Li, D., Harper, S.L., Tang, H.-Y., Maksimova, Y., Gallagher, P.G., Speicher, D.W., 2010. A comprehensive model of the spectrin divalent tetramer binding region deduced using homology modeling and chemical cross-linking of a mini-spectrin. J. Biol. Chem. 285, 29535–29545.

Li, H., Lykotrafitis, G., 2012. Two-Component Coarse-Grained Molecular-Dynamics Model for the Human Erythrocyte Membrane. Biophys. J. 102, 75–84. https://doi.org/https://doi.org/10.1016/j.bpj.2011.11.4012

Li, J., Dao, M., Lim, C.T., Suresh, S., 2005. Spectrin-level modeling of the cytoskeleton and optical tweezers stretching of the erythrocyte. Biophys. J. 88, 3707–3719.

Li, Jianzong, Feng, Y., Wang, X., Li, Jing, Liu, W., Rong, L., Bao, J., 2015. An overview of predictors for intrinsically disordered proteins over 2010–2014. Int. J. Mol. Sci. 16, 23446–23462.

Li, T., 2015. Cross-scale biophysics modelling of F-actin cytoskeleton in cell.

Li, T., 2008. A mechanics model of microtubule buckling in living cells. J. Biomech. 41, 1722–1729.

Li, T., Gu, Y., Feng, X.-Q., Yarlagadda, P.K.D. V, Oloyede, A., 2013. Hierarchical multiscale model for biomechanics analysis of microfilament networks. J. Appl. Phys. 113, 194701.

Lieleg, O., Schmoller, K.M., Claessens, M.M.A.E., Bausch, A.R., 2009. Cytoskeletal Polymer Networks: Viscoelastic Properties are Determined by the Microscopic Interaction Potential of Cross-links. Biophys. J. 96, 4725–4732. https://doi.org/https://doi.org/10.1016/j.bpj.2009.03.038

Liew, K.M., Xiang, P., Sun, Y., 2011. A continuum mechanics framework and a constitutive model for predicting the orthotropic elastic properties of microtubules. Compos. Struct. 93, 1809–1818. https://doi.org/https://doi.org/10.1016/j.compstruct.2011.01.017

Liew, K.M., Xiang, P., Zhang, L.W., 2015. Mechanical properties and characteristics of microtubules: a review. Compos. Struct. 123, 98–108.

Lindwall, G., Cole, R.D., 1984. Phosphorylation affects the ability of tau protein to promote microtubule assembly. J. Biol. Chem. 259, 5301–5305.

Liu, F., Iqbal, K., Grundke-Iqbal, I., Hart, G.W., Gong, C.-X., 2004. O-GlcNAcylation regulates phosphorylation of tau: A mechanism involved in Alzheimer's disease. Proc. Natl. Acad. Sci. U. S. A. 101, 10804 LP – 10809. https://doi.org/10.1073/pnas.0400348101

Luo, Y., Dinkel, P., Yu, X., Margittai, M., Zheng, J., Nussinov, R., Wei, G., Ma, B., 2013. Molecular insights into the reversible formation of tau protein fibrils. Chem. Commun. 49, 3582–3584.

Lyons, A.J., Gandhi, N.S., Mancera, R.L., 2014. Molecular dynamics simulation of the phosphorylation-induced conformational changes of a tau peptide fragment. Proteins Struct. Funct. Bioinforma. 82, 1907–1923.

Maccioni, R.B., Rivas, C.I., Vera, J.C., 1988. Differential interaction of synthetic peptides from the carboxyl-terminal regulatory domain of tubulin with microtubule-associated proteins. EMBO J. 7, 1957–1963.

MacKerell, A.D., Bashford, D., Bellott, M., Dunbrack, R.L., Evanseck, J.D., Field, M.J., Fischer, S., Gao, J., Guo, H., Ha, S., Joseph-McCarthy, D., Kuchnir, L., Kuczera, K., Lau, F.T.K., Mattos, C., Michnick, S., Ngo, T., Nguyen, D.T., Prodhom, B., Reiher, W.E., Roux, B., Schlenkrich, M., Smith, J.C., Stote, R., Straub, J., Watanabe, M., Wiórkiewicz-Kuczera, J., Yin, D., Karplus, M., 1998. All-Atom Empirical Potential for Molecular Modeling and Dynamics Studies of Proteins. J. Phys. Chem. B 102, 3586–3616. https://doi.org/10.1021/jp973084f

Mackerell Jr, A.D., Feig, M., Brooks III, C.L., 2004. Extending the treatment of backbone energetics in protein force fields: limitations of gas-phase quantum mechanics in reproducing protein conformational distributions in molecular dynamics simulations. J. Comput. Chem. 25, 1400–1415.

Mahadevan, L., Mitchison, T.J., 2005. Powerful curves. Nature 435, 895–897. https://doi.org/10.1038/435895a

Malka-Gibor, E., Kornreich, M., Laser-Azogui, A., Doron, O., Zingerman-Koladko, I., Harapin, J., Medalia, O., Beck, R., 2017. Phosphorylation-induced mechanical regulation of intrinsically disordered neurofilament proteins. Biophys. J. 112, 892–900.

Mandelkow, E.-M., Mandelkow, E., 1998. Tau in Alzheimer's disease. Trends Cell Biol. 8, 425–427.

Mandelkow, E., Song, Y.-H., Schweers, O., Marx, A., Mandelkow, E.-M., 1995. On the structure of microtubules, tau, and paired helical filaments. Neurobiol. Aging 16, 347–354. https://doi.org/https://doi.org/10.1016/0197-4580(95)00026-B

Marrink, S.J., Risselada, H.J., Yefimov, S., Tieleman, D.P., De Vries, A.H., 2007. The MARTINI force field: coarse grained model for biomolecular simulations. J. Phys. Chem. B 111, 7812–7824.

Matsushita, S., Adachi, T., Inoue, Y., Hojo, M., Sokabe, M., 2010. Evaluation of extensional and torsional stiffness of single actin filaments by molecular dynamics analysis. J. Biomech. 43, 3162–3167.

Matsushita, S., Inoue, Y., Adachi, T., 2012. Quantitative analysis of extension–torsion coupling of actin filaments. Biochem. Biophys. Res. Commun. 420, 710–713.

Matsushita, S., Inoue, Y., Hojo, M., Sokabe, M., Adachi, T., 2011. Effect of tensile force on the mechanical behavior of actin filaments. J. Biomech. 44, 1776–1781.

Mawal-Dewan, M., Henley, J., Van de Voorde, A., Trojanowski, J.Q., Lee, V.M., 1994. The phosphorylation state of tau in the developing rat brain is regulated by phosphoprotein phosphatases. J. Biol. Chem. 269, 30981–30987.

Mayo, S.L., Olafson, B.D., Goddard, W.A., 1990. DREIDING: a generic force field for molecular simulations. J. Phys. Chem. 94, 8897–8909.

Mazanetz, M.P., Fischer, P.M., 2007. Untangling tau hyperphosphorylation in drug design for neurodegenerative diseases. Nat. Rev. Drug Discov. 6, 464.

McCullough, B.R., Grintsevich, E.E., Chen, C.K., Kang, H., Hutchison, A.L., Henn, A., Cao, W., Suarez, C., Martiel, J.-L., Blanchoin, L., 2011. Cofilin-linked changes in actin filament flexibility promote severing. Biophys. J. 101, 151–159.

McQuaid, M.J., Sun, H., Rigby, D., 2004. Development and validation of COMPASS force field parameters for molecules with aliphatic azide chains. J. Comput. Chem. 25, 61–71.

Minami, Y., Sakai, H., 1986. Effects of microtubule-associated proteins on network formation by neurofilament-induced polymerization of tubulin. FEBS Lett. 195, 68–72.

Ming, D., Kong, Y., Wu, Y., Ma, J., 2003. Simulation of F-Actin Filaments of Several Microns. Biophys. J. 85, 27–35. https://doi.org/https://doi.org/10.1016/S0006-3495(03)74451-8

Mitra, A., Sept, D., 2008. Taxol Allosterically Alters the Dynamics of the Tubulin Dimer and Increases the Flexibility of Microtubules. Biophys. J. 95, 3252–3258. https://doi.org/https://doi.org/10.1529/biophysj.108.133884

Mofrad, M.R.K., 2008. Rheology of the Cytoskeleton. Annu. Rev. Fluid Mech. 41, 433–453. https://doi.org/10.1146/annurev.fluid.010908.165236

Molodtsov, M.I., Grishchuk, E.L., Efremov, A.K., McIntosh, J.R., Ataullakhanov, F.I., 2005. Force production by depolymerizing microtubules: A theoretical study. Proc. Natl. Acad. Sci. U. S. A. 102, 4353 LP – 4358. https://doi.org/10.1073/pnas.0501142102

Moon, R.T., McMahon, A.P., 1990. Generation of diversity in nonerythroid spectrins. Multiple polypeptides are predicted by sequence analysis of cDNAs encompassing the coding region of human nonerythroid alpha-spectrin. J. Biol. Chem. 265, 4427–4433.

Mortazavi, B., Rabczuk, T., 2015. Multiscale modeling of heat conduction in graphene laminates. Carbon N. Y. 85, 1–7.

Mortazavi, B., Yang, H., Mohebbi, F., Cuniberti, G., Rabczuk, T., 2017. Graphene or h-BN paraffin composite structures for the thermal management of Li-ion batteries: a multiscale investigation. Appl. Energy 202, 323–334.

Mukrasch, M.D., Von Bergen, M., Biernat, J., Fischer, D., Griesinger, C., Mandelkow, E., Zweckstetter, M., 2007. The “jaws” of the tau-microtubule interaction. J. Biol. Chem. 282, 12230–12239.

Mulder, C., Verwey, N.A., van der Flier, W.M., Bouwman, F.H., Kok, A., van Elk, E.J., Scheltens, P., Blankenstein, M.A., 2010. Amyloid-β (1–42), total tau, and phosphorylated tau as cerebrospinal fluid biomarkers for the diagnosis of Alzheimer disease. Clin. Chem. 56, 248–253.

Murakami, K., Yasunaga, T., Noguchi, T.Q.P., Gomibuchi, Y., Ngo, K.X., Uyeda, T.Q.P., Wakabayashi, T., 2010. Structural Basis for Actin Assembly, Activation of ATP Hydrolysis, and Delayed Phosphate Release. Cell 143, 275–287. https://doi.org/10.1016/j.cell.2010.09.034

Nagase, T., Ishikawa, K., Nakajima, D., Ohira, M., Seki, N., Miyajima, N., Tanaka, A., Kotani, H., Nomura, N., Ohara, O., 1997. Prediction of the coding sequences of unidentified human genes. VII.

The complete sequences of 100 new cDNA clones from brain which can code for large proteins in vitro. DNA Res. 4, 141–150.

Narita, A., Oda, T., Maéda, Y., 2011. Structural basis for the slow dynamics of the actin filament pointed end. EMBO J. 30, 1230–1237. https://doi.org/https://doi.org/10.1038/emboj.2011.48

Naydenov, N.G., Ivanov, A.I., 2011. Spectrin-adducin membrane skeleton: A missing link between epithelial junctions and the actin cytoskeletion? Bioarchitecture 1, 3506–3517.

Nestor, M.W., Cai, X., Stone, M.R., Bloch, R.J., Thompson, S.M., 2011. The actin binding domain of βI-spectrin regulates the morphological and functional dynamics of dendritic spines. PLoS One 6, e16197.

Niederman, R., Amrein, P.C., Hartwig, J., 1983. Three-dimensional structure of actin filaments and of an actin gel made with actin-binding protein. J. Cell Biol. 96, 1400–1413.

Nishimura, S., Nagai, S., Katoh, M., Yamashita, H., Saeki, Y., Okada, J., Hisada, T., Nagai, R., Sugiura, S., 2006. Microtubules modulate the stiffness of cardiomyocytes against shear stress. Circ. Res. 98, 81–87.

Nixon, R.A., Shea, T.B., 1992. Dynamics of neuronal intermediate filaments: a developmental perspective. Cell Motil. Cytoskeleton 22, 81–91.

Noble, W., Planel, E., Zehr, C., Olm, V., Meyerson, J., Suleman, F., Gaynor, K., Wang, L., LaFrancois, J., Feinstein, B., 2005. Inhibition of glycogen synthase kinase-3 by lithium correlates with reduced tauopathy and degeneration in vivo. Proc. Natl. Acad. Sci. 102, 6990–6995.

Nogales, E., Wolf, S.G., Downing, K.H., 1998. Erratum: Structure of the αβ tubulin dimer by electron crystallography. Nature 393, 191. https://doi.org/10.1038/30288

Oda, T., Iwasa, M., Aihara, T., Maéda, Y., Narita, A., 2009. The nature of the globular-to fibrous-actin transition. Nature 457, 441.

Okie, S., 2005. Traumatic brain injury in the war zone. N. Engl. J. Med. 352, 2043–2047.

Ono, T., Yamamoto, H., Tashima, K., Nakashima, H., Okumura, E., Yamada, K., Hisanaga, S.-I., Kishimoto, T., Miyakawa, T., Miyamoto, E., 1995. Dephosphorylation of abnormal sites of tau factor by protein phosphatases and its implication for Alzheimer's disease. Neurochem. Int. 26, 205–215.

Ortiz, V., Nielsen, S.O., Klein, M.L., Discher, D.E., 2005. Unfolding a linker between helical repeats. J. Mol. Biol. 349, 638–647.

Otterbein, L.R., Graceffa, P., Dominguez, R., 2001. The crystal structure of uncomplexed actin in the ADP state. Science (80-.). 293, 708–711.

Ouyang, H., Nauman, E., Shi, R., 2013. Contribution of cytoskeletal elements to the axonal mechanical properties. J. Biol. Eng. 7, 21. https://doi.org/10.1186/1754-1611-7-21

Pachenari, M., Seyedpour, S.M., Janmaleki, M., Shayan, S.B., Taranejoo, S., Hosseinkhani, H., 2014. Mechanical properties of cancer cytoskeleton depend on actin filaments to microtubules content: Investigating different grades of colon cancer cell lines. J. Biomech. 47, 373–379. https://doi.org/https://doi.org/10.1016/j.jbiomech.2013.11.020

Panda, D., Goode, B.L., Feinstein, S.C., Wilson, L., 1995. Kinetic Stabilization of Microtubule Dynamics at Steady State by Tau and Microtubule-Binding Domains of Tau. Biochemistry 34, 11117–11127. https://doi.org/10.1021/bi00035a017

Pant, H.C., 1988. Dephosphorylation of neurofilament proteins enhances their susceptibility to degradation by calpain. Biochem. J. 256, 665–668.

Paramore, S., Ayton, G.S., Voth, G.A., 2006. Extending a spectrin repeat unit. II: rupture behavior. Biophys. J. 90, 101–111.

Paramore, S., Voth, G.A., 2006. Examining the influence of linkers and tertiary structure in the forced

unfolding of multiple-repeat spectrin molecules. Biophys. J. 91, 3436–3445.

Pearce, C.W., Young, P.G., 2014. On the pressure response in the brain due to short duration blunt impacts. PLoS One 9, e114292.

Pelletier, O., Pokidysheva, E., Hirst, L.S., Bouxsein, N., Li, Y., Safinya, C.R., 2003. Structure of actin cross-linked with α-actinin: a network of bundles. Phys. Rev. Lett. 91, 148102.

Pelletier, V., Gal, N., Fournier, P., Kilfoil, M.L., 2009. Microrheology of microtubule solutions and actin-microtubule composite networks. Phys. Rev. Lett. 102, 188303.

Perrot, R., Eyer, J., 2009. Neuronal intermediate filaments and neurodegenerative disorders. Brain Res. Bull. 80, 282–295.

Peter, S.J., Mofrad, M.R.K., 2012. Computational modeling of axonal microtubule bundles under tension. Biophys. J. 102, 749–757.

Pettersen, E.F., Goddard, T.D., Huang, C.C., Couch, G.S., Greenblatt, D.M., Meng, E.C., Ferrin, T.E., 2004. UCSF Chimera--a visualization system for exploratory research and analysis. J. Comput. Chem. 25, 1605–1612. https://doi.org/10.1002/jcc.20084

Pfaendtner, J., Branduardi, D., Parrinello, M., Pollard, T.D., Voth, G.A., 2009. Nucleotide-dependent conformational states of actin. Proc. Natl. Acad. Sci. 106, 12723 LP – 12728. https://doi.org/10.1073/pnas.0902092106

Pfaendtner, J., De La Cruz, E.M., Voth, G.A., 2010a. Actin filament remodeling by actin depolymerization factor/cofilin. Proc. Natl. Acad. Sci. 107, 7299 LP – 7304. https://doi.org/10.1073/pnas.0911675107

Pfaendtner, J., Lyman, E., Pollard, T.D., Voth, G.A., 2010b. Structure and dynamics of the actin filament. J. Mol. Biol. 396, 252–263.

Pickhardt, M., Bergen, M. v, Gazova, Z., Hascher, A., Biernat, J., Mandelkow, E.-M., Mandelkow, E., 2005. Screening for inhibitors of tau polymerization. Curr. Alzheimer Res. 2, 219–226.

Plimpton, S., 1995. Fast Parallel Algorithms for Short-Range Molecular Dynamics. J. Comput. Phys. 117, 1–19. https://doi.org/https://doi.org/10.1006/jcph.1995.1039

Preuss, U., Biernat, J., Mandelkow, E.M., Mandelkow, E., 1997. The 'jaws' model of tau-microtubule interaction examined in CHO cells. J. Cell Sci. 110, 789–800.

Qian, X.S., Zhang, J.Q., Ru, C.Q., 2007. Wave propagation in orthotropic microtubules. J. Appl. Phys. 101, 84702. https://doi.org/10.1063/1.2717573

Qu, Y., Hahn, I., Webb, S.E.D., Pearce, S.P., Prokop, A., 2017. Periodic actin structures in neuronal axons are required to maintain microtubules. Mol. Biol. Cell 28, 296–308.

Rammensee, S., Janmey, P.A., Bausch, A.R., 2007. Mechanical and structural properties of in vitro neurofilament hydrogels. Eur. Biophys. J. 36, 661–668.

Rao, M. V, Houseweart, M.K., Williamson, T.L., Crawford, T.O., Folmer, J., Cleveland, D.W., 1998. Neurofilament-dependent radial growth of motor axons and axonal organization of neurofilaments does not require the neurofilament heavy subunit (NF-H) or its phosphorylation. J. Cell Biol. 143, 171–181.

Rao, M. V, Mohan, P.S., Kumar, A., Yuan, A., Montagna, L., Campbell, J., Espreafico, E.M., Julien, J.P., Nixon, R.A., 2011. The myosin Va head domain binds to the neurofilament-L rod and modulates endoplasmic reticulum (ER) content and distribution within axons. PLoS One 6, e17087.

Ravaglia, S., Bini, P., Sinforiani, E., Franciotta, D., Zardini, E., Tosca, P., Moglia, A., Costa, A., 2008. Cerebrospinal fluid levels of tau phosphorylated at threonine 181 in patients with Alzheimer's disease and vascular dementia. Neurol. Sci. 29, 417.

Rebello, C.A., Ludescher, R.D., 1998. Influence of tightly bound Mg2+ and Ca2+, nucleotides, and

phalloidin on the microsecond torsional flexibility of F-actin. Biochemistry 37, 14529–14538.

Rief, M., Pascual, J., Saraste, M., Gaub, H.E., 1999. Single molecule force spectroscopy of spectrin repeats: low unfolding forces in helix bundles. J. Mol. Biol. 286, 553–561.

Robertson, M.J., Tirado-Rives, J., Jorgensen, W.L., 2015. Improved Peptide and Protein Torsional Energetics with the OPLS-AA Force Field. J. Chem. Theory Comput. 11, 3499–3509. https://doi.org/10.1021/acs.jctc.5b00356

Rodney, D., Fivel, M., Dendievel, R., 2005. Discrete Modeling of the Mechanics of Entangled Materials. Phys. Rev. Lett. 95, 108004. https://doi.org/10.1103/PhysRevLett.95.108004

Rosenberg, K.J., Ross, J.L., Feinstein, H.E., Feinstein, S.C., Israelachvili, J., 2008. Complementary dimerization of microtubule-associated tau protein: Implications for microtubule bundling and tau-mediated pathogenesis. Proc. Natl. Acad. Sci. 105, 7445–7450.

Rosengren, L.E., Karlsson, Jan-Erik, Karlsson, Jan-Olof, Persson, L.I., Wikkelsø, C., 1996. Patients with amyotrophic lateral sclerosis and other neurodegenerative diseases have increased levels of neurofilament protein in CSF. J. Neurochem. 67, 2013–2018.

Roy, S., 2016. Waves, rings, and trails: The scenic landscape of axonal actin. J. Cell Biol. 212, 131.

Ruben, G.C., Iqbal, K., Grundke-Iqbal, I., Johnson Jr, J.E., 1993. The organization of the microtubule associated protein tau in Alzheimer paired helical filaments. Brain Res. 602, 1–13.

Rudrabhatla, P., Jaffe, H., Pant, H.C., 2011. Direct evidence of phosphorylated neuronal intermediate filament proteins in neurofibrillary tangles (NFTs): phosphoproteomics of Alzheimer's NFTs. FASEB J. 25, 3896–3905.

Runge, M.S., Laue, T.M., Yphantis, D.A., Lifsics, M.R., Saito, A., Altin, M., Reinke, K., Williams, R.C., 1981. ATP-induced formation of an associated complex between microtubules and neurofilaments. Proc. Natl. Acad. Sci. 78, 1431–1435.

Rycroft, C., 2009. Voro++: a three-dimensional Voronoi cell library in C++. United States. https://doi.org/10.2172/946741

Samsonov, A., Yu, J.-Z., Rasenick, M., Popov, S. V, 2004. Tau interaction with microtubules in vivo. J. Cell Sci. 117, 6129 LP – 6141. https://doi.org/10.1242/jcs.01531

Sandersius, S.A., Newman, T.J., 2008. Modeling cell rheology with the Subcellular Element Model. Phys. Biol. 5, 15002. https://doi.org/10.1088/1478-3975/5/1/015002

Sandvold, M.L., Mikkelsen, A., Elgsaeter, A., 1989. Frequency dependence of the shear moduli of spectrin studied using a multiple lumped resonator viscoelastometer. Acta Chem Scand 43, 783–786.

Santarella, R.A., Skiniotis, G., Goldie, K.N., Tittmann, P., Gross, H., Mandelkow, E.-M., Mandelkow, E., Hoenger, A., 2004. Surface-decoration of Microtubules by Human Tau. J. Mol. Biol. 339, 539–553. https://doi.org/https://doi.org/10.1016/j.jmb.2004.04.008

Sato, M., Leimbach, G., Schwarz, W.H., Pollard, T.D., 1985. Mechanical properties of actin. J. Biol. Chem. 260, 8585–8592.

Sato, M., Schwarz, W.H., Pollard, T.D., 1987. Dependence of the mechanical properties of actin/α-actinin gels on deformation rate. Nature 325, 828–830. https://doi.org/10.1038/325828a0

Saunders, M.G., Voth, G.A., 2012. Comparison between Actin Filament Models: Coarse-Graining Reveals Essential Differences. Structure 20, 641–653. https://doi.org/https://doi.org/10.1016/j.str.2012.02.008

Schaap, I.A.T., Carrasco, C., de Pablo, P.J., MacKintosh, F.C., Schmidt, C.F., 2006. Elastic Response, Buckling, and Instability of Microtubules under Radial Indentation. Biophys. J. 91, 1521–1531. https://doi.org/https://doi.org/10.1529/biophysj.105.077826

Schanus, E., Booth, S., Hallaway, B., Rosenberg, A., 1985. The elasticity of spectrin-actin gels at high

protein concentration. J. Biol. Chem. 260, 3724–3730.

Schmoller, K.M., Lieleg, O., Bausch, A.R., 2009. Structural and viscoelastic properties of actin/filamin networks: cross-linked versus bundled networks. Biophys. J. 97, 83–89.

Schramm, A.C., Hocky, G.M., Voth, G.A., Blanchoin, L., Martiel, J.-L., De La Cruz, E.M., 2017. Actin Filament Strain Promotes Severing and Cofilin Dissociation. Biophys. J. 112, 2624–2633. https://doi.org/https://doi.org/10.1016/j.bpj.2017.05.016

Scott, C.W., Blowers, D.P., Barth, P.T., Lo, M.M.S., Salama, A.I., Caputo, C.B., 1991. Differences in the abilities of human tau isoforms to promote microtubule assembly. J. Neurosci. Res. 30, 154–162. https://doi.org/10.1002/jnr.490300116

Scott, K.A., Batey, S., Hooton, K.A., Clarke, J., 2004. The folding of spectrin domains I: wild-type domains have the same stability but very different kinetic properties. J. Mol. Biol. 344, 195–205.

Seidler, P.M., Boyer, D.R., Rodriguez, J.A., Sawaya, M.R., Cascio, D., Murray, K., Gonen, T., Eisenberg, D.S., 2018. Structure-based inhibitors of tau aggregation. Nat. Chem. 10, 170.

Selkoe, D.J., 1991. The molecular pathology of Alzheimer's disease. Neuron 6, 487–498.

Senftle, T.P., Hong, S., Islam, M.M., Kylasa, S.B., Zheng, Y., Shin, Y.K., Junkermeier, C., Engel-Herbert, R., Janik, M.J., Aktulga, H.M., 2016. The ReaxFF reactive force-field: development, applications and future directions. npj Comput. Mater. 2, 1–14.

Sept, D., Baker, N.A., McCammon, J.A., 2003. The physical basis of microtubule structure and stability. Protein Sci. 12, 2257–2261. https://doi.org/10.1110/ps.03187503

Sept, D., MacKintosh, F.C., 2010. Microtubule elasticity: connecting all-atom simulations with continuum mechanics. Phys. Rev. Lett. 104, 18101.

SERRANO, L., MONTEJO DE GARCINI, E., HERNÁNDEZ, M.A., AVILA, J., 1985. Localization of

the tubulin binding site for tau protein. Eur. J. Biochem. 153, 595–600.

Setayandeh, S.S., Lohrasebi, A., 2016. Multi scale modeling of 2450 MHz electric field effects on microtubule mechanical properties. J. Mol. Graph. Model. 70, 122–128.

Seubert, P., Mawal-Dewan, M., Barbour, R., Jakes, R., Goedert, M., Johnson, G.V.W., Litersky, J.M., Schenk, D., Lieberburg, I., Trojanowski, J.Q., 1995. Detection of phosphorylated Ser262 in fetal tau, adult tau, and paired helical filament tau. J. Biol. Chem. 270, 18917–18922.

Shahinnejad, A., Haghpanahi, M., Farmanzad, F., 2013. Finite Element Analysis of Axonal Microtubule Bundle under Tension and Torsion. Procedia Eng. 59, 16–24. https://doi.org/https://doi.org/10.1016/j.proeng.2013.05.088

Shamloo, A., Manuchehrfar, F., Rafii-Tabar, H., 2015. A viscoelastic model for axonal microtubule rupture. J. Biomech. 48, 1241–1247.

Sharma, P., Barchi, J.J., Huang, X., Amin, N.D., Jaffe, H., Pant, H.C., 1998. Site-specific phosphorylation of Lys-Ser-Pro repeat peptides from neurofilament H by cyclin-dependent kinase 5: structural basis for substrate recognition. Biochemistry 37, 4759–4766.

Shen, H.-S., 2010a. Buckling and postbuckling of radially loaded microtubules by nonlocal shear deformable shell model. J. Theor. Biol. 264, 386–394. https://doi.org/https://doi.org/10.1016/j.jtbi.2010.02.014

Shen, H.-S., 2010b. Nonlocal shear deformable shell model for postbuckling of axially compressed microtubules embedded in an elastic medium. Biomech. Model. Mechanobiol. 9, 345–357. https://doi.org/10.1007/s10237-009-0180-3

Shen, H.-S., 2010c. Nonlocal shear deformable shell model for bending buckling of microtubules embedded in an elastic medium. Phys. Lett. A 374, 4030–4039. https://doi.org/https://doi.org/10.1016/j.physleta.2010.08.006

Shi, Y.J., Guo, W.L., Ru, C.Q., 2008. Relevance of Timoshenko-beam model to microtubules of low shear modulus. Phys. E Low-dimensional Syst. Nanostructures 41, 213–219.

Shultz, S.R., Wright, D.K., Zheng, P., Stuchbery, R., Liu, S.-J., Sashindranath, M., Medcalf, R.L., Johnston, L.A., Hovens, C.M., Jones, N.C., 2015. Sodium selenate reduces hyperphosphorylated tau and improves outcomes after traumatic brain injury. Brain 138, 1297–1313.

Sidenstein, S.C., D'Este, E., Böhm, M.J., Danzl, J.G., Belov, V.N., Hell, S.W., 2016. Multicolour Multilevel STED nanoscopy of Actin/Spectrin Organization at Synapses. Sci. Rep. 6, 26725. https://doi.org/10.1038/srep26725

Sihag, R.K., Nixon, R.A., 1989. In vivo phosphorylation of distinct domains of the 70-kilodalton neurofilament subunit involves different protein kinases. J. Biol. Chem. 264, 457–464.

Silber, J., Cotton, J., Nam, J.-H., Peterson, E.H., Grant, W., 2004. Computational models of hair cell bundle mechanics: III. 3-D utricular bundles. Hear. Res. 197, 112–130. https://doi.org/https://doi.org/10.1016/j.heares.2004.06.006

Sim, H., Sept, D., 2013. Properties of Microtubules with Isotropic and Anisotropic Mechanics. Cell. Mol. Bioeng. 6, 361–368. https://doi.org/10.1007/s12195-013-0302-y

Sjögren, M., Davidsson, P., Tullberg, M., Minthon, L., Wallin, A., Wikkelso, C., Granérus, A.-K., Vanderstichele, H., Vanmechelen, E., Blennow, K., 2001. Both total and phosphorylated tau are increased in Alzheimer's disease. J. Neurol. Neurosurg. Psychiatry 70, 624–630.

Smith, A.S., Nowak, R.B., Zhou, S., Giannetto, M., Gokhin, D.S., Papoin, J., Ghiran, I.C., Blanc, L., Wan, J., Fowler, V.M., 2018. Myosin IIA interacts with the spectrin-actin membrane skeleton to control red blood cell membrane curvature and deformability. Proc. Natl. Acad. Sci. 115, E4377 LP-E4385. https://doi.org/10.1073/pnas.1718285115

Sochocka, M., Ochnik, M., Sobczyński, M., Siemieniec, I., Orzechowska, B., Naporowski, P., Leszek, J.,

2019. New therapeutic targeting of Alzheimer's disease with the potential use of proline-rich polypeptide complex to modulate an innate immune response-preliminary study. J. Neuroinflammation 16, 137.

Soheilypour, M., Peyro, M., Peter, S.J., Mofrad, M.R.K., 2015. Buckling behavior of individual and bundled microtubules. Biophys. J. 108, 1718–1726.

SONCINI, M., VOTTA, E., APRODU, I., ENEMARK, S., REDAELLI, A., DERIU, M.A., MONTEVECCHI, F.M., 2009. MICROTUBULE-KINESIN MECHANICS BY MOLECULAR MODELING. Biophys. Rev. Lett. 04, 45–61. https://doi.org/10.1142/S1793048009000922

Splettstoesser, T., Holmes, K.C., Noé, F., Smith, J.C., 2011. Structural modeling and molecular dynamics simulation of the actin filament. Proteins Struct. Funct. Bioinforma. 79, 2033–2043.

Stevens, M.J., Hoh, J.H., 2011. Interactions between planar grafted neurofilament side-arms. J. Phys. Chem. B 115, 7541–7549.

Stevens, M.J., Hoh, J.H., 2010. Conformational dynamics of neurofilament side-arms. J. Phys. Chem. B 114, 8879–8886.

Stevenson, W., Chang, R., Gebremichael, Y., 2011. Phosphorylation-mediated conformational changes in the mouse neurofilament architecture: insight from a neurofilament brush model. J. Mol. Biol. 405, 1101–1118.

Stokke, B.T., Mikkelsen, A., Elgsaeter, A., 1986. Spectrin, human erythrocyte shapes, and mechanochemical properties. Biophys. J. 49, 319–327.

Stokke, B.T., Mikkelsen, A., Elgsaeter, A., 1985. Some viscoelastic properties of human erythrocyte spectrin networks end-linked in vitro. Biochim. Biophys. Acta (BBA)-Biomembranes 816, 111–121.

Stolarski, T., Nakasone, Y., Yoshimoto, S., 2018. Engineering analysis with ANSYS software. Butterworth-Heinemann.

Stricker, J., Falzone, T., Gardel, M.L., 2010. Mechanics of the F-actin cytoskeleton. J. Biomech. 43, 9–14.

Stukowski, A., 2010. Visualization and analysis of atomistic simulation data with OVITO–the Open Visualization Tool. Model. Simul. Mater. Sci. Eng. 18, 015012. https://doi.org/10.1088/0965-0393/18/1/015012

Suresh, S., 2007. Biomechanics and biophysics of cancer cells. Acta Mater. 55, 3989–4014.

Svetina, S., Kokot, G., Kebe, T.Š., Žekš, B., Waugh, R.E., 2016. A novel strain energy relationship for red blood cell membrane skeleton based on spectrin stiffness and its application to micropipette deformation. Biomech. Model. Mechanobiol. 15, 745–758.

Szaro, B.G., Strong, M.J., 2010. Post-transcriptional control of neurofilaments: New roles in development, regeneration and neurodegenerative disease. Trends Neurosci. 33, 27–37.

Tang-Schomer, M.D., Patel, A.R., Baas, P.W., Smith, D.H., 2010. Mechanical breaking of microtubules in axons during dynamic stretch injury underlies delayed elasticity, microtubule disassembly, and axon degeneration. FASEB J. 24, 1401–1410.

Taylor, P.A., Ford, C.C., 2009. Simulation of blast-induced early-time intracranial wave physics leading to traumatic brain injury. J. Biomech. Eng. 131, 61007.

Theisen, K.E., Desai, N.J., Volski, A.M., Dima, R.I., 2013. Mechanics of severing for large microtubule complexes revealed by coarse-grained simulations. J. Chem. Phys. 139, 09B629_1.

Theisen, K.E., Zhmurov, A., Newberry, M.E., Barsegov, V., Dima, R.I., 2012. Multiscale modeling of the nanomechanics of microtubule protofilaments. J. Phys. Chem. B 116, 8545–8555.

Tolomeo, J.A., Holley, M.C., 1997. Mechanics of microtubule bundles in pillar cells from the inner ear. Biophys. J. 73, 2241–2247. https://doi.org/https://doi.org/10.1016/S0006-3495(97)78255-9

Trinczek, B., Biernat, J., Baumann, K., Mandelkow, E.M., Mandelkow, E., 1995. Domains of tau protein, differential phosphorylation, and dynamic instability of microtubules. Mol. Biol. Cell 6, 1887–1902. https://doi.org/10.1091/mbc.6.12.1887

Tsuda, Y., Yasutake, H., Ishijima, A., Yanagida, T., 1996. Torsional rigidity of single actin filaments and actin–actin bond breaking force under torsion measured directly by in vitro micromanipulation. Proc. Natl. Acad. Sci. 93, 12937–12942.

Tuszyński, J.A., Brown, J.A., Crawford, E., Carpenter, E.J., Nip, M.L.A., Dixon, J.M., Satarić, M. V, 2005a. Molecular dynamics simulations of tubulin structure and calculations of electrostatic properties of microtubules. Math. Comput. Model. 41, 1055–1070. https://doi.org/https://doi.org/10.1016/j.mcm.2005.05.002

Tuszyński, J.A., Luchko, T., Portet, S., Dixon, J.M., 2005b. Anisotropic elastic properties of microtubules. Eur. Phys. J. E 17, 29–35. https://doi.org/10.1140/epje/i2004-10102-5

Tzikang, C., 2000. Determining a Prony series for a viscoelastic material from time varying strain data.

Unsain, N., Bordenave, M.D., Martinez, G.F., Jalil, S., Von Bilderling, C., Barabas, F.M., Masullo, L.A., Johnstone, A.D., Barker, P.A., Bisbal, M., 2018a. Remodeling of the actin/spectrin membrane-associated periodic skeleton, growth cone collapse and F-actin decrease during axonal degeneration. Sci. Rep. 8, 1–16.

Unsain, N., Stefani, F.D., Cáceres, A., 2018b. The actin/spectrin membrane-associated periodic skeleton in neurons. Front. Synaptic Neurosci. 10, 10.

Unterberger, M.J., Schmoller, K.M., Bausch, A.R., Holzapfel, G.A., 2013a. A new approach to model cross-linked actin networks: multi-scale continuum formulation and computational analysis. J. Mech. Behav. Biomed. Mater. 22, 95–114.

Unterberger, M.J., Schmoller, K.M., Wurm, C., Bausch, A.R., Holzapfel, G.A., 2013b. Viscoelasticity of

cross-linked actin networks: Experimental tests, mechanical modeling and finite-element analysis. Acta Biomater. 9, 7343–7353. https://doi.org/https://doi.org/10.1016/j.actbio.2013.03.008

Uversky, V.N., 2010. Targeting intrinsically disordered proteins in neurodegenerative and protein dysfunction diseases: another illustration of the D2 concept. Expert Rev. Proteomics 7, 543–564.

van den Bedem, H., Kuhl, E., 2015. Tau-ism: the Yin and Yang of microtubule sliding, detachment, and rupture. Biophys. J. 109, 2215.

VanBuren, V., Cassimeris, L., Odde, D.J., 2005. Mechanochemical Model of Microtubule Structure and Self-Assembly Kinetics. Biophys. J. 89, 2911–2926. https://doi.org/https://doi.org/10.1529/biophysj.105.060913

Vanmechelen, E., Vanderstichele, H., Davidsson, P., Van Kerschaver, E., Van Der Perre, B., Sjögren, M., Andreasen, N., Blennow, K., 2000. Quantification of tau phosphorylated at threonine 181 in human cerebrospinal fluid: a sandwich ELISA with a synthetic phosphopeptide for standardization. Neurosci. Lett. 285, 49–52.

Viel, A., 1999. K-Actinin and spectrin structures: an unfolding family story. FEBS Lett. 460, 394.

Vogt, B., 2008. Atomistic-based continuum constitutive relation for microtubules: elastic modulus prediction.

Vorobiev, S., Strokopytov, B., Drubin, D.G., Frieden, C., Ono, S., Condeelis, J., Rubenstein, P.A., Almo, S.C., 2003. The structure of nonvertebrate actin: implications for the ATP hydrolytic mechanism. Proc. Natl. Acad. Sci. 100, 5760–5765.

Wada, H., Netz, R.R., 2006. Non-equilibrium hydrodynamics of a rotating filament. EPL (Europhysics Lett. 75, 645.

Wagner, O.I., Rammensee, S., Korde, N., Wen, Q., Leterrier, J.-F., Janmey, P.A., 2007. Softness, strength and self-repair in intermediate filament networks. Exp. Cell Res. 313, 2228–2235.

Wakabayashi, K., Sugimoto, Y., Tanaka, H., Ueno, Y., Takezawa, Y., Amemiya, Y., 1994a. X-ray diffraction evidence for the extensibility of actin and myosin filaments during muscle contraction. Biophys. J. 67, 2422–2435. https://doi.org/https://doi.org/10.1016/S0006-3495(94)80729-5

Wakabayashi, K., Sugimoto, Y., Tanaka, H., Ueno, Y., Takezawa, Y., Amemiya, Y., 1994b. X-ray diffraction evidence for the extensibility of actin and myosin filaments during muscle contraction. Biophys. J. 67, 2422–2435. https://doi.org/https://doi.org/10.1016/S0006-3495(94)80729-5

Wang, C.Y., Ru, C.Q., Mioduchowski, A., 2006a. Vibration of microtubules as orthotropic elastic shells. Phys. E Low-dimensional Syst. Nanostructures 35, 48–56.

Wang, C.Y., Ru, C.Q., Mioduchowski, A., 2006b. Orthotropic elastic shell model for buckling of microtubules. Phys. Rev. E 74, 52901.

Wang, C.Y., Zhang, L.C., 2008. Circumferential vibration of microtubules with long axial wavelength. J. Biomech. 41, 1892–1896. https://doi.org/https://doi.org/10.1016/j.jbiomech.2008.03.029

Wang, G., Simon, D.J., Wu, Z., Belsky, D.M., Heller, E., O'Rourke, M.K., Hertz, N.T., Molina, H., Zhong, G., Tessier-Lavigne, M., 2019. Structural plasticity of actin-spectrin membrane skeleton and functional role of actin and spectrin in axon degeneration. Elife 8, e38730.

Wang, H., Wu, M., Zhan, C., Ma, E., Yang, M., Yang, X., Li, Y., 2012. Neurofilament proteins in axonal regeneration and neurodegenerative diseases. Neural Regen. Res. 7, 620.

Wang, J., Wolf, R.M., Caldwell, J.W., Kollman, P.A., Case, D.A., 2004. Development and testing of a general amber force field. J. Comput. Chem. 25, 1157–1174.

Watanabe, A., Hasegawa, M., Suzuki, M., Takio, K., Morishima-Kawashima, M., Titani, K., Arai, T., Kosik, K.S., Ihara, Y., 1993. In vivo phosphorylation sites in fetal and adult rat tau. J. Biol. Chem. 268, 25712–25717.

Wegmann, S., Schöler, J., Bippes, C.A., Mandelkow, E., Muller, D.J., 2011. Competing interactions

stabilize pro-and anti-aggregant conformations of human Tau. J. Biol. Chem. 286, 20512–20524.

Wells, D.B., Aksimentiev, A., 2010. Mechanical properties of a complete microtubule revealed through molecular dynamics simulation. Biophys. J. 99, 629–637.

Wen, G.Y., Wisniewski, H.M., 1984. Substructures of neurofilaments. Acta Neuropathol. 64, 339–343.

Witek, M.A., Fung, L.W.-M., 2013. Quantitative studies of caspase-3 catalyzed αII-spectrin breakdown. Brain Res. 1533, 1–15. https://doi.org/https://doi.org/10.1016/j.brainres.2013.08.010

Wu, J.Z., Herzog, W., Epstein, M., 1997. Evaluation of the finite element software ABAQUS for biomechanical modelling of biphasic tissues. J. Biomech. 31, 165–169.

Wu, S., Zhang, Y., 2007. LOMETS: a local meta-threading-server for protein structure prediction. Nucleic Acids Res. 35, 3375–3382.

Wu, Y.-T., Adnan, A., 2018. Damage and failure of axonal microtubule under extreme high strain rate: an in-silico molecular dynamics study. Sci. Rep. 8, 12260.

Wu, Z., Nogales, E., Xing, J., 2012. Comparative studies of microtubule mechanics with two competing models suggest functional roles of alternative tubulin lateral interactions. Biophys. J. 102, 2687–2696.

Wu, Z., Wang, H.-W., Mu, W., Ouyang, Z., Nogales, E., Xing, J., 2009. Simulations of Tubulin Sheet Polymers as Possible Structural Intermediates in Microtubule Assembly. PLoS One 4, e7291.

Xiang, P., Liew, K.M., 2013. A computational framework for transverse compression of microtubules based on a higher-order Cauchy–Born rule. Comput. Methods Appl. Mech. Eng. 254, 14–30. https://doi.org/https://doi.org/10.1016/j.cma.2012.10.013

Xiang, P., Liew, K.M., 2012. Dynamic behaviors of long and curved microtubules based on an atomistic-continuum model. Comput. Methods Appl. Mech. Eng. 223, 123–132.

Xu, J., Schwarz, W.H., Käs, J.A., Stossel, T.P., Janmey, P.A., Pollard, T.D., 1998a. Mechanical Properties of Actin Filament Networks Depend on Preparation, Polymerization Conditions, and Storage of Actin Monomers. Biophys. J. 74, 2731–2740. https://doi.org/https://doi.org/10.1016/S0006-3495(98)77979-2

Xu, J., Wirtz, D., Pollard, T.D., 1998b. Dynamic Cross-linking by α-Actinin Determines the Mechanical Properties of Actin Filament Networks. J. Biol. Chem. 273, 9570–9576.

Xu, K., Zhong, G., Zhuang, X., 2013. Actin, spectrin, and associated proteins form a periodic cytoskeletal structure in axons. Science (80-.). 339, 452–456.

Yao, N.Y., Broedersz, C.P., Lin, Y.-C., Kasza, K.E., MacKintosh, F.C., Weitz, D.A., 2010. Elasticity in ionically cross-linked neurofilament networks. Biophys. J. 98, 2147–2153.

Yates, D.M., Manser, C., De Vos, K.J., Shaw, C.E., McLoughlin, D.M., Miller, C.C.J., 2009. Neurofilament subunit (NFL) head domain phosphorylation regulates axonal transport of neurofilaments. Eur. J. Cell Biol. 88, 193–202.

Yogurtcu, O.N., Kim, J.S., Sun, S.X., 2012. A mechanochemical model of actin filaments. Biophys. J. 103, 719–727.

Yoon, G., Kwak, J., Kim, J.I., Na, S., Eom, K., 2011. Mechanical Characterization of Amyloid Fibrils Using Coarse-Grained Normal Mode Analysis. Adv. Funct. Mater. 21, 3454–3463.

Yuan, A., Rao, M. V, Nixon, R.A., 2012a. Neurofilaments at a glance.

Yuan, A., Rao, M. V, Sasaki, T., Chen, Y., Kumar, A., Liem, R.K.H., Eyer, J., Peterson, A.C., Julien, J.-P., Nixon, R.A., 2006. α-Internexin is structurally and functionally associated with the neurofilament triplet proteins in the mature CNS. J. Neurosci. 26, 10006–10019.

Yuan, A., Sasaki, T., Kumar, A., Peterhoff, C.M., Rao, M. V, Liem, R.K., Julien, J.-P., Nixon, R.A., 2012b. Peripherin is a subunit of peripheral nerve neurofilaments: implications for differential

vulnerability of CNS and peripheral nervous system axons. J. Neurosci. 32, 8501–8508.

Yuzwa, S.A., Macauley, M.S., Heinonen, J.E., Shan, X., Dennis, R.J., He, Y., Whitworth, G.E., Stubbs, K.A., McEachern, E.J., Davies, G.J., Vocadlo, D.J., 2008. A potent mechanism-inspired O-GlcNAcase inhibitor that blocks phosphorylation of tau in vivo. Nat. Chem. Biol. 4, 483.

Zakharov, P., Gudimchuk, N., Voevodin, V., Tikhonravov, A., Ataullakhanov, F.I., Grishchuk, E.L., 2015. Molecular and Mechanical Causes of Microtubule Catastrophe and Aging. Biophys. J. 109, 2574–2591. https://doi.org/https://doi.org/10.1016/j.bpj.2015.10.048

Zeiger, A.S., Layton, B.E., 2008. Molecular modeling of the axial and circumferential elastic moduli of tubulin. Biophys. J. 95, 3606–3618.

Zhang, J., Wang, C., 2014. Molecular structural mechanics model for the mechanical properties of microtubules. Biomech. Model. Mechanobiol. 13, 1175–1184.

Zhang, R., Zhang, C., Zhao, Q., Li, D., 2013. Spectrin: structure, function and disease. Sci. China Life Sci. 56, 1076–1085.

Zhang, Y., 2008. I-TASSER server for protein 3D structure prediction. BMC Bioinformatics 9, 40.

Zhang, Y., Skolnick, J., 2004a. Automated structure prediction of weakly homologous proteins on a genomic scale. Proc. Natl. Acad. Sci. 101, 7594–7599.

Zhang, Y., Skolnick, J., 2004b. SPICKER: a clustering approach to identify near-native protein folds. J. Comput. Chem. 25, 865–871.

Zhang, Y., Skolnick, J., 2004c. Scoring function for automated assessment of protein structure template quality. Proteins Struct. Funct. Bioinforma. 57, 702–710.

Zheng, X., Diraviyam, K., Sept, D., 2007. Nucleotide Effects on the Structure and Dynamics of Actin. Biophys. J. 93, 1277–1283. https://doi.org/https://doi.org/10.1529/biophysj.107.109215

Zhong, G., He, J., Zhou, R., Lorenzo, D., Babcock, H.P., Bennett, V., Zhuang, X., 2014. Developmental mechanism of the periodic membrane skeleton in axons. Elife 3, e04581. https://doi.org/10.7554/eLife.04581

Zhu, Q., Asaro, R.J., 2008. Spectrin Folding versus Unfolding Reactions and RBC Membrane Stiffness. Biophys. J. 94, 2529–2545. https://doi.org/https://doi.org/10.1529/biophysj.107.119438

Zhu, X., Raina, A.K., Rottkamp, C.A., Aliev, G., Perry, G., Boux, H., Smith, M.A., 2001. Activation and redistribution of c-jun N-terminal kinase/stress activated protein kinase in degenerating neurons in Alzheimer's disease. J. Neurochem. 76, 435–441.

Zhulina, E.B., Leermakers, F.A.M., 2010. The polymer brush model of neurofilament projections: effect of protein composition. Biophys. J. 98, 462–469.

Zhulina, E.B., Leermakers, F.A.M., 2007a. Effect of the ionic strength and pH on the equilibrium structure of a neurofilament brush. Biophys. J. 93, 1452–1463.

Zhulina, E.B., Leermakers, F.A.M., 2007b. A self-consistent field analysis of the neurofilament brush with amino-acid resolution. Biophys. J. 93, 1421–1430.

VITA

VITA

MD ISHAK KHAN

Md Ishak Khan was born in Dhaka, Bangladesh on October 11, 1991. He spent his childhood in his hometown and obtained his high school graduation from Dhaka City College. In 2009, he began his undergraduate studies at Bangladesh University of Engineering and Technology (BUET) which is considered as the top engineering institution in the nation. In September 2015, he completed his bachelor's degree in Mechanical Engineering from BUET. In Fall 2016, he joined the Multiscale Mechanics and Physics Laboratory (MMPL) to pursue his Doctor of Philosophy in Mechanical Engineering from The University of Texas at Arlington under the supervision of Professor Dr. Ashfaq Adnan (Fellow, ASME). Details of the subject matter along with the understanding of nanoscale mechanics of disordered biomolecules in brain using atomistic modeling and simulations are contained herein. Khan completed his PhD in December 2020.